^{17}O HYPERFINE SPECTROSCOPY TO INVESTIGATE WATER BINDING TO ORGANIC RADICALS

Dissertation

for the award of the degree

Doctor rerum naturalium

of the Georg-August-Universität Göttingen

within the doctoral program

Physics of Biological and Complex Systems

of the Georg-August University School of Science (GAUSS)

MAX PLANCK INSTITUTE
FOR MULTIDISCIPLINARY SCIENCES

GEORG-AUGUST-UNIVERSITÄT
GÖTTINGEN

submitted by

Fabian Hecker

from Essen

Göttingen 2022

PhD examination committee

Prof. Dr. Marina Bennati - *TAC member and 1st referee*
Research Group EPR Spectroscopy
Max Planck Intitute for multidisciplinary Sciences, Göttingen
Institute for Organic and Biomolecular Chemistry
Georg-August-Universität Göttingen

Prof. Dr. Christian Griesinger - *TAC member and 2nd referee*
Department of NMR-based Structural Biology
Max Planck Intitute for multidisciplinary Sciences, Göttingen

Prof. Dr. Martin A. Suhm - *TAC member*
Physical Chemistry II
Georg-August-Universität Göttingen

Dr. Stefan Glöggler
Research Group NMR Signal Enhancement
Center for Biostructural Imaging of Neurodegeneration, Göttingen

Prof. Dr. Kai Tittmann
Department of Molecular Enzymology
Georg-August-Universität Göttingen

Date of oral examination: May 18, 2022

Abstract

Hyperfine spectroscopy experiments detect nuclear spins around paramagnetic centers. They reveal magnetic interactions that contain valuable structural information on distance and orientation of the coupling partners. One can therefore use them, to study the magnetic nuclei in water molecules around organic radicals. Such radicals occur as important intermediates in enzymatic reactions.^{17}O is a particularly interesting target nucleus to detect water molecules, since it does not exchange with other oxygen moieties in protein environments, allowing for unambiguous assignment of spectral signatures to $H_2{}^{17}O$. It has already been used to study water coordination around transition metal ions. The low gyromagnetic ratio and high nuclear spin have, however, discouraged the use of ^{17}O hyperfine spectroscopy to study water around organic radicals so far.

This thesis shows the application of ^{17}O hyperfine spectroscopy to organic nitroxides and tyrosyl radicals. The Mims ENDOR experiment is used at 94 and 263 GHz to detect small, isotropic hyperfine couplings in a range of $0.5 - 0.7$ MHz at three trapped tyrosyl intermediates in "active" complexes of *E. coli* ribonucleotide reductase. The sharp spectral features give the first direct experimental evidence of hydrogen-bound water molecules at the radical intermediates, which are part of a long range proton-coupled electron transfer chain across different subunits of the enzyme. Small theoretical models are used to link the observed hyperfine couplings to a well defined, in-plane coordination of the water molecules. Very small amounts of spin density (~ 0.01 %) on the oxygen nucleus, facilitated by the hydrogen-bond, are enough to cause detectable hyperfine splitting in the spectra. The exquisite capability of very high-field ENDOR spectroscopy to produce narrow spectral lines is shown and rationalized, allowing a reevaluation of our previous models of the tyrosyl radical intermediate $Y^{\bullet}_{356}$.

The thesis then answers the previously open question: *Which hyperfine spectroscopy experiment is best suited to study ^{17}O water around organic radicals ?* The performance of three different types of hyperfine spectroscopy, recorded at 34 and 94 GHz EPR frequency, is compared for two nitroxide radicals as well as one tyrosyl radical. While all techniques

detect ^{17}O signals, the HYSCORE experiments at 34 GHz best show the presence of large hyperfine couplings in the range of $1 - 8$ MHz for the two nitroxide radicals. Mims ENDOR experiments at 94 GHz best reveal small, isotropic couplings of $0.6 - 0.8$ MHz for the nitroxide radical with a five-membered ring as well as the tyrosyl radical. Theoretical models and molecular dynamics simulations are used to show that large, anisotropic ^{17}O couplings correspond to out-of-plane coordination while small isotropic couplings indicate in-plane coordination for all three radicals.

All experiments performed in this thesis show that ^{17}O hyperfine spectroscopy is a well suited method to detect water molecules at organic radicals. The strong dependence of ^{17}O hyperfine coupling parameters on the hydrogen-bond geometry results in easily recognizable coupling structures, i.e. *fingerprint* signatures, of in-plane water binding.

Contents

Abbreviations and symbols

Abbreviations

2D	two-dimensional
ATP	adenosine triphosphate
BDPA	α,γ-bisdiphenylene-β-phenylallyl
CDP	cytidine diphosphate
cw	continuous wave
DFT	density functional theory
(d)ND(T)P	(deoxy) nucleoside di(tri)phosphate
DOPA	3,4-dihydroxyphenylalanine
DEER	double electron-electron resonance
EDTA	ethylenediaminetetraacetic acid
EPR	electron paramagnetic resonance
ENDOR	electron-nuclear double resonance
ESE	electron spin echo
EFG	electric field gradient
ELDOR	electron-electron double resonance
EDNMR	electron-electron double resonance detected nuclear magnetic resonance
ESEEM	electron spin echo envelope modulation
E. coli	*Escherichia coli*
FID	free inducion decay
(F)FT	(fast) Fourier transformation
FWHM	full width at half maximum
HWHM	half width at half maximum
H-bond	hydrogen-bond
HTA	high turning angle

hf	hyperfine
HEPES	4-(2-hydroxyethyl)-1-piperazineethanesulfonic acid
HYSCORE	hyperfine sublevel corrrelation spectroscopy
ID	inner diameter
mw	microwave
MD	molecular dynamics
NA	natural abundance
NMWL	nominal molecular weight limit
NMR	nuclear magnetic resonance
NRMSD	normalized root mean square deviation
OEC	oxygen-evolving complex
OD	outer diameter
PAS	principle axis system
P.D.	point dipole
PELDOR	pulsed electron double resonance
PSII	photosystem II
PC	paramagnetic center
PCET	proton-coupled electron transfer
PS	polystyrene
rf	radio-frequency
RNR	ribonucleotide reductase
RT	radical transfer
SAM	S-adenosyl-L-methionine
SDSL	site-directed spin labelling
SG	Savitzky-Golay
SRT	shot repetition time
TEMPOL	4-hydroxy-2,2,6,6-tetramethylpiperidin-1-oxy
TEMPYL	3-Hydroxymethyl-(1-oxy-2,2,5,5-tetramethylpyrroline)
TM	transition metal
UAA	unnatural amino acid
wt	wild type
X-band	$8 - 12\,\mathrm{GHz}$
Q-band	$26 - 40\,\mathrm{GHz}$
W-band	$75 - 110\,\mathrm{GHz}$
mm-band	$110 - 300\,\mathrm{GHz}$

Symbols

$\hat{H}$	spin Hamiltonian in energy units
$\hat{\mathcal{H}}$	spin Hamiltonian in angular frequency units ($\hat{H}/\hbar$)
$\hat{H}_0$,$\hat{\mathcal{H}}_0$	static spin Hamiltonian
$\hat{H}_1$,$\hat{\mathcal{H}}_1$	microwave (perturbation) spin Hamiltonian
S,m_S	electron sin quantum number and corresponding projection quantum number
$\hat{\boldsymbol{S}}$,$\hat{S}_{x,y,z}$	electron spin angular momentum operator and individual components
I,m_I	electron sin quantum number and corresponding projection quantum number
$\hat{\boldsymbol{I}}$,$\hat{I}_{x,y,z}$	electron spin angular momentum operator and individual components
tr{}	trace of a matrix
T	Temperature
k_B	*Boltzmann* constant
μ_B	*Bohr* magneton
μ_N	Nuclear magneton
h	*Planck* constant
$\hbar$	reduced *Planck* constant
g_e	g-value of a free electron
g_n	g-value of a nucleus
γ_e	gyromagnetic ratio of an electron
γ_n	gyromagnetic ratio of a nucleus
μ_0	Vacuum permeability
$\boldsymbol{B}$	static magnetic field vector
B_0	static magnetic field amplitude
B_1	microwave field amplitude
B_2	radio-frequency field amplitude
ω_S	electron Zeeman/Larmor frequency
ω_I	nuclear Zeeman/Larmor frequency
ω_0	resonance frequency
ω_mw	microwave frequency
ω_rf	radiowave frequency
ω_1	electron *Rabi* nutation frequency
ω_2	nuclear *Rabi* nutation frequency
$\mathbb{1}$	identity matrix
$\boldsymbol{g}$, $g_{1,2,3}$	g-tensor and principle axis values
g_iso	isotropic g-value
$\boldsymbol{A}$, $A_{1,2,3}$	hyperfine coupling tensor and principle axis values

$\boldsymbol{T}$	dipolar hyperfine coupling tensor
A,B	secular and pseudo-secular hyperfine coupling constant
a_{iso}	isotropic hyperfine coupling constant
$\boldsymbol{P}$, $P_{1,2,3}$	quadrupole coupling tensor and principle axis values
eq	electric field gradient
eQ	quadrupole moment
$\hat{\sigma}$	density operator
$\hat{\sigma}_{\mathrm{eq}}$	thermal equilibrium density operator
$\hat{\sigma}_0$	density operator at the beginning of pulse sequences
$\hat{U}$	propagator
$\boldsymbol{R}$	rotation matrix
$T_{1\mathrm{e}}$	longitudinal relaxation time of electron spins
$T_{2\mathrm{e}}$	transverse relaxation time of electron spins
T_{m}	phase memory time
$\mathcal{P}$	fractional population
p	transition matrix element

List of figures

List of tables

1 Introduction

The interaction between electron and nuclear spins is called hyperfine (hf) interaction. Hyperfine interactions contain valuable information about the relative distance and orientation of the coupled spins and typically lie in the radio- to microwave frequency range, i.e. MHz to GHz. Nuclear magnetic resonance (NMR) and electron paramagnetic resonance (EPR) spectroscopy, which operate in these frequency ranges and directly detect either nuclear or electron magnetic moments, are therefore the techniques of choice to resolve hyperfine interactions. A large variety of NMR techniques has been developed to detect the influence of hyperfine coupling on magnetic nuclei.[1,2] However, fast electron relaxation and strong electron-nuclear interaction complicate the detection of closely bound nuclei around paramagnetic centers (PC). EPR spectroscopy can harness the large magnetic moment of electron spins for signal detection as well as cope with their fast relaxation times and is consequently often the method of choice. In many cases, hyperfine interactions strongly influence the lineshape of EPR spectra and can be resolved as distinct singularities. The large abundance of nuclear spins around PCs in bulk samples can, however, significantly complicate the assignment of spectral signatures and lead to broadened EPR spectra, from which an analysis of the hf structure becomes impossible.

A subset of EPR experiments, termed hyperfine spectroscopy, has therefore been specifically designed to detect the hyperfine coupled nuclei. The first among them was continuous wave (cw) electron-nuclear double resonance (ENDOR), in which electrons and nuclei are separately manipulated by microwave (mw) and radio-frequency (rf) irradiation.[3] The development of pulsed microwave technology led to the Mims[4] and Davies[5] ENDOR experiments, in which the spin system is manipulated by short mw and rf pulses on the nanosecond and microsecond scale, respectively. Subsequently, electron spin-echo envelope modulation (ESEEM) with its two-dimensional variant hyperfine sublevel correlation spectroscopy (HYSCORE),[6,7] as well as electron-electron double resonance detected NMR (EDNMR)[8] were introduced. Both techniques utilize only microwave pulses and rely on the excitation and detection of forbidden EPR transitions to detect nuclear resonance

frequencies. Technological advancements continue to drive the research in hyperfine spectroscopy methods, which now utilize high-powered microwave sources at frequencies of 34 GHz and higher,[9,10] broadband excitation with arbitrary waveform generators[11] and high-field EPR at frequencies of up to 263 GHz.[12–16]

Hyperfine spectroscopy has been applied in a large variety of systems to investigate the structure of nuclei around paramagnetic centers. Biological systems such as large enzymes are of particular interest, since they often contain PCs in the form of transition metal ions or highly reactive radical intermediates. A few recent examples[(a)] that highlight the application of hf spectroscopy in biological machines are studies of photosystem II (PSII),[17,18] nitrogenase,[19] [FeFe] hydrogenases,[20,21] radical S-adenosyl-L-mehionine (SAM) enzymes,[22,23] and ribonucleotide reductases (RNR).[24–28]

One aspect of structural biology, which has gained significant interest in recent years, is the involvement of water molecules in biological transformations (Figure 1.1).[29] Especially the involvement in electron transfer processes,[30–33] proton-wires[34–36] and proton-coupled electron transfer (PCET)[24,25,37,38] has been studied. The identification of internal waters in proteins can be achieved by X-ray crystallography.[39–41] The crystallization of transient

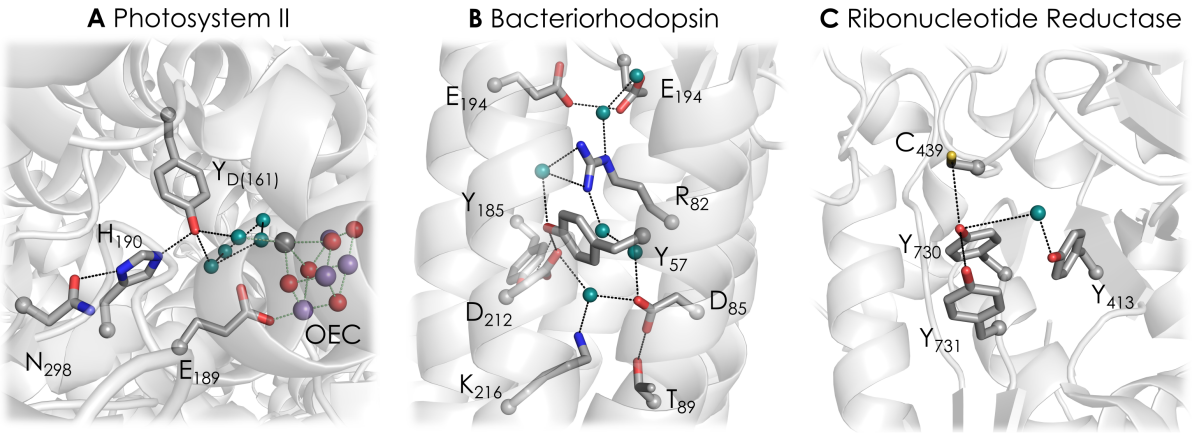

Figure 1.1: Water molecules (cyan) in important biological machines. **A**: Water-cluster between the oxygen-evolving complex (OEC) and the mechanistically relevant tyrosine D (Y_D) in PSII (pdb: 3WU2).[37,41] **B**: Proton-wire in bacteriorhodopsin (pdb: 1C3W).[34] **C**: Water molecule at the PCET pathway residue Y_{730} in the isolated α-subunit of *E. coli* class Ia ribonucleotide reductase (pdb:1RLR).[39] Hydrogen bonds are indicated with black dotted lines.

protein complexes is however difficult. Hyperfine sprctrosopy, on the other hand, is not limited to protein crystals as it can detect PCs in frozen solutions. The use of hyperfine spectroscopy to detect water molecules requires a careful choice of the target nucleus. Water offers three options of detectable nuclear spins: ^{1}H, ^{2}H and ^{17}O.[(b)] The ^{1}H nucleus has almost 100 % natural abundance (NA) and the largest gyromagnetic ratio, but it's

[(a)] This list is by no means complete and is limited to the last decade.
[(b)] Not counting the radioactive ^{3}H nucleus for practical purposes.

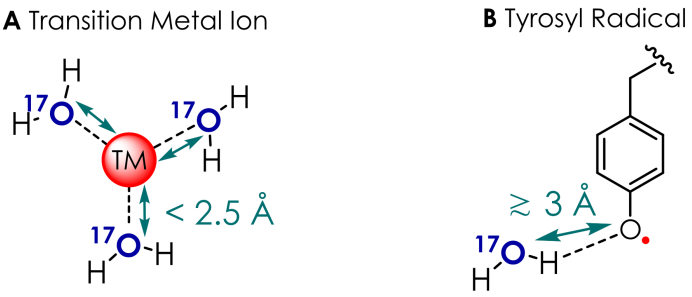

Figure 1.2: Water coordination to transition metal ions (**A**) and organic radicals (**B**). Direct coordination to TM via the ^{17}O atom results in short ($< 2.5\,Å$) PC···O_{H_2O} distances (cyan) while hydrogen-bond coordination to organic radicals leads to longer ($\gtrsim 3\,Å$) PC···O_{H_2O} distances.

abundance in any bulk system can make signal assignment to water molecules ambiguous. The ^{2}H nucleus offers increased specificity due to its low NA ($\sim 0.01\,\%$) and is readily introduced into bulk systems by buffer exchange. Nevertheless, its tendency for fast exchange with amino- or hydroxyl-hydrogens leaves a small uncertainty in the assessment of spectral signatures. The ^{17}O nucleus has a similarly low NA ($\sim 0.04\,\%$) but shows very slow chemical exchange with other organic molecules,[42] offering the high specificity needed to unambiguously assign spectral signatures to ^{17}O-labelled water molecules. Two important properties of the ^{17}O nucleus challenge the acquisition and interpretation of hf spectra: Firstly, it's low gyromagnetic ratio ($\gamma_{^1H}/\gamma_{^{17}O} \approx 7.4$)[43] leading to low sensitivity and secondly, it's high nuclear spin ($I = 5/2$) leading to a large number of signals as well as quadrupolar signal broadening.

Despite these drawbacks, the ability to directly link spectral ^{17}O signatures to isotopically-labelled $H_2{}^{17}O$ water molecules has inspired hf spectroscopy studies of transition metal (TM)-water complexes with ENDOR,[44,45] EDNMR[46,47] and ESEEM[48,49] experiments. Similar studies of water molecules coordinated to organic radicals as paramagnetic centers have been scarce. A single EDNMR study has so far used of ^{17}O water to determine the hydration state of a nitroxide radical. But hyperfine couplings were neither reported nor resolved in the EDNMR or ENDOR spectra.[50] This lack of detection is related to the different coordination geometry of water molecules to transition metals vs. organic radicals (see Fig. 1.2). TMs usually directly coordinate the oxygen nucleus at short PC···O_{H_2O} distances, resulting in large hyperfine couplings. Organic radicals, on the other hand, coordinate water via hydrogen-bonds, leading to longer PC···O_{H_2O} distances and smaller couplings which are intrinsically harder to detect

The motivation to explore ^{17}O hyperfine spectroscopy for organic radicals came from a previous ENDOR study of a radical intermediate in the active enzyme complex of *Escherichia coli* (*E. coli*) class Ia ribonucleotide reductase. It showed the spectroscopic signature of hydrogen-bound ^{1}H nuclei, which were proposed to originate from two coordinated

water molecules to the essential tyrosyl radical.[26] The water molecules were deemed mechanistically relevant for the proton-coupled electron transfer mechanism of the enzyme. The open question remained: *Can we give direct experimental evidence for water binding?* Prior to this work, it was not clear whether ^{17}O hyperfine couplings to organic radicals can be resolved and if so, which method is best suited to the task. This thesis shows the journey towards the answer:

Chapter 2 gives a general theoretical description of coupled electron-nuclear spin systems and the different hyperfine spectroscopy experiments to investigate them. It also highlights important aspects for their application to the ^{17}O nucleus.

Chapter 3 gives a brief overview of the materials and methods used throughout the thesis.

Chapter 4 describes the development of numerical simulation algorithms for ^{17}O ENDOR spectra to understand and compare state-of-the-art simulation programs used by the EPR community.

Chapter 5 gives an introduction into the world of *E. coli* ribonucleotide reductase with a brief overview of the current mechanistic understanding. It then shows the application of Mims ENDOR spectroscopy at 94 and 263 GHz to detect ^{17}O-labelled water hydrogen-bound to three tyrosyl radical intermediates in the RNR enzyme. Small density functional theory (DFT) models of the tyrosyl and amino-tyrosyl radicals are introduced. They link the spectroscopic results to a clearly defined binding structure of the water molecules in the plane of the radicals. This part of the chapter has been published in the *Journal of the American Chemical Society*. The final part of this chapter gives additional information on the analysis of ^{17}O Mims ENDOR spectra and show how the new spectroscopic and structural information may be used for models of the radical intermediates in RNR.

Chapter 6 shows an optimization and comparison of the three hyperfine spectroscopy techniques HYSCORE, EDNMR and ENDOR. Experiments performed at 34 and 94 GHz EPR frequency with samples of three different, biologically relevant, organic radicals in ^{17}O-labelled water are displayed and explained. Distinct differences and similarities in the spectroscopic signatures of water molecules coordinated to nitroxides and tyrosyl radicals are discussed. The same DFT methodology is used to rationalize the observed hyperfine couplings and derive a clearly defined hydrogen-bond structure around the tyrosyl radical vs. structural heterogeneity around the two nitroxide radicals. The chapter then shows how molecular dynamics simulations of nitroxide radicals can be used to qualitatively

link this structural variety with broad coupling features. It highlights, how the hyperfine spectroscopy is able to reveal distinct structural differences between nitroxide radicals with different ring structures. This chapter is being prepared for submission.

Chapter 7 summarizes the hyperfine spectroscopy experiments performed throughout this thesis, highlighting the great potential of ^{17}O nuclei to link spectroscopic signatures to structural information. It gives an outlook on future applications to other molecular systems and radicals as well as the use of new spectroscopy methods such as multi nuclear correlations experiments to increase structural information gained from ^{17}O signals.

2 Theory of hyperfine spectroscopy

This chapter gives a brief summary of the basic theory necessary to understand EPR hyperfine spectroscopy experiments. It provides an overview of the physical basis of magnetic interactions and shows the mathematical tools to describe and simulate spectroscopy experiments. The knowledge is summarized in a number of great textbooks and reviews. Two books which are of particular value to EPR spectroscopists are the works of Schweiger and Jeschke[51] as well as Goldfarb and Stoll.[52]

2.1 Static EPR Hamiltonian

The energetic structure of a paramagnetic center in the ground state, surrounded by nuclear spins, can be described by a spin Hamiltonian $\hat{\mathcal{H}}_S$,[(a)] which is a sum of individual magnetic interaction Hamiltonians:

$$\hat{\mathcal{H}}_S = \hat{\mathcal{H}}_{\mathrm{EZ}} + \hat{\mathcal{H}}_{\mathrm{ZFS}} + \hat{\mathcal{H}}_{\mathrm{EE}} + \hat{\mathcal{H}}_{\mathrm{NZ}} + \hat{\mathcal{H}}_{\mathrm{HF}} + \hat{\mathcal{H}}_{\mathrm{NQ}} \tag{2.1}$$

The contributions to the spin Hamiltonian are:

$\hat{\mathcal{H}}_{\mathrm{EZ}}$ – the electron Zeeman interaction
$\hat{\mathcal{H}}_{\mathrm{ZFS}}$ – the zero field splitting
$\hat{\mathcal{H}}_{\mathrm{EE}}$ – the electron-electron interaction
$\hat{\mathcal{H}}_{\mathrm{NZ}}$ – the nuclear Zeeman interaction
$\hat{\mathcal{H}}_{\mathrm{HF}}$ – the hyperfine interaction between electron and nuclear spins
$\hat{\mathcal{H}}_{\mathrm{NQ}}$ – the nuclear quadrupole interaction

[(a)] $\hat{\mathcal{H}}$ denotes Hamiltonians in angular frequency units while $\hat{H}$ indicates energy units

For the understanding of magnetic resonance experiments, the investigated system can be treated by an effective Hamiltonian, which neglects interactions irrelevant to the system. All systems investigated in this thesis are isolated organic radicals with a $S = 1/2$ ground state in dilute solutions. Zero-field splitting $\hat{\mathcal{H}}_{\mathrm{ZFS}}$ and electron-electron interactions $\hat{\mathcal{H}}_{\mathrm{EE}}$ can usually be neglected in such systems and will not be discussed in detail.

2.1.1 Electron Zeeman interaction $\mathcal{H}_{\mathbf{EZ}}$

The interaction of the magnetic moment $\boldsymbol{\mu}_{\mathrm{e}}$[b] of an electron spin $\hat{\boldsymbol{S}} = (\hat{S}_x, \hat{S}_y, \hat{S}_z)$

$$\boldsymbol{\mu}_{\mathrm{e}} = -\mu_{\mathrm{B}} \boldsymbol{g} \hat{\boldsymbol{S}} \tag{2.2}$$

with an external magnetic field vector $\boldsymbol{B}$ is described by the electron Zeeman Hamiltonian (in angular frequency units):

$$\hat{\mathcal{H}}_{\mathrm{EZ}} = \frac{\mu_{\mathrm{B}}}{\hbar} \boldsymbol{B}^{\mathrm{T}} \boldsymbol{g} \hat{\boldsymbol{S}} \tag{2.3}$$

where μ_{B} is the Bohr magneton and $\hbar$ is the reduced Planck constant. The orientation dependence of the magnetic interaction is encoded in the symmetric $\boldsymbol{g}$-tensor.[c] It stems from the spin-orbit coupling of excited electronic states, which causes deviations from the g-value of the free electron g_{e}.[53] This deviation is small for organic radicals but can get large for transition metals. The orientation dependence is directly linked to the electronic structure defined by the molecular environment. A coordinate system in which the g-tensor is diagonal

$$\boldsymbol{g} = \begin{pmatrix} g_1 & 0 & 0 \\ 0 & g_2 & 0 \\ 0 & 0 & g_3 \end{pmatrix} \tag{2.4}$$

i.e. its principle axis system (PAS)[d], is therefore generally chosen as the molecular frame of reference. Other magnetic interaction tensors will also be discussed in their respective PAS and can be transferred into the molecular by rotation with three Euler angles α, β and γ.[e] Three cases of g-tensor symmetry can be distinguished: cubic symmetry ($g_1 = g_2 = g_3$), also called isotropic g-tensor, axial symmetry ($g_1 = g_2 \neq g_3$) and rhombic symmetry ($g_1 \neq g_2 \neq g_3$). The g-tensor symmetry reflects on the shape of the molecular frame and so organic radicals most commonly have rhombic symmetry while symmetric

[b] vectors and matrices are indicated bold throughout this thesis

[c] in the course of this thesis, all 3x3 interaction matrices will be called tensors as is the convention in magnetic resonance

[d] the indices 1,2 and 3 are used to denote the principle axis values of the tensors

[e] the z,x',z'' convention is used here

transition metal complexes often show axial or even cubic symmetry. If a strong, external magnetic field with the magnitude B_0 is applied, the Zeeman energy of an electron spin with a particular orientation to the external field and therefore an effective g-value g_{eff} is described by the electron Larmor frequency ω_S

$$\hat{\mathcal{H}}_{\text{EZ}} = \frac{\mu_{\text{B}}}{\hbar} g_{\text{eff}} B_0 \hat{S}_z = \omega_S \hat{S}_z \tag{2.5}$$

A common measure of the interaction strength is the electrons gyromagnetic ratio defined for the free electron by:

$$\gamma_{\text{e}} = \frac{\mu_{\text{B}}}{\hbar} g_{\text{e}} \tag{2.6}$$

2.1.2 Nuclear Zeeman interaction $\mathcal{H}_{\text{NZ}}$

The interaction of nuclear magnetic moments with external magnetic fields is described in analogy to the electron Zeeman interaction by:

$$\hat{\mathcal{H}}_{\text{NZ}} = -\frac{\mu_{\text{N}}}{\hbar} g_{\text{n}} \boldsymbol{B}^{\top} \hat{\boldsymbol{I}} \tag{2.7}$$

where μ_{N} is the nuclear magneton and g_{n} is the isotope specific nuclear g-value. The major difference lies in the negative sign, which indicates the reversal of energetic order associated with the spin states of electrons and nuclei for positive nuclear g-values (^{1}H,^{2}H,^{14}N,^{19}F...). For negative nuclear g-values as observed for ^{17}O ($g_{\text{n}} = -0.757516$), the energetic order is equivalent to that of the electron. The g_{n}-value's orientation dependence, which is described by the chemical shielding tensor and often called chemical shift anisotropy, is orders of magnitude smaller than the electron's g-anisotropy. Therefore it is usually neglected in hyperfine spectroscopy experiments, even though our recent studies have shown that it has to be considered for applications at very high EPR frequencies.[54] For an external field B_0, the Zeeman energy can be described by the nuclear Larmor frequency ω_I

$$\hat{\mathcal{H}}_{\text{NZ}} = -\frac{\mu_{\text{N}}}{\hbar} g_{\text{n}} B_0 \hat{I}_z = -\omega_I \hat{I}_z \tag{2.8}$$

The gyromagnetic ratio for a specific nucleus is defined as:

$$\gamma_{\text{n}} = \frac{\mu_{\text{N}}}{\hbar} g_{\text{n}} \tag{2.9}$$

2.1.3 Hyperfine interaction $\mathcal{H}_{\mathrm{HF}}$

The interaction between electrons and nuclei is described by the hyperfine Hamiltonian

$$\hat{\mathcal{H}}_{\mathrm{HF}} = \hat{\boldsymbol{S}}^{\top}\boldsymbol{A}\hat{\boldsymbol{I}} \tag{2.10}$$

The interactions are summarised in the hyperfine coupling tensor $\boldsymbol{A}$:

$$\boldsymbol{A} = a_{\mathrm{iso}}\mathbb{1} + \boldsymbol{T} \tag{2.11}$$

which contains the isotropic hyperfine coupling constant a_{iso} (multiplied by the unity matrix $\mathbb{1}$ because it is a scalar) and the dipolar coupling tensor $\boldsymbol{T}$. Both contributions are based on the magnetic dipole interaction between electron and nuclear spins and thus contain the product of the two gyromagnetic ratios.[55] Isotropic hyperfine coupling entails finite spin-density $\rho^{\alpha-\beta}$ at the position of the coupled nucleus n, making the dipole interaction distance independent.[56]

$$a_{\mathrm{iso}} = \frac{2\mu_0}{3\hbar} g_{\mathrm{e}}\mu_{\mathrm{B}} g_{\mathrm{n}}\mu_{\mathrm{N}}\rho_{\mathrm{n}}^{\alpha-\beta} \tag{2.12}$$

The through-space dipolar interaction is described by the coupling tensor $\boldsymbol{T}$. The elements of the tensor T_{kl} reflect the general r^{-3} distance dependence of dipole interactions. The nucleus is assumed as a point in space but the distribution of the electron spin is considered by integrating over the ground state electron spin density distribution Ψ_0

$$T_{kl} = \frac{\mu_0}{4\pi\hbar} g_{\mathrm{e}}\mu_{\mathrm{B}} g_{\mathrm{n}}\mu_{\mathrm{N}} \left\langle \Psi_0 \middle| \frac{3r_k r_l}{r^5} - \frac{\delta_{kl}}{r^3} \middle| \Psi_0 \right\rangle \tag{2.13}$$

For larger inter-spin distances ($r \gtrsim 3\,\text{Å}$), the point-dipole approximation can usually be applied to the electron as well and $\boldsymbol{T}$ can be simplified to a traceless tensor of the form:

$$\boldsymbol{T} = \frac{\mu_0}{4\pi\hbar} g_{\mathrm{e}}\mu_{\mathrm{B}} g_{\mathrm{n}}\mu_{\mathrm{N}} \frac{1}{r^3} \begin{pmatrix} -1 & 0 & 0 \\ 0 & -1 & 0 \\ 0 & 0 & 2 \end{pmatrix} \tag{2.14}$$

2.1.4 Nuclear quadrupole interaction $\mathcal{H}_{\mathrm{NQ}}$

The nuclear quadrupole coupling is described by the quadruple coupling Hamiltonian

$$\hat{\mathcal{H}}_{\mathrm{NQ}} = \hat{\boldsymbol{I}}^{\top}\boldsymbol{P}\hat{\boldsymbol{I}} \tag{2.15}$$

The non-spherical charge distribution in nuclei with spin $I > 1/2$ is described by the quadrupole moment eQ. Its interaction with the surrounding electric field gradient (EFG) eq is parameterized by the traceless quadrupole coupling tensor:[57]

$$\boldsymbol{P} = \frac{e^2 qQ}{4I(2I-1)\hbar} \begin{pmatrix} -(1-\eta_P) & 0 & 0 \\ 0 & -(1+\eta_P) & 0 \\ 0 & 0 & 2 \end{pmatrix} \tag{2.16}$$

The symmetry of the quadrupole coupling tensor is directly related to the shape of the EFG tensor and so its asymmetry parameter is defined as $\eta_P = (V_1 - V_2)/V_3$[(f)] where $V_{1,2,3}$ are the EFG tensors PAS values. The quadruple coupling in itself is a purely electrostatic interaction but is relevant to the spin Hamiltonian due to a perturbation of the nuclear angular momentum.

2.2 Spin dynamics

Multiple models can be used to describe the time evolution of electron or nuclear spins during magnetic resonance experiments. For didactic purposes, the vector model comes in handy to describe simple spin echo experiments. Complex pulse sequences, however, require a quantum mechanical treatment with the density operator formalism, which will be explained in the following section. It follows the description of Schweiger and Jeschke[51] as well as Feintuch and Vega.[58] A detailed description is essential for EPR experiments, where the electron and nuclear Zeeman interaction are not always dominant, resulting in Hamiltonians that are not diagonal (see previous Section).

2.2.1 Expectation values

An isolated spin system can be described by the wave function $|\Psi\rangle$ which is a sum of its orthogonal eigenfunctions $|\psi_i\rangle$ that span the N-dimensional *Hilbert* space:

$$|\Psi\rangle = \sum_{i=1}^{N} c_i |\psi_i\rangle \tag{2.17}$$

The time evolution of the quantum mechanical system follows the time-dependent *Schrödinger* equation

$$\frac{\partial}{\partial t} |\Psi(t)\rangle = -\mathrm{i}\hat{\mathcal{H}} |\Psi(t)\rangle \tag{2.18}$$

(f) the asymmetry parameter is given here with the subscript P to differentiate it from another asymmetry parameter used in a subsequent chapter

Physical properties of quantum mechanical systems are called observables and are expressed as the expectation value of Hermetian operators $\hat{Q}$ (e.g. a Hamiltonian) acting on the system:

$$\left\langle \hat{Q} \right\rangle = \langle \Psi | \hat{Q} | \Psi \rangle \tag{2.19}$$

which can be written in terms of the eigenfunctions:

$$\langle \Psi | \hat{Q} | \Psi \rangle = \sum_{kl} c_k^* c_l \langle \psi_k | \hat{Q} | \psi_l \rangle \tag{2.20}$$

The relevant information about the system is encoded in the coefficient products $c_k^* c_l$, making it convenient to define a density operator $\hat{\rho}$:

$$\hat{\rho} = |\Psi\rangle \langle \Psi| \tag{2.21}$$

which has the coefficient products as expectation values:

$$\langle \psi_l | \hat{\rho} | \psi_k \rangle = c_k^* c_l \tag{2.22}$$

The operators expectation value can therefore be expressed as

$$\begin{aligned} \left\langle \hat{Q} \right\rangle &= \sum_{lk} \langle \psi_l | \hat{\rho} | \psi_k \rangle \langle \psi_k | \hat{Q} | \psi_l \rangle \\ &= \sum_{lk} \langle \psi_l | \hat{\rho} \hat{Q} | \psi_k \rangle \\ &= \mathrm{tr}\{\hat{\rho}\hat{Q}\} = \mathrm{tr}\{\hat{Q}\hat{\rho}\} \end{aligned} \tag{2.23}$$

The density operator contains the full information of the isolated spin state:

- diagonal elements $\rho_{kk} = c_k^* c_k = |c_k|^2$ describe *populations* of states
- off-diagonal elements $\rho_{kl} = c_k^* c_l$ describe *coherences* between states

2.2.2 Ensemble description

Magnetic resonance has recently made great advances in the detection of single spins, yet the majority of experiments detect spin ensembles. Therefore, the system needs to be described by an ensemble of wave functions $|\Psi_i\rangle$ and fractional populations $\mathcal{P}_i$ that describe the contribution of the individual spin states i. The expectation value of an operator can then be calculated by summing over the weighted expectation values of the whole ensemble:

$$\left\langle \hat{Q} \right\rangle_{\text{ensemble}} = \sum_i \mathcal{P}_i \left\langle \hat{Q}_i \right\rangle = \sum_i \mathcal{P}_i \langle \Psi_i | \hat{Q} | \Psi_i \rangle \tag{2.24}$$

If the wavefunctions of the ensemble components $|\Psi\rangle$ can be expressed by the same basis vectors $|\psi\rangle$, the expectation values can be derived from a statistical average of the coefficient products:

$$\left\langle \hat{Q} \right\rangle_{\text{ensemble}} = \sum_{kl} \overline{c_k^* c_l} \langle \psi_k | \hat{Q} | \psi_l \rangle \tag{2.25}$$

The ensemble averaged density operator $\hat{\sigma}$ is then formulated in analogy to equation (2.21):

$$\hat{\sigma} = \sum_i \mathcal{P}_i \left| \Psi_i \right\rangle \left\langle \Psi_i \right| = \sum_{lk} \overline{c_l c_k^*} \left| \psi_l \right\rangle \left\langle \psi_k \right| \tag{2.26}$$

2.2.3 Time evolution of the density operator

The time derivative of the density operator describes the time evolution of the spin system. It can be calculated with the time-dependent *Schrödinger* equation (Eq. (2.18)):

$$\begin{aligned} \frac{\partial}{\partial t}\hat{\sigma} &= \frac{\partial}{\partial t}\left(\left|\Psi\right\rangle\left\langle\Psi\right|\right) \\ &= \left(\frac{\partial}{\partial t}\left|\Psi\right\rangle\right)\left\langle\Psi\right| + \left|\Psi\right\rangle\left(\frac{\partial}{\partial t}\left\langle\Psi\right|\right) \\ &= -\mathrm{i}\hat{\mathcal{H}}\left|\Psi\right\rangle\left\langle\Psi\right| - \mathrm{i}\left|\Psi\right\rangle\left\langle\Psi\right|\hat{\mathcal{H}} \\ &= -\mathrm{i}\hat{\mathcal{H}}\hat{\sigma} - \mathrm{i}\hat{\sigma}\hat{\mathcal{H}} \\ \frac{\partial}{\partial t}\hat{\sigma} &= -\mathrm{i}\left[\hat{\mathcal{H}},\hat{\sigma}\right] \end{aligned} \tag{2.27}$$

This is commonly known as the *Liouville-von Neumann* equation. Distinct evolutions of the density operator are described by unitary transformations with propagators $\hat{U}$, which represent a rotation in the Hilbert space:

$$\hat{\sigma}(t) = \hat{U}\hat{\sigma}\hat{U}^{-1} \tag{2.28}$$

For time-independent Hamilton operators, the propagator takes the form $\hat{U} = \exp\left(-\mathrm{i}\hat{\mathcal{H}}t\right)$ so that one can write:

$$\hat{\sigma}(t) = \exp\left(-\mathrm{i}\hat{\mathcal{H}}t\right)\hat{\sigma}(0)\exp\left(\mathrm{i}\hat{\mathcal{H}}t\right) \tag{2.29}$$

This is often conveniently represented as:

$$\hat{\sigma}(0) \xrightarrow{\hat{\mathcal{H}}t} \hat{\sigma}(t) \tag{2.30}$$

This methodology can be used to describe pulsed magnetic resonance experiments, but requires two further mathematical manipulations. Hamilton operators in magnetic resonance

are intrinsically time-dependent, which prevent the use of Equation (2.29). A transformation of the system into a frame where the Hamiltonians are time-independent solves this problem and will be described in Section 2.2.5. Additionally, pulse sequences are made up of time intervals with differing Hamiltonians and can not be described by a singe evolution step. This problem can be solved by subdividing pulse experiments into small time intervals, in which the Hamiltonian and therefore the propagator is time-independent. For i steps, the evolution of $\hat{\sigma}$ can then be written as:

$$\hat{\sigma}(t_i) = \hat{U}_i ... \hat{U}_2 \hat{U}_1 \hat{U} \hat{\sigma} \hat{U}^{-1} \hat{U}_1^{-1} \hat{U}_2^{-1} ... \hat{U}_i^{-1} \tag{2.31}$$

or equivalently:

$$\hat{\sigma}(0) \xrightarrow{\hat{\mathcal{H}}_1 t_1} \xrightarrow{\hat{\mathcal{H}}_2 t_2} ... \xrightarrow{\hat{\mathcal{H}}_i t_i} \hat{\sigma}(t_i) \tag{2.32}$$

The expectation value of any operator can be probed by calculating:

$$\left\langle \hat{Q} \right\rangle = \mathrm{tr}\left\{ \hat{\sigma} \hat{Q} \right\} \tag{2.33}$$

2.2.4 Product operator formalism

The density operator can be written as a linear combination of orthogonal basis operators $\hat{O}_i$, called product operators:

$$\hat{\sigma} = \sum_i c_i \hat{O}_i \tag{2.34}$$

The transformation of the individual product operators follows the same rules explained for the density operator. The evolution of a product operator $\hat{A}$ under another product operator $\hat{B}$ leads to a third product operator $\hat{C}$:

$$\hat{C} = \exp\left\{ -\mathrm{i}\varphi \hat{B} \right\} \hat{A} \exp\left\{ \mathrm{i}\varphi \hat{B} \right\} \qquad \text{or} \qquad \hat{A} \xrightarrow{\varphi \hat{B}} \hat{C} \tag{2.35}$$

The general solution for time-independent propagators is known as the *Baker-Hausdorff* formula:

$$\hat{C} = \begin{cases} \hat{A} \cos\varphi - \mathrm{i} \left[\hat{A}, \hat{B} \right] \sin\varphi & \text{if } \left[\hat{A}, \hat{B} \right] \neq 0 \\ \hat{A} & \text{if } \left[\hat{A}, \hat{B} \right] = 0 \end{cases} \tag{2.36}$$

Conveniently, basis sets describing isolated spins can be chosen as the basis set of the density operator for magnetic resonance experiments. Several choices are available:

Cartesian operators $\{\hat{S}_x,\hat{S}_y,\hat{S}_z,\mathbb{1}\}$

The angular momentum operators of the individual spins form the *Cartesian* basis and are a convenient choice, since they follow the cyclic permutation rules:

$$\begin{aligned}\left[\hat{S}_x,\hat{S}_y\right] &= \mathrm{i}\hat{S}_z\\ \left[\hat{S}_y,\hat{S}_z\right] &= \mathrm{i}\hat{S}_x\\ \left[\hat{S}_z,\hat{S}_x\right] &= \mathrm{i}\hat{S}_y\end{aligned} \tag{2.37}$$

Single transition operators $\{\hat{S}^+,\hat{S}^-,\hat{S}^\alpha,\hat{S}^\beta\}$

If selective excitation of single transitions need to be described, as is the case in hyperfine spectroscopy experiments in particular (see Sec. 2.3.3), the polarization operators are highly useful:

$$\begin{aligned}\hat{S}^\alpha &= \frac{1}{2}(\mathbb{1}+2\hat{S}_z)\\ \hat{S}^\beta &= \frac{1}{2}(\mathbb{1}-2\hat{S}_z)\end{aligned} \tag{2.38}$$

Additionally, the raising $\hat{S}^+$ and lowering $\hat{S}^-$ operators can be defined to describe transfers between states:

$$\begin{aligned}\hat{S}^+ &= \hat{S}_x+\mathrm{i}\hat{S}_y\\ \hat{S}^- &= \hat{S}_x-\mathrm{i}\hat{S}_y\end{aligned} \tag{2.39}$$

If the *Cartesian* basis is chosen for the product operator description of magnetic resonance experiments, it is important to know the equilibrium density operator $\hat{\sigma}_{\mathrm{eq}}$ before the beginning of the pulse sequence. This may be written as:

$$\hat{\sigma}_{\mathrm{eq}} = \frac{1}{Z}\exp\left\{-\frac{\hbar\hat{\mathcal{H}}}{k_{\mathrm{B}}T}\right\} \tag{2.40}$$

where Z is the partition function:

$$Z = \mathrm{tr}\left\{\exp\left(-\frac{\hbar\hat{\mathcal{H}}}{k_{\mathrm{B}}T}\right)\right\} \tag{2.41}$$

In the high temperature approximation, i.e. when $k_{\mathrm{B}}T$ is larger than the largest energy difference between two states, the equilibrium density operator can be approximated as

$$\hat{\sigma}_{\mathrm{eq}} \approx \mathbb{1} - \frac{\hbar\hat{\mathcal{H}}}{k_{\mathrm{B}}T} \tag{2.42}$$

At the beginning of an EPR pulse sequence, the energy level distribution is dominated by the Zeeman Hamiltonian $\hat{\mathcal{H}} = \omega_S \hat{S}_z$. Substituting this into equation (2.42) and dropping the invariant term results in:

$$\hat{\sigma}_{\text{eq}} \approx -\hat{S}_z \tag{2.43}$$

2.2.5 Rotating frame transformation

Time-independent Hamilton operators are necessary to conveniently describe pulse sequences with the product operator formalism. The Hamiltonian for magnetic resonance experiments is therefore split into a static component $\hat{\mathcal{H}}_0$ and a dynamic component $\hat{\mathcal{H}}_1$:

$$\hat{\mathcal{H}} = \hat{\mathcal{H}}_0 + \hat{\mathcal{H}}_1 \tag{2.44}$$

For a single-electron spin Hamiltonian, the static component is the electron Zeeman interaction with the external magnetic field and the dominant dynamic component is the interaction with oscillating magnetic fields, i.e. continuous of pulsed microwave irradiation:

$$\hat{\mathcal{H}} = \hat{\mathcal{H}}_{\text{EZ}} + \hat{\mathcal{H}}_{\text{mw}} = \omega_S \hat{S}_z + 2\omega_1 \hat{S}_x \cos(\omega_{\text{mw}} t + \phi_{\text{mw}}) \tag{2.45}$$

with $2\omega_1 = \frac{\mu_B}{\hbar} g_e B_1$ expressing the amplitude and ϕ_{mw} the phase of the linearly oscillating microwave field vector B_1. The Hamiltonian can be made time-independent by transforming the density operator and the spin Hamiltonian into a frame, that rotates with the frequency of the microwave irradiation. This is done by the unitary transformation with the operator:

$$\hat{U}^R = \exp\left(-\mathrm{i}\omega_{\text{mw}} t \hat{S}_z\right) \tag{2.46}$$

The rotating frame density operator can then be calculated as:

$$\hat{\sigma}^R = \hat{U}^R \hat{\sigma} \hat{U}^{R,-1} \tag{2.47}$$

and the rotating frame Hamiltonian as:

$$\hat{\mathcal{H}}^R = \hat{U}^R \hat{\mathcal{H}} \hat{U}^{R,-1} - \omega_{\text{mw}} \hat{S}_z \tag{2.48}$$

The unitary transformation can be calculated by the recipe given in equation (2.36):

$$\begin{aligned} \hat{U}^R \hat{\mathcal{H}} \hat{U}^{R,-1} &= \omega_S \hat{S}_z + 2\omega_1 \left(\hat{S}_x \cos\omega_{\text{mw}} t - \hat{S}_y \sin\omega_{\text{mw}}\right) \cos(\omega_{\text{mw}} t + \phi_{\text{mw}}) \\ &= \omega_S \hat{S}_z + \omega_1 \left(\hat{S}_x \cos\phi_{\text{mw}} - \hat{S}_y \sin\phi_{\text{mw}}\right) \\ &\quad + \omega_1 \left\{\hat{S}_x \cos(2\omega_{\text{mw}} t + \phi_{\text{mw}}) - \hat{S}_y \cos(2\omega_{\text{mw}} t + \phi_{\text{mw}})\right\} \end{aligned} \tag{2.49}$$

The time-dependent terms that oscillate with twice the microwave frequency are usually neglected, assuming that they do not interact with the spins. This is called the *rotating wave approximation* and is usually justified when $2\omega_{\mathrm{mw}} \gg \omega_1$. Small deviations of the transition frequency ω_S are still occasionally observed and this is called the *Bloch-Siegert-shift*. The full rotating frame Hamiltonian can then be written as:

$$\begin{aligned}\hat{\mathcal{H}}^R &= \omega_S \hat{S}_z + \omega_1 \left(\hat{S}_x \cos\phi_{\mathrm{mw}} - \hat{S}_y \sin\phi_{\mathrm{mw}}\right) - \omega_{\mathrm{mw}} \hat{S}_z \\ &= \Delta\omega_S + \omega_1 \left(\hat{S}_x \cos\phi_{\mathrm{mw}} - \hat{S}_y \sin\phi_{\mathrm{mw}}\right)\end{aligned} \tag{2.50}$$

With this, the time evolution of the density operator in the rotating frame can be calculated by the *Liouville-von Neumann* equation:

$$\frac{\partial}{\partial t}\hat{\sigma}^R = -\mathrm{i}[\hat{\mathcal{H}}^R, \hat{\sigma}^R] \tag{2.51}$$

In the following chapters, the rotation index ^{R} will be omitted from the density operator and the Hamiltonian and only indicated by the use of the offset term $\Delta\omega_S = \omega_S - \omega_{\mathrm{mw}}$ for the electron Zeeman Hamiltonian. Experiments of coupled spin systems, which utilize irradiation with more than one frequency ω_{mw}, e.g. ENDOR, are sometimes described in the doubly-rotating frame. The transformation rules for this frame are identical to the aforementioned singly-rotating frame, with an additional unitary transformation $U^{R2} = \exp\left(-\mathrm{i}\omega_{\mathrm{rf}} t \hat{I}_z\right)$. The use of this frame will be indicated by the equivalent nuclear offset $\Delta\omega_I = \omega_I - \omega_{\mathrm{rf}}$.

2.2.6 Relaxation

The product operator formalism and *Liouville-von Neumann* equation given under (2.27) disregard processes, which destroy coherences or return polarization back to equilibrium. In short, they disregard relaxation. This can be remedied by the introduction of a *relaxation superoperator* $\hat{\hat{\Gamma}}$, which returns the system back do equilibrium $\hat{\sigma}_{\mathrm{eq}}$ and is described by the aptly named *quantum mechanical master equation*:

$$\frac{\partial}{\partial t}\hat{\sigma} = -\mathrm{i}[\hat{\mathcal{H}}, \hat{\sigma}] + \hat{\hat{\Gamma}}\left(\hat{\sigma} - \hat{\sigma}_{\mathrm{eq}}\right) \tag{2.52}$$

Relaxation theories belong to the more complex mathematical construct in magnetic resonance and require large computational power to describe even small systems. A numerically accurate description will therefore not be given but a phenomenological approach will be used. In this approach, relaxation is mainly described by two processes, *spin-lattice* and *spin-spin* relaxation, described by the T_1 and T_2 relaxation times, respectively. These relaxation times come from the solutions of the *static Bloch equation* and describe how

quickly magnetization returns to the equilibrium state.
Spin-lattice relaxation returns z-magnetization, i.e. polarization, to thermal equilibrium while *spin-spin* relaxation destroys x and y magnetization, i.e. coherences. As evident from the name, the T_1 mechanism is mainly the exchange of energy with the surrounding lattice or thermal bath. In practice however, more complicated processes such as spectral diffusion also cause the destruction of out-of-equilibrium polarization. Likewise, the name of the T_2 process indicates that interactions between different spins in the system cause the dephasing of electron coherences. Once again, this might be the main contribution but other effects such as *nuclear spin diffusion* enter into the process and therefore the experimentally measured relaxation time of coherences is named *phase memory time* and denoted by T_m.

2.3 Hyperfine spectroscopy experiments

EPR spectroscopy experiments that focus on the detection of electron-nuclear spin interactions are generally summarized as hyperfine spectroscopy experiments. Modern hf spectroscopy is performed almost exclusively as pulsed experiments and can be categorized into three families: 1. microwave single resonance techniques such as HYSCORE, the 2D variation of ESEEM;[6,7] 2. microwave double resonance techniques based on the EDNMR experiment;[8] 3. microwave radio-frequency double resonance techniques based on the ENDOR experiments.[4,5] The hf spectroscopy techniques all aim at the detection of nuclear resonance frequencies via the EPR signal but differ in the excitation of and detection schemes. ENDOR experiments detect exclusively allowed electron and nuclear transitions, while EDNMR and HYSCORE require the excitation of generally forbidden EPR transitions and coherences. The following sections will show the working principles of the techniques and the requirements of the spin system described with the density operator formalism. This is essential to understand the different hyperfine spectra and the influence of experimental parameters on them.

2.3.1 The coupled S=1/2, I=1/2 spin system

The following sections will describe the hyperfine spectroscopy experiments with the aid of the simplest possible coupled spin system: an electron spin $S = 1/2$ coupled to a nuclear spin $I = 1/2$. This leads to the best understanding of the mechanisms of the hf spectroscopy experiments. Higher nuclear spins quickly lead to calculations, for which analytical solutions are no longer feasible. Since the main focus of this work is the hf spectroscopy of ^{17}O with a nuclear spin $I = 5/2$, important deviations from the described behaviour of nuclear spin one-half will be mentioned. These are mostly associated with the nuclear quadrupole

coupling. In practice, numerical simulations are the method of choice for dealing with high nuclear spins, which will be shown in chapter 3.
The static spin Hamiltonian of the model system can be written as:

$$\hat{\mathcal{H}}_0 = \frac{\mu_\mathrm{B}}{\hbar}\boldsymbol{B}^\top \boldsymbol{g}\hat{\boldsymbol{S}} - \frac{\mu_\mathrm{N}}{\hbar} g_\mathrm{n}\boldsymbol{B}^\top \hat{\boldsymbol{I}} + \hat{\boldsymbol{S}}^T \boldsymbol{A}\hat{\boldsymbol{I}} \tag{2.53}$$

These assumptions will be made:

- the electron spin can be described with a single effective g-value
- the nuclear spin has a positive nuclear g-value
- the electron is fully quantized along the external magnetic field $\boldsymbol{B} = (0,0,B_0)$
- the nuclear spin is quantized along an arbitrary direction determined by the relative size of the nuclear Zeeman and hyperfine fields

If the last two assumptions are true, the spin system is treated in the so called *general high magnetic field case*. The Hamiltonian can then be written as:

$$\hat{\mathcal{H}}_0 = \omega_S \hat{S}_z - \omega_I \hat{I}_z + A_{zz}\hat{S}_z\hat{I}_z + A_{zx}\hat{S}_z\hat{I}_x + A_{zy}\hat{S}_z\hat{I}_y \tag{2.54}$$

This can be further simplified by turning the nuclear coordinate systems so that $A_{zy} = 0$:

$$\hat{\mathcal{H}}_0 = \omega_S \hat{S}_z - \omega_I \hat{I}_z + A\hat{S}_z\hat{I}_z + B\hat{S}_z\hat{I}_x \tag{2.55}$$

where A is then called the *secular* and $B = \sqrt{A_{zx}^2 + A_{zy}^2}$ the *pseudo-secular* hyperfine coupling. For a system with a hyperfine tensor composed of an isotropic and an axially symmetric dipolar coupling contribution (see Sec. 2.1.3), they can be described as:

$$A = a_\mathrm{iso} + T(3\cos^2\theta - 1) \tag{2.56}$$

$$B = 3T\sin\theta\cos\theta \tag{2.57}$$

where θ is one of the Euler angles describing the relative orientation of the hyperfine tensor to the g-tensor, i.e. the molecular frame. The pseudo-secular hyperfine coupling contributes off-diagonal elements to the static spin Hamiltonian, thus it needs to be diagonalized to obtain the eigenvalues, i.e. the energy levels, of the system. The Hamiltonian can first be rewritten in terms of the previously mentioned single transition operators:

$$\hat{\mathcal{H}}_0 = \omega_S \hat{S}_z + \left(\omega_I + \frac{A}{2}\right)\hat{S}^\alpha\hat{I}_z + \frac{B}{2}\hat{S}^\alpha\hat{I}_x + \left(\omega_I - \frac{A}{2}\right)\hat{S}^\beta\hat{I}_z - \frac{B}{2}\hat{S}^\beta\hat{I}_x \tag{2.58}$$

The unitary transformation that diagonalizes the Hamiltonian can then be rationalized as consecutive rotations of the individual spin manifolds around the y axis by the respective angles η_α and η_β :

$$\hat{U}_{\text{diag}} = \hat{U}_y^\alpha \hat{U}_y^\beta = \exp\Big\{-\mathrm{i}\left(\eta_\alpha \hat{S}^\alpha \hat{I}_y + \eta_\beta \hat{S}^\beta \hat{I}_y\right)\Big\} \tag{2.59}$$

The same transformation can also be written in the cartesian operator basis with the angles ξ and η as:

$$\hat{U}_{\text{diag}} = \exp\Big\{-\mathrm{i}\left(\xi \hat{I}_y + \eta 2\hat{S}_z \hat{I}_y\right)\Big\} \tag{2.60}$$

The angles η_α and η_β result from the geometric relation of the nuclear Zeeman field with respect to the secular and pseudo-secular hyperfine field (Fig. 2.1, A and D):

$$\eta_\alpha = \arctan\left(\frac{-B/2}{A/2+\omega_I}\right) \qquad \text{and} \qquad \eta_\beta = \arctan\left(\frac{-B/2}{A/2-\omega_I}\right) \tag{2.61}$$

The sum and difference of the two form the angles for the cartesian transformation:

$$\xi = \frac{\eta_\alpha - \eta_\beta}{2} \qquad \text{and} \qquad \eta = \frac{\eta_\alpha + \eta_\beta}{2} \tag{2.62}$$

The angles essentially describe the effective magnetic fields experienced by the nuclear spin within each different spin manifold. Fig. 2.1 shows this for two specific limiting cases, which are relevant for all hyperfine spectroscopy experiments.
In the weak coupling case (left), the nuclear Zeeman field ω_I dominates and the hyperfine fields ($A/2$ and $B/2$) cause a deviation from the z axis. The opposite is the strong coupling case (right), in which the hyperfine fields dominate and the Zeeman field causes a deviation. The geometric representation clearly shows, that the pseudo-secular part of the hyperfine coupling is the reason for the deviation from the z quantization axis. The diagonalized spin Hamiltonian in the *tilted frame* can then be written as:

$$\begin{aligned}\hat{\mathcal{H}}_0^{\text{tilted}} &= \omega_S \hat{S}_z + \omega_{12} \hat{S}^\alpha \hat{I}_z + \omega_{34} \hat{S}^\beta \hat{I}_z \\ &= \omega_S \hat{S}_z + \frac{\omega_+}{2} \hat{I}_z + \frac{\omega_-}{2} 2\hat{S}_z \hat{I}_z\end{aligned} \tag{2.63}$$

The basic nuclear transition frequencies, which can also be imagined as the effective nuclear fields can be written as:

$$\omega_{12} = \omega_\alpha = \left(\omega_I + \frac{A}{2}\right)\cos\eta_\alpha - \frac{B}{2}\sin\eta_\alpha \tag{2.64}$$

$$\omega_{34} = \omega_\beta = \left(\omega_I - \frac{A}{2}\right)\cos\eta_\beta + \frac{B}{2}\sin\eta_\beta \tag{2.65}$$

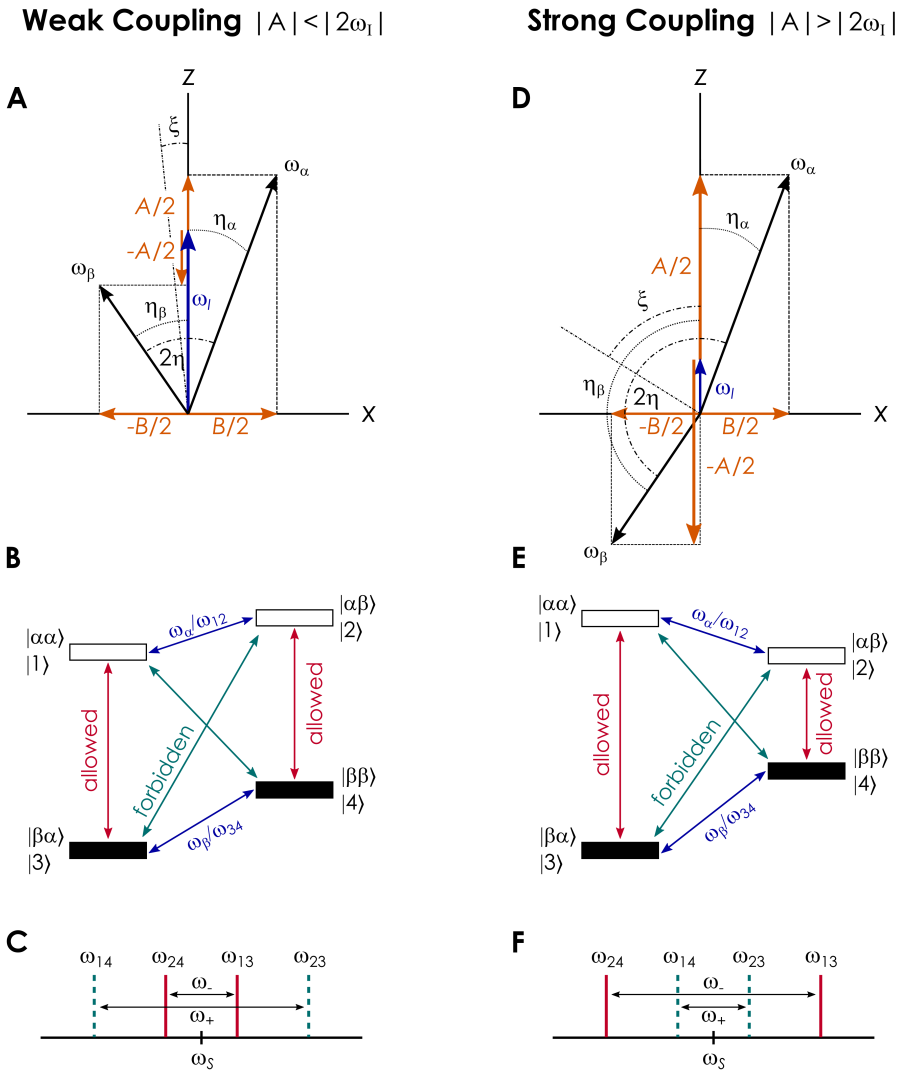

Figure 2.1: The coupled $S = 1/2, I = 1/2$ spin system in the weak (left) and strong (right) coupling cases. **A**/**D**: Relative orientations of the nuclear Zeeman (blue) and hyperfine (orange) fields that determine the quantization axis of the basic nuclear transition frequencies ω_α and ω_β. Angles for the single transition operators are marked by dotted circles while angles for the Cartesian operators are marked by dash-dotted circles. **B**/**E**: Energy level diagrams with arrows marking the allowed (red) and forbidden (cyan) EPR transitions as well as the allowed nuclear transitions (blue). Boltzmann distribution is marked by the coloring (filled/unfilled) of the boxes. **C**/**F**: EPR spectra with relative position of the allowed (solid red) and forbidden (dashed cyan) EPR transition frequencies.

In the Cartesian basis, they are written as the sum and difference frequencies:

$$\omega_+ = \omega_{12} + \omega_{34} \qquad \text{and} \qquad \omega_- = \omega_{12} - \omega_{34} \tag{2.66}$$

From this Hamiltonian, the energy level diagram of the coupled spin system can be derived. It is shown in Fig. 2.1, B and E for the strong and weak coupling case, respectively. Six transitions are possible between the four levels: two allowed EPR transitions (red) ω_{13} and ω_{24} with $\Delta m_S = 1, \Delta m_I = 0$, two forbidden EPR transitions (cyan) ω_{14} and ω_{23} with $\Delta m_S = 1, \Delta m_I = 1$ and two allowed nuclear (NMR) transitions (blue) ω_{12} and ω_{34} with $\Delta m_S = 0, \Delta m_I = 1$. This color code will be kept throughout the figures in this work. The schematic EPR spectra for the two coupling cases are given in Fig. 2.1, C and F.
For the description of the hyperfine spectroscopy experiments, it is also necessary to transform the dynamic Hamiltonian, i.e. the microwave Hamiltonian that induces transitions, into the tilted frame. This is done by the same unitary transformation used for the static Hamiltonian. For a set microwave phase (x) in the rotating frame, this means:

$$\hat{\mathcal{H}}_1^{\mathrm{R,tilted}} = \hat{U}_{\mathrm{diag}}^{-1} \hat{\mathcal{H}}_1^{\mathrm{R}} \hat{U}_{\mathrm{diag}} = \omega_1 \hat{U}_{\mathrm{diag}}^{-1} \hat{S}_x \hat{U}_{\mathrm{diag}} \tag{2.67}$$

Because this transformation occurs in the Cartesian base, expression (2.60) is used to get:

$$\omega_1 \hat{S}_x \xrightarrow{\xi \hat{I}_y + \eta 2 \hat{S}_z \hat{I}_y} \omega_1 \left(\hat{S}_x \cos\eta + 2 \hat{S}_y \hat{I}_y \sin\eta \right) \tag{2.68}$$

The matrix representation of this Hamiltonian clearly shows how allowed (red) and forbidden (cyan) transitions are induced by terms with $\cos\eta$ and $\sin\eta$, respectively:

$$\hat{\mathcal{H}}_1^{\mathrm{R,tilted}} = \omega_1 \begin{pmatrix} 0 & 0 & \cos\eta & -\sin\eta \\ 0 & 0 & \sin\eta & \cos\eta \\ \cos\eta & \sin\eta & 0 & 0 \\ -\sin\eta & \cos\eta & 0 & 0 \end{pmatrix} \tag{2.69}$$

From this, and from the previous geometric considerations for the diagonalization, the transition probabilities and intensities of the EPR transitions can be derived. The normalized intensities/transition probabilities for the allowed (I_{a}) and forbidden (I_{f}) transitions are given as:

$$I_{\mathrm{a}} = \cos^2\eta = \frac{\left|\omega_I^2 - \frac{1}{4}\omega_-^2\right|}{\omega_\alpha \omega_\beta} \qquad \text{and} \qquad I_{\mathrm{f}} = \sin^2\eta = \frac{\left|\omega_I^2 - \frac{1}{4}\omega_+^2\right|}{\omega_\alpha \omega_\beta} \tag{2.70}$$

Generally, the larger the anisotropy of the hyperfine interaction, the larger the intensity of the forbidden EPR transitions. While the forbidden EPR transitions might not be resolved

in EPR spectra or their contribution might be very small, they form the basis of two of the three hf spectroscopy methods, namely EDNMR and HYSCORE.

2.3.2 Experiment overview

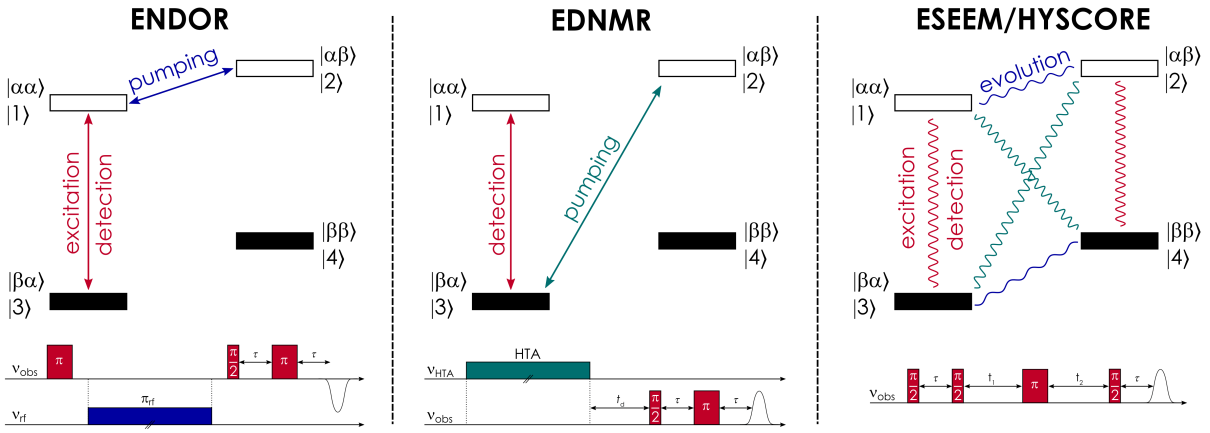

Figure 2.2: Overview of hyperfine spectroscopy experiments for a coupled $S = 1/2$, $I = 1/2$ system in the weak coupling case. **A**: ENDOR, which utilizes the excitation of allowed EPR transitions to prepare the spin system and rf irradiation to detect the nuclear transitions via the EPR signal. **B**: EDNMR, which uses long microwave excitation to drive forbidden EPR transitions and detect the effect via the EPR signal. **C**: ESEEM/HYSCORE, which utilizes broadband microwave pulses to excite allowed and forbidden electron coherences and detect the evolution of nuclear coherences via the EPR signal.

Figure 2.2 shows an overview of the three hf spectroscopy methods with the pulse sequences and their working principles illustrated for the weakly coupled spin system. It highlights the main difference between the three methods: while ENDOR utilizes the excitation, pumping and detection of allowed EPR transitions, EDNMR and ESEEM utilize the excitation of allowed and also forbidden transitions. ENDOR and EDNMR are considered *pump-probe* experiments, which record the spectra in the direct frequency dimension while ESEEM/HYSCORE is a time-domain experiment in which evolution of nuclear coherences is detected via the EPR signal and the frequency domain spectrum is generated via Fourier transformation (FT). Finally, ENDOR and EDNMR rely on the selective excitation of transitions, while ESEEM utilizes broadband excitation. Exceptions to this last point exist both for ENDOR and EDNMR and will be discussed in the respective sections (*vide infra*).

2.3.3 ENDOR

Pulsed ENDOR spectroscopy is generally performed with one of two pulse sequences: Davies[5] or Mims[4] ENDOR, each named after the respective inventor. Many more elaborate pulse sequences exist, but the general working principle is best explained using these two. The Davies experiment is based on a refocused electron spin echo (Fig. 2.3)

while the Mims experiment utilizes a stimulated echo (Fig. 2.4). Both aim for the generation of electron-nuclear double spin order, a mixed state described by the $2\hat{S}_z\hat{I}_z$ operator, which is the condition when one of the EPR transitions is inverted.

Davies ENDOR In the Davies ENDOR sequence (Fig. 2.3, A) this is achieved by a selective π-pulse that acts only on the allowed $1 \leftrightarrow 3$ or α transition ($\pi\hat{S}_x\hat{I}^\alpha$):

$$\hat{\sigma}_{\text{eq}} = -\hat{S}_z = -\hat{S}_z\hat{I}^\alpha - \hat{S}_z\hat{I}^\beta \xrightarrow{\pi\hat{S}_x\hat{I}^\alpha} = \hat{S}_z\hat{I}^\alpha - \hat{S}_z\hat{I}^\beta = 2\hat{S}_z\hat{I}_z = \hat{\sigma}_{\text{prep}}^{\text{sel}} \tag{2.71}$$

After the preparation, a selective radio-frequency pulse with the flip angle φ is applied on one of the nuclear transitions:

$$\begin{aligned}\hat{\sigma}_{\text{prep}}^{\text{sel}} &\xrightarrow{\varphi\hat{S}^\alpha\hat{I}_x} \left(\hat{S}_z\hat{I}^\alpha - \hat{S}_z\hat{I}^\beta\right)\left[\frac{1}{2}(1+\cos\varphi)\right] \\ &-\hat{I}_z\left[\frac{1}{2}(1-\cos\varphi)\right] - \hat{S}^\alpha\hat{I}_y\sin\varphi = \hat{\sigma}_{\text{ENDOR}}\end{aligned} \tag{2.72}$$

In the case of full inversion of a nuclear transition ($\varphi = \pi$) the spin system is in a state of nuclear polarization, i.e. $-\hat{I}_z$, while it remains in its state of electron-nuclear double spin order, if the rf pulse has no effect. The latter case is true for off resonant irradiation. The final selective spin echo sequence acts as a read out of the $1 \leftrightarrow 3$ transition:[59]

$$\hat{\sigma}_{\text{ENDOR}} \xrightarrow{\frac{\pi}{2}\hat{S}_x\hat{I}^\alpha} \xrightarrow{\tau\hat{\mathcal{H}}_0} \xrightarrow{\pi\hat{S}_x\hat{I}^\alpha} \xrightarrow{\tau\hat{\mathcal{H}}_0} \frac{1}{2}(1+\cos\varphi)\hat{S}_y\hat{I}^\beta = \hat{\sigma}_{\text{echo}} \tag{2.73}$$

The Davies pulse sequence and polarization transfer is illustrated in Fig. 2.3. The ENDOR spectrum is detected by sweeping the rf frequency range and monitoring the intensity of the EPR echo. This can be expressed by calculating the expectation value of transverse magnetization (here $\hat{S}_y$ magnetization) at the time of the echo:

$$I_{\text{echo}} = \left\langle \hat{S}_y(t_{\text{echo}}) \right\rangle = \text{tr}\left\{\hat{\sigma}_{\text{echo}}\hat{S}_y\right\} = -\frac{1}{4}(1+\cos\varphi) \tag{2.74}$$

The echo intensity is directly linked to the effective flip angle of the rf pulse φ and therefore reports on on- vs off-resonant irradiation. Equation (2.74) shows that the echo intensity for full inversion of a nuclear transition drops to zero, while an echo intensity of 0.5 is detected when the rf pulse has no effect.
Since the absolute echo intensity is affected by many more experimental parameters, the ENDOR effect is usually quantified by the relative ENDOR efficiency F_{ENDOR}:

$$F_{\text{ENDOR}}^{\text{Davies}} = \frac{1}{2}\left|\frac{I_{\text{echo}}(\text{off res.}) - I_{\text{echo}}(\text{on res.})}{I_{\text{echo}}(\text{off res.})}\right| \tag{2.75}$$

This description assumes ideally selective microwave pulses and is thus valid for the

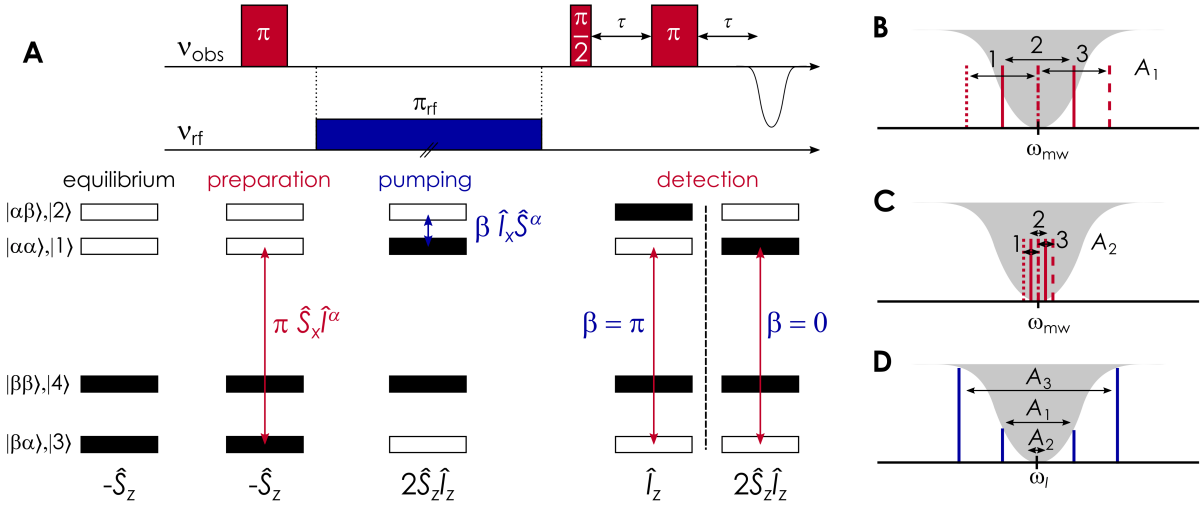

Figure 2.3: The Davies ENDOR experiment. **A**: Pulse sequence (top) and polarization transfer (bottom) for a $S = 1/2, I = 1/2$ four level spin system during the three stages of a selective Davies ENDOR experiment. EPR transitions and mw pulses are marked in red while nuclear transitions and rf pulses are marked blue. Populations are indicated by the fill-color of the boxes. Adapted from [5]. **B**/**C**: Distribution of spin packets (1,2,3) with the same hyperfine coupling within the powder EPR spectrum. Excitation profile of the preparation pulse is marked as grey area. **D**: ENDOR spectrum with three different hyperfine couplings ($A_3 > A_1 > A_2$) with their intensities effected by the central blindspot (grey area).

description of a single spin packet. In practice however, ENDOR is most often performed on poly-crystalline powders with an inhomogeneously broadened EPR line consisting of all possible molecular orientations and with microwave pulses of a finite length. In that case, Davies ENDOR can be considered as a so called *hole-burning* experiment and the previous description has to be altered slightly.

First, the length and shape of the "selective" microwave pulse needs to be considered: The excitation profile of a rectangular microwave pulse is described by a sinc-function, as that is the Fourier transformation of a rectangular time signal. The excitation bandwidth and therefore the width of the hole burned into the EPR line can be estimated by its pulselength t_p as:

$$\Delta\nu_{1/2} \approx \frac{1}{t_p} \tag{2.76}$$

Next, the distribution of resonance frequencies in the powder sample needs to be considered: In a broad EPR line, it is possible to excite either of the two (or both) EPR transitions for spin packets with the same hyperfine coupling but different resonance frequencies (Fig. 2.3, B and C). At the beginning of the Davies sequence, all transitions inside the excitation function are inverted with an efficiency, corresponding to the excitation profile. If the hyperfine coupling is large enough, i.e. larger than the excitation width of the

preparation pulse, spin packets where only one of the EPR transition is inverted exist (Fig. 2.3, B). If the hyperfine coupling is however smaller than the width of the excitation function (Fig. 2.3, C), both EPR transitions are excited at the same time.
After the preparation pulse, and if only one EPR transition was excited, the radio-frequency pulse transfers the inverted polarization from the *central hole* to a *side hole*. This reduces the depth of the *central hole*, which is detected as a reduction in echo intensity. If both EPR transitions are excited at the same time, no ENDOR effect is detected. Therefore, Davies ENDOR spectra of powder samples have a hole at the Larmor frequency[(g)] of the investigated nucleus, which suppresses small hyperfine couplings, that is directly related to the length of the preparation pulse (Fig. 2.3, D). Longer preparation pulses can be used to minimize the hole width, but this also has its drawbacks. Smaller excitation bandwidths reduce the overall number of spin packets excited and reduce the signal intensity. It is therefore mainly used for medium to large hyperfine couplings.

Mims ENDOR The preparation in Mims ENDOR is achieved by two non-selective $\pi/2$ pulses, separated by a time interval τ:

$$\begin{aligned} -\hat{S}_z \xrightarrow{\frac{\pi}{2}\hat{S}_x} \hat{S}_y \xrightarrow{\tau\hat{\mathcal{H}}_0} \xrightarrow{\frac{\pi}{2}\hat{S}_x} \hat{S}_z \cos\left(\frac{A}{2}\tau\right)\cos(\Delta\omega_S\tau) - \\ 2\hat{S}_z\hat{I}_z \sin\left(\frac{A}{2}\tau\right)\sin(\Delta\omega_S\tau) = \hat{\sigma}_{\text{prep}}^{\text{nonsel}} \end{aligned} \tag{2.77}$$

The generated electron nuclear double spin order $2\hat{S}_z\hat{I}_z$ contains modulation terms of the hyperfine interaction A and a resonance offset $\Delta\omega_S$. While the first is relatively obvious in an ENDOR experiment, the second means that the Mims ENDOR sequence is inherently designed for broadened EPR lines. After preparation, a selective rf pulse is applied in analogy to the Davies experiment:

$$\begin{aligned} \hat{\sigma}_{\text{prep}}^{\text{nonsel}} \xrightarrow{\varphi\hat{S}^\alpha\hat{I}_x} \hat{S}_z \cos\left(\frac{A}{2}\tau\right)\cos(\Delta\omega_S\tau) - \\ \Bigg\{ 2\hat{S}_z\hat{I}_z\left[\frac{1}{2}(1+\cos\varphi)\right] + \\ \hat{I}_z\left[\frac{1}{2}(1-\cos\varphi)\right] + \hat{I}_y\left[\frac{1}{2}\sin\varphi\right] + \\ 2\hat{S}_z\hat{I}_y\left[\frac{1}{2}\sin\varphi\right]\Bigg\} \sin\left(\frac{A}{2}\tau\right)\sin(\Delta\omega_S\tau) = \hat{\sigma}_{\text{ENDOR}} \end{aligned} \tag{2.78}$$

[(g)] this is true for the weak coupling case

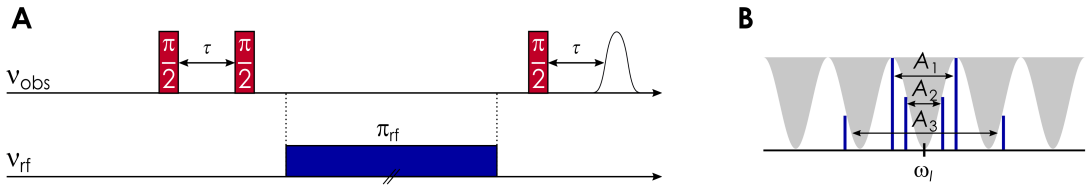

Figure 2.4: The Mims ENDOR experiment. **A**: Mims pulse sequence. Microwave pulses are marked in red while rf pulses are marked blue. **B**: ENDOR spectrum with three different hyperfine couplings ($A_3 > A_1 > A_2$) with their intensities effected by the Mims blindspot function (grey area).

The readout is achieved with a stimulated echo through another $\pi/2$ pulse:

$$\hat{\sigma}_{\text{ENDOR}} \xrightarrow{\frac{\pi}{2}\hat{S}_x} \xrightarrow{\tau\hat{\mathcal{H}}_0} -\hat{S}_y \Bigg\{ \cos^2\left(\frac{A}{2}\tau\right)\cos^2(\Delta\omega_S\tau) + \frac{1}{2}\sin^2\left(\frac{A}{2}\tau\right)\sin^2(\Delta\omega_S\tau)(1+\cos\varphi)\Bigg\} = \hat{\sigma}_{\text{echo}} \tag{2.79}$$

The echo intensity for on resonant rf irradiation ($\varphi = \pi$) and for the average over all excited resonance offsets $\Delta\omega_S$ can then be expressed as:

$$I_{\text{echo}} = \frac{1}{4}[1+\cos(A\tau)] \tag{2.80}$$

and the ENDOR efficiency becomes:

$$F_{\text{ENDOR}}^{\text{Mims}} = \frac{1}{2}\sin^2\left(\frac{A}{2}\tau\right) \tag{2.81}$$

The Mims ENDOR efficiency depends on the hyperfine coupling constant A and the chosen time interval τ in a periodic fashion, which means that it reaches maximum for $\tau = (2n+1)\pi/A$ and is zero for $\tau = 2n\pi/A$ with $n = 0,1,2,\ldots$. These zero intensities are usually called the *Mims blindspots*, which are mapped directly onto the ENDOR spectrum. Figure 2.4 B depicts the situation for three hyperfine couplings $A_{1,2,3}$, which would normally have equal intensity but are attenuated by the blindspot function (grey area) to yield three different intensities. Because hyperfine couplings in solids are most often tensors and not isotropic values, this blindspot function can lead to significant deviation of the ENDOR lineshapes from the original tensor shapes (e.g. dipolar Pake patterns). To make sure, that no spectral features are lost, Mims therefore needs to be performed with multiple τ-values, sometimes called τ-*average* Mims.

The non-selective preparation gives Mims ENDOR an overall sensitivity advantage over Davies ENDOR, since a lot more spin packets are excited and contribute to the overall echo intensity. Like in Davies ENDOR, the Mims ENDOR blindspot function causes a spectral hole at the center of the ENDOR spectrum, i.e. $\omega_I = 0$ in the weak coupling case.

This blindspot, as well as the periodic blind spots to either side, can however be adjusted by the choice of τ-value. In general, longer τ-values lead to a smaller hole and a shorter spacing between periodic blindspots. This means, that small hyperfine couplings may be investigated by the choice of very long preparation intervals (up to 4 µs).[14,60] The limiting factor for the choice of τ is however the phase memory time of the investigated PC, as the overall ENDOR sensitivity S_{ENDOR} is a product of the ENDOR efficiency and the echo intensity determined by relaxation:

$$S_{\mathrm{ENDOR}} = F_{\mathrm{ENDOR}}^{\mathrm{Mims}} \cdot I_{\mathrm{echo}}^{T_{\mathrm{m}}} = \frac{1}{2}\sin^2\left(\frac{A}{2}\tau\right) \cdot I_0 \exp\left(-\frac{\tau}{T_{\mathrm{m}}}\right) \tag{2.82}$$

This means, that a maximum τ-value exists, which is equivalent to the phase memory time of the system.[61]

The blind spot behaviour of nuclear spins $I > 1/2$ is different from the described formula, as the direct mapping of hyperfine coupling to the ENDOR spectrum is lost when nuclear quadrupole coupling comparable to the hyperfine coupling is present. An analytical derivation for nuclear spin $I = 1$ has been reported but the same for $I > 3/2$ was deemed unfeasible.[62] This point will be discussed for $I = 5/2$ nuclei in detail under Section 4.3.

Apart from the distortions caused by the blindspot functions, ENDOR spectra show the exact shape of the hyperfine and quadruple coupling tensors, since radio-frequency irradiation is used to directly drive the nuclear transitions. The spectral resolution of experimental ENDOR spectra is limited by the excitation bandwidth of the radio-frequency pulse and the intrinsic linewidth of the individual hyperfine or quadrupole transition.

2.3.4 EDNMR

The electron-electron double resonance (ELDOR)-detected NMR experiment[8] aims at the detection of forbidden EPR transitions and consists of two steps. The first part of the pulse sequence (Fig. 2.5) is a long microwave pulse, performed at variable microwave frequencies ν_{HTA}. Because of its length and microwave strength, it can no longer be considered as an ideal microwave pulse and treatment with the density operator formalism is not feasible.[51] Instead, a description of the individual EPR transitions is generally chosen to descibe the experiment. The pulse rotates the allowed and forbidden EPR transitions of the system by the angle $\varphi_{\mathrm{a,f}}$, determined by their transition probabilities defined under (2.70):

$$\varphi_{\mathrm{a,f}} = \omega_1 t_{\mathrm{HTA}} \sqrt{I_{\mathrm{a,f}}} = \varphi_0 \sqrt{I_{\mathrm{a,f}}} \tag{2.83}$$

Since the transition probability for forbidden EPR transitions is generally rather low, long irradiation times are necessary to invert them, i.e. to achieve $\varphi_{\mathrm{f}} \approx \pi$. Such long t_{HTA}

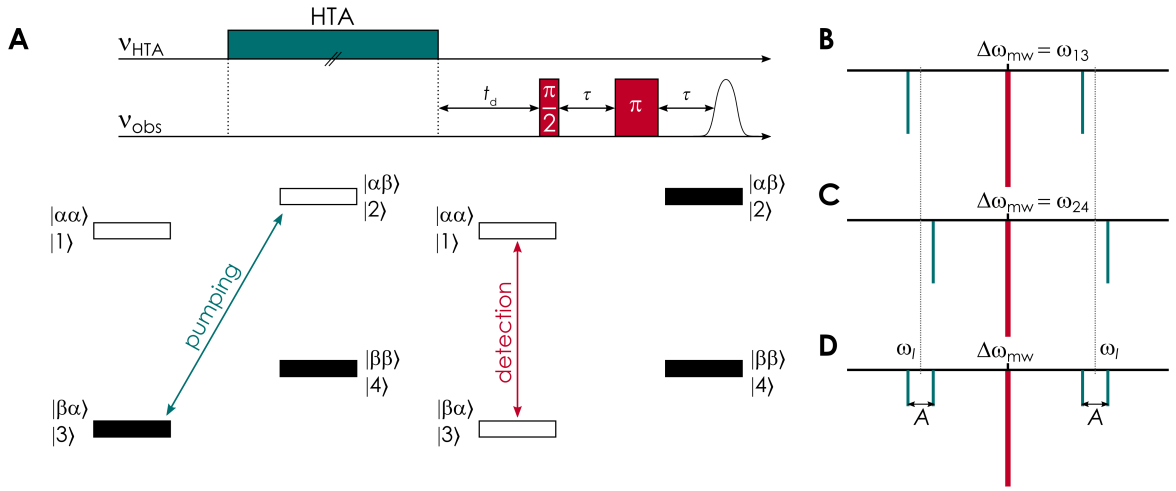

Figure 2.5: The EDNMR experiment. **A**: Pulse sequence (top) and polarization transfer (bottom) for a $S = 1/2, I = 1/2$ four level spin system during the two stages of an EDNMR experiment. Allowed EPR transitions and selective mw pulses are marked in red while forbidden EPR transitions and the HTA pulse are marked in cyan. Populations are indicated by the fill-color of the boxes. **B**/**C**/**D**: EDNMR spectra for selective detection on the allowed ω_{13} (**B**) or ω_{24} (**C**) transitions, as well as for detection in the powder (**D**). Adapted from [63].

causes high turning angles (HTA) for the allowed transitions, which is the reason for the name of the pulse. The thus created polarization difference is probed by a selective spin echo acting on the allowed EPR transitions. The EDNMR signal is then detected as a drop in echo intensity as a function of the HTA frequency. If the HTA pulse is on resonance with the allowed EPR transition that is also used for detection, the said transition is saturated and the echo intensity drops to 0. This is shown in Figure 2.5, B and C as the red signal at the center of the spectrum. If the HTA pulse is on resonance with one of the two forbidden transitions, the echo intensity is reduced in proportion to the turning angle φ_f (cyan signals).

As for the Davies ENDOR experiment, it is necessary to describe EDNMR of broad EPR lines as a *hole-burning* experiment. The hole of long microwave pulses is best described by a Lorentzian with a full width at half maximum (FWHM) of $\sim 2\omega_1$. The depth of this hole h can be described by the following expression:

$$h = 1 - I_a \cos\left(\omega_1 t_{HTA}\sqrt{I_f}\right) - I_f \cos\left(\omega_1 t_{HTA}\sqrt{I_a}\right) \tag{2.84}$$

Also in analogy to the Davies ENDOR description, the overlap of spin packets with the same hyperfine coupling but different resonance offsets leads to EDNMR spectra, which are the sum of the spectra expected for selective excitation of only one EPR transition (Fig. 2.5, D). Powder EDNMR spectra are dominated by the so called *central hole*, produced when the HTA pulse is on resonance with the allowed transitions and therefore equivalent to the hole

in the EPR line.

In the weak coupling case, the nuclear transitions are detected as doublets, split by the hyperfine coupling A around the nuclear Larmor frequencies ω_I symmetric around the *central hole*. In the case of strong coupling, they appear centered at half the hyperfine coupling and split by the nuclear Larmor frequency. If the hyperfine coupling is large enough to be resolved in the EPR line, signals can appear exclusively on one side of the EDNMR spectrum. This happens when the HTA pulse selects a specific nuclear spin manifold within the EPR spectrum. If the nuclear transitions fall inside the central hole, they are obscured by it and can no longer be detected.

The spectral shape of the anisotropic hyperfine patterns is distorted in the EDNMR spectra, because the transition probability of the forbidden EPR transitions depends on the angle θ, which describes the relative orientation of the hyperfine and g-tensors. It drops to 0 for the canonical orientations, obscuring the typical singularities of e.g. dipolar Pake patterns. Nuclear quadrupole coupling contributes to the non-secular terms of the spin Hamiltonian and can therefore increase the transition probabilities of the observed transitions in the EDNMR spectra.

The spectral resolution ν_R of EDNMR performed with rectangular HTA pulses is determined by the integration length t_int of the detected echo and can be described empirically by $\nu_\mathrm{R}(\mathrm{MHz}) = 1.4/t_\mathrm{int}(\mu\mathrm{s})$.[64] This means, that spectral resolution and signal-to-noise ratio of EDNMR spectra are intrinsically linked, since longer echo integration necessitates longer evolution times τ to avoid the overlap of echo and microwave pulses or spectrometer deadtime.

2.3.5 ESEEM/HYSCORE

The HYSCORE experiment, which is a two-dimensional version of the ESEEM experiment, aims at the detection of nuclear coherences via the EPR signal.[6,7] It consists of four steps depicted in Figure 2.6. The first part of the pulse sequence is comprised of two non-selective microwave pulses, separated by an evolution time τ. They prepare the spin system by producing allowed ($\mathrm{EC_a}$, red) and forbidden ($\mathrm{EC_f}$, cyan) electron coherences after the first pulse. As for the EDNMR experiment, this is only possible in the presence of pseudo-secular hyperfine coupling:

$$\hat{\sigma}_\mathrm{eq} = -\hat{S}_z \xrightarrow{\frac{\pi}{2}\left(\hat{S}_x \cos\eta + 2\hat{S}_y\hat{I}_y \sin\eta\right)} \hat{S}_y \cos\eta - 2\hat{S}_x\hat{I}_y \sin\eta = \hat{\sigma}_1 \tag{2.85}$$

The evolution time τ under the tilted Hamiltonian (Eq. 2.63) generates:

$$\begin{aligned}\hat{\sigma}_1 \xrightarrow{\tau\hat{\mathcal{H}}_0^{\text{tilted}}} & \hat{S}_y \cos\eta \cos(\Delta\omega_S\tau)\cos\left(\frac{\omega_-}{2}\tau\right) - \hat{S}_x \cos\eta \sin(\Delta\omega_S\tau)\cos\left(\frac{\omega_-}{2}\tau\right) \\ & -2\hat{S}_x\hat{I}_z \cos\eta\cos(\Delta\omega_S\tau)\sin\left(\frac{\omega_-}{2}\tau\right) + 2\hat{S}_y\hat{I}_z\cos\eta\sin(\Delta\omega_S\tau)\sin\left(\frac{\omega_-}{2}\tau\right) \\ & -2\hat{S}_x\hat{I}_y \sin\eta\cos(\Delta\omega_S\tau)\cos\left(\frac{\omega_+}{2}\tau\right) + 2\hat{S}_x\hat{I}_x\sin\eta\cos(\Delta\omega_S\tau)\sin\left(\frac{\omega_+}{2}\tau\right) \\ & +2\hat{S}_y\hat{I}_y\sin\eta\sin(\Delta\omega_S\tau)\cos\left(\frac{\omega_+}{2}\tau\right) - 2\hat{S}_y\hat{I}_x\sin\eta\sin(\Delta\omega_S\tau)\sin\left(\frac{\omega_+}{2}\tau\right) = \hat{\sigma}_2\end{aligned} \tag{2.86}$$

And the second $\pi/2$ pulse produces the following density operator:

$$\begin{aligned}\hat{\sigma}_2 \xrightarrow{\frac{\pi}{2}\left(\hat{S}_x\cos\eta + 2\hat{S}_y\hat{I}_y\sin\eta\right)} & \cos(\Delta\omega_S\tau)\left[\cos^2\eta\cos\left(\frac{\omega_-}{2}\tau\right) + \sin^2\eta\cos\left(\frac{\omega_+}{2}\tau\right)\right]\hat{S}_z \\ & + \sin(\Delta\omega_S\tau)\left[\cos^2\eta\sin\left(\frac{\omega_-}{2}\tau\right)2\hat{S}_z\hat{I}_z + \sin^2\eta\sin\left(\frac{\omega_+}{2}\tau\right)\hat{I}_z\right] \\ & - \sin(\Delta\omega_S\tau)\sin(2\eta)\sin\left(\frac{\omega_\beta}{2}\tau\right)\left[\cos\left(\frac{\omega_\alpha}{2}\tau\right)\hat{S}^\alpha\hat{I}_x + \sin\left(\frac{\omega_\alpha}{2}\tau\right)\hat{S}^\alpha\hat{I}_y\right] \\ & - \sin(\Delta\omega_S\tau)\sin(2\eta)\sin\left(\frac{\omega_\alpha}{2}\tau\right)\left[\cos\left(\frac{\omega_\beta}{2}\tau\right)\hat{S}^\beta\hat{I}_x + \sin\left(\frac{\omega_\beta}{2}\tau\right)\hat{S}^\beta\hat{I}_y\right]\end{aligned} \tag{2.87}$$

The first two terms describe nuclear polarization, while the last two terms describe nuclear coherences (NC, light and dark blue) in the two nuclear sub-manifolds α and β. During the first evolution interval t_1, the nuclear coherences evolve. The third microwave pulse inverts the electron spin manifolds, which also exchanges the nuclear coherences. After a second evolution time t_2 the nuclear coherences are converted to detectable electron coherences by the final microwave pulse. The modulations of the stimulated echo are then recorded as a function of the two evolution times. As evident from expression (2.87), many different pathways contribute to the overall echo modulation V:

$$V = 1 - \frac{k}{4}\sum V_i \tag{2.88}$$

For a single spin packet, the intensity of the modulation is determined by the modulation depth parameter k:

$$k = \sin^2(2\eta) = \left(\frac{B\omega_I}{\omega_\alpha\omega_\beta}\right)^2 \tag{2.89}$$

The important modulation contributions for the HYSCORE experiment are contained in two terms:

$$V_a = C(\tau)\cos^2\eta\left[\cos\left(\omega_\alpha t_1 + \omega_\beta t_2 + \omega_+\tau/2\right) + \cos\left(\omega_\beta t_1 + \omega_\alpha t_2 + \omega_+\tau/2\right)\right] \tag{2.90}$$

$$V_b = -C(\tau)\sin^2\eta\left[\cos\left(\omega_\alpha t_1 - \omega_\beta t_2 + \omega_-\tau/2\right) + \cos\left(\omega_\beta t_1 - \omega_\alpha t_2 - \omega_-\tau/2\right)\right] \tag{2.91}$$

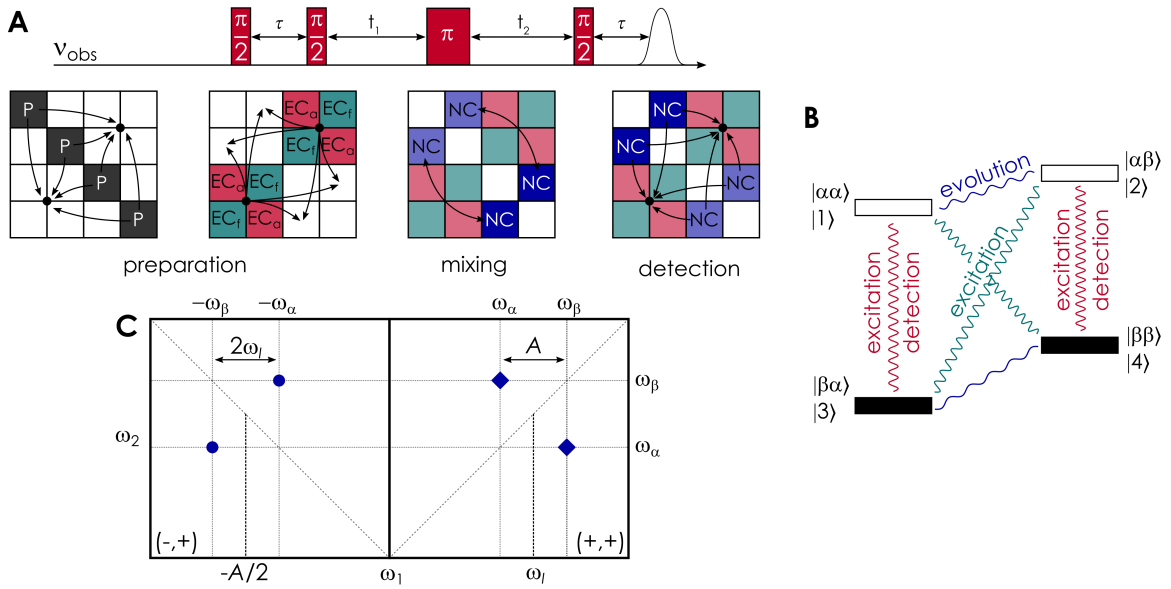

Figure 2.6: The HYSCORE experiment. **A**: Pulse sequence (top) and polarization/coherence transfer scheme (bottom). Microwave pulses are shown in red. The transfer scheme depicts a graphic representation of the spin Hamiltonian with polarizations (P) marked in grey at the beginning of the pulse sequence. Allowed (EC_a) and forbidden (EC_f) electron coherences are shown in red and cyan, respectively. Nuclear coherences (NC) are shown in dark and light blue to distinguish between the two electron spin manifolds. Transfers and evolutions are marked by black arrows. **B**: Energy level diagram with coherences shown in the same color scheme. **C**: HYSCORE spectrum with two signals. Signal in the weak coupling case (blue squares) appear centered at ω_I in the (+,+)-quadrant, while signal in the strong coupling case (blue circles) appear cantered at half the hyperfine coupling $A/2$ in the (-,+)-quadrant. Figure adapted from [65].

A HYSCORE spectrum is then generated by the discrete Fourier transformation of the experimental time trace. It can be split into the four quadrants, denoted by the relative sign of the frequency axis. Out of the four quadrants, two pairs are mutually symmetric ((+,+) and (-,-)/(-,+) and (+,-)) and so it is enough to inspect only two of them. Figure 2.6, C shows a hypothetical HYSCORE spectrum with two contributions in either of the two quadrants. The contributions to the (+,+)-quadrant originate from the V_a modulation term, because it has a positive phase modulation ω_+. This dominates when $\eta \approx 0/\pi$, which describes the weak coupling case. Due to the 2D nature of the experiment, signals appear split along the anti-diagonal by the hyperfine coupling A centered at ω_I.

Signals in the (-,+)-quadrant originate from the V_b modulations due to its negative phase modulation ω_-, which dominates for $\eta \approx \pi/2$, i.e. in the strong coupling case. Signals here appear to be split along the anti diagonal by twice the nuclear Larmor frequency, while being centred at half the hyperfine coupling.

The τ-dependent factor C in in the modulation terms (Eq. (2.90) and (2.91)) accounts for the first evolution interval, which introduces blindspots into the HYSCORE spectrum, similar to the situation in Mims ENDOR. Since HYSCORE is a FT method, these blindspots

are fixed at the same frequencies for a given evolution time τ, regardless of the hyperfine coupling. To gain the full correlation pattern, multiple HYSCORE experiments with different τ-values have to be recorded.

In analogy to EDNMR, HYSCORE does not display the full shape of the hyperfine or quadrupole coupling tensors, because the modulation depth depends on the pseudo-secular coupling B, which vanishes at the canonical orientations of the coupling tensors. Broad coupling features appear as so called *ridges* in the HYSCORE spectrum, whose extent across the anti-diagonal gives information about the coupling size while the curvature can be analyzed to get information about the dipolar hyperfine coupling.

HYSCORE spectra of nuclei with quadrupole coupling become significantly more complicated, since the number of nuclear transitions that can evolve increases. An essential feature of HYSCORE is the separation of hyperfine and quadrupole coupling in two different dimensions. Quadruple coupling separates the individual frequencies along the diagonal while the hyperfine coupling causes broad features across the anti-diagonal. More detailed information about HYSCORE of $I = {}^5/_2$ nuclei is given in Chapter 6.

The spectral resolution of HYSCORE is determined by the sampling interval and the length of the detected time traces. Longer evolution times and smaller time intervals lead to increased resolution but also to longer acquisition times. This means that spectral resolution and signal-to-noise ratio are linked.

3 Materials and methods

This chapter will describe the materials and methods used throughout this work. Certain aspects will be repeated in the following chapters since they were included for the respective publications.

3.1 Sample preparation

3.1.1 Protonated and deuterated BDPA

Protonated α,γ-bisdiphenylene-β-phenylallyl (BDPA, Fig. 3.1, A) was purchased from Sigma Aldrich as 1:1 complex with benzene. Deuterated BDPA was synthesized by the facility for synthetic chemistry of the MPI for biophysical chemistry in Göttingen in 2012, following the synthesis procedure for protonated BDPA.[66] Both radicals were dispersed in polystyrene (PS, Sigma Aldrich, 35000 average molecular weight) by dissolution of radical and matrix in $CHCl_3$, followed by drying under nitrogen gas and grinding to a fine powder. This was performed by B. Angerstein in our research group.

3.1.2 Nitroxide radicals

4-hydroxy-2,2,6,6-tetramethylpiperidin-1-oxyl radical (TEMPOL, $T_6^{\bullet}$, Fig. 3.1, B) and 90 % ^{17}O labelled water ($H_2{}^{17}O$) was purchased from Sigma Aldrich. 3-Hydroxymethyl-(1-oxy-2,2,5,5-tetramethylpyrroline) (TEMPYL, $T_5^{\bullet}$, Fig. 3.1, C) was purchased from Santa Cruz Biotechnology. TEMPOL and TEMPYL were dissolved in $H_2{}^{17}O$ and mixed with glycerol to yield a concentration of 200 µM radical in a solution of 80 % $H_2{}^{17}O$ and 20 % glycerol (v/v).

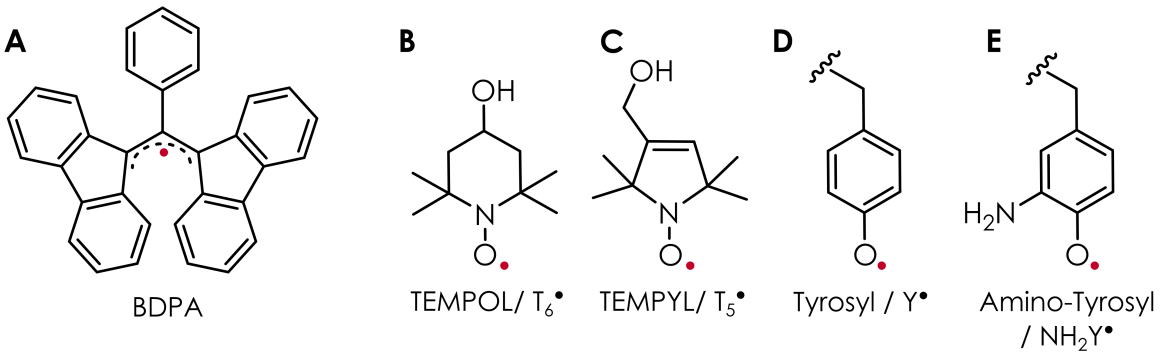

Figure 3.1: Overview of investigated radicals. **A**: BDPA/α,γ-bisdiphenylene-β-phenylallyl **B**: TEMPOL/4-hydroxy-2,2,6,6-tetramethylpiperidin-1-oxyl radical **C**: TEMPYL/3-Hydroxymethyl-(1-oxy-2,2,5,5-tetramethylpyrroline) **D**: Tyrosyl radical **E**: Amino-tyrosyl radical.

3.1.3 Radical intermediates in E. coli RNR

The incorporation of unnatural amino acids (UAAs) into *E. coli* ribonucleotide reductase followed the previously reported protocols.[67,68] Proteins with UAAs were expressed and purified by Brandon Greene and Chang Cui (MIT). Wild-type (wt) protein was expressed and purified by myself during a stay at MIT.

Purified α_2 (wt, $Y_{730}F$, NH_2Y_{731} and NH_2Y_{730}) was exchanged into 5 mM 4-(2-hydroxyethyl)-1-piperazineethanesulfonic acid (HEPES) buffer (pH 7.6) containing 1.5 mM $MgSO_4$, 0.1 mM ethylenediaminetetraacetic acid (EDTA) and 1 mM β-mercaptoethanol with Amicon spin filters (30 000 NMWL). 100 µL protein solution was supplemented with 300 µL buffer and spun at 12 000 g for 5 min. This process was repeated 6 times. Adenosine triphosphate (ATP) and cytidine diphosphate (CDP) were added and the protein concentration was adjusted with assay buffer (50 mM HEPES, pH 7.6, 15 mM $MgSO_4$, 1 mM EDTA) to yield a final concentration of 30 µM α_2, 500 µM ATP and 167 µM CDP. 100 µL quantities of this solution were frozen in liquid nitrogen and lyophilized overnight.

The samples were rehydrated in 10 µL $H_2{}^{17}O$ to yield solutions of 300 µM α_2, 5 mM ATP and 1.67 mM CDP in assay buffer. Recovery of wild-type (wt) α_2 activity after the lyophilization procedure was checked by spectrophotometric activity assay and found to be 90 - 100 % (data not shown).

Purified β_2 (wt, F_3Y_{122}, $F_3Y_{122}/E_{52}Q$) was exchanged into assay buffer with the aforementioned protocol and had the following concentrations: 890 µM wt-β_2, 980 µM F_2Y_{122}-β_2, 1600 µM $F_3Y_{122}/E_{52}Q$.

EPR samples were prepared by mixing the previously described α_2 solutions containing substrate and effector with the corresponding β_2 solution (Table 5.2) and addition of $H_2{}^{17}O$ to a final concentration of 180 µM $\alpha_2\beta_2$, 3 mM ATP and 1 mM CDP. The final amount of $H_2{}^{17}O$ was approx. 80 %. The reaction mixtures were hand quenched in liquid N_2 inside

EPR tubes. The quench times followed the previously established protocols for maximum radical yield.[25,26,69]

EPR samples containing only β_2 with $H_2{}^{17}O$ were prepared by diluting the aforementioned solutions of β_2 (wt and F_3Y_{122}) with $H_2{}^{17}O$ to a final protein concentration of 180 µM and approx. 90 % $H_2{}^{17}O$. The β_2 solution was left to incubate for 10 min at 4°C to allow for sufficient exchange of water molecules within the protein, i.e. close to Y_{122}, and subsequently frozen in liq. N_2 inside the EPR tubes.

3.1.4 EPR samples

1.6 mm outer diameter (OD)/1.1 mm inner diameter (ID) quartz tubes (WG-221T) and 0.9 mm OD/0.5 mm ID suprasil tubes (WG-213ST9S) were purchased from Wilmad-Lab Glass. 0.33 mm OD/0.2mm ID (CV2033-S-100) suprasil capillaries were purchased from CM scientific. Q-band samples contained $10 - 12$ µL solution in 1.6 mm OD/1.1 mm ID quartz tubes. W-band samples contained 2 µL solution in 0.9 mm OD/0.5 mm ID suprasil tubes. 263 GHz samples contained $30 - 50$ nL solution in 0.33 mm OD/0.2 mm ID suprasil capillaries.

3.2 Experimental setup

3.2.1 Spectrometers

Q-band: 1.2 T, 34 GHz 34 GHz experiments were performed on a Bruker E580 pulsed Q-band spectrometer with a 170 W microwave amplifier (AIE 187Ka-13402) leading to typical π-pulse lengths of $\sim$ 12 ns at maximum output power. The ENDOR resonator (Model EN5107D2) was placed in a liquid helium fed cryostat (Oxford Instruments). Radio-frequency pulses were generated by a two-channel rf pulse forming unit (Bruker Dice-II) and amplified by a 600 W rf amplifier (Amplifier Research, Model 600A600A).

W-band: 3.4 T, 94 GHz 94 GHz experiments were performed on a Bruker E680 pulsed W-band spectrometer with a 2 W microwave amplifier (Quinstar) leading to typical π-pulse lengths of $\sim$ 20 ns at maximum output power. The ENDOR resonator (Model EN600-1021H) was placed in a liquid helium fed cryostat (Oxford Instruments). Radio-frequency pulses were generated by a two-channel rf pulse forming unit (Bruker Dice-I/II) and amplified by a 250 W rf amplifier (Amplifier Research, Model 250A250A).

mm-band: 9.4 T, 263 GHz 263 GHz experiments were performed on a prototype Bruker E780 spectrometer with a 100 mW microwave amplifier multiplier chain (AMC, Virginia

Diodes) leading to typical π-pulse lengths of $\sim 32\,\mathrm{ns}$ at maximum output power. The ENDOR resonator (Model E9501510) was placed in a liquid helium fed cryostat (Oxford Instruments). Radio-frequency pulses were generated by a two-channel rf pulse forming unit (Bruker Dice-II) and amplified by a 125 W rf amplifier (Amplifier Research, Model 125W1000).

3.2.2 EPR measurements

Pulse sequences for the EPR experiments are given in the following section. General experimental details including the number of scans, shot repetition time (SRT), shots/point, pulse lengths (mw and rf) and delay times are given in the captions of the figures or in specific sections of the following chapters.

3.2.2.1 Echo-detected EPR (ESE)

Pulse sequence: $\pi/2 - \tau - \pi - \tau -$ echo
x-axis: magnetic field B_0

3.2.2.2 Microwave nutation

Pulse sequence: $t_\mathrm{p} - t_\mathrm{d} - \pi/2 - \tau - \pi - \tau -$ echo
x-axis: time increment of the the first pulse t_p. For the optimization of selective pulses in the range of hundreds of nanoseconds, delay times t_d of more than 10 µs were chosen to avoid overlap of different echos. The mw nutation experiment was used to determine the bandwidth, i.e. Q value of the resonators used for EDNMR experiments at the Q- and W-band spectrometers. For this, a series of mw nutation experiments were performed with a sample of protonated BDPA (0.1 % in PS) while varying the detection frequency and resonance field in a range of $\sim 200 - 500\,\mathrm{MHz}$ around the center of the resonator dip. Results are shown in Appendix A.

3.2.2.3 Relaxation measurements

Inversion recovery Pulse sequence: $\pi - t_\mathrm{d} - \pi/2 - \tau - \pi - \tau -$ echo
x-axis: delay time t_d between the first two pulses. The *spin-lattice* relaxation time was determined from a bi-exponential fit to the experimental time trace as the larger time constant:

$$I = I_{0,1} \exp\left(-\frac{t_\mathrm{d}}{T_\mathrm{1e}}\right) + I_{0,2} \exp\left(-\frac{t_\mathrm{d}}{T_\mathrm{SD}}\right) + C \qquad \text{with } T_\mathrm{1e} > T_\mathrm{SD} \qquad (3.1)$$

Phase memory time Pulse sequence: $\pi/2 - \tau - \pi - \tau -$ echo or $\pi/2 - \tau - \pi/2 - T - \pi/2 - \tau -$ echo

x-axis: delay time 2τ. For phase memory time measurements using the stimulated echo, the delay time T between the second and third pulse greatly influences the outcome (see Sec. 5.5.1.3) and needs to be chosen carefully. The phase memory time T_m was determined from a mono-exponential fit[(a)] to the experimental time trace:

$$I = I_0 \exp\left(-\frac{\tau}{T_m}\right) + C \tag{3.2}$$

3.2.2.4 Radio-frequency nutation

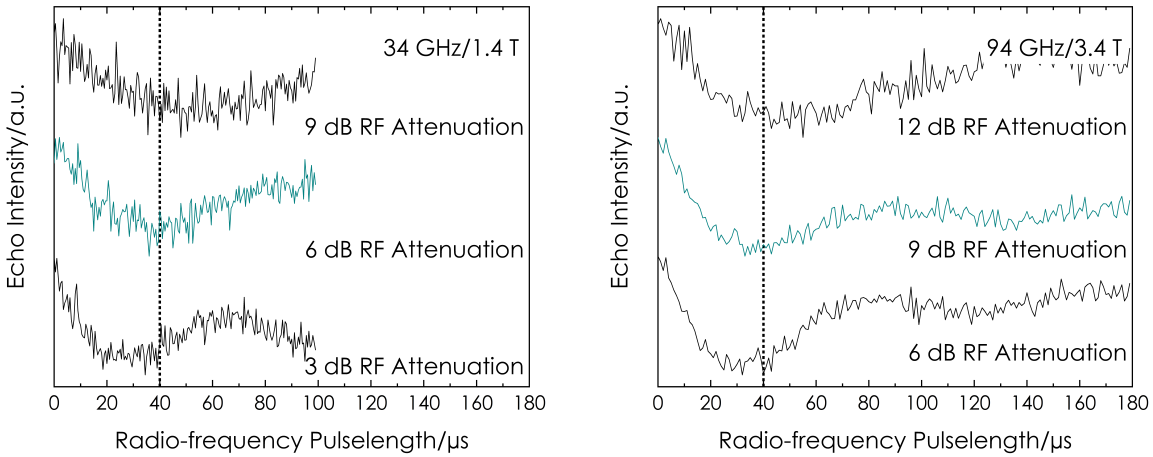

Figure 3.2: Radio-frequency nutation experiments of ^{17}O nuclei at varying rf attenuations at 1.2 T (Q-band, left) and 3.4 T (W-band, right). The nutation with the experimentally used attenuation is colored in cyan and the used radio-frequency pulse length is marked by a dotted line. Experimental parameters: 50 K, $\pi/2 = 6/10$ ns, $\tau = 390$ ns, RF = $1 \rightarrow 100/180$ µs, 30 shots/point, 5 ms SRT.

Pulse sequence: $\pi/2 - \tau - \pi/2 - t_p(\mathrm{rf}) - t_d - \pi/2 - \tau -$ echo

x-axis: length of the rf-pulse $t_p(\mathrm{rf})$. Radio-frequency nutation experiments were performed with the Mims ENDOR sequence to achieve the highest possible sensitivity. Experiments were recorded on- and off-resonance and divided to yield the background free nutation. The protein sample of $Y^{\bullet}_{356}$ (Y_{730}F-α) was used to record the measurements at 34 and 94 GHz, with the signal at $\nu_n(^{17}\mathrm{O}) = +0.3$ MHz used for the on-resonance measurements and off-resonance measurements performed at $\nu_n(^{17}\mathrm{O}) = +5$ MHz. The sample was chosen, since it had the most defined ^{17}O coupling features and showed the highest protein radical yield. The power was adjusted to yield 40 µs rf pulses at both fields. Figure 3.2 shows the power dependent rf nutations.

[(a)] because the phase memory time contains many different contributions, a fit is often not very successful and a qualitative judgement is more reasonable

3.2.2.5 ENDOR

Mims Pulse sequence: $\pi/2 - \tau - \pi/2 - \pi(\mathrm{rf}) - t_\mathrm{d} - \pi/2 - \tau - \mathrm{echo}$
x-axis: frequency of π(rf)-pulse. Mims ENDOR experiments were performed with either full microwave power (6, 10 and 32 ns at 34, 94 and 263 GHz, respectively) to maximize signal intensity, or with 40 ns pulses for an increased and constant orientation selectivity. The τ-value used in Mims ENDOR was 390 ns across all measurements. This value was optimized, based on simulations of the ^{17}O ENDOR spectrum of the $Y^{\bullet}_{356}$ radical and its phase-memory time. See Sections 4.3 and 5.5.1.5.

Davies Pulse sequence: $\pi_\mathrm{sel.} - \pi(\mathrm{rf}) - t_\mathrm{d} - \pi/2 - \tau - \pi - \tau - \mathrm{echo}$
x-axis: frequency of π(rf)-pulse. Davies ENDOR experiments were performed with a 400 ns preparation pulse as a compromise between overall signal intensity and minimal size of the central blindspot. The detection was performed with selective pulses (200/400 ns) for the nitroxide radicals and with non-selective pulses (20/40 ns) for the protein radicals. Selective read-out gave slightly higher signal-to-noise in the ENDOR spectra, if the phase memory time of the radicals was long enough (data not shown).

All ENDOR experiments were performed with $10 - 20\,\mu\mathrm{s}$ delay time t_d between the rf pulse and the subsequent read-out sequence to reduce the effects of rf heating , which can lead to baseline distortions (see Appendix B). The radio-frequency was swept stochastically to reduce heating and saturation effects and the entire echo was integrated to yield the ENDOR spectra. Experiments were recorded in batches of 5 - 100 scans as a 2D dataset. The batches were individually phase corrected to account for phase drifts during long acquisition and then summed. The sum spectra were baseline corrected (first-order polynomial) and normalized to the maximum intensity.

3.2.2.6 HYSCORE

Pulse sequence: $\pi/2 - \tau - \pi/2 - t_1 - \pi - t_2 - \pi/2 - \tau - \mathrm{echo}$
x/y-axis: pulse delays t_1 and t_2. HYSCORE experiments were recorded with with maximum microwave power resulting in 6 ns and 12 ns $\pi/2$ pulses at 34 and 94 GHz, respectively. A 16-step phase cycle was used to remove unwanted echo contributions. Experiments were performed with two inter-pulse delays τ chosen to either maximize ($\tau = n/\nu_\mathrm{n}$) or minimize ($\tau = (n + 0.5)/\nu_\mathrm{n}$) the signal at the respective nuclear Larmor frequency of ^{17}O. The center of the produced echo (32 ns) was integrated to yield the time traces. The experimental datasets comprised a total of 300 by 300 data points. The time domain data was baseline corrected (third-order polynomial), apodized with a hamming function,

zero-filled and Fourier transformed to yield the frequency spectrum with a resolution of 0.1 MHz. Frequency spectra were normalized to the ^{17}O signal.

3.2.2.7 EDNMR

Pulse sequence: $t_{\mathrm{HTA}} - t_{\mathrm{d}} - \pi/2 - \tau - \pi - \tau -$ echo
x-axis: frequency of HTA-pulse. The microwave frequency of the detection echo was set to the operating frequency of the resonator and the power adjusted to produce $\pi/2$-pulses of 100 ns and π-pulses of 200 ns, checked by mw nutation experiments. The power of the HTA pulse was adjusted for each experiment individually and the $\omega_1/2\pi$ determined as the half-width at half maximum (HWHM) of a Lorentz fit to the central blindspot. Experiments were performed with 20 µs HTA pulses at 34 GHz and 30 µs HTA pulses at 94 GHz. A long delay t_{d} of 10 µs was chosen to allow a full relaxation of any coherences produced by the HTA pulse. Experiments with shorter delays showed no significant loss in EDNMR signal (data not shown).
The τ-value in the detection echo was set to 1400 ns, which ensures a sufficient delay between the end of the spectrometer dead time and the echo ($\sim$ 1000 ns), while limiting signal loss due to relaxation. The experiments were performed with a 2-step phase cycle of the $\pi/2$-pulse to remove artefacts from long free induction decays (FIDs) produced by the π-pulse in combination with the narrow hole of the HTA pulse. The echo was integrated in a range of $\pm$1000 ns around its maximum to increase the spectral resolution.

3.3 Spectral simulations

Spectral simulations were performed using software implemented on the *MATLAB* programming platform. Most simulations used the *EasySpin* 5.2.33 spectral simulation package. Home-written simulation codes were developed on the same programming platform to understand and validate the *EasySpin* simulations of ^{17}O hyperfine experiments (see Chapter 4).

3.3.1 EPR simulations

Echo-detected field sweep spectra were simulated using the `pepper` function with a matrix diagonalization method (`Opt.method='matrix'`). Simulations used the experimentally determined microwave frequency, while the resonance fields of the canonical *g*-tensor orientations were determined relative to the $B_0 \| g_3$ singularity in the spectra. This was done to compensate for incorrect measurement of the magnetic fields.

3.3.2 ENDOR simulations

Davies ENDOR simulations used the `salt` function with a matrix diagonalization method (`Opt.method='matrix'`) if not declared otherwise.[70] Mims ENDOR simulations used the `saffron` function.[71] Simulations were restricted to the ENDOR nuclei to reduce calculation time significantly. Simulated ENDOR spectra were normalized to the maximum intensity.

3.3.3 EDNMR simulations

EDNMR was simulated with a code initially described by *Cox et al.*[12] and further developed by *Wili et al.*[72] It is implemented into *EasySpin* by the function *horseradish*, which is available from the electronic supplementary information of reference [72]. The code was optimized as described under Section 4.4. EDNMR simulations were normalized to the maximum intensity of the ^{17}O signal.

3.3.4 HYSCORE simulations

HYSCORE simulations used the `saffron` function. Simulated time traces were treated identical to the experimental traces using apodization and zero filling. Fourier transformed spectra were normalized to the ^{17}O signal.

3.4 Density functional theory calculations

DFT models were calculated using the *Orca* 4.0.1.2 software package.[73] Geometry optimization was performed using the BP86[74,75] combined with Ahlrichs' triple-ζ quality basis set def2-TZVP[76,77] and the RIJCOSX[78] approximation (def 2/J auxiliary basis set). The SCF calculations were supplemented with Grimmes dispersion correction (d3bj).[79,80] SCF energies, magnetic properties and coupling parameters were calculated from the geometry optimized structures using the hybrid B3LYP[75,81,82] combined with the EPR-II basis set[83] for the all atoms except sulfur, for which the IGLO-II functional was used. The RIJCOSX approximation and dispersion correction were also used.
The water and protein environment was approximated by a conductor-like polarization model (CPCM) with polarity epsilon of 80 and 24 for the nitroxides and the tyrosyl radicals, respectively.[25,26] For the large model of $NH_2Y^{\bullet}_{730}$ an epsilon of 4 was used in accordance with the previous model.[24]

Simulation of ^{17}O hf spectroscopy experiments

4

The extraction of coupling parameters from hyperfine spectra is generally only possible with the aid of accurate numerical simulations. Today, multiple programs are available for the simulation of EPR experiments. Most popular among those are *EasySpin*[70,71] and *Spinach*[84], both implemented on the *Matlab* programming platform. These programs have been developed and maintained for many years and are designed to perform a large number of different simulations in the most time efficient way. This necessitates in a number of *simplifications* or *shortcuts*, which need to be evaluated for every investigated system. The nature of these programs, however, make it difficult to follow the entire simulation and to directly correlate changes in the input of the simulations to the resulting spectra. In this particular case, the simulation of ^{17}O ENDOR experiments of tyrosyl radicals using *EasySpin* resulted in asymmetric spectra and the explanation for this behaviour was not readily found. Home-written simulation routines were developed for the calculation of ^{17}O ENDOR to find the nature of the asymmetry and to validate the *EasySpin* simulation approach for the investigated systems.

Generally, two different simulation approaches can be distinguished: A) Static simulations, in which the transition energies/frequencies between the energy states are calculated and evaluated with respect to the desired experiments; B) dynamic simulations, in which the evolution of the density matrix throughout the steps of the experiment is explicitly calculated by the *Liouville-von Neumann* equation (see Sec. 2.2).[58] The following sections will show both approaches:

4.1 Home-written static EPR/ENDOR simulations

The home-written code contains multiple approaches for the simulation of ENDOR spectra to compare their validity for the case of ^{17}O nuclei. The code is based on the separation of coupled spin systems with an electron coupled to multiple nuclei. These are separated

into EPR and ENDOR active, i.e. strongly and weakly coupled, nuclei. This requires the high-field approximation for the electron spin, which entails the following:[51]

- much larger electron Zeeman energy compared to the hyperfine-coupling terms $E_{\mathrm{EZ}} \gg E_{\mathrm{HF}}$
- small g-anisotropy $g_{\mathrm{max}}/g_{\mathrm{min}} \approx 1$

Both conditions are met for the organic radicals at the magnetic fields investigated in this thesis. The full Hamiltonian is therefore treated as sum of separable sub-Hamiltonians.

$$\hat{\mathcal{H}}_S = \hat{\mathcal{H}}_S^{\mathrm{EPR}} + \hat{\mathcal{H}}_S^{\mathrm{ENDOR}} \tag{4.1}$$

with the Zeeman and coupling tensors (see Sec 2.1):

$$\begin{aligned}\hat{\mathcal{H}}_S^{\mathrm{EPR}} &= \frac{\mu_{\mathrm{B}}}{\hbar}\boldsymbol{B}^{\mathsf{T}}\boldsymbol{g}\hat{\boldsymbol{S}} + \frac{\mu_{\mathrm{N}}}{\hbar}g_{\mathrm{n}}^{\mathrm{EPR}}\boldsymbol{B}^{\mathsf{T}}\hat{\boldsymbol{I}}^{\mathrm{EPR}} + \hat{\boldsymbol{S}}\boldsymbol{A}\hat{\boldsymbol{I}}^{\mathrm{EPR}} + \hat{\boldsymbol{I}}^{\mathrm{EPR}}\boldsymbol{P}\hat{\boldsymbol{I}}^{\mathrm{EPR}} \\ \hat{\mathcal{H}}_S^{\mathrm{ENDOR}} &= \frac{\mu_{\mathrm{B}}}{\hbar}\boldsymbol{B}^{\mathsf{T}}\boldsymbol{g}\hat{\boldsymbol{S}} + \frac{\mu_{\mathrm{N}}}{\hbar}g_{\mathrm{n}}^{\mathrm{ENDOR}}\boldsymbol{B}^{\mathsf{T}}\hat{\boldsymbol{I}}^{\mathrm{ENDOR}} + \hat{\boldsymbol{S}}\boldsymbol{A}\hat{\boldsymbol{I}}^{\mathrm{ENDOR}} + \hat{\boldsymbol{I}}^{\mathrm{ENDOR}}\boldsymbol{P}\hat{\boldsymbol{I}}^{\mathrm{ENDOR}}\end{aligned} \tag{4.2}$$

The EPR and ENDOR sub-Hamiltonians can then be individually diagonalized to determine the relevant energy states of the system. This cuts down the calculation time of numerical matrix diagonalization significantly, as it depends on the matrix-dimension. E.g. full Hamiltonian of a coupled spin system: $S = {}^1/_2$, $I^{\mathrm{EPR}} = 1$, $I^{\mathrm{ENDOR}} = {}^5/_2$ - 36x36 matrix, EPR Hamiltonian - 6x6, ENDOR Hamiltonian - 12x12.
In the code, all transition frequencies between two states k and l of the sub-system are calculated. The relevant EPR or ENDOR transitions are selected by computing the transition matrix elements p_{kl}:

$$p_{\mathrm{kl}}^{\mathrm{EPR}} \propto \left\langle k|\hat{S}_x|l\right\rangle^2 \qquad \text{and} \qquad p_{\mathrm{kl}}^{\mathrm{ENDOR}} \propto \left\langle k|\hat{I}_x|l\right\rangle^2 \tag{4.3}$$

In addition to the diagonalization approach, the Hamiltonian of the EPR or ENDOR spin system can be calculated in the high-field approximation for both electron and nucleus. In this case, both spins are assumed to be fully quantified along the external magnetic field. The spin Hamiltonian can then be expressed purely by the z-Operators:[(a)]

$$\hat{\mathcal{H}}_S^{\mathrm{ENDOR}} = \frac{\mu_{\mathrm{B}}}{\hbar}g_{\mathrm{eff}}B_0\hat{S}_z + \frac{\mu_{\mathrm{N}}}{\hbar}g_{\mathrm{n}}B_0\hat{I}_z + A_{zz}\hat{S}_z\hat{I}_z + \frac{1}{2}\hat{P}_{zz}\left(3\hat{I}_z^2 - I(I+1)\right) \tag{4.4}$$

In this case, the Hamiltonian is always diagonal and analytical expressions for the electron or nuclear transition frequencies can be used. Such simulations are significantly faster making them desirable to use but the following section will comment on its applicability to ^{17}O ENDOR spectra.

[(a)] the ENDOR/EPR superscript of operators is omitted to make it easier to read

Both approaches result in a theoretical frequency spectra without the consideration of spectral blindspots. As described under Section 2.3.3, these blindspots significantly effect the shape of the detected ENDOR spectra and therefore need to be considered. This is done by multiplying the theoretical ENDOR spectra (S_{theory}) with either a Lorentzian hole function with a FWHM corresponding to the preparation pulse of Davies ENDOR or with the Mims blindspot function (2.82) for Mims ENDOR (F_{prep}). In a semi-empirical approach, the blindspot functions are scaled by a factor x specific to the individual spectrum, that accounts for effects such as imperfect preparation pulses or spectral diffusion:

$$S_{\text{final}} = (1 - x) \cdot S_{\text{theory}} + x \cdot S_{\text{theory}} \cdot F_{\text{prep}} \tag{4.5}$$

The structure of the home-written simulation program is summarized in the following *pseudo-code*:

```
1) Definition of spin systems:
    a) spin system: EPR spectrum and orientation selection
    b) spin system: ENDOR spectrum
2) Definition of simulation parameters
3) Definition of spin operators
4) Rotation of coupling tensors:
    Hyperfine and quadrupole tensor in g-frame:
        A_g=R^-1(alpha,beta,gamma)*A*R(alpha,beta,gamma) (P tensor equivalently)
5)Generation of orientation list:
    for theta, phi
        generate list of all orientations with equal weight
6)Calculation of the EPR frequency spectrum:
    for all orientations
        calculate effective coupling tensors A/P(theta,phi)
        for individual EPR nuclei
            calculate the spin Hamiltonian
            numerically diagonalize the Hamiltonian
            calculate all transition frequencies between Hamiltonian elements
            calculate transition probabilities of all Hamiltonian elements with the S_x
                operator
            for all transition frequencies
                if transition probability > 0
                    add transition to the total spectrum
                    save all parameters into a list
7) Orientation selection:
    for all orientations
        for all EPR resonances
            if transition probability > 0
                calculate excitation_function and compare to EPR resonance
                    if excitation_function value > threshold
```

```
                        add parameters to list of excited orientations
                    else
                        discard result
8)Calculation of ENDOR spectrum:
    for excited orientations
        for all ENDOR nuclei
            calculate the spin Hamiltonian of the subsystem
            numerically diagonalize the Hamiltonian
            calculate all transition frequencies between Hamiltonian elements
            calculate transition probabilities of all Hamiltonian elements with the I_x
                operator
            for all transition frequencies
                if transition probability > 0
                    add transition to the total spectrum
9) Convolution of EPR and ENDOR spectra with Lorentzian/Gaussian line shapes
10) Convolution ENDOR spectrum with spectral blindspot_function
```

The full code is shown in Appendix C. It was tested against *EasySpin* EPR (`pepper` routine) and ENDOR (`salt` routine) simulations performed with matrix diagonalization (`Opt.method='matrix'`) and with perturbation theory (`Opt.method='perturb1'`), which is equivalent to the high-field approximation.

The home-written and *EasySpin* simulations produce nearly identical results for both the full tensor treatment as well as the high-field approximation (see Fig. 4.1). Minor deviations can be assigned to differences in the used excitation functions as well as numerical rounding

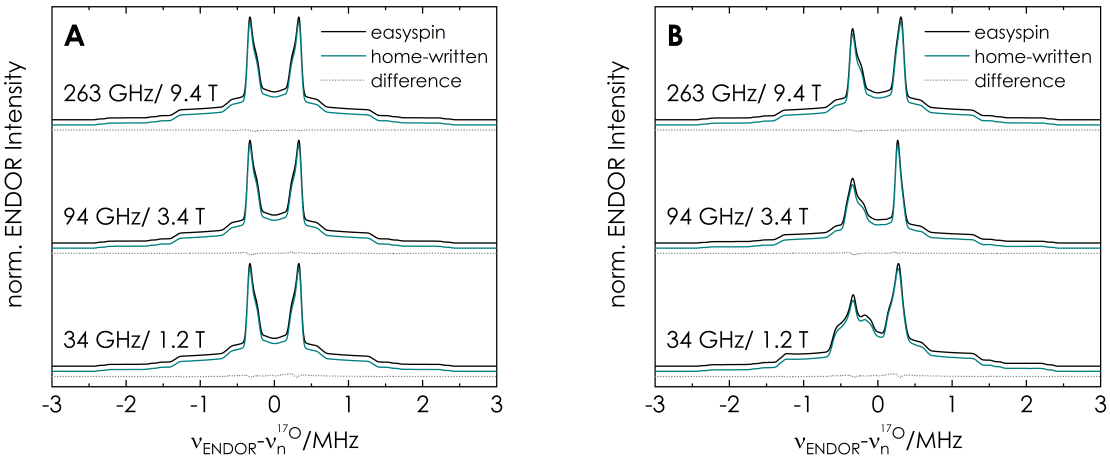

Figure 4.1: Comparison of *EasySpin* (black) and home-written (cyan) simulation code. Simulations were performed in the high-field approximation (**A**) and with full Hamiltonian diagonalization (**B**). Subtractions of the simulations (gray dotted lines) show only minor deviations of the two approaches, most likely due to different excitation functions and numerical rounding errors. Spin system: $S = 1/2$, $\boldsymbol{g} = [2.0081; 2.0062; 2.0022]$, $I^{\mathrm{EPR}}(^{14}\mathrm{N}) = 1$, $\boldsymbol{A} = [13; 13; 94]$ MHz, $\boldsymbol{P} = [1.3; 0.5; -1.8]$ MHz, $I^{\mathrm{ENDOR}}(^{17}\mathrm{O}) = 5/2$, $\boldsymbol{A} = 0.6 + [-0.2; 0.1; 0.1]$ MHz, $\boldsymbol{P} = [-0.02; -0.32; 0.34]$ MHz, all EPR resonances are excited.

errors. Therefore, the diagonalization routine for the EPR Hamiltonian was used in our recent publication: A. Kehl, M. Hiller, F. Hecker, I. Tkach, S. Dechert, M. Bennati, A. Meyer "Resolution of chemical shift anisotropy in ^{19}F ENDOR spectroscopy at 263 GHz/9.4 T" *J. Magn. Res.*, **2021**, *333*, 107091.
At the time of the code development, *EasySpin* was not an open-source software package and therefore the exact theoretical treatment of the spin Hamiltonian was not clear, despite the extensive and excellent documentation, publications and numerous applications. The software package has since then been made open-source, which is a great asset to the EPR community at large. The code is modular, since the software package is designed for a very broad application range, and therefore it is advantageous to have a single simulation file in which the theoretical treatment can be read by someone, who is not necessarily a software engineer. It should be pointed out, that since *EasySpin* is significantly faster in simulating ENDOR spectra of ^{17}O nuclei and was programmed by experts that made it exceptionally simple to use, it was utilized for the majority of the spectral simulations shown in this work.

4.2 High-field approximation vs. full tensor diagonalization

Most ENDOR experiments of this thesis were performed at a W-Band spectrometer with a magnetic field of 3.4 T, which is usually considered as a high-field in EPR spectroscopy. ENDOR studies at this field utilized the high-field approximation for very fast ENDOR simulations, using the analytical solutions for the transition frequencies. This proved to be accurate for high-γ nuclei such as ^{1}H[85] and ^{19}F[14] but also for the low-γ nucleus ^{2}H[24–26,86], which has a gyromagnetic ratio similar to ^{17}O ($\gamma_{2H}/\gamma_{17O} = -1.13$[43]). It was justified, since in all cases, the hyperfine and quadrupole interactions were small compared to the nuclear Zeeman interaction, but also importantly, the nuclear quadrupole coupling was small, compared to the hyperfine coupling.
Figure 4.2 shows the simulated ^{17}O ENDOR spectra for a series of spin systems (Table 4.1) with hyperfine coupling values relevant to this work simulated with high-field approximation (HF) and full tensor diagonalization (Matrix) at a magnetic field of 3.4 T. No spectral blindspot function was added to the theoretical ENDOR spectra. The individual nuclear transitions (color) and the full spectrum (black) are shown to better illustrate the effect of nuclear quadrupole coupling on the spectral line shape. Significant deviations between the two simulation approaches indicate the breaking down of the the high-field approximation.
The first three spin systems (A, B and C) have very small quadrupole coupling constants and purely dipolar (A), purely isotropic (B) or combined (C) hyperfine coupling tensors. The nuclear transitions within the two electron spin manifolds have almost identical frequencies

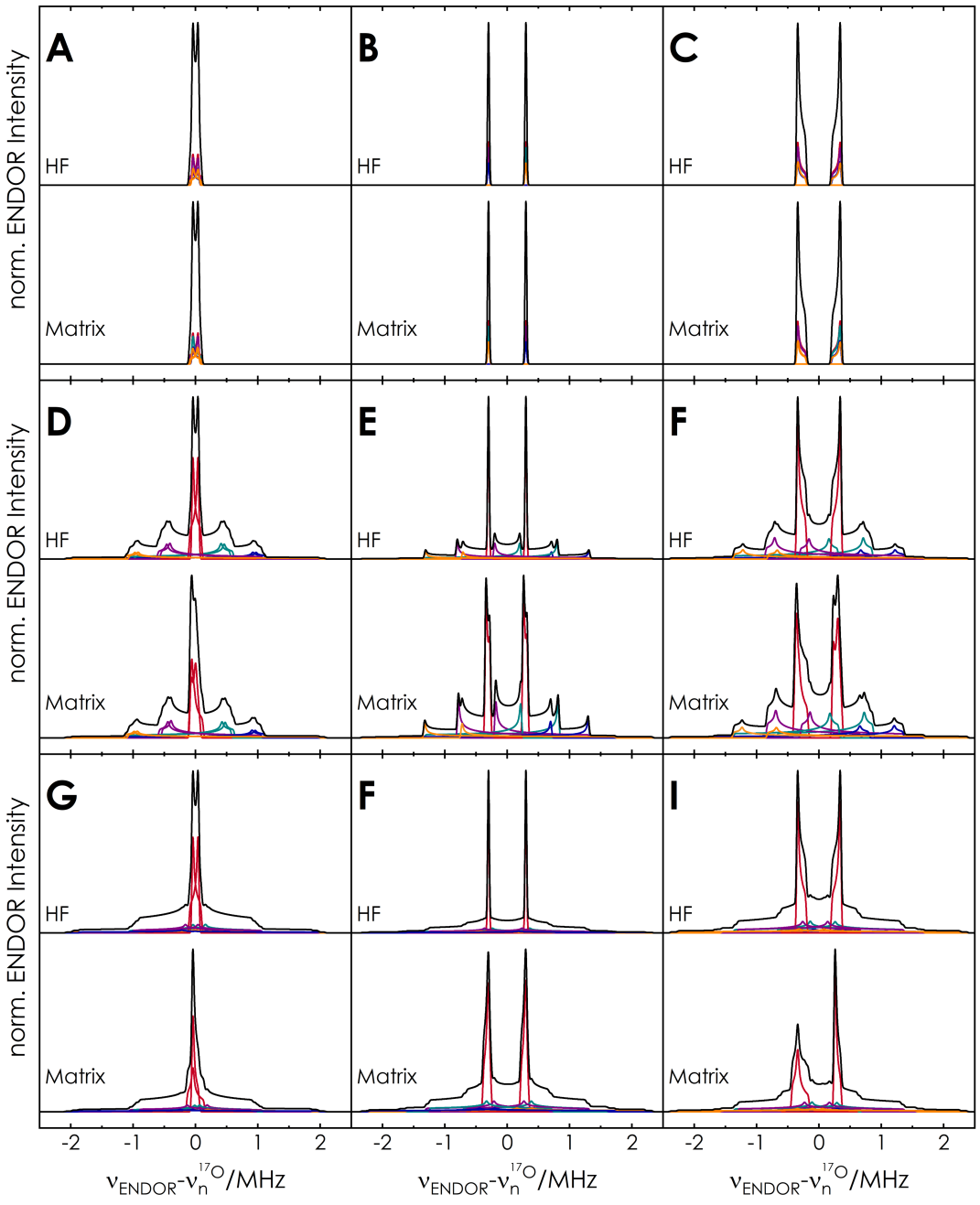

Figure 4.2: Simulated ENDOR spectra (black) and individual nuclear transitions (color) for coupled $S = 1/2, I = 5/2$ spin systems calculated in high-field approximation with 1st order perturbation theory (HF) and with full tensor diagonalization (Matrix). Coupling parameters are given in Table 4.1.

Table 4.1: Hyperfine and quadrupole coupling parameters for Fig. 4.2.

Simulation	a_{iso}	T_1	T_2	T_3	P_1	P_2	P_3
A	0	-0.2	0.1	0.1	-0.001	-0.001	0.002
B	0.6	0	0	0	-0.001	-0.001	0.002
C	0.6	-0.2	0.1	0.1	-0.001	-0.001	0.002
D	0	-0.2	0.1	0.1	-0.17	-0.17	0.34
E	0.6	0	0	0	-0.17	-0.17	0.34
F	0.6	-0.2	0.1	0.1	-0.17	-0.17	0.34
G	0	-0.2	0.1	0.1	-0.02	-0.32	0.34
H	0.6	0	0	0	-0.02	-0.32	0.34
I	0.6	-0.2	0.1	0.1	-0.02	-0.32	0.34

* All coupling values in MHz.

and only vary in intensity due to different transition probabilities. The simulated spectra for purely dipolar hf coupling show in both cases a small doublet structure close to the Larmor frequency (A). In case of isotropic hf coupling (B) the signals are very sharp and only broadened by the ENDOR linewidth. In case of the rhombic hf tensor (C) the signals are additionally broadened by the dipolar hf coupling. For these systems, both methods yield the same result, justifying the high-field approximation.

The second set of spin systems (D, E and F) have axial quadrupole tensors in the size observed experimentally and either dipolar (D), isotropic (E) or combined (F) hyperfine coupling tensors. Even though this quadrupole tensor shape is not expected in the systems of this study, the simulations are shown here to better illustrate the impact of quadrupole coupling on the ENDOR spectra. The individual nuclear transitions in the two electron spin manifolds are no longer energetically equivalent and the simulated ENDOR spectra contain sharp central signals (red) split by the hyperfine coupling, which correspond to the $m_I = -1/2 \rightarrow m_I = 1/2$ nuclear transition as well as broad signals corresponding to the other nuclear transitions. The central transitions are not affected by quadrupole coupling in the high-field approximation, so they have the same line shape as in A, B and C. The simulations performed with matrix diagonalization show that the central transitions are affected by the quadrupole coupling and become broadened and in case of a hf coupling tensor with dipolar coupling contribution (D and F) also asymmetric around the ^{17}O Larmor frequency. For a small, purely dipolar tensor (D) the small doublet structure is lost and the signal at the Larmor frequency becomes a single asymmetric peak.

The third set of spin systems has rhombic quadrupole coupling tensors (G, H and I), equivalent to the systems we investigated in this work. The quadrupole transitions become much broader and therefore less intense due to their rhombic tensor shape. In case of small dipolar coupling (G) the effect observed in the previous section is amplified and all hf

coupling information is lost in the spectrum within a single central peak. For the case of isotropic hf coupling (H) the broadening effect on the central transition is limited while a significant broadening and asymmetry is observed for rhombic hf and quadrupole tensor (I). In conclusion. the high-field approximation fails for the coupling sizes observed in this work , requiring full matrix diagonalization for all spectral simulations. Additionally, the asymmetry of the ENDOR spectra is caused by the size and relative orientation of the hyperfine and quadrupole tensors and therefore has to be considered during simulation.

4.3 Dynamic ENDOR simulations

The static ENDOR simulations described in Section 4.1 consider the Mims blindspot function by multiplying the ENDOR frequency spectrum with the theoretical Mims ENDOR efficiency. As discussed under section 2.3.3, this convenient treatment breaks down, as soon as the direct mapping of hyperfine coupling A to the spectral radio-frequency axis is perturbed due to the presence of significant nuclear quadrupole coupling. An analytical approach by *Hoffman et al.* was adapted for $I = 1$ nuclei, calculating A_{eff} from a combination of hyperfine and quadrupole coupling.[62] They concluded however, that a similar treatment for $I = 5/2$ nuclei was unfeasible. The alternative to this approach is dynamic simulation of the Mims ENDOR experiment in the density operator formalism, from which the spectral shape including the spectral blindspots will emerge without the need of additional treatment. *EasySpin* offers this option in the `saffron` function, albeit with several alterations to the general density operator formalism described under 2.2.4. Most important among those are:

- separation of the full spin Hamiltonian and density operator into sub-spaces for electron α and β states
- pre-calculation of relevant coherence transfer pathways
- calculation of the frequencies and amplitudes of the coherence transfer pathways and Fourier transforming them to gain the time domain signal

These are well founded in theory and have been applied to a large variety of EPR experiments. However, a simulation-routine that treats the density operator in the exact product operator formalism was used to validate the *EasySpin* approach for Mims ENDOR experiments of ^{17}O. The simulation algorithm is based on the code developed by S. Glaser and R. Zeier (TU Munich) as well as I. Bejenke and M. Bennati (MPI NAT).[86] The Mims ENDOR routine was written in collaboration with A. Kehl in our research group and is summarized in the following *pseudo-code*:

```
1) Definition of spin systems:
    a) spin system: EPR spectrum and orientation selection
    b) spin system: ENDOR spectrum
2) Definition of simulation parameters
3) Definition of spin operators
4) Rotation of coupling tensors:
    Hyperfine and quadrupole tensor in g-frame:
        A_g=R^-1(alpha,beta,gamma)*A*R(alpha,beta,gamma) (P tensor equivalently)
5)Calculation of the EPR frequency spectrum
    for theta, phi
        calculate g_eff/A_zz/P_zz(theta,phi) explicitly
        calculate EPR transitions explicitly
        for all EPR transitions
            calculate excitation_function and compare to resonance position
                if excitation_function value > threshold
                        add magnetic parameter to list of excited orientations
                else
                    discard result
6)Calculation of ENDOR spectrum
    for excited orientations
        for ENDOR nuclei
            for m_I values
                set electron resonance offset to ENDOR resonance
                        calculate Hamiltonians in the doubly rotating frame
                        calculate propagators
                        calculate density operator evolution
                        calculate echo intensity and add value to ENDOR spectrum
7)Convolve EPR and ENDOR spectra with Lorentzian/Gaussian line shapes
```

The full simulation code is given in Appendix D. For the density operator treatment, the pulse sequence is split into time intervals during which the Hamiltonian acting on the system can be considered time-independent. The density operator is then calculated by successive evolution of the eight time intervals in the Mims ENDOR pulse sequence (see Fig. 4.3, A). Three different Hamiltonians are necessary: firstly, the Hamiltonian during free evolution times $\hat{\mathcal{H}}_{\text{free}}$, secondly, the Hamiltonian during microwave pulses $\hat{\mathcal{H}}_{\text{nonsel}}$ and thirdly, the Hamiltonian during the radio-frequency pulses $\hat{\mathcal{H}}_{\text{rf}}$. For this approach, the Hamiltonians have to be time-independent and are therefore considered in the doubly-rotating frame.

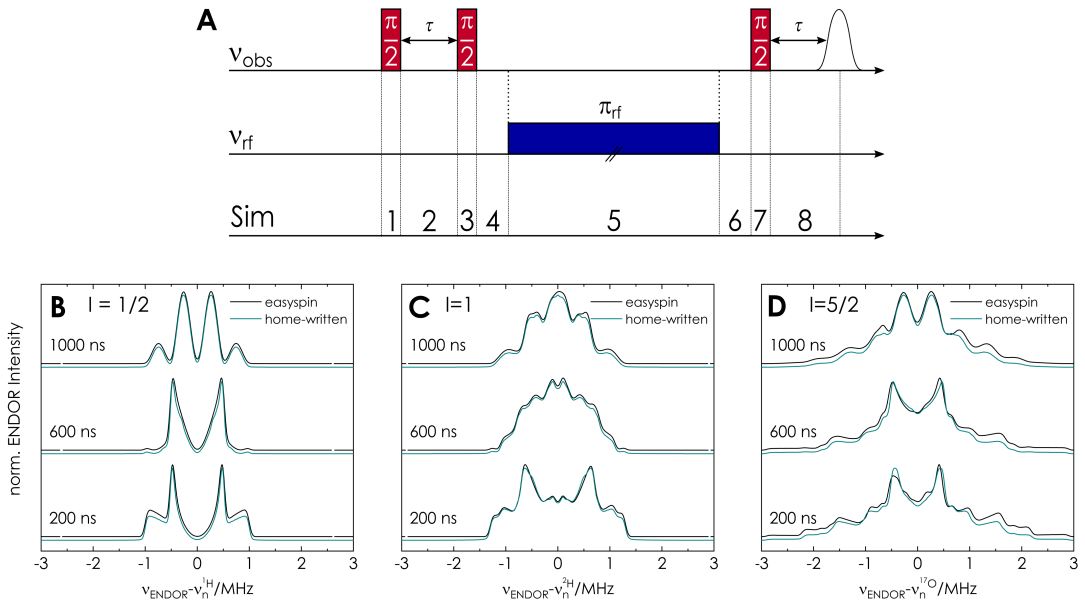

Figure 4.3: Dynamic Mims ENDOR simulations. **A**: Mims ENDOR pulse sequence with numbered time intervals used for density operator simulations. **B**/**C**/**D**: Comparison of *EasySpin* (black) and home-written (cyan) simulation code for representative nuclear spins $I(^1\mathrm{H}) = 1/2$ (**B**), $I(^2\mathrm{H}) = 1$ (**C**) and $I(^{17}\mathrm{O}) = 5/2$ (**D**). Spin system: $S = 1/2, g = 2.0023, \boldsymbol{A} = [-2; 1; 1]$ MHz, $\boldsymbol{P}(^2\mathrm{H},^{17}\mathrm{O}) = [-0.2; -0.2; 0.4]$ MHz, all EPR resonances excited.

This requires coupling Hamiltonians that commute with the $\hat{S}_z$ and $\hat{I}_z$ operators, which is only given for the full high-field approximation:

$$\hat{\mathcal{H}}_{\mathrm{free}}(2,4,6,8) = \Delta\omega_S\hat{S}_z + \Delta\omega_I\hat{I}_z + A_{zz}\hat{S}_z\hat{I}_z + \frac{1}{2}\hat{P}_{zz}(3\hat{I}_z^2 - I(I+1)) \tag{4.6}$$

$$\hat{\mathcal{H}}_{\mathrm{nonsel}}(1,3,7) = \hat{\mathcal{H}}_{\mathrm{free}} + \omega_1\hat{S}_x \tag{4.7}$$

$$\hat{\mathcal{H}}_{\mathrm{rf}}(5) = \hat{\mathcal{H}}_{\mathrm{free}} + \omega_2\hat{I}_y \tag{4.8}$$

The microwave pulses can be considered as either ideal pulses by neglecting $\hat{\mathcal{H}}_{\mathrm{free}}$ or as real pulses by including it.

The result of Mims ENDOR simulations with *EasySpin* (black) and home-written code (cyan) are compared for three representative τ-values in Figure 4.3, B-D for three different nuclear spins. They show, that both simulation approaches produce nearly identical results for all three nuclear spins. It should be noted, that only simulations using ideal microwave pulses, produced results comparable with *EasySpin*. Minor deviations occur for the $I = 5/2$ simulations and can be explained by the different treatment of the spin Hamiltonian. *EasySpin* simulations with `saffron` consider the full coupling Hamiltonians, i.e. use tensor diagonalization, while the home-written code uses the high-field approximation.

It is currently being developed by A. Kehl to include the pseudo-secular hyperfine coupling B, which requires a different treatment of the radio-frequency pulse. Since such a spin

Hamiltonian no longer commutes with the $\hat{I}_z$ operator, it is also no longer time-independent in the doubly rotating frame. To solve this, the rf pulse can be split into small time increments, during which the Hamiltonian can be considered time-independent, which can then be calculated in sequence. The drawback of this approach is an increased calculation time.
For the purposes of this work, the density operator approach utilized by *EasySpin* is adequate for the simulation of ^{17}O Mims ENDOR spectra, while at the same time being much faster than the home-written simulation code.

4.4 Static EDNMR simulations

The general principle of the EDNMR simulation code developed by *Cox et al.*[12] and *Wili et al.*[72] is similar to the ENDOR simulation code described in the previous section. It is contained in the *EasySpin* function `horseradish`.
For every orientation of the g-tensor with respect to the external field, all coupling tensors are calculated and the full spin Hamiltonian is diagonalized to determine the energy eigenstates and the transition frequencies between them. Subsequently, the inversion efficiency W_i of every transition i, i.e. its relative weight in the EDNMR spectrum, is calculated. Therefore, selective excitation with the HTA pulse is assumed and the time evolution of the individual transition $\boldsymbol{M}_i$ is calculated using the *Bloch* equations in the rotating frame, including relaxation T_m and relative transition probabilities I_i (see Sec. 2.3.4):

$$\frac{\partial}{\partial t}\boldsymbol{M}_i = \begin{pmatrix} -1/T_\mathrm{m} & 0 & 0 \\ 0 & -1/T_\mathrm{m} & -\omega_1 \cdot \sqrt{I_i} \\ 0 & \omega_1 \cdot \sqrt{I_i} & 0 \end{pmatrix} \cdot \boldsymbol{M}_i(t) \tag{4.9}$$

The inversion efficiency after the HTA pulse results as

$$W_i = \frac{1 - M_{z,i}(t_\mathrm{HTA})}{2} \tag{4.10}$$

if only z magnetization is assumed at the beginning of the high turning angle pulse.[12] The main bottleneck of this simulation code is also the numerical diagonalization of the static spin Hamiltonian, which needs to be repeated for every orientation of the g-Tensor, and scales dramatically with the dimension of the Hamiltonian.
Therefore, the strategy of separating the spin system into EPR and EDNMR nuclei was employed for the selection of excited orientations. These were calculated, in analogy to the ENDOR code in Section 4.1, with the reduced spin system, containing only the EPR active nuclei (here either ^{14}N for the nitroxides or ^{1}H for the tyrosyl radical). The `orisel` function implemented in *EasySpin* was used for this[70]. It calculates the EPR transitions

of the spin system and uses a Gaussian excitation function with a bandwidth corresponding to the microwave $\pi/2$-pulse to select the excited orientations and their relative weights. For the excited orientations, defined by the polar angles θ and ϕ, the EDNMR resonances are calculated with the `horseradish` function. Here, full spin system, containing EPR and EDNMR active nuclei are considered. This is important, since all nuclei influence the transition probabilities in the diagonalized Hamiltonian. The adapted simulation code described here was created by L. Fries in the course of her Master thesis, which I supervised.

Water molecules in E. coli ribonucleotide reductase

5

Summary The role of water in biological proton-coupled electron transfer is emerging as a key for understanding mechanistic details at atomic resolution. Here we demonstrate ^{17}O high-frequency electron-nuclear double resonance in conjunction with $H_2{}^{17}O$ labelled protein buffer to establish the presence of ordered water molecules at three radical intermediates in an "active" enzyme complex, the $\alpha_2\beta_2$ *E. coli* ribonucleotide reductase. Our data give unambiguous evidence that all three, individually trapped, intermediates are hyperfine coupled to one water molecule with Tyr-O$\cdots{}^{17}O$ distances in the range $2.8 - 3.1$ Å. The availability of this structural information will allow for quantitative models of PCET in this prototype enzyme. The results also provide a spectroscopic signature for water H-bonded to a tyrosyl radical.

The first part of the chapter is an introduction to the studied enzyme and the investigated radicals (Sec. 5.1-5.3). The second part of the chapter describes our 94 and 263 GHz Mims ENDOR study (Sec. 5.4-5.5). The third part of the chapter contains additional information on the analysis of ^{17}O Mims ENDOR spectra of the radical intermediates (Sec. 5.6) and in the final part we will discuss perspectives for the future investigation of PCET in RNR (Sec. 5.7).

Acknowledgement Sec. 5.4-5.5 of this chapter have been published as a Communication in the Journal of the American Chemical Society. They are reprinted here with permission from: F. Hecker, J. Stubbe, M. Bennati, "Detection of Water Molecules on the Radical Transfer Pathway of Ribonucleotide Reductase by ^{17}O Electron-Nuclear Double Resonance Spectroscopy" *J. Am. Chem. Soc.* **2021**, *143* (19), 7237-7241 [15]. Copyright 2021 American Chemical Society. Brandon Greene (MIT) is acknowledged for the purification of RNR protein and help in the production of ^{17}O-labelled protein samples. The experiments, DFT calculations and simulations in this chapter were performed by the author. The manuscript was conceptualized by the author and M. Bennati and written in conjunction with J. Stubbe. All figures were designed and produced by the author.

5.1 E. coli ribonucleotide reductase

Ribonucleotide reductases (RNRs) are a family of enzymes that catalyze the reduction of nucleotides (ND(T)P) to 2'-deoxyribonucleotides (dND(T)P), which are needed for the production and repair of DNA.[87–91] Nucleotide reduction occurs in the active pocket of the RNR enzyme, where a cystein radical is formed, which enables the reaction (Fig. 5.1).[92] All ribonucleotide reductases share a common active site motive, which contains three cystein residues, one of which is transiently oxidized while the other two provide the necessary reduction equivalents.[39,93,94] The protein that harbors the active site is referred to as the α-subunit.

Different classes of RNR enzymes are mainly distinguished by their metallo-cofactors (class I, II and III), which enable the cystein oxidation. In class I RNRs, a µ-oxo-dimetallo radical cofactor is located in another protein, the β-subunit, and transferred to the active site over a long distance. Recently, another type of RNRs without a metal cofactor but rather a 3,4-dihydroxyphenylalanine (DOPA) radical has been discovered, however due to the similarity in long range radical transfer it is also counted as a class I.[27,28,95] In class II RNRs, the radical is generated from an adenosyl cobalamin and in class III RNRs, the cofactor is an S-adenosyl-L-methionin and an FeS cluster. The subclass Ia, which contains a diferric tyrosyl cofactor, is found in human, mouse or yeast cells and due to its large similarity, *E. coli* class Ia RNR[(a)] is studied as a model system for these enzymes. The research on RNRs has been going on for over 70 years and there is no sign of stopping. Several excellent reviews summarize the state of research[92,96–99] and this chapter will focus on the most important aspects necessary to understand the research conducted during this thesis.

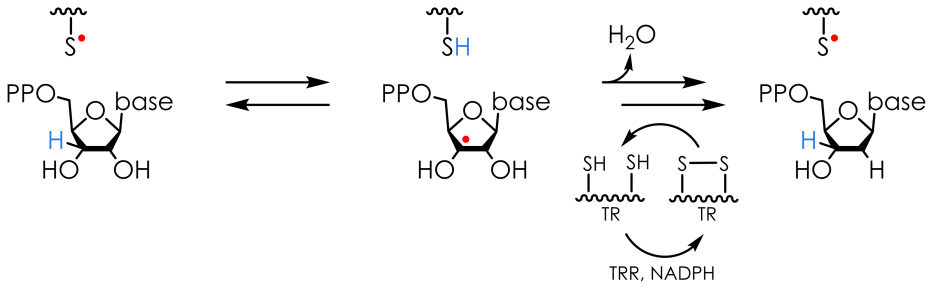

Figure 5.1: Mechanism of ribonucleotide reduction in all classes of ribonucleotide reductase. A cystein radical (red, C_{439} in *Escherichia coli*) formed in the active site of the enzyme initiates reduction by abstraction of the ND(T)Ps 3' proton (blue). The reaction is driven towards the dND(T)P by the rapid loss of water. In the process, two cystein residues within the enzyme are oxidized. These are re-reduced by thioredoxin (TR) which in turn gets reduced by thioredoxin reductase (TRR) with the aid of NADPH. In the final step, the hydrogen atom is transferred back from the cystein to the deoxynucleotide, recovering the cystein radical. Figure adapted from Ref. [92].

[(a)] *E. coli* contains multiple classes of RNR, but all future mentions of the enzyme refer to class Ia

5.2 Proton-coupled electron transfer in E. coli RNR

The *E. coli* class Ia RNR enzyme is composed of two homodimeric subunits α_2 and β_2. The α_2-subunit (Fig. 5.2, A) is a 172 kDa protein, which contains the enzyme's catalytic site, as well as the activity and specificity binding sites.[39,40] The β_2-subunit (Fig. 5.2, B) is a 87 kDa protein that contains the diferric metal cofactor and the stable tyrosyl radical at position Y_{122}.[100]. Regulated by the relative concentrations of NDPs and dNDPs in the cell environment, the enzyme can adopt multiple quartanary structures, including the dissociated state of the two subunits, an inactive $\alpha_4\beta_4$ structure, generated by dATP binding to the activity site, as well as the active $\alpha_2\beta_2$, generated upon ATP binding to the activity site.[101] In the presence of the correct substrate and effector combination, the enzyme begins its catalytic cycle, in which the tyrosyl radical cofactor $Y^{\bullet}_{122}$ in β is reduced and the active site cystein C_{439} in α is oxidized. After reduction of a nucleotide, the enzyme returns to its $Y^{\bullet}_{122}$ resting state. The $\alpha_2\beta_2$ state of the active complex was hypothesized early on upon discovery of RNR, but it took nearly 30 years until a structure was proposed. This so called *docking model* is based on the shape complementarity of the individual β_2 and α_2 crystal structures (Figure 5.2, C).[39] To date, no X-ray structure of $\alpha_2\beta_2$ is available, since crystallization is prevented by the transient nature of the complex, but the *in silico* docking model has been well established by a large number of biochemical and biophysical studies.[99,102–105]

It showed the remarkable distance of ~ 35 Å between the diferric radical cofactor $Y^{\bullet}_{122}$ in β and the active cystein residue C_{439} in α. Based on this distance, a radical transfer (RT) pathway involving redox-active residues was proposed: $Y^{\bullet}_{122}[\beta] \rightleftarrows (W_{48}[\beta]) \rightleftarrows Y_{356}[\beta] \rightleftarrows Y_{731}[\alpha] \rightleftarrows Y_{730}[\alpha] \rightleftarrows C_{439}[\alpha]$ (Fig. 5.2, F).[107,108] The participation of the tyrosyl residues Y_{356}, Y_{731} and Y_{730} was initially established by phenylalanine mutations of RNR at the respective positions, which retained the protein structure but lost enzyme activity.[109–111] Participation of the tryptophan residue W_{48} was proposed but no direct experimental evidence of its RT involvement exists.[112–114] The radical transfer mechanism proceeds as a series of distinct proton-coupled electron transfer steps (Fig. 5.2, F), which avoids the occurrence of high energy intermediates.[24–26,115,116] A feature of RNR functionality and its reaction mechanism is its half-sites reactivity, which means that RT initially occurs only in one of the two α/β pairs.[117] A conformational or chemical transformation that occurs during or after product formation then allows the RT in the other α/β pair.

Recently, a cryo-EM structure of a stabilized $\alpha_2\beta_2$ ($F_3Y^{\bullet}_{122}/E_{52}Q$-$\beta_2$: α_2-wt) (Fig. 5.2, D) was recorded with a resolution of 3.6 Å and has shed new light into the RNR mechanism. For the first time, the entire radical transfer pathway (Fig. 5.2, E) was observed and confirmed the hypothesized position of Y_{356} (disordered in all β_2 crystal structures) at the subunit interface between β_2 and α_2.[106] The complex's asymmetry, in contrast to the

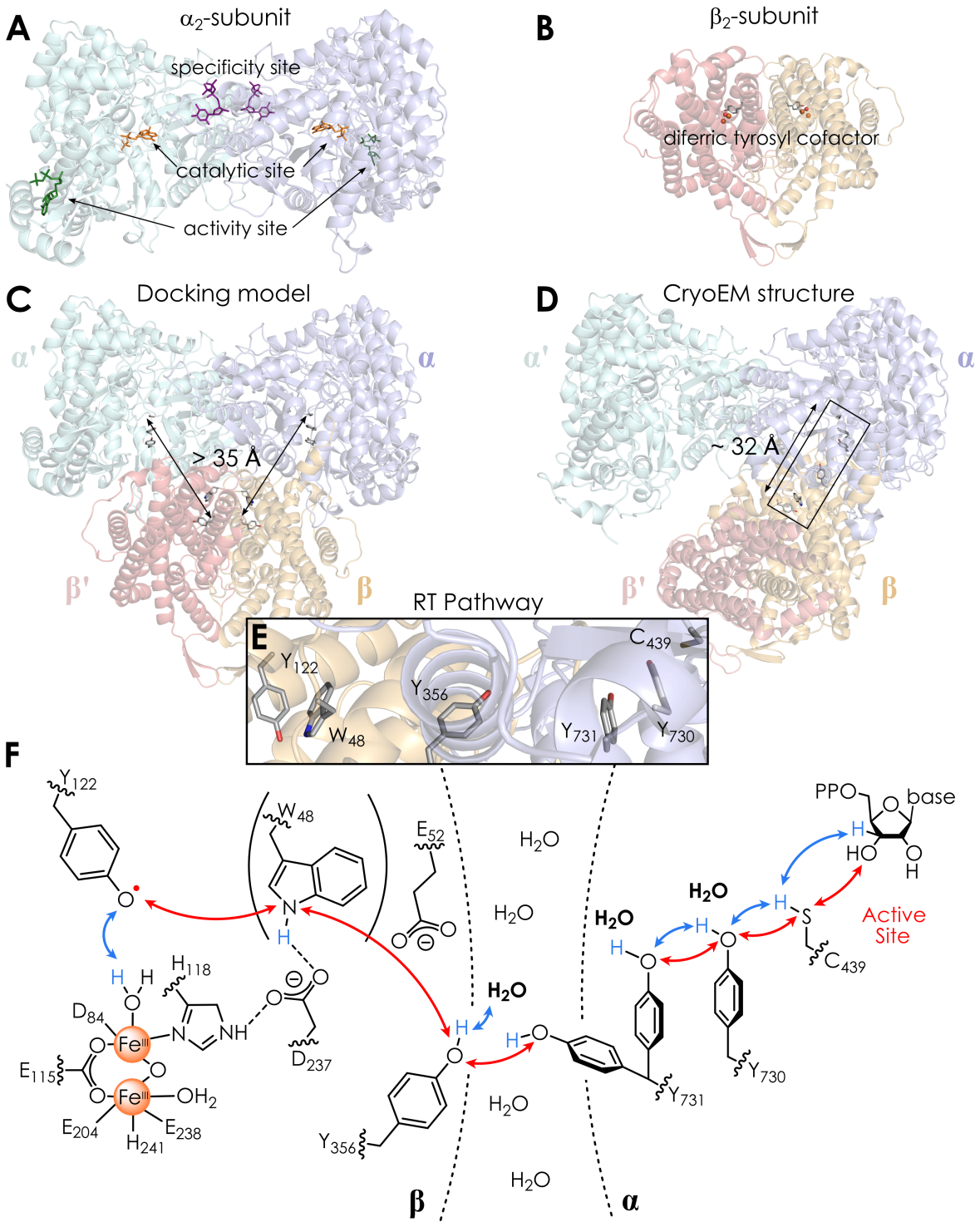

Figure 5.2: *E. coli* ribonucleotide reductase. **A**: α-subunit with marked specificity (purple), catalytic (orange) and activity (green) site. **B**: β-subunit with marked diferric tyrosyl cofactor. **C**: In silico *docking model* of the $\alpha_2\beta_2$ complex based on shape complementarity of the individual subunit crystal structures.[39] **D**: Cryo-EM structure of the $F_3Y_{122}/E_{52}Q$-β_2 : α_2−wt complex.[106] **E**: Resolved radical transfer pathway in the closely bound $\alpha\beta$ pair of the cryo-EM structure. **F**: Proposed mechanism of proton-coupled electron transfer. Proton transfer marked as blue arrows, electron transfer marked as red arrows. Water molecules detected in this thesis are marked bold.

symmetric *docking model*, is consistent with the half-sites reactivity, since one of the two possible RT transfer pathways (Fig. 5.2, D α'/β') is interrupted by a large gap between the subunits.

5.3 Investigation of radical intermediates

The current knowledge of PCET in *E. coli* RNR is based on the detailed structural investigation of the individual radical intermediates on the RT pathway. EPR spectroscopy can directly detect radical intermediates and is therefore the ideal tool for this task. The stable tyrosyl cofactor $Y^{\bullet}_{122}$ in *E. coli* RNR was the first enzyme radical ever detected by EPR spectroscopy.[118] Its molecular structure and magnetic properties have since been investigated in great detail[119,120] and new information continues to be revealed with advances in EPR spectroscopy.[13,121,122] The thermodynamically uphill RT mechanism (> 200 mV)[69] and the conformational gating prevent the direct detection of other pathway radicals in the wild-type enzyme. This hurdle was overcome by the site-specific incorporation of unnatural amino acids, which alter the thermodynamic landscape of the radical transfer pathway.[105,123,124] Two main strategies can be employed: The redox potential of the stable tyrosyl cofactor can be raised by ~ 120 mV by replacing it with 2,3,5-F_3Y (or $\gtrsim 300$ mV by using NO_2Y), which traps the radical at position $Y^{\bullet}_{356}$ after initiation of the enzyme reaction (Figure 5.3, red).[67,125] Alternatively, the residue at the desired radical position can be replaced with NH_2Y, which has a drastically lower redox potential (~ 590 mV) and

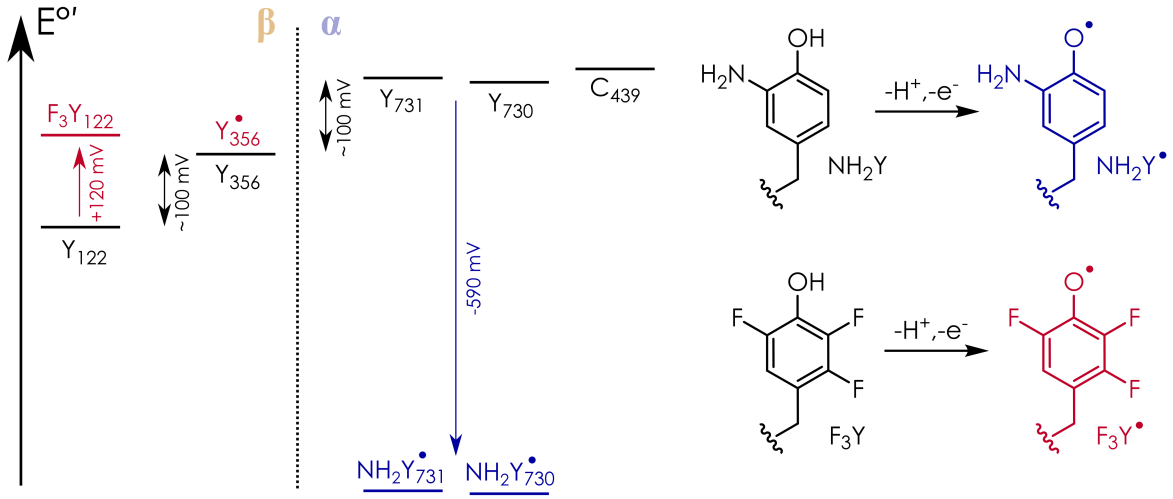

Figure 5.3: Radical trapping in *E. coli* RNR. $Y^{\bullet}_{356}$ can be trapped by replacing Y_{122} with 2,3,5-F_3Y, which raises the redox potential by ~ 120 mV (red), and prevents the immediate re-oxidation of Y_{122} after turnover. $NH_2Y^{\bullet}_{731}$ and $NH_2Y^{\bullet}_{730}$ can be trapped by replacing the tyrosines at either position with 3-NH_2Y, which lowers the redox potential by ~ 590 mW, trapping the radical in the thermodynamic minimum (blue). Figure adapted from Ref. [68, 69].

therefore acts as a spin trap producing $NH_2Y^{\bullet}_{731}$ or $NH_2Y^{\bullet}_{730}$ after initiation (Figure 5.3, blue).[68,105] Radicals are trapped with maximum yields of $\lesssim 50\,\%$ due to the half-site reactivity, leaving at least 50 % radical in the Y_{122} resting position.

EPR was used to identify the trapped radicals, distinguishing them by their altered hyperfine structure, electrostatic environment or relaxation behaviour.[26,67,105,123,125] The diagonal distances between the radical in the resting β-subunit and the radicals trapped at different positions in the RT transfer pathway was measured by pulsed electron double resonance (PELDOR/DEER) spectroscopy, confirming the pathway intermediates and giving support for the *docking model*.[104] High-field ENDOR studies of the the amino-tyrosyl radicals $NH_2Y^{\bullet}_{730}$[24] and $NH_2Y^{\bullet}_{731}$[25] revealed the hydrogen-bonding environment that exists around and between the two essential pathway residues. The ENDOR spectra gave the basis for

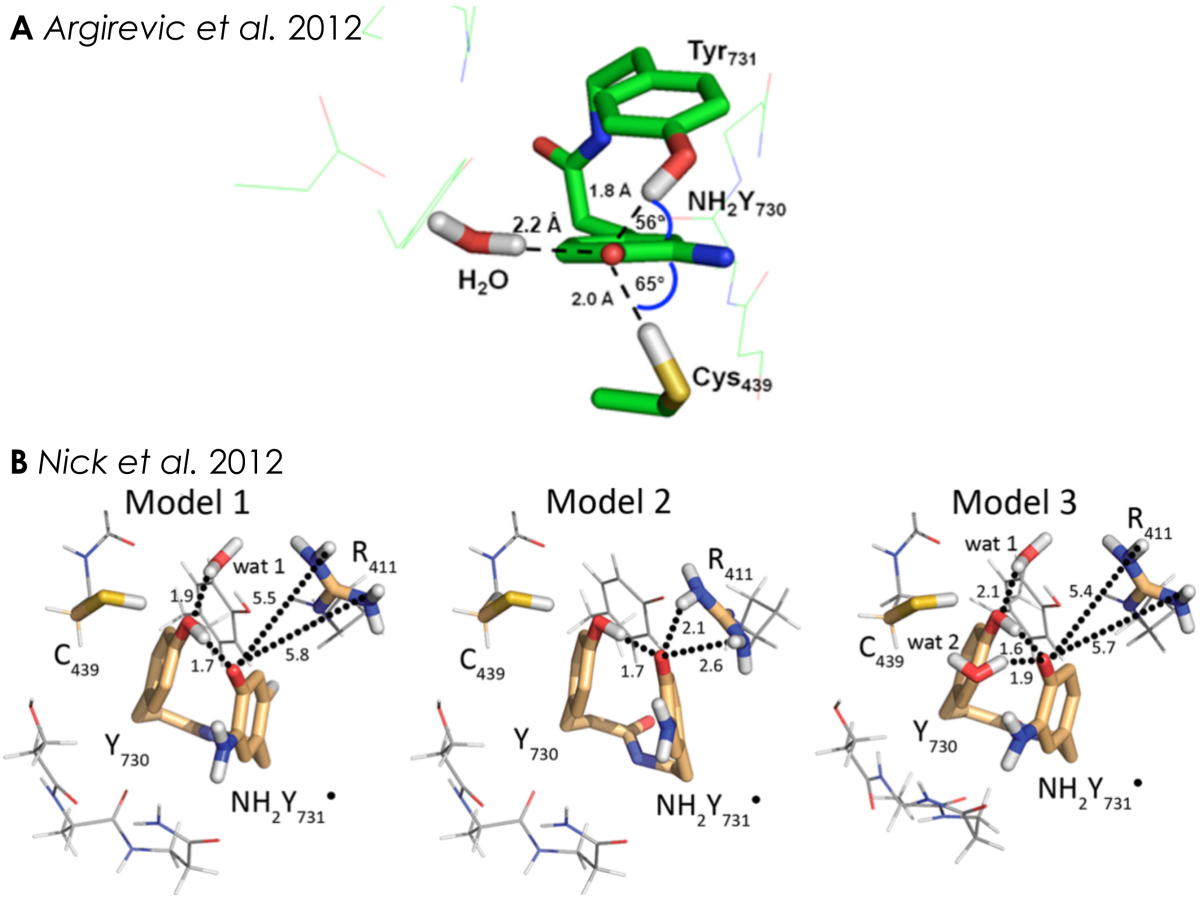

Figure 5.4: Combined EPR and DFT models for the H-bond network around $NH_2Y^{\bullet}_{730}$ (**A**) and $NH_2Y^{\bullet}_{731}$ (**B**). **A**: Model of $NH_2Y^{\bullet}_{730}$ in α as reported in *Argirevic et al.*[24] The water and its mechanistic significance was proposed in that study, but direct experimental evidence was missing. Hf coupling parameters of the water molecule are reported Table 5.1 as DFT_{large}. **B**: Models of $NH_2Y^{\bullet}_{731}$ as reported in *Nick et al.*[25] Left: Model 1 includes only the water molecule wat1. Center: Model 2 has no water molecules. Model 3 contains a second water molecule wat2, which is observed in some X-ray structures. Residues in interaction distance are bold. All distances are given in Å.

large scale atomic models of PCET intermediates in RNR (see Fig. 5.4). These models, in conjunction with independent theoretical models[126,127] led to the conclusion, that co-linear PCET, i.e. transfer of electron and hydrogen between the same donor and acceptor, is the mechanism of radical transfer within the α_2 subunit. The hydrogen-bonding (H-bonding) environment of $NH_2Y^{\bullet}_{730}$ included a water molecule at a distance of $r(O\cdots H) = 2.2\,Å$ (Fig. 5.4, A) whose mechanistic importance for PCET has been hypothesized.[24]

Recently, the focus of the EPR studies in *E. coli* RNR has shifted towards the radical transfer mechanism across the subunit. The PELDOR-derived diagonal distances suggested a distance of at least $\sim 8\,Å$ between the RT intermediates $Y^{\bullet}_{356}$ and $NH_2Y^{\bullet}_{731}$ and the recent cryo-EM structure shows a distance of 8.3 Å, in line with the PELDOR study.[104,106] The flexibility of Y_{731}, first observed as flipped conformations in the crystal structure of NH_2Y_{731}-α_2[128], was investigated using PELDOR[129] and later also by HYSCORE spectroscopy and transient optical spectroscopy with the photo-β_2-method.[130] Both experiments revealed a stable, flipped conformation of the $NH_2Y^{\bullet}_{731}$ radical, if a close arginine residue (R_{411}-α) was was mutated to an alanine, hinting at a possible mechanism of PCET across the subunit interface. A recent molecular dynamics (MD) study based on the cryo-EM structure also concludes flexibility of Y_{731}.[131]

The trapped $Y^{\bullet}_{356}$ radical allows the investigation of an unperturbed radical intermediate at the β_2 side of the subunit interface. PELDOR spectroscopy of multiple biochemical constructs has shown consistent diagonal distances of $Y^{\bullet}_{356}$ to $Y^{\bullet}_{122}$ and therefore suggest little flexibility of the residue, despite the flexibility that the β-tail exhibits in isolated β_2-subunits.[26] High-field EPR of the radical showed a remarkably small g_1-value (2.0062), pointing to a strongly polar environment, consistent with the placement of $Y^{\bullet}_{356}$ at the subunit interface. Finally, ENDOR experiments of a fully deuterated $Y^{\bullet}_{356}$ radical gave the first indication of a hydrogen-bonding network, which was assigned to water molecules at the subunit interface.[26]

The question of PCET across the subunit interface remains of great interest and our recent studies are focused on the $Y^{\bullet}_{356}$ perspective. The ^1H and ^2H ENDOR studies of $Y^{\bullet}_{356}$ and $NH_2Y^{\bullet}_{730}$ suggested the presence of water molecules at the radical intermediates, and recent MD[132] and biochemical[133] studies all hint at the importance of water for PCET in RNR. Water molecules have only been observed crystallographically in inactive α_2's with out the presence of β_2[39,40,67,125], but the direct experimental proof of water molecules in the $\alpha_2\beta_2$ complex has thus far been missing. In the following sections, we will show, how water molecules can be directly detected using ^{17}O ENDOR spectroscopy.

5.4 Results and discussion

Here, we explored the capability of H^{17}_2O ENDOR spectroscopy by exchanging the RNR buffer with $H_2{}^{17}O$. $\alpha_2\beta_2$-$Y^{\bullet}_{356}$ was generated by a 2,3,5-$F_3Y^{\bullet}_{122}$ mutation in β_2[67] whereas radicals at Y_{731} and Y_{730} were trapped by replacing the respective residue with 3-amino tyrosine (NH_2Y),[68] leading to $\alpha_2\beta_2$-$NH_2Y^{\bullet}_{731}$and $\alpha_2\beta_2$-$NH_2Y^{\bullet}_{730}$. The individual variants were mixed with the complementary α_2 or β_2 protein, CDP as substrate and ATP as effector. The reaction was then quenched after a few seconds inside EPR tubes. Details on sample preparation are given in Sec. 5.5.1 and 5.5.2. Figure 5.5 displays representative 94 GHz ^{17}O Mims[4] ENDOR spectra of the radical intermediates.

Each spectrum shows a sharp doublet centred on the ^{17}O Larmor frequency (19.3 MHz at 3.4 Tesla), which can be assigned to the central spin transition ($m_I(^{17}O) = +1/2 \rightarrow -1/2$) of one coupled ^{17}O nucleus. As ^{17}O is contained only in the water of the protein buffer, these sharp signals must arise from water molecules coupled to the radicals. Control experiments with only β_2 protein confirmed that the signal is associated to the radicals generated in $\alpha_2\beta_2$ (Sec. 5.5.3). The broad resonances between ± 2.5 MHz are attributed to other nuclear transitions of the $I = 5/2$ spin system, broadened by nuclear quadrupole coupling (Fig. 5.5, A). Additionally, we note asymmetry of the doublet, which arises from second order effects of the quadrupole coupling (Section 4.2). A comparison of the ENDOR spectra at the low ($B_0 \| g_1$) and high-field ($B_0 \| g_3$) edges of the EPR line (Sec. 5.5.4) indicates an almost isotropic hf coupling, with the dipolar contribution dominating the line width of the central doublet. The ^{17}O ENDOR spectra could be simulated with one ^{17}O nucleus, from which the asymmetry of the central peaks resulted using full diagonalization of the spin Hamiltonian (Fig. 5.5). Parameters are in Table 5.1. The spectra of $Y^{\bullet}_{356}$ and $NH_2Y^{\bullet}_{731}$ additionally contain signals close to the Larmor frequency not reproduced in the simulations, which likely originate from second sphere water molecules at the subunit interface. Additional broadening is also observed, particularly at $NH_2Y^{\bullet}_{731}$. It might be caused by conformational distribution of this residue, which was found to have flexibility.[129–131]

To rationalize the coupling, we began with a DFT optimized small model (25 atoms, details in Sec. 5.5.1) of $Y^{\bullet}_{356}$, as previous ENDOR revealed ^1H couplings consistent with one water at a H-bond distance $r_{O\text{-}H} \sim 1.8$ Å.[26] The ^{17}O coupling from this model was $A_{max}(^{17}O) \sim 1$ MHz, slightly exceeding the present experimental value of 0.6 ± 0.05 MHz. To optimize the model, we computed dihedral $\theta(C_3\text{-}C_4\text{-}O\cdots H)$ and distance scans for ^{17}O couplings, including the quadrupole tensor and the relative energies (Sec. 5.5.5). The DFT equilibrium distance always resulted in $r_{O\text{-}H} \sim 1.8$ Å. We found that hf coupling and energies vary significantly with θ, while the quadrupole coupling is less affected (Fig. 5.14, A, B and C). Values of $A_{1,2,3}$ of $\lesssim 1$ MHz are found for θ in the range $\lesssim \pm 30°$ (or equivalently $150° \lesssim \theta \lesssim 240°$), i.e. close to the ring plane. Water coordination in the ring plane also

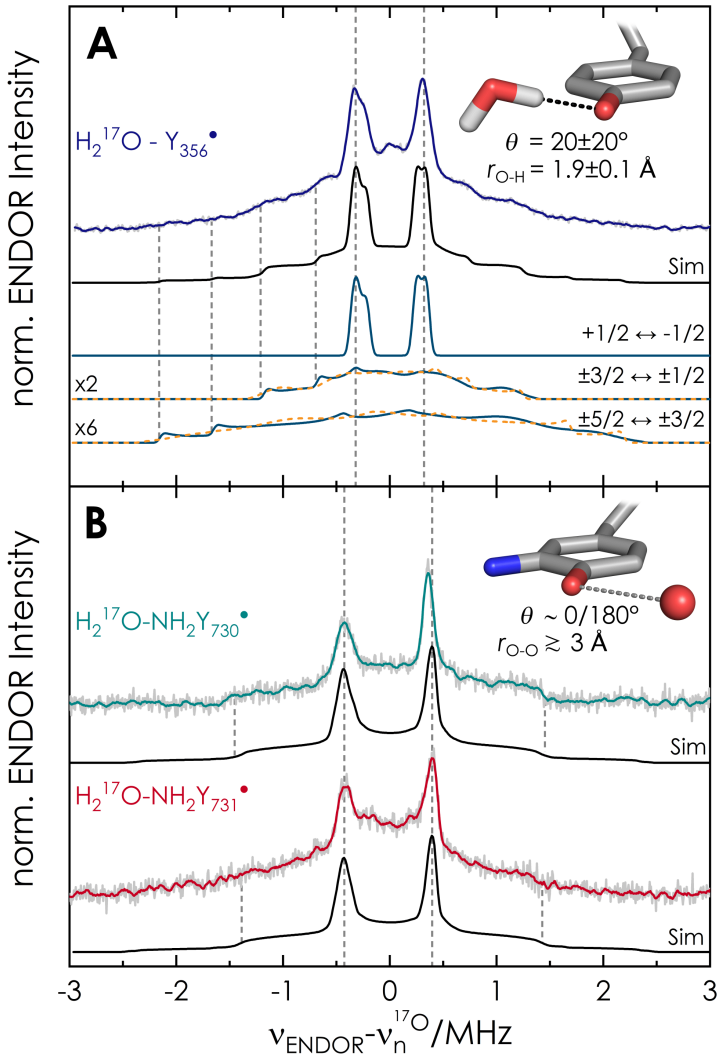

Figure 5.5: 94 GHz ^{17}O Mims[4] ENDOR spectra of the intermediate $Y_{356}^{\bullet}$ (**A**) and $NH_2Y_{731}^{\bullet}$ and $NH_2Y_{730}^{\bullet}$ (**B**) at $B_0 \parallel g_2$ in the EPR line; T = 50 K, τ_{Mims} = 390 ns. Acquisition time: 46 h ($Y_{356}^{\bullet}$), 40 h ($NH_2Y_{731}^{\bullet}$) and 18 h ($NH_2Y_{730}^{\bullet}$). $Y_{356}^{\bullet}$ is from β_2-$F_3Y_{122}^{\bullet}/\alpha_2$−$Y_{730}F$, which gives highest radical yield (Section 5.5.2). Experimental spectra are in gray, with Savitzky-Golay (SG) filter (4th order polynomial, 20 point-window) in color. Simulations used *EasySpin*[70] (Sec. 5.5.1.6) with parameters in Table 5.1 transitions among $m_I > 0$ manifolds, dashed lines (orange) among $m_I < 0$ manifolds. Simulation does not distinguish between dihedral $\theta = 0$ or 180°.

Table 5.1: Simulation and DFT parameters for ^{17}O-H_2O and ^{1}H hf couplings of water in RNR intermediates.

	$Y^{\bullet}_{356}$ Sim./ DFT$_{small}$	$NH_2Y^{\bullet}_{731}$ Sim.	$NH_2Y^{\bullet}_{730}$ Sim./DFT$_{large}$[(a)]
A_1 (^{17}O)	0.43/0.19	0.70	0.65/0.24
A_2 (^{17}O)	0.66/0.59	0.84	0.80/0.6
A_3 (^{17}O)	0.70/0.65	0.89	0.89/0.6
A (^{1}H)	6.2[26]/7.4	$\lesssim 2.5$[(a)]	2.7[(a)]/4.2
ρ(^{17}O)[(b)]	0.05 %	-	0.03 %
r(O$\cdots^{17}$O)	2.9 ± 0.1 Å	~ 3.0 Å	~ 3.0 Å

* Coupling values are in MHz. Simulated quadrupole coupling values for ^{17}O were $[P_1; P_2; P_3] = [-0.02; -0.32; 0.34]$ MHz with $e^2qQ/h = 6.8$ MHz and $\eta = 0.93$.[134]

(a) Values from ^{2}H couplings in Ref.[25] and Ref.[24] using $\gamma_{^1H}/\gamma_{^2H} \sim 6.526$.

(b) Loewdin spin density[135] from DFT. Uncertainties in coupling constants are less than 10 % for simulations and up to 20 % for DFT.

results in minimal relative energies (Fig. 5.14, B). Importantly, predicted spin densities on ^{17}O are < 0.1 %, but sufficient for producing a marked ^{17}O isotropic splitting. The spin density transfer or spin polarization is likely related to the H-bond nature.

A distance scan for the optimized dihedral of +20° predicts A_{max}(^{17}O) in the range $0.75 - 0.56$ MHz (Fig. 5.15, A) for $r_{O\text{-}H} = 1.8 - 2.0$ Å. Consideration of the DFT predicted ^{1}H couplings (Fig. 5.15, B) and comparison with the experimental values[25] of ~ 6.2 (H_1) and ~ 1.6 MHz (H_2) indicates that the water is located at r(Tyr-O$\cdots^{17}$O) = 2.9 ± 0.1 Å, corresponding to $r_{O\text{-}H}$ of 1.9 ± 0.1 Å. Notably, the DFT predicted dipolar coupling ($T_{\parallel} \sim$ 0.3 MHz, Sec. 5.5.5) is consistent with the point-dipole model and the above-mentioned broadening of the sharp peaks.

Analogous DFT calculations were performed on an isolated amino-tyrosyl $NH_2Y^{\bullet}$.[24,25,68] We observed a trend for the ^{17}O hf coupling in the dihedral and distance scans (Sec. 5.5.6) very similar to the $Y^{\bullet}$ model. The calculation predicts that a_{iso}(^{17}O) of $NH_2Y^{\bullet}$ is slightly larger (10-15 %) than in $Y^{\bullet}$ at similar Tyr-O$\cdots^{17}$O distance and orientation, which could explain the experimental observation. The amino group introduces an asymmetry in the radical and the energetically most favoured water orientation is found at the opposite side of the amino group (Fig. 5.16, B). Nevertheless, this small model could not account simultaneously for the ^{17}O and ^{1}H couplings observed for these two intermediates (Fig. 5.17). As noted in a previous g_1 calculation,[24] the coordination of the water molecule to $NH_2Y^{\bullet}$s is influenced by the surrounding second sphere residues, as these two intermediates are buried in $\alpha_2\beta_2$ (Figure 5.2).

Having established that at least one water molecule is hf coupled to each of the three intermediates, we examine their current molecular models in light of this finding. First, we consider the radical site $Y^{\bullet}_{356}$ (Figure 5.2). To explain the unprecedented g_1 value of $Y^{\bullet}_{356}$ (g_1 = 2.0062), we previously proposed that two almost equivalent waters might

be simultaneously bonded to $Y^{\bullet}_{356}$.[25] While the present results are most consistent with the distance and orientation proposed for one water, the 94 GHz ^{17}O ENDOR spectra (Fig. 5.5, A) cannot resolve a second water. We note that the spectral line shape and ^{17}O hf coupling in Fig. 5.5, A are conserved in other RNR constructs that generate $Y^{\bullet}_{356}$ (Section 5.5.7), including the $F_3Y^{\bullet}_{122}/E_{52}Q$-$\beta_2$ double mutant used to solve a recent cryo-EM structure.[136] To gain spectral resolution, we recorded ^{17}O ENDOR spectra of $Y^{\bullet}_{356}$ at 263 GHz/9.4 T, Figure 5.6.[13,137,138]

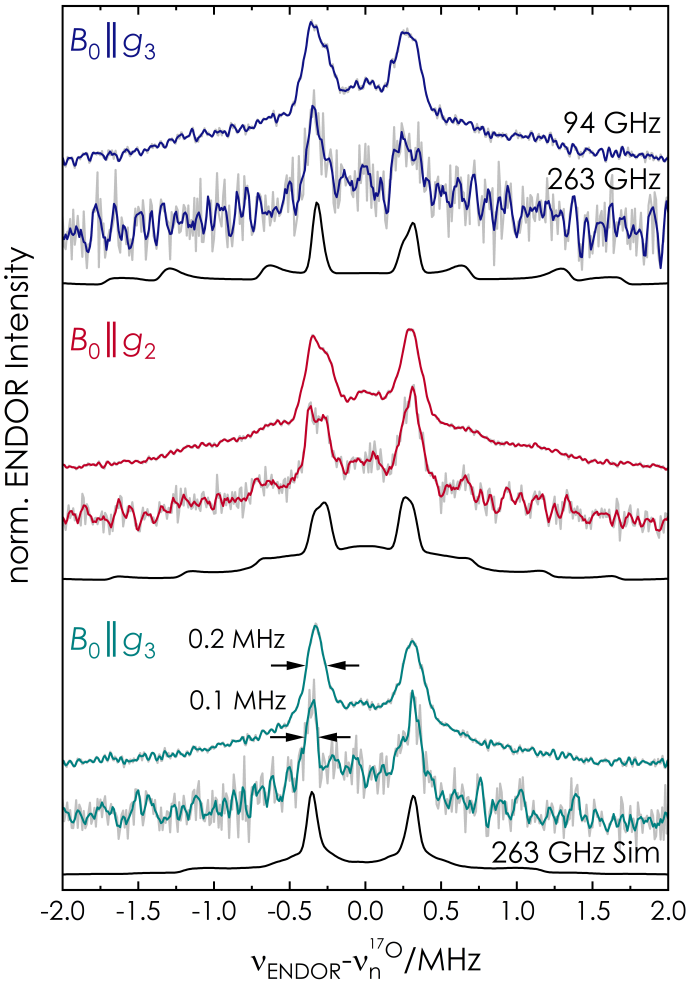

Figure 5.6: Comparison of 94 and 263 GHz Mims ENDOR of $Y^{\bullet}_{356}$ at the three canonical positions in the EPR line. For 263 GHz ($T = 20$ K): Total acquisition time: 18 h ($B_0 \| g_1$), 10 h ($B_0 \| g_2$) and 11 h ($B_0 \| g_3$). Experimental spectra are in gray, with SG filter (4^{th} order polynomial, 10 point window) in color. Simulations of 263 GHz spectra are in black with parameters as for 94 GHz (see Table 5.1 and Section 5.5.4).

The results illustrate that the line width of the central doublet substantially narrows, particularly at $B_0 \| g_3$ (Fig. 5.6). Despite the narrowing, a factor of approximately two from 94 to 263 GHz, we cannot discern two distinct ^{17}O contributions. Simulations of the 263 GHz spectra with the same parameters used at 94 GHz reproduce the line narrowing and

support the analysis at 94 GHz. The lack of evidence for a second, almost equivalent water H-bonded to $Y^{\bullet}_{356}$ strongly suggests that the two-water model has become very unlikely and alternative explanations for the shifted g_1 value of $Y^{\bullet}_{356}$ will have to be examined. The precise location of second sphere residues might play a role,[38] which will require further experimental and computational investigation.

For the radical intermediates in the subunit α_2 a previous combined ENDOR/DFT model of $NH_2Y^{\bullet}_{730}$ proposed a water molecule coordinated in plane at a distance $r(NH_2Y_{730}\text{-O}\cdots{}^{17}\text{O}) \sim 3.0$ Å.[24] The present results are consistent with this model and provide direct evidence for this postulated water in the enzyme complex $\alpha_2\beta_2$-$NH_2Y^{\bullet}_{730}$. The DFT predicted hf parameters (DFT_{large}) for this large model (140 atoms) are reported in Table 5.1 and the model is displayed in Fig. 5.4, A. Finally, for $\alpha_2\beta_2$-$NH_2Y^{\bullet}_{731}$, large-scale (215 atoms) DFT calculations previously proposed three models of the trapped intermediate. Among these models, only one (model 3, Fig. 5.4, B) contained a water molecule in H-bond distance. The DFT predicted ^{17}O hf couplings of model 3 (~ 2.5 MHz), however, largely exceed the present experimental values (Table 5.6). Albeit, this DFT model did not include residues from the β_2 subunit, which we now know are close to this residue in the active complex.[136] Therefore, the model will require further refinement. Nevertheless, the present results give evidence for a water molecule coordinated almost in plane of $NH_2Y^{\bullet}_{731}$.

In conclusion, we have reported the capability of ^{17}O high-frequency ENDOR to detect H-bonded water to tyrosyl radicals. The spectroscopic approach led to the first detection of ordered water molecules at three trapped radicals proposed to be representative of $Y^{\bullet}$ intermediates in the PCET of *E. coli* RNR. These results verify previous hypothesis on the presence and role of water in the RNR mechanism and provide a new starting point for computational studies. Knowledge of this ^{17}O signature will be generally useful also for many other biological systems, in which tyrosyl radicals are involved.

5.5 Supporting information

5.5.1 Experimental procedure

5.5.1.1 Sample preparation

90 % ^{17}O labelled water was purchased from Sigma Aldrich. The incorporation of unnatural amino acids into *E. coli* ribonucleotide reductase followed the previously reported protocols.[67,68] Purified α_2 (wild-type, $Y_{730}F$, NH_2Y_{731} and NH_2Y_{730}) was exchanged into 5 mM HEPES buffer (pH 7.6) containing 1.5 mM $MgSO_4$, 0.1 mM EDTA and 1 mM β-mercaptoethanol with Amicon spin filters (30 000 NMWL). 100 µL protein solution was supplemented with 300 µL buffer and spun at 12 000 g for 5 min. This process was repeated 6 times. ATP and CDP were added and the protein concentration was adjusted with assay buffer (50 mM HEPES pH 7.6, 15 mM $MgSO_4$, 1 mM EDTA) to yield a final concentration of 30 µM α_2, 500 µM ATP and 167 µM CDP. 100 µL quantities of this solution were frozen in liquid nitrogen and lyophilized overnight. The samples were rehydrated in 10 µL $H_2{}^{17}O$ to yield solutions of 300 µM α_2, 5 mM ATP and 1.67 mM CDP in assay buffer. Recovery of wild-type (wt) α_2 activity after the lyophilization procedure was checked by spectrophotometric activity assay and found to be 90 - 100 % (data not shown). Purified β_2 (wt, F_3Y_{122}, $F_3Y_{122}/E_{52}Q$) was exchanged into assay buffer with the abovementioned protocol and had the following concentrations: 890 µM wt-β_2, 980 µM F_2Y_{122}-β_2, 1600 µM $F_3Y_{122}/E_{52}Q$. EPR samples were prepared by mixing the previously described α_2 solutions containing substrate and effector with the corresponding β_2 solution (Table 5.2) and addition of $H_2{}^{17}O$ to a final concentration of 180 µM $\alpha_2\beta_2$, 3 mM ATP and 1 mM CDP. The final amount of $H_2{}^{17}O$ was approx. 80 %. The reaction mixtures were hand quenched in liq. N_2 inside EPR tubes. The quench times followed the previously established protocols for maximum radical

Table 5.2: Subunit combinations, quench times and radical yields.

α_2-subunit	β_2-subunit	Radical	Quench Time	Radical Yield[(a)]
$Y_{730}F$	2,3,5-F_3Y_{122}	$Y^{\bullet}_{356}$	10 − 20 s	40 %
wt	2,3,5-F_3Y_{122}	$Y^{\bullet}_{356}$	10 − 20 s	25 %
$Y_{730}F$	2,3,5-$F_3Y_{122}/E_{52}Q$	$Y^{\bullet}_{356}$	120 s	40 %
wt	2,3,5-$F_3Y_{122}/E_{52}Q$	$Y^{\bullet}_{356}$	120 s	35 %
F_2Y_{731}	2,3,5-$F_3Y_{122}/E_{52}Q$	$Y^{\bullet}_{356}$	20 s	5 %
NH_2Y_{731}	wt	$NH_2Y^{\bullet}_{731}$	10 − 20 s	10 %
NH_2Y_{730}	wt	$NH_2Y^{\bullet}_{730}$	10 − 20 s	30 %
-	wt	$Y^{\bullet}_{122}$	10 min	100 %
-	2,3,5-F_3Y_{122}	2,3,5-$F_3Y^{\bullet}_{122}$	10 min	100 %

[(a)] Method for radical determination is explained under Section 5.5.2.

yield.[25,26,69] EPR samples containing only β_2 with $H_2{}^{17}O$ were prepared by diluting the abovementioned solutions of β_2 (wt and F_3Y_{122}) with $H_2{}^{17}O$ to a final protein concentration of 180 µM and approx. 90 % $H_2{}^{17}O$. The β_2 solution was left to incubate for 10 min at 4°C to allow for sufficient exchange of water molecules within the protein, i.e. close to Y_{122}, and subsequently frozen in liq. N_2 inside the EPR tubes. W-band samples contained 2 µL protein mixture in 0.9 mm OD/0.5 mm ID suprasil tubes. 263 GHz samples contained 30 − 50 nL protein mixture in 0.33 mm OD/0.2 mm ID suprasil capillaries.

5.5.1.2 EPR spectroscopy

3.4 T EPR experiments were performed on a Bruker E680 pulsed W-band spectrometer with 2 W microwave power output. The optimal pulse length was determined by a Rabi nutation to 8 − 10 ns for a $\pi/2$ pulse at maximum output power. Echo detected EPR spectra for radical yield determination were recorded with a Hahn echo pulse sequence ($\pi/2 - \tau - \pi - \tau -$ echo) with τ = 290 ns. Shot repetition time (SRT) and shots/point varied for different temperatures and radicals and are given in the figure captions. 9.4 T experiments were performed on a Bruker E780 pulsed 263 GHz quasi-optical spectrometer with 100 mW microwave power output. The optimal pulse length was determined by a Rabi nutation to 30 − 32 ns for a $\pi/2$ pulse at maximum output power.

5.5.1.3 Relaxation measurements

To optimize ENDOR experiments at 50 K, we measured the relaxation properties of each radical. All relaxation experiments were recorded at the maximum of the EPR line, i.e. $B_0 \| g_2$. The electron spin-lattice relaxation time (T_{1e}) was determined via an inversion recovery experiment ($\pi - t - \pi/2 - \tau - \pi - \tau -$ echo, inset Fig 5.7). A bi-exponential fit (Eq. (5.1)) to the echo intensity as a function of the time-interval t yielded T_{1e} as the largest time constant, while the smaller time constant was assigned to spectral diffusion T_{SD}.

$$I = I_{0,1} \exp\left(-\frac{t}{T_{1e}}\right) + I_{0,2} \exp\left(-\frac{t}{T_{SD}}\right) + C \qquad \text{with} T_{1e} > T_{SD} \qquad (5.1)$$

At 50 K, T_{1e} is 1.6 ms for the tyrosyl radical $Y^{\bullet}_{356}/Y_{730}F\text{-}\alpha_2$ and 2.9 ms and 4.6 ms for the two amino-tyrosyl radicals $NH_2Y^{\bullet}_{731}$and $NH_2Y^{\bullet}_{730}$, respectively. Therefore all 50 K ENDOR experiments of $Y^{\bullet}_{356}$ were performed with 5 ms SRT, while 10 ms SRT was used for the two amino-tyrosyl radicals. The phase memory time T_m strongly influences the Mims ENDOR sensitivity (see Section 5.5.1.5). It was measured by recording the stimulated echo intensity as a function of the time delay τ ($\pi/2 - \tau - \pi/2 - T - \pi/2 - \tau -$ echo, inset Fig. 5.8).

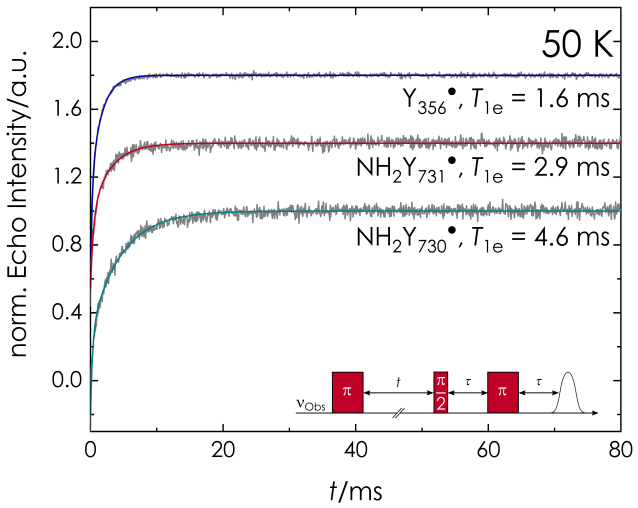

Figure 5.7: 50 K inversion recovery experiments of the three radical intermediates $Y_{356}^{\bullet}/Y_{730}F\text{-}\alpha_2$ (top, blue), $NH_2Y_{731}^{\bullet}$ (middle, red) and $NH_2Y_{730}^{\bullet}$ (bottom, cyan) in gray and bi-exponential fits (Eq. (5.1)) in color. Largest time constant are given in the figure. Inset: microwave pulse sequence.

T_m is the time constant of a mono-exponential decay fit to the experimental data (data not shown):

$$I = I_0 \exp\left(-\frac{t}{T_m}\right) + C \tag{5.2}$$

This experiment was repeated for increasing times T, i.e. the separation of the second and third $\pi/2$ pulse. The experiments show that initially, T_m decreases almost exponentially

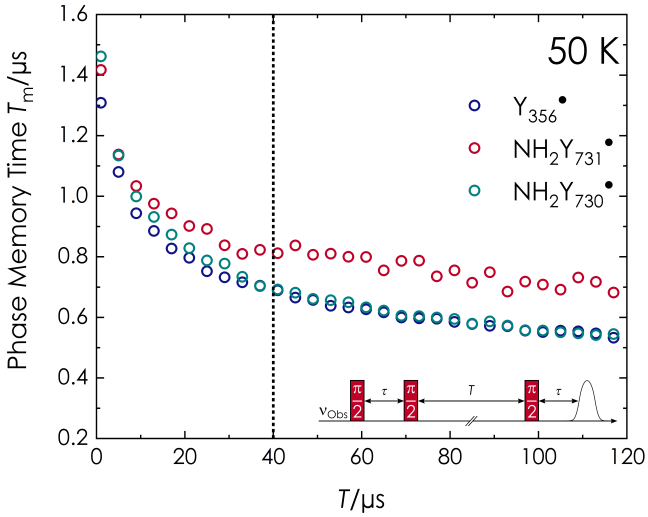

Figure 5.8: Phase memory times T_m as a function of the time T. Experimental values at 50 K for the three radicals $Y_{356}^{\bullet}/Y_{730}F\text{-}\alpha_2$ (blue), $NH_2Y_{731}^{\bullet}$ (red) and $NH_2Y_{730}^{\bullet}$ (cyan). The time $T = 40\,\mu s$, used in ENDOR experiments, is marked by a dotted line. Inset: microwave pulse sequence.

with increasing pulse separation time T for all investigated radicals. At $T = 40\,\mu s$, which was used for all ENDOR experiments, the phase memory time is approximately 700 - 800 ns for the three trapped radical intermediates.

5.5.1.4 ENDOR spectroscopy

ENDOR experiments at 94 and 263 GHz were recorded with the Mims[4] pulse sequence ($\pi/2 - \tau - \pi/2 - \text{rf} - \pi/2 - \tau - \text{echo}$) most sensitive to small hyperfine couplings. The microwave power at both instruments was reduced to produce $\pi/2$-pulses of 40 ns with an excitation bandwidth of 25 MHz/ 0.7 mT for increased orientation-selectivity. The τ-value was set as explained in the following Section (5.5.1.5). A 250 W rf-amplifier (250A250A, Amplifier research) was used to increase the rf pulse power. Rf pulse length was optimized with a rf Rabi nutation experiment (see Fig. 5.9). At W-band frequency, 40 µs rf pulses with an excitation bandwidth of 25 kHz were used, while 75 µs pulses with an excitation bandwidth of 13 kHz were used at 263 GHz. The difference in experimental setup at 3.4 T vs 9.4 T is caused by the different ENDOR resonator design and efficiency as well as varying output powers of the amplifier at the different frequencies.
All ENDOR experiments were recorded using stochastic rf acquisition with 30 shots-per-point .[139–141] Comparison of experiments with 1 shots/point vs 30 shots/point showed negligible saturation effects (data not shown), while a significant shortening of measurement time was observed for the latter method. This is caused by the reprogramming time of the spectrometer upon change of the rf frequency (i.e. between each x-axis data point),

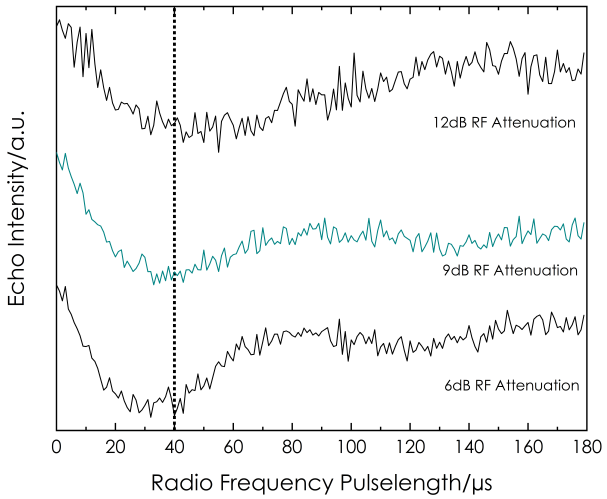

Figure 5.9: Rf Rabi nutation experiments of ^{17}O nuclei at 6, 9 and 12 dB radio frequency attenuation at 3.4 T (W-band). The nutation with the experimentally used attenuation is colored in cyan and the used radio frequency pulse length is marked by a dotted line. Experimental parameters: 50 K, pulse sequence: $\pi/2 - \tau - \pi/2 - \text{rf} - \pi/2 - \tau - \text{echo}$, $\pi/2 = 10$ ns, $\tau = 390$ ns, rf = $1 \rightarrow 180$ µs, 30 shot/point, 5 ms SRT.

which is around 30 ms and does not occur between shots at the same frequency. ENDOR experiments were recorded at 50 K at W-band and 20 K at 263 GHz. The temperature was chosen to achieve the best compromise between high signal intensity and short relaxation time for quick experimental shot repetition.

5.5.1.5 Choice of τ - value for Mims ENDOR

The sensitivity S of the Mims ENDOR experiment is described by the product of the ENDOR efficiency (F_{ENDOR}) and the echo intensity I_{echo}:

$$S = F_{\mathrm{ENDOR}} \cdot I_{\mathrm{echo}} \tag{5.3}$$

The Mims ENDOR efficiency for a nuclear spin $I = 1/2$ system can be described by a periodic function, depending on the effective hyperfine coupling A_{eff}:

$$F_{\mathrm{ENDOR}} = \frac{1}{2}\sin^2\left(\frac{A_{\mathrm{eff}}}{2}\tau\right) \tag{5.4}$$

This formula breaks down for nuclear spins $I > 1/2$, if the quadrupole coupling is on the order of the hyperfine coupling.[62] The approach was adapted for $I = 1$ nuclei by calculating A_{eff} from a combination of hyperfine and quadrupole coupling by Hoffman and coworkers. A similar treatment to $I = 5/2$ nuclei was however deemed unfeasible.[62] Therefore, the blind spots in a ^{17}O Mims ENDOR spectrum have to be treated within the

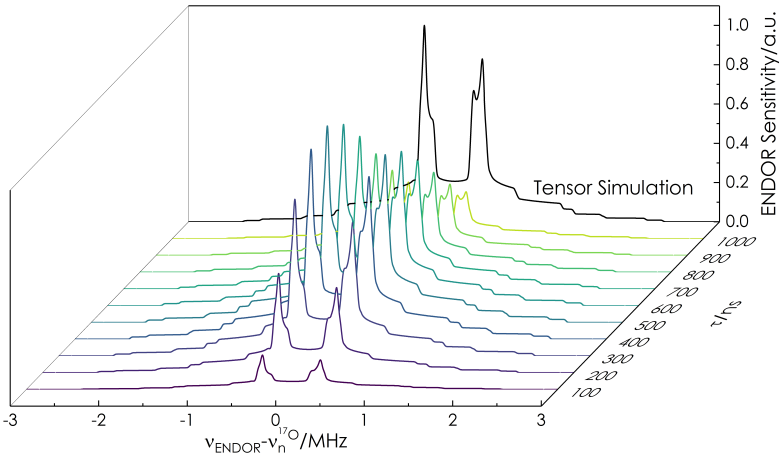

Figure 5.10: Comparison of ENDOR spectra of $Y^{\bullet}_{356}$ simulated with different τ-values (color) and with pure tensor simulation (black). Simulations are scaled by the experimentally determined phase memory time T_{m} = 0.7 µs.

density matrix formalism and an explicit calculation of the coherence transfer pathway of the Mims sequence for each individual spin system of interest. This can be achieved with the *EasySpin* routine `saffron`[142] (vide infra).

The second term on the right side of equation (5.3) nevertheless is true and has to be considered, since I_{echo} decays exponentially as a function of the phase memory time T_m (see Eq. (5.2)). The choice of the optimal τ–value therefore depends on T_m (here $\sim 0.7\,\mu s$, see Fig. 5.8) and the expected coupling parameters (A and P). Fig. 5.10 shows the simulated ENDOR spectrum of $Y^{\bullet}_{356}$with blind spots (color, Mims ENDOR simulation) and with pure tensor simulation (black). The ENDOR spectra are scaled by the phase memory time. The simulations show that no periodic blind spots are clearly visible in the simulated spectra. The shape of the central nuclear transitions depends slightly on τ but the main difference is the change in overall signal intensity. The overall maximum ENDOR signal can be achieved with values between 400 and 600 ns. In this study, we chose a τ-value of 390 ns to give the best compromise between ENDOR sensitivity and echo intensity, since the latter also influences the overall signal-to-noise of the spectra.

5.5.1.6 Simulation of ENDOR spectra

All ENDOR spectra were simulated using the *EasySpin* software package.[70] The simulated spin system was based on the literature g-values of the radicals $Y^{\bullet}_{356}$,[26] $NH_2Y^{\bullet}_{731}$ and $NH_2Y^{\bullet}_{730}$[25] as well as the nuclei with the largest hyperfine coupling constants (Table 5.3). In case of $Y^{\bullet}_{356}$, this was only the β-methylene proton, while the amino nitrogen was included for $NH_2Y^{\bullet}_{731}$ and $NH_2Y^{\bullet}_{730}$. Additional couplings were neglected, since they significantly prolong calculation times while their contribution to the orientation-selection and therefore the simulated ^{17}O ENDOR spectra was found to be negligible. ^{17}O ENDOR spectra were calculated with the `saffron` routine employing full tensor diagonalization (See 4.2). An excitation bandwidth of 25 MHz was used to select the orientations. A uniform ENDOR linewidth of 60 kHz was used for all simulations. All simulated ENDOR spectra were normalized to unity for comparison with equally treated experimental spectra.

Table 5.3: Spin system parameters for EPR simulations.[25,26]

Radical	g_1	g_2	g_3	Nuclei	A_1	A_2	A_3
$Y^{\bullet}_{356}$	2.0062	2.0045	2.0022	H_β	61	52	57
$NH_2Y^{\bullet}_{731}$	2.0051	2.0040	2.0022	H_β N_{amino}	23 2	22 3	22 31
$NH_2Y^{\bullet}_{731}$	2.0054	2.0042	2.0022	H_β N_{amino}	31 2	29 3	28 31

* Hyperfine coupling values in MHz.

The quadrupole coupling size calculated by DFT was generally too large. The deviation can in part be explained by the absence of other H-bonding partners to the water molecule in the small DFT models, which are known to reduce the quadrupole coupling constant.[134] Therefore, the literature known coupling constants for pure water in ice: $\boldsymbol{P} = [-0.02; -0.32; 0.34]$ MHz[134] was chosen and found to be in good agreement with the data of this work.

5.5.1.7 DFT calculations

DFT models were calculated using the *Orca* 4.0.1.2 software package.[73] Geometry optimization was performed using the BP86 functional[74,75] in combination with the Ahlrichs' def2-TZVP basis set of triple-ζ quality[76,77] for all atoms and the RIJCOSX approximation[78] (def 2/J auxiliary basis set). Grimmes dispersion correction (`d3bj`)[79,80] was applied on top of the SCF calculations. Single point energies and EPR parameters were calculated from the geometry optimized structures employing the B3LYP[75,81,82] functional in conjunction with the EPR-II basis set[83] for all nuclei. The abovementioned RIJCOSX approximation and dispersion correction were also used. The protein environment was approximated by a conductor–like polarization model (CPCM) with polarity $\epsilon = 24$.

The geometry of the small models of a tyrosyl and amino-tyrosyl radical model was initially optimized without a water molecule and only restricted to the experimentally known β-H dihedral angles (C_2–C_1–C_β-$H_{\beta 1}$) of 70° and -120° for $Y^\bullet_{356}$ and $NH_2Y^\bullet_{731}$, respectively.[25,26] A water molecule was added and its geometry was optimized while the C_3-C_4-$O_{Tyr}\cdots H_{H_2O}$ dihedral angle θ and the coordinates of all the radical atoms were fixed. In case of the amino-tyrosyl radical, the amino protons were not fixed, since they are potential hydrogen-bond partners for the water molecule. 36 individual models were calculated with θ values in increments of 10° from 0° to 350°. The $O_{Tyr}\cdots H_{H_2O}$ distance r was not fixed in the models.

5.5.2 Radical yield determination

Due to the half-site reactivity of *E. coli* RNR,[104,143] the EPR spectra of hand quenched samples contain the contribution of two radicals. One signal is the trapped radical in the RT pathway of one α/β pair of the "active" $\alpha_2\beta_2$ complex: $Y^\bullet_{356}/Y_{730}$F-α_2 (Fig. 5.11, A), $NH_2Y^\bullet_{731}$ (Fig. 5.11, B) or $NH_2Y^\bullet_{730}$ (Fig. 5.11, C). The second signal is $Y^\bullet_{122}$ or $F_3Y^\bullet_{122}$ in the unreacted α/β pair. The two radical species have very different relaxation times due to their different environments. The signal associated with the radical at residue 122 relaxes very fast due their proximity to the di-iron center, making it fully visible only at very low temperatures.[144]

Therefore, echo-detected EPR spectra of the samples were recorded at 10 K (Fig. 5.11, red lines) and the EPR spectrum of the respective tyrosyl radical at residue 122 (Fig. 5.11, blue lines) was subtracted.[145] The relative amount of radical trapped was then determined from the integral of the full EPR signal versus the integral of the subtracted spectrum (Fig. 5.11, cyan lines). The resulting radical yields are displayed in Fig. 5.11 and Table 5.2.

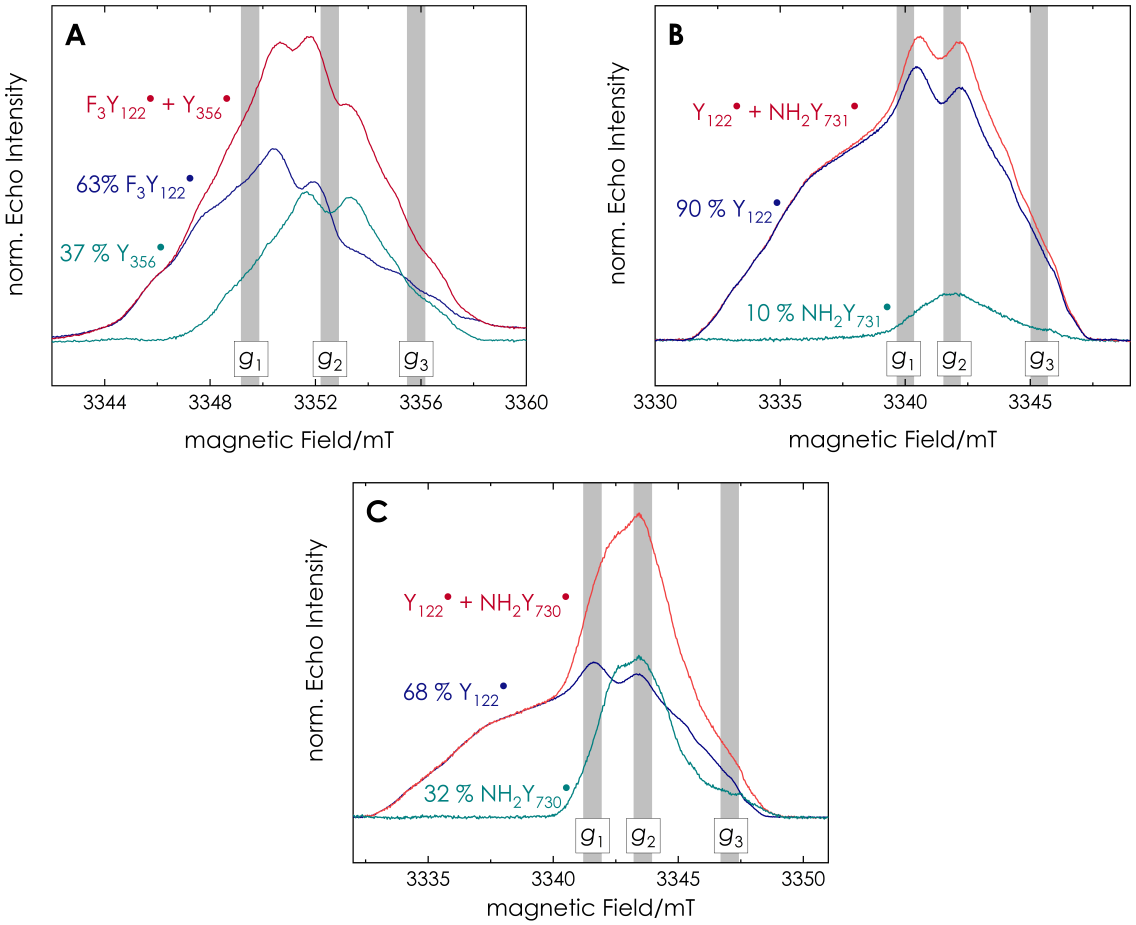

Figure 5.11: Echo-detected EPR spectra of reaction mixtures (red) with the radicals $Y_{356}^{\bullet}/Y_{730}$F-$\alpha_2$ (**A**), $NH_2Y_{731}^{\bullet}$ (**B**) and $NH_2Y_{730}^{\bullet}$ (**C**). Reference spectra of the respective resting β_2 (blue) and subtraction of the two spectra (cyan). Relative amounts of radical determined by integration and given in the figure. Canonical g-tensor orientations ($B_0 \| g_1$, $B_0 \| g_2$ and $B_0 \| g_3$), at which the orientation-selective ENDOR spectra were recorded, are marked by gray areas. Experimental parameters: 10 K, pulse sequence: $\pi/2 - \tau - \pi - \tau -$ echo, $\pi/2 = 10$ ns, $\tau = 290$ ns, 5 shot/point, 100 ms SRT.

5.5.3 Mims ENDOR spectra of $Y^{\bullet}_{122}$ and $F_3Y^{\bullet}_{122}$

The ^{17}O ENDOR experiments in this study were performed on radical mixtures that contain more than 50 % unreacted tyrosyl radical $Y^{\bullet}_{122}$ or $F_3Y^{\bullet}_{122}$ at the diiron cofactor. (See Figure 5.11 and Table 5.2). To exclude ^{17}O hf contributions of this radical, Mims ENDOR experiments of $Y^{\bullet}_{122}$ and $F_3Y^{\bullet}_{122}$ in the spectral region investigated in all other ENDOR experiments (19.3 ± 3 MHz) were recorded. These ENDOR experiments were performed at 10 K due to the fast relaxation properties of the two radicals caused by the adjacent di-iron cluster (see 5.5.2). Experiments were performed at the maximum of the EPR signal, i.e. $B_0 \| g_2$ and with full microwave power to increase the ENDOR signal.

The ENDOR spectra show a small amount of a mostly featureless signal in a range of ±0.2 MHz around the ^{17}O Larmor frequency. This contribution is smaller at temperatures higher than 10 K due to the fast relaxation properties which cause signal loss. The results confirm that the distinct coupling features detected in the ^{17}O ENDOR experiments of the pathway radical intermediates originate from water molecules at the intermediates themselves and not from the tyrosyl radicals associated with the di-iron cofactor.

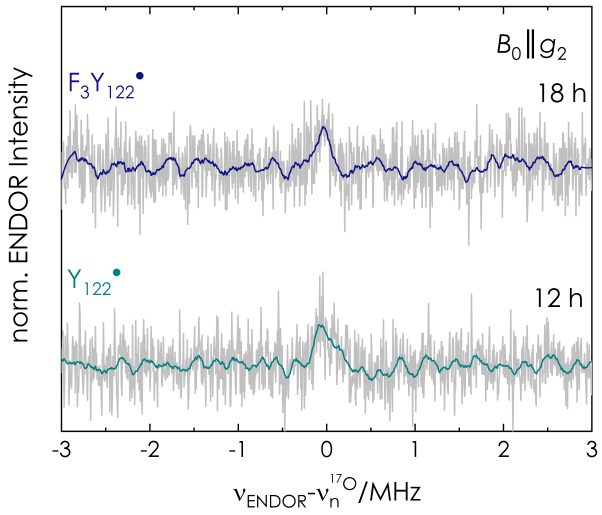

Figure 5.12: Mims ENDOR spectra of $Y^{\bullet}_{122}$ (cyan) and $F_3Y^{\bullet}_{122}$ (blue) in a region of ±3 MHz around the ^{17}O Larmor frequency recorded at the maximum EPR intensity, i.e. $B_0 \| g_2$. Experimental parameters: 10 K, pulse sequence: $\pi/2-\tau-\pi/2-$rf$-\pi/2-\tau-$echo, $\pi/2 = 8$ ns, $\tau = 390$ ns, rf = 40 µs, 5 shot/point, random rf acq., 30 ms SRT, 6 kHz rf sweep interval. Acquisition time of the spectra is written in the figure.

5.5.4 Orientation-selective Mims ^{17}O ENDOR spectra of the radical intermediates

Mims ENDOR spectra of the three radical intermediates $Y^{\bullet}_{356}/Y_{730}F\text{-}\alpha_2$ (A), $NH_2Y^{\bullet}_{731}$ (B) and $NH_2Y^{\bullet}_{730}$ (C) were recorded at the field positions corresponding to the three canonical g-tensor orientations marked in Fig. 5.11: $B_0 \| g_1$ (blue), $B_0 \| g_2$ (red) and $B_0 \| g_3$ (cyan). Baseline corrected (1st order polynomial) spectra are shown in light gray and 4th order SG filtered spectra (20 pt window) are shown in color. The difference in signal-to-noise in the spectra is a consequence of several factors: a) radical yield of the sample with the lowest overall S/N for $NH_2Y^{\bullet}_{731}$, b) different EPR signal intensity at the field positions with $B_0 \| g_2$ giving the best S/N since it is the maximum of the EPR spectrum, c) different ENDOR sensitivity at the specific g-tensor orientations with $B_0 \| g_3$ having more ENDOR sensitivity than $B_0 \| g_1$ for the $Y^{\bullet}_{356}$ radical, whiles this is reversed for the amino-tyrosyl radicals. This is caused by the smaller difference of g_1 and g_2 in the amino-tyrosyl radicals, resulting in the excitation of more orientations and the larger similarity of the spectra. Orientation-selective ENDOR simulations with the spin system parameters specified under Section 5.5.1.6 and the ^{17}O coupling parameters from Table 5.4 are shown in black.

Table 5.4: Simulated and DFT calculated ^{17}O hyperfine and quadrupole parameters.

Radical	A_1	A_2	A_3	α	β	γ	P_1	P_2	P_3	α	β	γ
$Y^{\bullet}_{356}$	0.43 0.19	0.66 0.59	0.70 0.65	49	168	-67	-0.02	-0.32	0.34	-39	87	-22
$NH_2Y^{\bullet}_{731}$	0.70	0.84	0.89	84	109	-68	-0.02	-0.32	0.34	50	82	-27
$NH_2Y^{\bullet}_{730}$	0.65 0.24	0.80 0.6	0.89 0.6	84	109	-68	-0.02	-0.32	0.34	50	82	-27

* DFT values are shown in blue. All coupling constants given in MHz. Euler angles given in degrees and defined from the $\boldsymbol{A}$ and $\boldsymbol{P}$ to the g-tensor based on the y-convention. $\boldsymbol{A}$ and $\boldsymbol{P}$ tensors are chosen so that $|A_1/P_1| < |A_2/P_2| < |A_3/P_3|$.

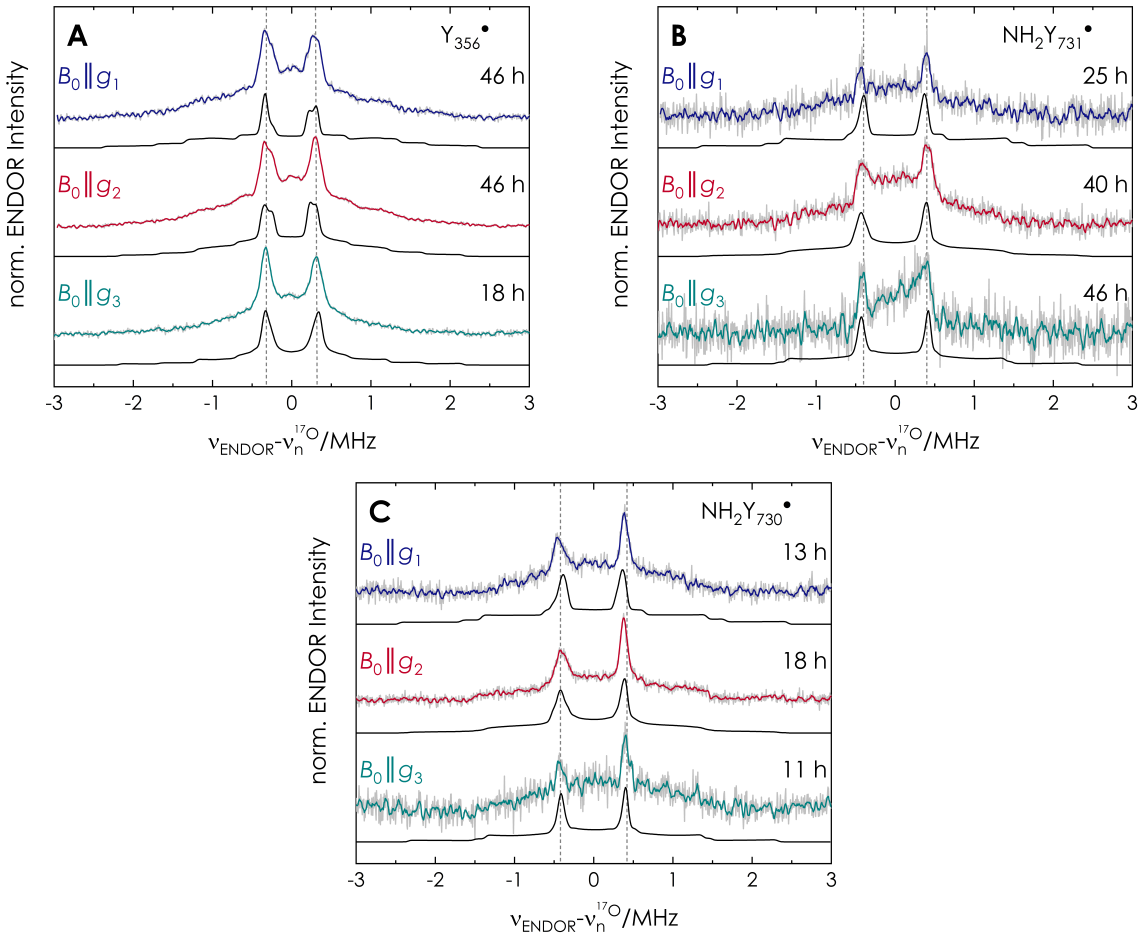

Figure 5.13: Orientation-selective Mims ENDOR spectra of $Y_{356}^{\bullet}$/Y_{730}F-α_2 (**A**), $NH_2Y_{731}^{\bullet}$ (**B**) and $NH_2Y_{730}^{\bullet}$ (**C**) recorded at field positions corresponding to the three canonical g-tensor orientations $B_0 \| g_1$ (blue), $B_0 \| g_2$ (red) and $B_0 \| g_3$ (cyan). Simulations given in black. Experimental parameters: 50 K, pulse sequence: $\pi/2-\tau-\pi/2-\text{rf}-\pi/2-\tau-\text{echo}$, $\pi/2 = 40$ ns, $\tau = 390$ ns, rf = 40 µs, 30 shot/point, random rf acquisition, 5 ms ($Y_{356}^{\bullet}$); 10 ms ($NH_2Y_{731/730}^{\bullet}$) SRT, 6 kHz rf sweep interval. Acquisition time of the spectra is written in the figure. Simulation parameters given in Section 5.5.1.6 and Table 5.4.

5.5.5 DFT models of an isolated tyrosyl radical with one coordinated water molecule

Small scale models of an isolated tyrosyl radical with a single water molecule were geometry optimized for restricted dihedral angles θ. From these, the single point energies and hyperfine as well as quadrupole coupling parameters were calculated. The results are shown in the following figure.

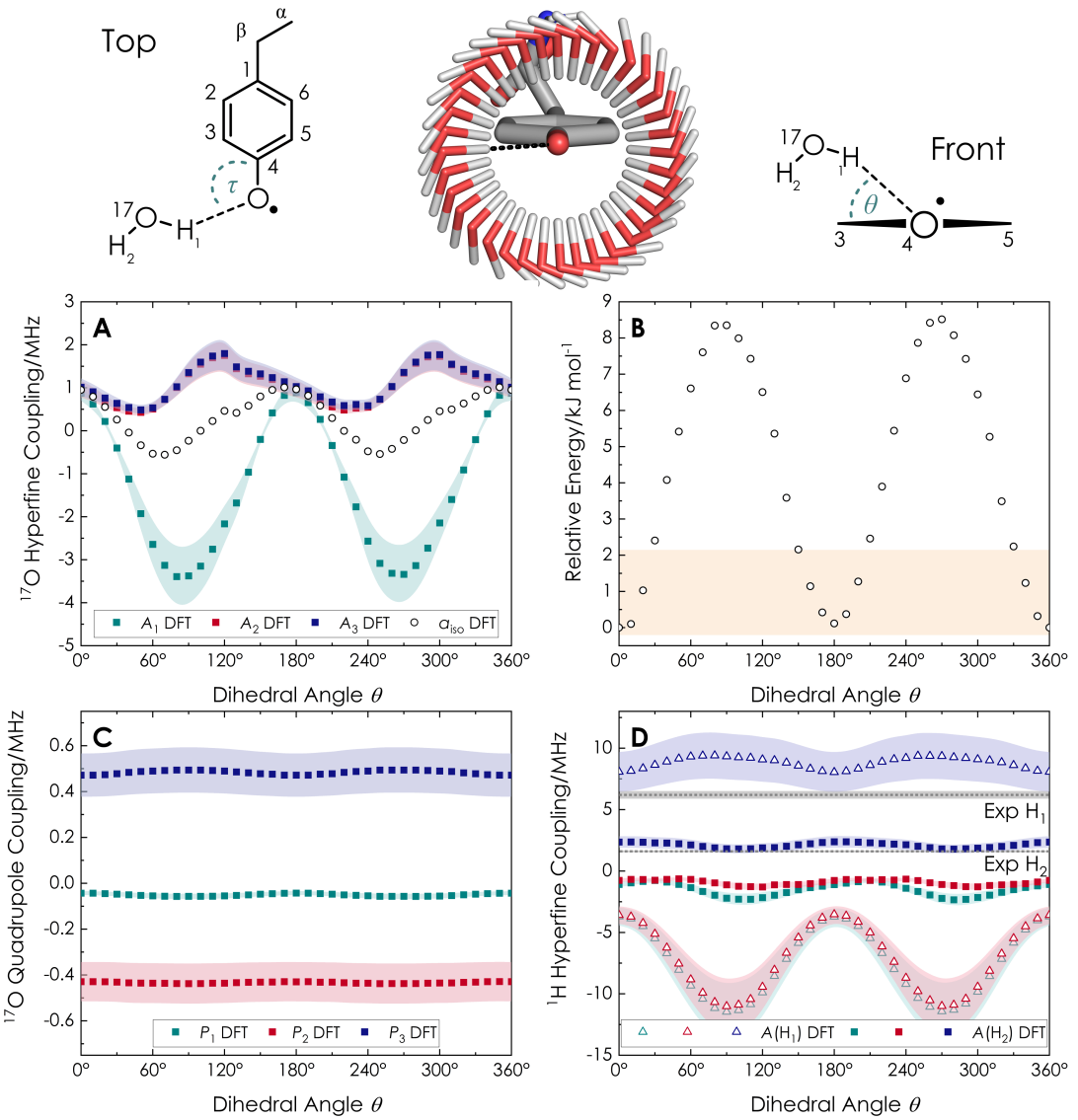

Figure 5.14: Angle scan for a tyrosyl radical with one water molecule. Top: Small (26 atoms) DFT models with one water molecule fixed at $\tau = 120°$ and dihedral angles $\theta(C_3\text{-}C_4\text{-}O_{Tyr}\cdots H_{H_2O})$ at DFT optimized distances of $r(O_{Tyr}\cdots H_{H_2O}) = 1.8$ Å. 0° structure is marked by black dashed line. Calculation method described under Section 5.5.1.7. **A**: Calculated ^{17}O hf coupling tensor components $A_{1,2,3}$ as well as isotropic coupling constant a_{iso}. Almost isotopic coupling in the experimental range $\lesssim 1$ MHz is found for θ in the range $\lesssim \pm 30°$ and $150° \lesssim \theta \lesssim 240°$. **B**: Relative energy of the calculated structures. $\theta = 0°$ structure set as the zero-point. Orange area represents an interval of thermal energy ($k_B T$) at 298 K. Coordination with $\theta = 0°$ and 180° results in equivalent energetic minima. **C**: Calculated ^{17}O quadrupole coupling tensor components $P_{1,2,3}$. The values change only slightly as a function of θ. **D**: Calculated ^{1}H hf coupling tensors components $A_{1,2,3}$ for H_1 (open triangles) and H_2 (full squares). Experimental values A from previous study[26] marked by dashed lines with 5 % confidence interval marked by grey areas. Couplings close to the experimental values are observed for $\theta = 0°$ and 180°. 20 % confidence interval of DFT calculated coupling constants are marked by colored areas.

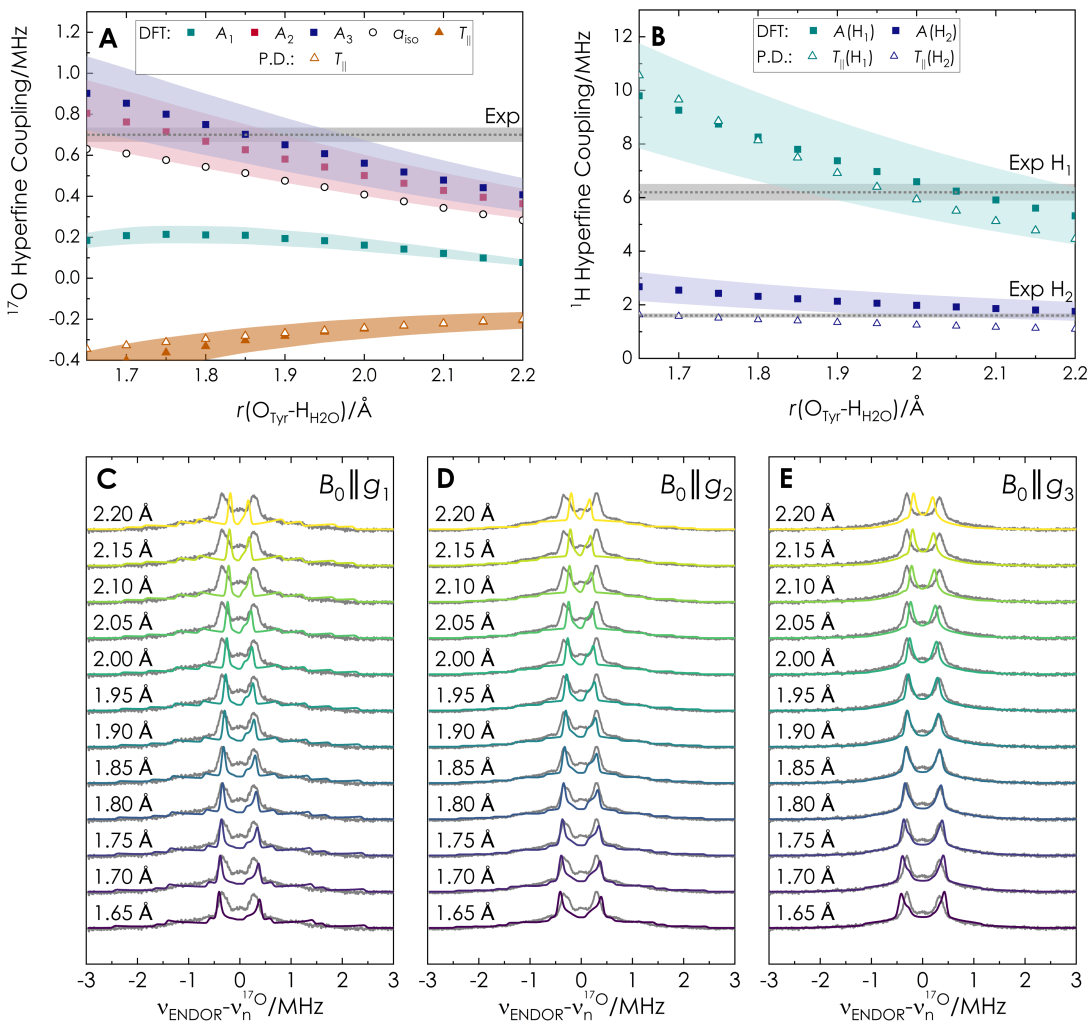

Figure 5.15: Distance scan for a tyrosyl radical with one water coordinated at $\theta = 20°$. **A**: DFT calculated ^{17}O hyperfine coupling tensor components and point-dipole (P.D.) approximated $T_{\parallel}$ components using a spin density $\rho = 0.3$ on the oxygen atom of $Y^{\bullet}$. **B**: DFT calculated ^{1}H hf coupling tensor components and point-dipole (P.D.) approximated $T_{\parallel}$ components with spin density $\rho = 0.3$. Experimental values are shown as gray dashed lines with a 5 % confidence interval marked as grey area. 20 % confidence interval of DFT calculated coupling constants are marked by colored areas. Orientation-selective ^{17}O Mims ENDOR simulations at **C**: $B_0 \| g_1$, **D**: $B_0 \| g_2$, **E**: $B_0 \| g_3$ for the calculated coupling tensors as a function of the $r(O_{Tyr} \cdots H_{H_2O})$ distance.

Figure 5.15 displays the distance dependence of the ^{17}O (A) and ^{1}H hf (B) couplings calculated by the DFT distance scan as well as by a simple point-dipole model. The dipolar coupling contribution from the point-dipole (P.D.) model was estimated as:

$$T_{\parallel}(\text{P.D.}) = 2 \cdot T = 2 \cdot \frac{\mu_0}{4\pi h} g_e \mu_B g_n \mu_N \frac{1}{r^3} \cdot \rho \tag{5.5}$$

where r is the inter spin distance and ρ the spin density. Since the water molecule is coordinated almost in plane, we assumed an interaction only with the spin density ρ on the oxygen atom, which was estimated from the DFT Loewdin spin population[135] analysis

calculation to be 0.3 for the tyrosyl radical. Nuclear g_n-values used were: $g_n(^{17}O) = -0.7575$ and $g_n(^{1}H) = 5.5857$.[43]

$$T_{\parallel}(^{17}O) = -2 \cdot 10.722 \frac{\text{Å}}{r^3_{O\cdots O}} \cdot 0.3 \qquad \text{and} \qquad T_{\parallel}(^{1}H) = 2 \cdot 79.064 \frac{\text{Å}}{r^3_{O\cdots H}} \cdot 0.3 \qquad (5.6)$$

We note that the point-dipole model agrees well with the dipolar contribution of ^{17}O computed by DFT (Figure 5.15, A). For the ^{1}H coupling, the experimental values A correspond to $T_{\parallel}$, as the tensors are almost purely dipolar. For the two ^{1}H tensors, the DFT computed values slightly exceed the point-dipolar approximation. The experimental values are found right between these two (Figure 5.15, B).
Overall, the distance analysis shows that a H-bond distance of 1.85 ± 0.05 Å leads to the best agreement of the ^{17}O couplings detected in this work, while a distance of $\sim 1.95 \pm 0.05$ Å leads to the best agreement with the ^{1}H couplings detected in *Nick et al.*[25] Taken this information together, we conclude that the H-bond distance is 1.9 ± 0.05 Å.
Figure 5.15, C/D/E illustrates that simulation of the ^{17}O ENDOR spectra with hf couplings predicted for a distance of 1.9 Å shows peaks and line shapes well compatible with the data.

5.5.6 DFT models of an isolated amino-tyrosyl radical with one coordinated water molecule

Small scale models of an isolated amino-tyrosyl radical with a single water molecule were geometry optimized for restricted dihedral angles θ. From these, the single point energies and hyperfine as well as quadrupole coupling parameters were calculated. The results are shown in the following figure.
Overall, the angle sweep for the amino-tyrosyl radical shows that coordination with $\theta = 180°$, i.e. in ring plane opposite to the NH_2-group results in the energetic minimum and ^{17}O hyperfine couplings compatible with the experimental data. A distance sweep for this coordination angle shows that the experimental ^{17}O couplings of $NH_2Y^{\bullet}_{730}$ and $NH_2Y^{\bullet}_{731}$ would be most compatible with $r(O_{Tyr}\cdots H_{H_2O}) = 2.8$ Å. (Fig. 5.17, A) This distance is however not compatible with the experimentally observed ^{1}H hf couplings for $NH_2Y^{\bullet}_{730}$ (Fig. 5.17, B) (and also not with those of $NH_2Y^{\bullet}_{731}$ since they are even smaller. See Table 5.1). We conclude that the small model cannot describe the amino-tyrosyl radicals sufficiently due to the absence of surrounding second sphere residues.

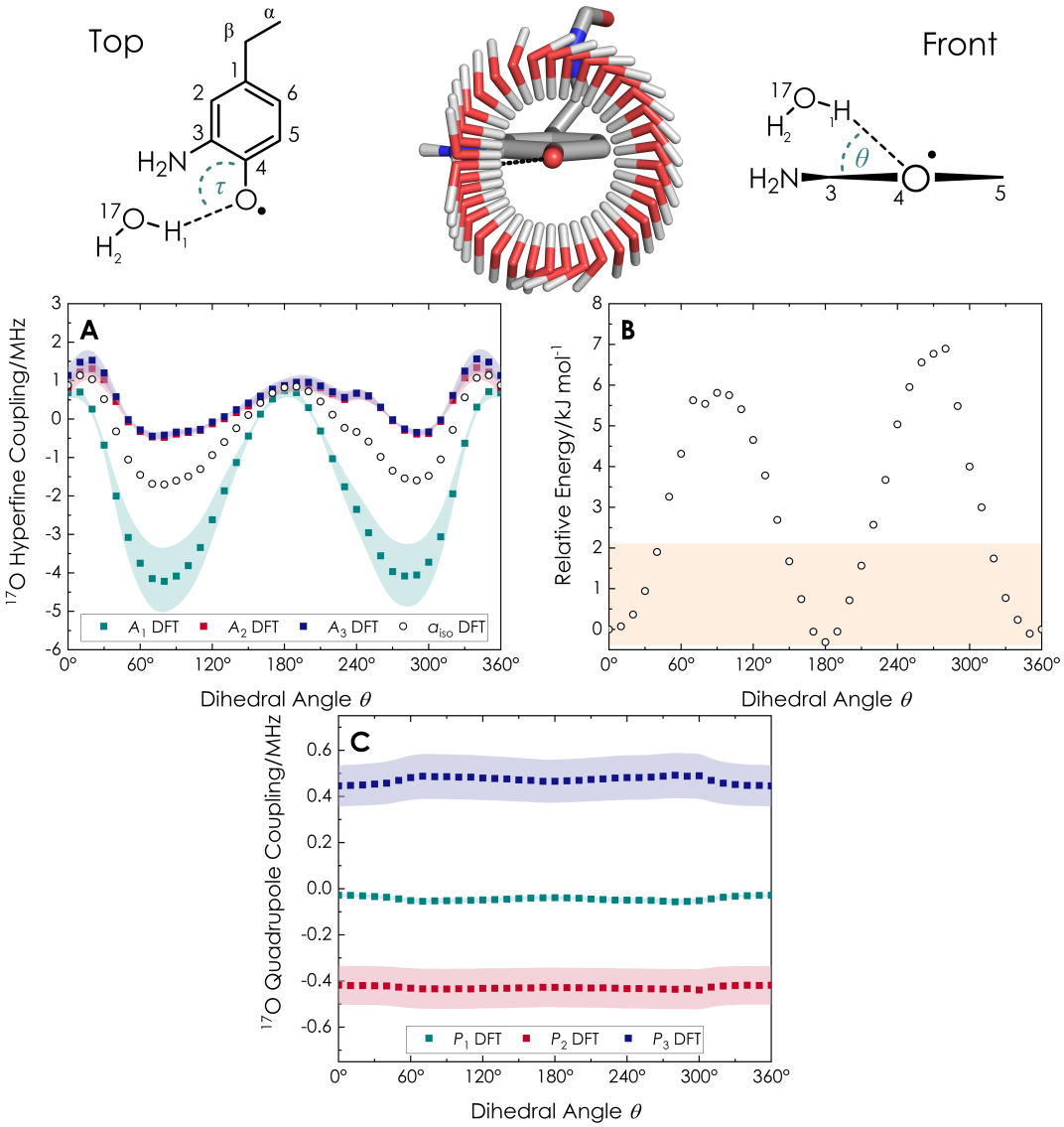

Figure 5.16: Angle scan for an amino-tyrosyl radical with one water molecule. Top: Small (28 atoms) DFT models with one water molecule fixed at $\tau = 120°$ and dihedral angles $\theta(C_3\text{-}C_4\text{-}O_{Tyr}\cdots H_{H_2O})$ at DFT optimized distances of $r(O_{Tyr}\cdots H_{H_2O}) = 1.8$ Å. 0° structure is marked by black dashed line. Calculation method described under Section 5.5.1.7. **A**: Calculated ^{17}O hf coupling tensor components $A_{1,2,3}$ as well as isotropic coupling constant a_{iso}. Almost isotopic coupling in the experimental range $\lesssim 1$ MHz is found for θ in the range $\lesssim \pm 10°$ and $150° \lesssim \theta \lesssim 240°$. **B**: Relative energy of the calculated structures, $\theta = 0°$ structure set as the zero-point. Orange area represents an interval of thermal energy ($k_B T$) at 298 K. Coordination with $\theta = 180°$, i.e. opposite to the NH_2-group, results in the energetic minimum. **C**: Calculated ^{17}O quadrupole coupling tensor components $P_{1,2,3}$. The values change only slightly as a function of θ. 20 % confidence interval of DFT calculated coupling constants are marked by colored areas.

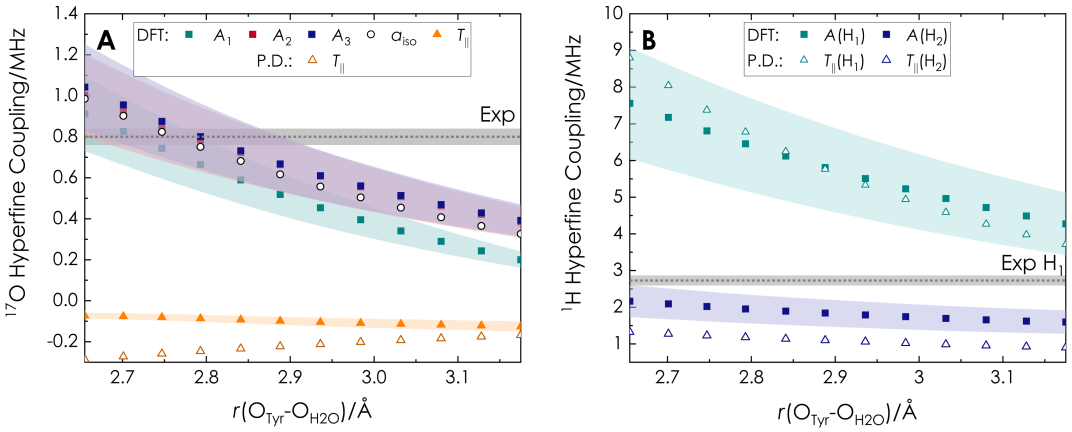

Figure 5.17: Distance scan for an amino-tyrosyl radical with one water coordinated at $\theta = 180°$. **A**: Calculated ^{17}O hyperfine coupling tensor components and P.D. approximated $T_{||}$ components (Eq. (5.5)) with a calculated spin density $\rho = 0.25$ on the oxygen atom of $NH_2Y^{\bullet}$. **B**: DFT calculated ^{1}H hf coupling tensor components and P.D. approximated $T_{||}$ components with a calculated spin density $\rho = 0.25$. Experimental values are shown as gray dashed lines with a 5 % confidence interval marked as grey area. 20 % confidence interval of DFT calculated coupling constants are marked by colored areas.

5.5.7 ^{17}O ENDOR on different mutants to generate $Y^{\bullet}_{122}$

The intermediate $Y^{\bullet}_{356}$ is accessible from different biochemical constructs which share the mutation, β_2-F_3Y_{122}. An additional mutation of $Y_{730}F$ in the pathway results in the highest radical yield. The F_3Y_{122}-β_2/$Y_{730}F$-α_2 construct was thus investigated both at 94 and 263 GHz. The F_3Y_{122}/$E_{52}Q$-β_2 was also studied as this double mutation leads to a tight $\alpha_2\beta_2$ complex that is active[136] which gave rise to the first high-resolution structure of the holocomplex by cryo-EM.[106] Additionally, the F_3Y_{122}-β_2/F_2Y_{731}-α_2 construct is planned for measurement of the distances between Y_{356} and the fluorines in F_2Y_{731}.[16] Figure 5.18 shows 94 GHz Mims ENDOR experiments for four possible combinations of subunit pairs prepared under similar conditions. The ^{17}O ENDOR line shape and position of the peaks do not vary significantly. Minor differences in asymmetry can be explained by slight variations in field positions. The spectra generally show that a specific coordination of one water molecule exists and is conserved across the biochemical constructs.

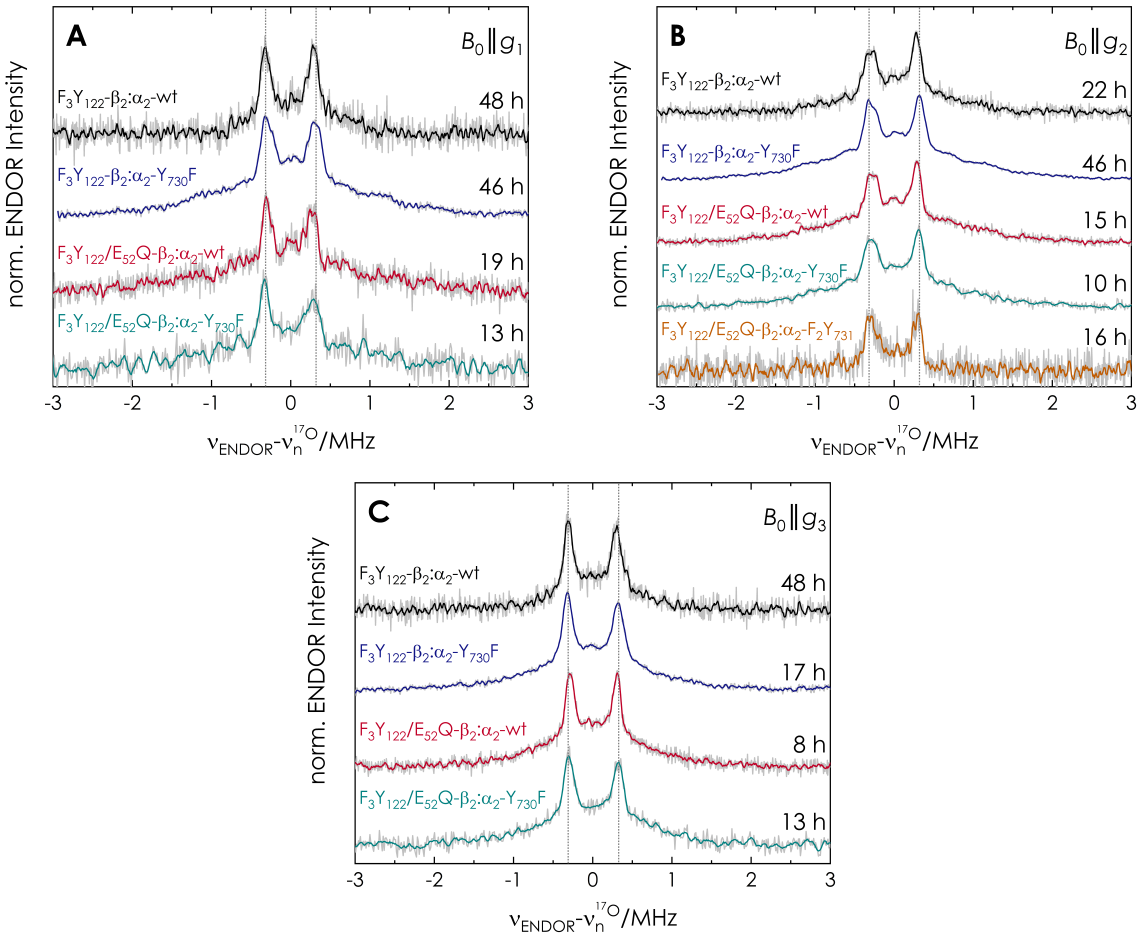

Figure 5.18: Orientation-selective Mims ENDOR spectra of $Y_{356}^{\bullet}$ produced by different biochemical constructs. **A**: $B_0 \| g_1$, **B**: $B_0 \| g_2$, **C**: $B_0 \| g_3$. Black: F_3Y_{122}-β_2 with wt-α_2. Blue: F_3Y_{122}-β_2 with $Y_{730}F$-α_2. Red: $F_3Y_{122}/E_{52}Q$-β_2 with wt-α_2. Cyan: $F_3Y_{122}/E_{52}Q$-β_2 with $Y_{730}F$-α_2. Orange: $F_3Y_{122}/E_{52}Q$-β_2 with F_2Y_{731}-α_2. S/N ratios across the spectra vary due to different radical yields at position 356 and different total acquisition times of the experiments. The radical yields are 25 % for F_3Y_{122}-β_2:α_2-wt, 40 % for F_3Y_{122}-β_2:α_2-$Y_{730}F$, 35 % $F_3Y_{122}/E_{52}Q$-β_2:α_2-wt, 30 % $F_3Y_{122}/E_{52}Q$-β_2:α_2-$Y_{730}F$ and 5 % $F_3Y_{122}/E_{52}Q$-β_2:α_2-F_2Y_{731}. Experimental parameters: 50 K, pulse sequence: $\pi/2 - \tau - \pi/2 - \text{rf} - \pi/2 - \tau - \text{echo}$, $\pi/2 = 40$ ns, $\tau = 390$ ns, rf = 40 µs, 30 shot/point, random rf acq., 5 ms SRT, 6 kHz rf sweep interval. Acquisition time of the spectra is written in the figure.

5.6 Additional information

The following was not included in the published SI.

5.6.1 Sensitivity of spectral shape on ^{17}O hyperfine parameters

The analysis of ENDOR experiments by spectral simulation might be viewed as a least square fitting procedure. The major difficulty lies in the number of fitting parameters to

the experimental data. In the case of ^{17}O ENDOR described in the previous chapter, the parameters for a single nucleus that need to be fitted to the experimental spectra are: three hyperfine tensor components $A_{1,2,3}$, three quadrupole tensor components $P_{1,2,3}$ and Euler angles α, β and γ for both coupling tensors, i.e. 12 parameters. If the desired outcome of the simulation is not just the reproduction of the experimental spectra but structural information, quantum mechanical modelling is the method of choice.

Recently, *Pribitzer et al.* have reported a fitting strategy for ^{1}H ENDOR spectra at X-band frequency, where they reduced the fitting parameter space to two, the nuclear distance and the isotropic hyperfine coupling, and introduced DFT model based regularization. This strategy showed great success for these particular nuclei with only two nuclear transitions and at low field, where orientation-selectivity can be neglected, but was nevertheless computationally very expensive.[146] Our group has recently been working on a Bayesian optimization approach for the simulation of ^{1}H/^{19}F ENDOR spectra, in which DFT calculated hf couplings are used as a Prior to fit the experimental ENDOR spectra. Once again, a key to the success of such a simulation approach is fast ENDOR spectra simulation and a good prior knowledge of the molecular structure, both of which were not available in this work. Instead, systematic DFT modelling was chosen to find a good structural parameter for investigation.

For the tyrosyl radicals investigated in this work, the dihedral angle θ was chosen for systematic study, since the ^{17}O hyperfine coupling varies significantly while the nuclear quadrupole coupling does not change (See Fig. 5.14). What does however change, is the relative orientation of the hyperfine and quadrupole coupling parameters, i.e. their Euler angles. This leaves 9 coupling parameters for optimization if a fixed quadrupole coupling is assumed. The hyperfine and quadrupole coupling tensors are linked to and defined by the the molecular frame of the water molecule, while the *g*-tensor is linked to the molecular frame of the radical. Hence, the dihedral angle θ can (in the simple models used here) be used as a substitute fitting parameter, which defines all 9 coupling parameters at once.

Simulations of the $Y^{\bullet}_{356}$ and $NH_2Y^{\bullet}_{730}$ Mims ENDOR spectra with the DFT calculated hyperfine coupling parameters and Euler angles are shown in Figures 5.19 and 5.20. They show the large changes in spectral shape observed for even small changes in the dihedral angle θ, which can be observed even without a trained eye. Quantitative analysis was performed by calculating the normalized root-mean square deviation (NRMSD) between simulations and experimental spectra.

$$\mathrm{NRMSD} = \sqrt{\frac{1}{N_{\mathrm{points}}} \sum_{i=1}^{N_{\mathrm{points}}} \left(y_i^{\mathrm{sim}} - y_i^{\mathrm{exp}}\right)^2} \tag{5.7}$$

Here, N_{points} are the total number of data points and y_i^{sim} and y_i^{exp} are the individual simulated and experimental data points, respectively. These show clearly defined minima at the angles of 160/340° for $Y^{\bullet}_{356}$ and 180° for $NH_2Y^{\bullet}_{730}$. It is also apparent, that the $B_0 \| g_3$ spectra are most sensitive to even small changes (cyan dots in NRMSD figures). From this analysis, the Euler angles of the hyperfine and quadrupole coupling tensors were chosen, reducing the number of fitting parameters to three. Thus can be handled manually and resulted in the parameters reported in Table 5.1. This analysis allowed us to give small confidence intervals for the dihedral angles ($\pm$10/20°).

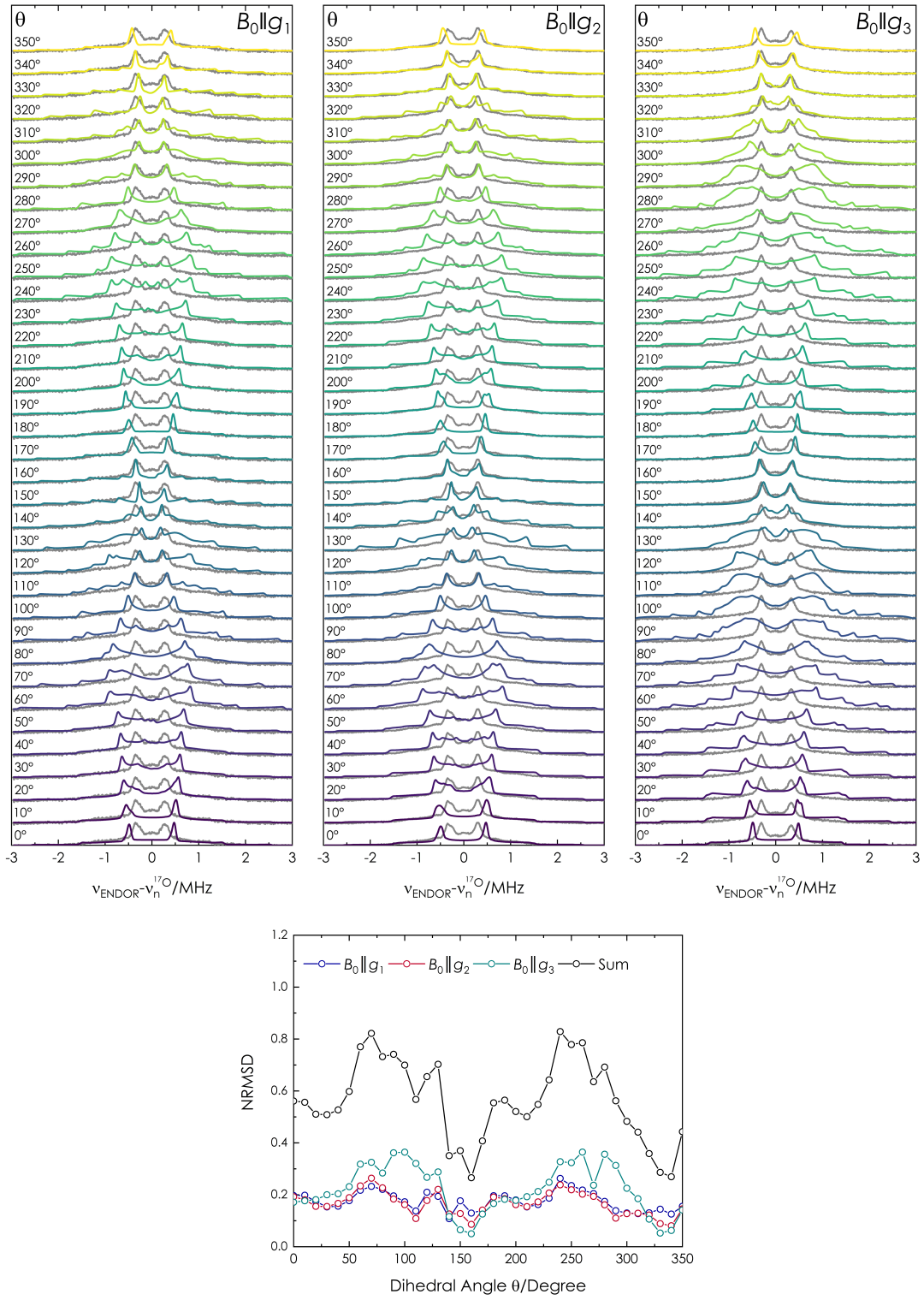

Figure 5.19: Top: Simulated (color) and experimental (grey) $Y_{356}^{\bullet}$ ENDOR spectra at $B_0 \| g_1$ (left), $B_0 \| g_2$ (middle) and $B_0 \| g_3$ (right). Bottom: Calculated NRMSD between simulation and experimental $Y_{356}^{\bullet}$ ENDOR spectra recorded at $B_0 \| g_1$ (blue), $B_0 \| g_2$ (cyan) and $B_0 \| g_3$ (red) and the sum of all three (black).

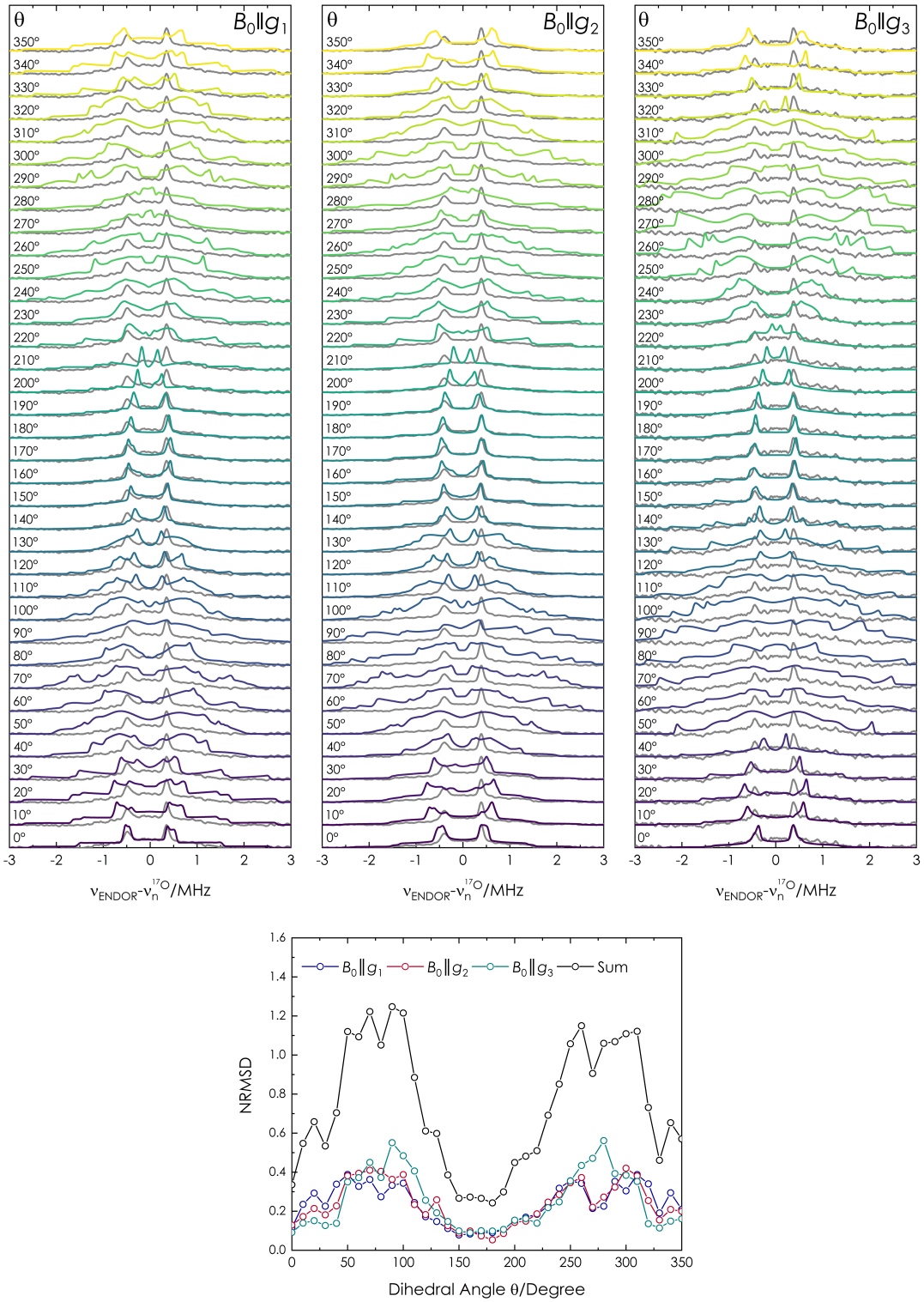

Figure 5.20: Top: Simulated (color) and experimental (grey) $NH_2Y^{\bullet}_{730}$ ENDOR spectra at $B_0 \| g_1$ (left), $B_0 \| g_2$ (middle) and $B_0 \| g_3$ (right). Bottom: Calculated NRMSD between simulation and experimental $Y^{\bullet}_{356}$ ENDOR spectra recorded at $B_0 \| g_1$ (blue), $B_0 \| g_2$ (cyan) and $B_0 \| g_3$ (red) and the sum of all three (black).

5.6.2 $Y^{\bullet}_{356}$ models with multiple water molecules

The ^{17}O Mims ENDOR spectra of $Y^{\bullet}_{356}$ showed very sharp spectroscopic features at 94 and especially at 263 GHz with linewidths $\sim$ 0.2 and $\sim$ 0.1 MHz, respectively, recorded at the $B_0 \| g_3$ position (see Fig. 5.6). This observation led us to reconsider our earlier model of two in-plane water molecules, which was used to explain the strongly shifted g_1 value of $Y^{\bullet}_{356}$.[26] In light of the strong dependence of ^{17}O hyperfine coupling parameters on small changes of dihedral angle θ (see previous section) it seemed unlikely that the narrow ENDOR spectra would be compatible with two water molecules. To test this hypothesis, we calculated a series of DFT models (Fig. 5.21) with two water molecules (Model C-F) and compared them to the best fitting single water model (Model A).

The hydrogen-bond distances, dihedral angles and calculated hyperfine coupling parameters for ^{17}O and ^{1}H are summarized in Table 5.5. Model B is our previously published model based on the ^{1}H ENDOR experiments, with wat1 at 20° and wat2 at 15°. Despite the small difference in coordination angle, the resulting ^{17}O couplings differ by more than 0.1 MHz, which is not compatible with the experimental observations. Model C was optimized by

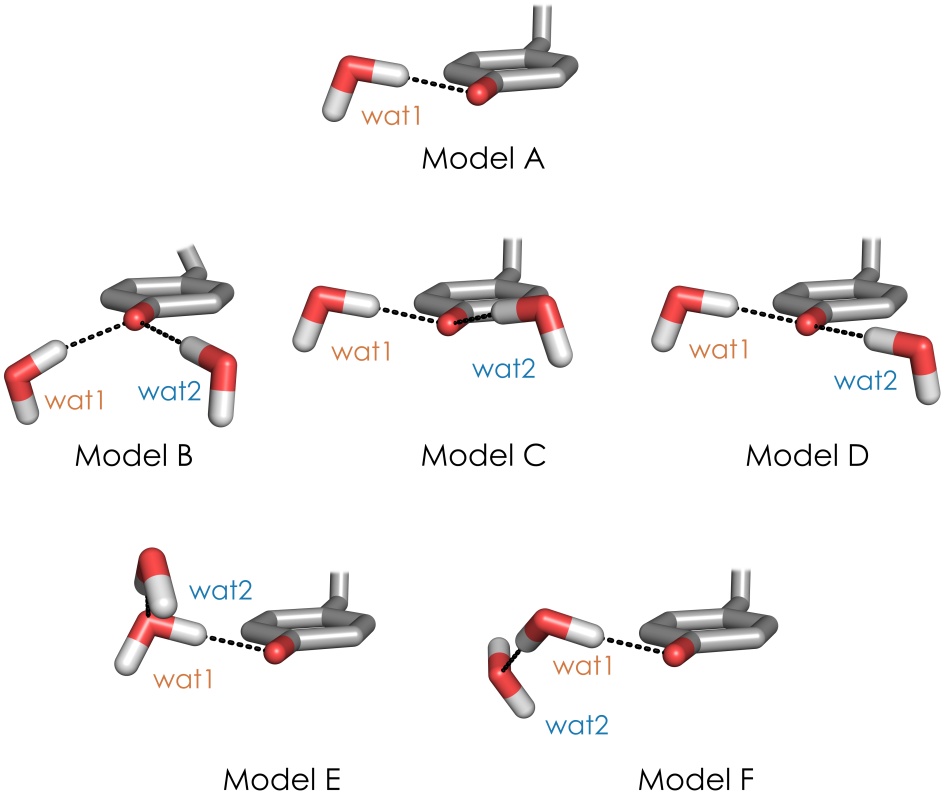

Figure 5.21: $Y^{\bullet}_{356}$ models with multiple water molecules. Model A is the best fitting single water model with a dihedral angle of 20°. Model B is our previous model from *Nick et al.*[26] Models C-F are described in the text. The structure parameters and calculated ^{17}O and ^{1}H hyperfine couplings are summarized in Table 5.5.

restricting both water molecules to the same dihedral angle of 20°, resulting in a fully symmetric structure. The calculated hyperfine couplings are nearly identical and smaller than for the single water Model A, showing that an absolutely symmetric coordination would be compatible with the experimental data. Such a situation is however unlikely in an asymmetric protein environment. Model D was optimized by restricting wat1 to a dihedral angle of 20° while wat2 was unrestricted. In the resulting structure, wat2 assumes an angle of 5°, which results in significantly different hyperfine coupling ($\Delta A_3 \sim 0.3\,\mathrm{MHz}$).

Finally, the influence of additional hydrogen-bonding to the H-bound wat1 was investigated in Model E and F. In Model E, wat2 forms a hydrogen-bond with one of the lone-pairs of wat2 while the opposite situation is shown in Model F. Both models were calculated by restricting the dihedral angle of wat1 and placing the wat2 in the desired hydrogen-bond orientation before optimization. In both models, the distant water molecules (wat2) show ^{17}O hyperfine couplings smaller than 0.15 MHz, which would fall into the center of the ENDOR spectra. The coupling of wat1 is influenced by the water coordination, becoming larger if one of its lone-pairs is coordinated (Model E) and becoming smaller if it coordinates a lone-pair of wat2 itself (Model F).

The models with two water molecules show, that small differences in binding geometry can cause large differences in hyperfine coupling, which is not in agreement with the sharp signals observed in the ENDOR spectra. We thus concluded that a coordination with two water molecules is unlikely. The models also show, that hydrogen-bonding of wat1 with

Table 5.5: Structure parameters and hyperfine couplings of the $Y^{\bullet}_{356}$ models with multiple water molecules.

Model	Water	r(O-H)/Å	θ/°	$A_1(^{17}O)$	$A_2(^{17}O)$	$A_3(^{17}O)$	$A_3(H_1)$	$A_3(H_2)$
A	1	1.8	20	0.29	0.68	0.81	8.2	2.5
B	1	1.8	20	0.58	0.90	0.98	7.5	2.2
	2	1.8	15	0.18	1.03	1.15	7.8	2.4
C	1	1.8	20	0.20	0.61	0.73	7.7	2.4
	2	1.8	20	0.22	0.61	0.74	7.7	2.4
D	1	1.8	20	0.24	0.59	0.72	7.7	2.4
	2	1.8	5	0.73	0.90	1.00	7.0	2.4
E	1	1.8	20	0.35	0.74	0.91	8.0	2.2
	2	3.6	50	0.07	0.08	-0.13	1.5	1.0
F	1	1.8	20	0.01	0.64	0.73	8	2.5
	2	4.1	20	-0.12	0.11	0.14	1.6	1.3
Sim.	-	1.9	20	0.43	0.66	0.7	6.2	1.6

* All coupling values given in MHz.

water molecules influences the ^{17}O hyperfine coupling even if the dihedral angle is kept constant, motivating larger models of $Y^{\bullet}_{356}$ within its protein environment.

5.7 Perspectives

The current understanding of the proton-coupled electron transfer mechanism in *E. coli* ribonucleotide reductase is a result of countless biochemical, biophysical and computational studies, which range from kinetic investigations to detailed structure analysis. Ultimately, an understanding of the RT transfer pathway requires full atomistic models of the individual intermediates. Experimentally determined EPR parameters can be used to validate such models. Our group has previously published two models of the aminotyrosyl radicals and their immediate protein environment (Fig. 5.4), which were built based on the crystal structures of the individual α_2-subunits.[24,25] The models were in agreement with the experimental *g*-values as well as the ^2H hyperfine and quadrupole coupling tensors of the exchangeable protons surrounding the radical intermediates. Both models contained water molecules in the vicinity of the respective radical intermediate and were therefore in principle suited to reproduce the experimental ^{17}O hyperfine couplings recorded in this study. Calculation of the ^{17}O hyperfine coupling parameters from these structures resulted in reasonable agreement for the $NH_2Y^{\bullet}_{730}$ model, while the $NH_2Y^{\bullet}_{731}$ values did not agree with the simulations (see Table 5.6).

The recent cryo-EM structure of the "active" $\alpha_2\beta_2$ RNR complex showed, that part of the closely bound β-subunit, referred to as the β-*tail*, protrudes into the α-subunit close to the RT residues.[106] Specifically the residues β-P_{348} and -Q_{349} are of particular interest as they come close to α-Y_{731} in the cryo-EM structure and it is therefore prudent to assume that they influence the radical's surroundings, most notably the placement of water molecules around them. Additionally, the residue α-P_{621} was not included in the previous models, which is however in close vicinity to the α-$Y_{731}Y_{730}$ dyad and therefore also likely relevant for the structure.

5.7.1 Models of $NH_2Y^{\bullet}_{730}$ and $NH_2Y^{\bullet}_{731}$

To create new models, atomic coordinates of the α-$Y_{731}Y_{730}$ dyad from the previous models were fitted to the corresponding atoms in the cryo-EM structure. The closest surrounding residues were then chosen: α-$A_{696}N_{695}S_{694}$, -P_{621}, -C_{439}, -Y_{413}, -R_{411}, -D_{334} and β-$Q_{349}P_{348}$. For single residues, the backbone atoms were truncated at the C_α and replaced by hydrogen atoms to reduce the overall atom count of the models. For adjacent residues, the connecting backbone atoms were included. Two water molecules (wat_1 and wat_2) were added, one at each radical, at dihedral angles of 180 degrees. The models

included a total of 200 atoms. The models were geometry optimized under the following restrictions:

- All backbone carbon, oxygen and nitrogen atoms were fixed
- The C_α-C_β-C_1-C_2 dihedral angles of the respective amino-tyrosyl radicals were fixed at the experimental values
- The angles and distances of the radicals' hydrogen-bond donors (except the water molecules) were fixed at the previously reported values

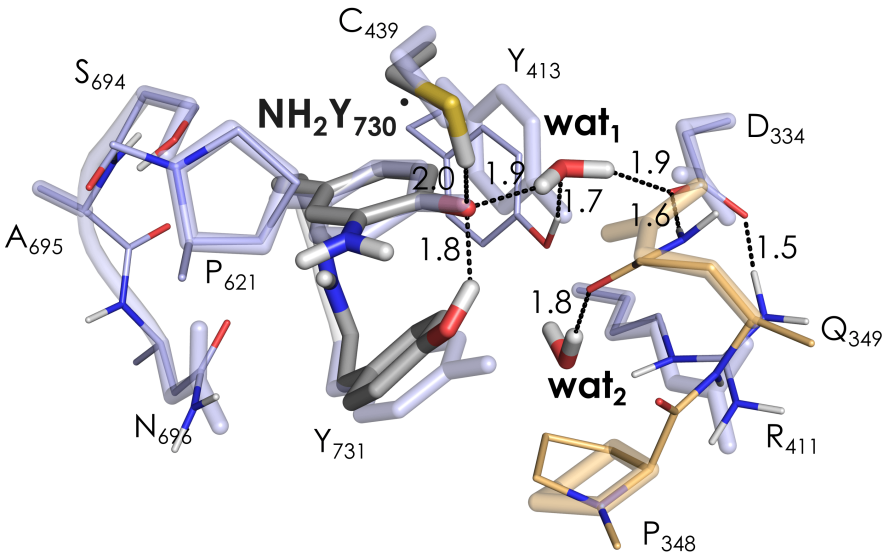

Figure 5.22: Large scale model of $NH_2Y^\bullet_{730}$ based on the cryo-EM structure. Residues belonging to the α-subunit are shown in blue and belonging to the β-subunit are shown in orange. Redox-active residues on the radical transfer pathway are shown in grey sticks. Cryo-EM arrangement is shown as transparent sticks while the geometry optimized arrangement is shown as wires. Hydrogen-bonding interactions are shown as black dashed lines and distances given in Å.

From the geometry optimized structures, the ^{17}O hyperfine coupling parameters of the water molecule were calculated. The resulting structures of $NH_2Y^\bullet_{730}$ and $NH_2Y^\bullet_{731}$ are shown in Figure 5.22 and 5.23, respectively, where they are compared to the residue placement within the cryo-EM structure.

Both models show, that the β-residues do not come close enough to the radical intermediates for direct hydrogen-bonding. They are however close enough to define the coordination space around the radicals and influence the placement of the two water molecules. A residue that has particular importance is β-Q_{349}, as it forms a tight hydrogen-bond or salt bridge with β-D_{334} and a H-bond with wat_1 in the $NH_2Y^\bullet_{730}$ or wat_2 in the $NH_2Y^\bullet_{731}$ models, accompanied by a twisting of the head-group between the two models. The wat_1 molecule, bound to $NH_2Y^\bullet_{730}$ at 1.9 Å is additionally bound by α-Y_{413} and α-D_{334} in this

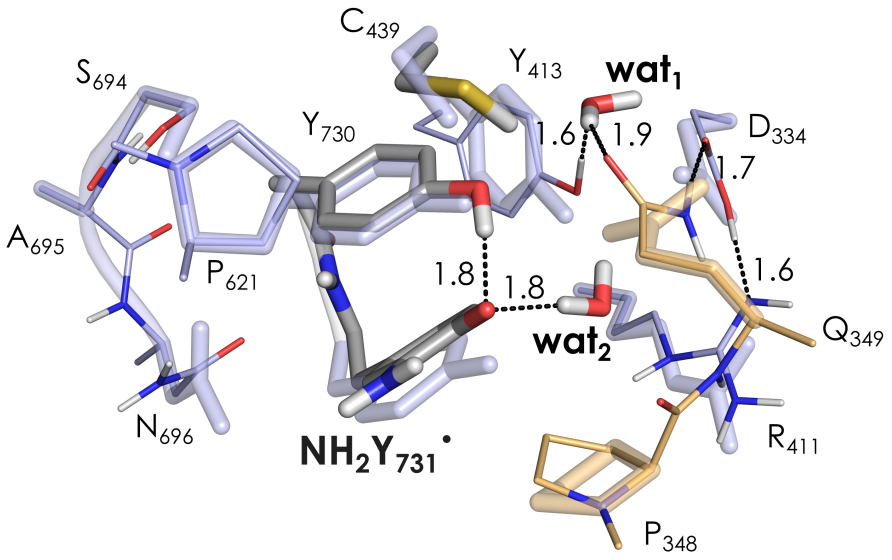

Figure 5.23: Large scale model of $NH_2Y^{\bullet}_{731}$ based on the cryo-EM structure. Residues belonging to the α-subunit are shown in blue and belonging to the β-subunit are shown in orange. Redox-active residues on the radical transfer pathway are shown in grey sticks. Cryo-EM arrangement is shown as transparent sticks while the geometry optimized arrangement is shown as wires. Hydrogen-bonding interactions are shown as black dashed lines and distances given in Å.

as well as the precious model (Fig. 5.22 and *Argirevic et al.*), explaining the very defined position in accordance with the sharp spectroscopic features. The orientation with respect to the ring plane of the amino-tyrosyl is 5°, in excellent agreement with our small model investigation. The calculated ^{17}O coupling parameters are given in Table 5.6 under DFT_{large} and are in good agreement with the experimental data. They are generally larger and fit the experimental ^{17}O data better than in the previous model, a result of the shorter hydrogen-bond distance.

The wat_2 molecule in the $NH_2Y^{\bullet}_{731}$ model (Fig. 5.23) is bound to the radical intermediate at a distance of 1.8 Å and an angle of 30°, both slightly outside the boundaries set by our small model investigation. This appears to be influenced by a long distance hydrogen-bond to α-Y_{413} of $\sim$ 2.4 Å. The coupling parameters of this model (DFT_{large}), given in Tab. 5.6, fit to the experimental spectra much better than the previous model (*Nick et al.*). Compared to the small model however, the deviation of A_1 is significant and requires further optimization. In contrast to the protein pocket housing wat_1 near $NH_2Y^{\bullet}_{730}$, the coordination space at the subunit interface, defined mainly by β-$Q_{349}P_{348}$ and α-R_{411}, allows for multiple water molecules, which might additionally influence the placement of wat_2. Due to the large amounts of structural freedom in the computation of water cluster geometry, this would however also require the inclusion of more residues. Such calculations are computationally very expensive and go beyond the current scope of this work. The advancement of fast QM

calculations and ever larger computational resources make it however feasible to extent the models in the future.

Table 5.6: Calculated ^{17}O hyperfine coupling parameters for $NH_2Y^\bullet$ models.

$NH_2Y^\bullet_{730}$	A_1	A_2	A_3	α	β	γ
Argirevic et al.[24]	0.24	0.57	0.61	80	54	−29
DFT_{small}[15]	0.69	0.89	0.94	81	109	−68
DFT_{large}	0.47	0.84	0.93	−85	105	−46
Simulation	0.65	0.80	0.89	81	109	−68
$NH_2Y^\bullet_{731}$	A_1	A_2	A_3	α	β	γ
Nick et al.[25]	0.37	0.59	−2.59	9	85	−40
DFT_{small}[15]	0.69	0.89	0.94	81	109	−68
DFT_{large}	−0.02	0.58	0.85	−30	29	−90
Simulation	0.70	0.84	0.89	81	109	−68

* All coupling values given in MHz. All angles given in degree.

5.7.2 Model of $Y^\bullet_{356}$

The mechanism of proton-coupled electron transfer across the subunit interface has been a mystery for many years. The current hypothesis of water-mediated PCET was first proposed in the ^1H ENDOR study of *Nick et al.*[26] and our ^{17}O experiments gave the direct experimental proof of water at all radical intermediates. Molecular dynamics by *Reinhardt et al.* based on the cryo-EM structure showed these water molecules at the subunit interface and concluded the importance of them for proton transfer across the interface.[131] Additionally, experiments with photo-RNRs have highlighted the role of the interface residue E_{52} in gating the transfer of protons to the bulk solution via a water channel.[133] But even though the experiments and simulations suggest water involvement, no direct experimental evidence for water-mediated PCET exists. The cryo-EM structure resolves no water molecules[106] and our ENDOR experiments only detect defined coupling structures for nuclei in the first coordination sphere.[15,26]

Recent experiments performed by A. Meyer in our group have revealed a possible new PCET mechanism different to all previous proposals. High-field ^{19}F ENDOR measurements of the trapped $Y^\bullet_{356}$ radical in an "active" $\alpha_2\beta_2$ complex with fluorine labels at the Y_{731} position (β_2-F_3Y_{122}($E_{52}Q$):F_2Y_{731}-α_2) indicate the presence of a *flipped* Y_{731} conformation in addition to the previously known *stacked* conformation.[16] Figure 5.24 shows the two models representing the *stacked* (red) and *flipped* (cyan) conformation within the cryo-EM surrounding (blue and orange wires, representing α and β residues). The $O_{Tyr}\cdots O_{Tyr}$ distance between $Y^\bullet_{356}$ and Y_{731} is ~ 8 Å in the *stacked* conformation, too large for direct

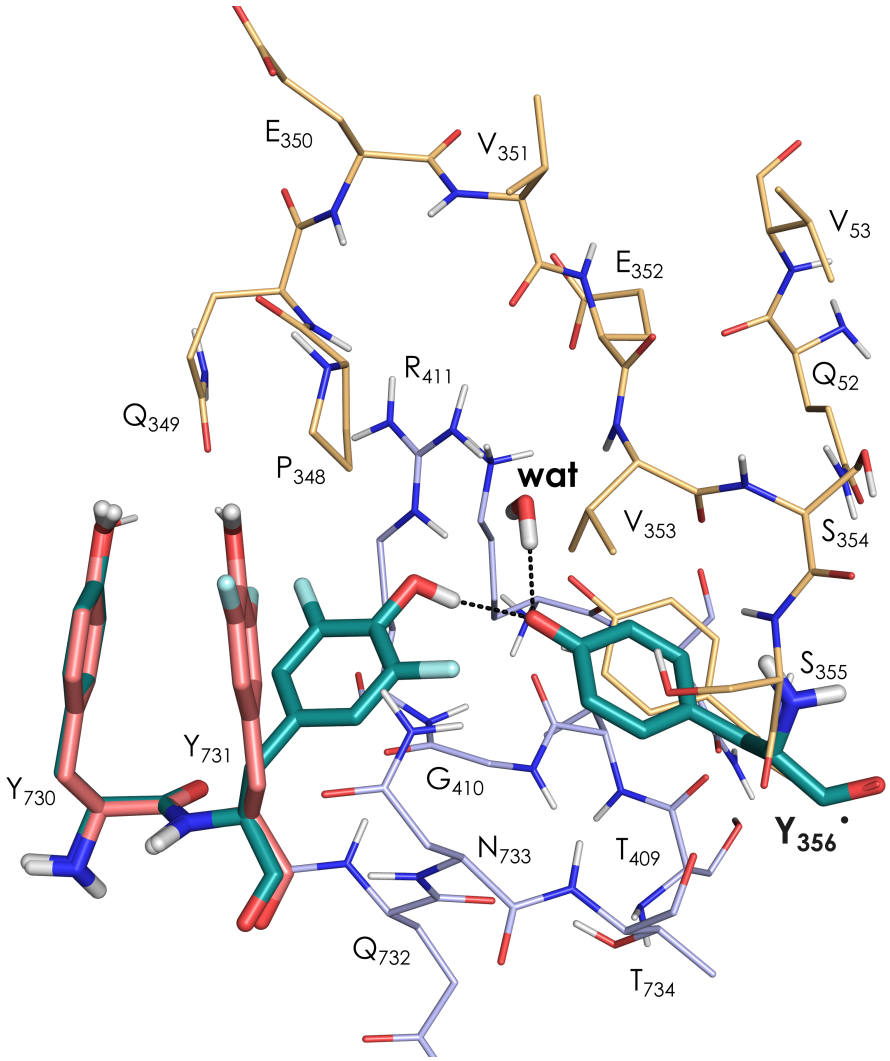

Figure 5.24: Large scale model of $Y_{356}^{\bullet}$ based on the cryo-EM structure. Residues belonging to the α-subunit are shown in blue and belonging to the β-subunit are shown in orange. Redox-active residues on the radical transfer pathway are shown as sticks. Important hydrogen-bonding interactions are shown as black dashed lines and distances given in Å. Models based on the ^{19}F ENDOR experiments are shown in red (*stacked* conformation) and cyan (*flipped* conformation).[16]

PCET, but only ~ 3 Å in the *flipped* conformation. This short distance allows co-linear PCET between the two tyrosines, as was proposed for the $Y_{731}[\alpha] \rightleftarrows Y_{730}[\alpha] \rightleftarrows C_{439}[\alpha]$ pathway. Importantly, water coordination to $Y^{\bullet}_{356}$ was detected by ^{17}O Mims ENDOR in samples of the enzyme with the fluorine mutation on Y_{731} (see Fig. 5.5.7, B), in which the flipped conformation was also detected.

These findings and the available cryo-EM structure can form the basis of a large scale model of the $Y^{\bullet}_{356}$ radical within its protein environment. Figure 5.24 shows the beginnings of such a model, but two important aspects need to be addressed: Firstly, the 8 Å distance between Y_{356} and Y_{731} requires the modelling of a lot of residues. Currently the model contains 360 atoms which pushes the upper boundary of DFT calculations and requires many restrictions to arrive at a converged model. Secondly, the coordination space around $Y^{\bullet}_{356}$ leaves a lot of room for water molecules. A combined MD/DFT approach will be necessary to find a sensible arrangement of water molecules in this space, but the defined ^{17}O coupling features in all biochemical constructs suggest that a preferred motif has to exist in the trapped radical state. Once a model in agreement with all spectroscopic observations can be found, it may be used to calculate the influence of the water molecules on the PCET mechanism.

Our previous theoretical investigation of $NH_2Y^{\bullet}_{730}$ had shown that water coordination to radical intermediates could influence the RT kinetics by up to 1 order of magnitude.[24] A mechanistic importance of water molecules in co-linear PCET between Y_{356} and Y_{731} might thus be shown on the basis of the ^{17}O ENDOR experiments.

The cryo-EM structure and the new PCET model also open up new avenues for EPR spectroscopy investigations: One striking fact of the model shown is the close distance of the water molecule to residue R_{411}. The importance of this residue for the conformation of $NH_2Y^{\bullet}_{731}$ (see Sec. 5.3) was already shown and a possible coordination of the same water molecule coordinated to $Y^{\bullet}_{356}$ may be investigated by similar strategy of using α_2-R_{411}A. Additionally, the arginine residue can be labelled with ^{15}N and its coupling to $Y^{\bullet}_{356}$ may be detected by hyperfine spectroscopy methods.

^{17}O hyperfine spectroscopy to detect water binding to biologically relevant radicals

6

Summary Nitroxide and tyrosyl radicals are important spin probes and intermediates in electron transfer mechanisms. Binding of water molecules can have direct influence on their magnetic parameters or influence the energetics and mechanism of the molecular machines, which they are embedded in. Here we investigate the capabilities of different hyperfine spectroscopy techniques to detect ^{17}O signals of labelled water molecules around three representative organic radicals: nitroxide radicals with six- ($T^{\bullet}_{6}$) and five-membered ($T^{\bullet}_{5}$) rings and a tyrosyl radical intermediate ($Y^{\bullet}_{356}$) in *E. coli* ribonucleotide reductase. We use quantum mechanical calculations on the DFT level as well as molecular dynamics simulations to rationalize the observed hyperfine spectra. Our experiments are able to resolve a distribution of couplings in the range of $1-8$ MHz for the two nitroxide radicals, which originate from hydrogen-bound water molecules coordinated perpendicular to the two nitroxides ring plains. They also show that Mims ENDOR is the only technique capable of resolving small ^{17}O couplings in the range of $0.6-0.8$ MHz, which originate from hydrogen-bound water molecules coordinated in-plane of the two radicals. Systematic DFT modelling and coupling parameter calculations were required to derive the aforementioned binding motifs. We also show how MD simulations can be used compute and reproduce a distribution of radical-water complexes in bulk solutions for simulation of the hyperfine spectra.

Acknowledgements At the time of thesis submission, the results of this chapter are not published. The chapter is planned for submission as: F. Hecker, L. Fries, M. Hiller, M. Chiesa, M. Bennati, "^{17}O hyperfine spectroscopy to detect water binding to biologically relevant radicals: a comparative study of nitroxide and tyrosyl radicals", *to be submitted*. M. Chiesa (University of Turin) is acknowledged for his introduction to ^{17}O HYSCORE spectroscopy during a research stay in Turin. M. Hiller designed and performed molecular dynamics simulations and contributed to their analysis. L. Fries optimized and performed HYSCORE experiments on the $T^{\bullet}_{6}$ radical during the course of her Bachelor thesis. She

also performed hyperfine spectroscopy on the $T_5^{\bullet}$ radical and contributed to the EDNMR simulation code during the course of her Master thesis. Both theses were supervised by Prof. M. Bennati and myself. All other experiments, DFT calculations and simulations were performed by myself. Text and figures were designed and written by myself.

6.1 Introduction

Pulsed hyperfine spectroscopy techniques in EPR can be sorted into three classes of experiments: 1.mw single resonance experiments such as HYSCORE based on the ESEEM effect,[6,7] 2. mw double resonance experiments such as EDNMR[8] and 3. mw-rf double resonance experiments such as ENDOR[4,5] (Fig. 6.1). While they all differ significantly in the required experimental setup, they share the common goal of detecting nuclear frequencies via the EPR signal. It is then the spectroscopist's task to find the experiment best suited to the research question at hand.

A question that has been of increasing interest over the last years is the involvement of water molecules in a large variety of chemical and biological transformations.[29] Hyperfine spectroscopy is particularly well suited for this task, since it detects only nuclei in close vicinity to the paramagnetic centers within bulk solutions or enzymatic environments. The use of ^{17}O hyperfine spectroscopy has specific challenges (see Chapter 1 and 5) but experiments

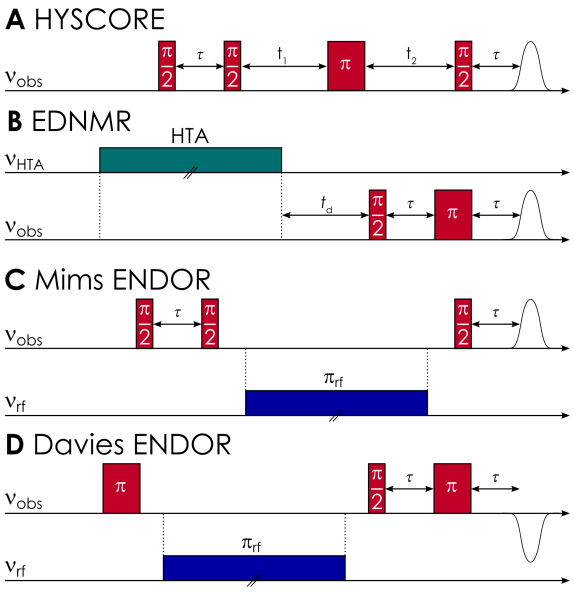

Figure 6.1: Pulse sequences of common hyperfine spectroscopy experiments. **A**: HYSCORE - echo intensity is monitored as a function of the two inter-pulse delays t_1 and t_2. **B**: EDNMR - echo intensity is monitored as a function of the HTA frequency ν_{HTA}. **C**/**D**: Mims (**C**) and Davies (**D**) ENDOR - the echo intensity is monitored as a function of the radio-frequency ν_{rf}. E: Four level scheme of a coupled $S = 1/2$, $I = 1/2$ spin system in the weak coupling case (A,$B > 0$, $2\omega_I > A$).

from all three aforementioned categories have been applied to ^{17}O-labelled water molecules around transition metal ions such as Mn(II)[44,46,47,103,147], Fe(III)[48,148,149], Cu(II)[49] and Gd(III)[150]. The hyperfine couplings in these studies lie in a range of $\sim 1 - 35$ MHz, with the majority in the $5 - 10$ MHz range (Table 6.2).

The use of ^{17}O hyperfine spectroscopy for organic radicals faces additional challenges due to the altered coordination of the water molecule to the paramagnetic center (see Ch. 1). Nevertheless, *Nalepa et al.* have reported the use of 94 GHz ^{17}O EDNMR of a nitroxide radical to quantify the local water exchange in bacterial photosynthetic reaction centers. ^{17}O hyperfine and quadrupole couplings were, however, not resolved and the binding structure was not investigated.[50] We have recently reported the first ^{17}O ENDOR study of water molecules coordinated to tyrosyl radicals in *E. coli* class Ia ribonucleotide reductase, in which we found that hydrogen-bonding induces small amounts of spin density transfer (< 0.1 %) onto the waters oxygen nucleus, sufficient for resolvable isotropic hyperfine coupling.[15] We have therefore set out to systematically study the coordination of water molecules to three oxygen-centered organic radicals (Fig. 6.2), namely the nitroxide radicals TEMPOL/$T_6^\bullet$ and TEMPYL/$T_5^\bullet$ as well as the tyrosyl radical $Y_{356}^\bullet$, with ^{17}O hyperfine spectroscopy in an effort to compare the capabilities of the different methods available.

Stable nitroxide radicals like $T_6^\bullet$ and $T_5^\bullet$ belong to the most important spin probes used in structural biology today.[151,152] The ability for site-directed spin labelling (SDSL) with nitroxides allows the study of diamagnetic biological systems with EPR spectroscopy.[153]

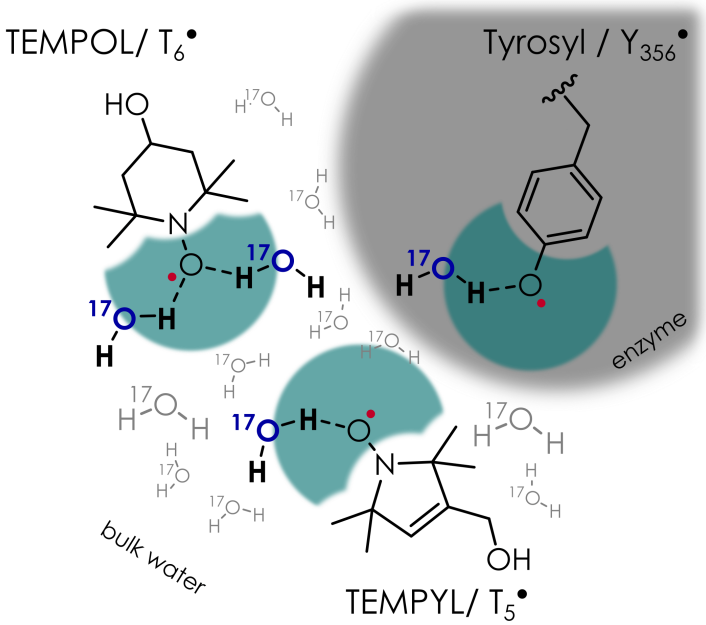

Figure 6.2: Overview of three biologically relevant oxygen-centered radicals in ^{17}O labelled water. Cyan areas indicate the approximate coordination space that can be probed by hyperfine spectroscopy. Grey area indicates an enzyme environment.

They are also used as spin probes for paramagnetic NMR experiments[1,2] and as important polarizers in dynamic nuclear polarization experiments.[154,155] Tyrosyl radicals, on the other hand, are among the most common radicals occurring in enzymatic catalysis[156,157] and we have previously established the presence of a coordinated water molecule at the $Y^{\bullet}_{356}$ radical with ^{17}O Mims ENDOR (Chapter 5).

6.2 Experimental results

The following section will summarize the experimental results of the ^{17}O hyperfine spectroscopy experiments. We will however begin with a generalized discussion about design of the experiments and set expectations for the results that will be discussed.
Four different commercial pulsed EPR spectrometers are available in the range from 9.5 to 263 GHz (Table 6.1), with the X-band spectrometers most abundant across laboratories. Q-band spectrometers have spread in recent years due to their application value for PELDOR/DEER spectroscopy and are therefore present in most dedicated EPR laboratories. W-band spectrometers can be found in a few specialized laboratories, while the mm-band spectrometer remains a rarity. Our choice of spectrometer for ^{17}O hyperfine spectroscopy

Table 6.1: Overview of commercially available fields for EPR spectroscopy with corresponding electron and ^{17}O nuclear Larmor frequencies.

mw-band	EPR frequency/GHz	magnetic field/T	^{17}O Larmor frequency/MHz
X	9.5	0.34	1.96
Q	34	1.21	6.99
W	94	3.34	19.28
mm	263	9.38	54.16

* Resonance frequencies shown for $g = g_e = 2.0023$.

experiments can be rationalized by looking at the Larmor frequency of the nucleus if we assume the previously discussed small hyperfine couplings. At X-band frequency, it is less than 2 MHz, which provides challenges for all three hf spectroscopy experiments: HYSCORE - poor resolution of small frequencies (< 2 MHz) due to phase-cycling and background artefacts; EDNMR - overlap of small frequencies (< 4 MHz) with the *central hole*; ENDOR - weak power of radio-frequency circuits at small frequencies (< 4 MHz). The higher Larmor frequencies of ~ 7 and ~ 19 MHz at the magnetic fields of Q- and W-band make these spectrometers the better choice that is still available to a good number of EPR laboratories.
Performance of the hf spectroscopy techniques at different fields are a balance between overall signal intensity and spectral resolution. With increasing magnetic field, signal intensity will generally drop but resolution will increase, both due to the larger spread of

EPR resonances and increased orientation-selectivity (see Fig. 6.13). Generally, we expect HYSCORE to perform best at 34 GHz, since the modulation depth and therefore signal intensity also scales with the relative size of Larmor frequency and hyperfine coupling (see Eq. (2.89)), reaching a maximum at the *exact cancellation* condition when $A \sim 2\omega_I$. EDNMR transition probabilities are equally field dependent and will be larger at the 34 GHz, but due to reduced signal overlap with the *central hole* and increased separation of Larmor frequencies, performance at 94 GHz is expected to be better. ENDOR transition probabilities are not field dependent, therefore rf circuit performance and increased spectral resolution at higher field make 94 GHz the expected choice. Apart from these considerations, we have previously shown that higher magnetic fields reduce the influence of nuclear quadrupole broadening on ENDOR signals. The combination of reduced linewidth and increased orientation selection leads to an overall increase of spectral resolution.[15]
All hyperfine spectroscopy experiments of the three radicals were performed at a temperature of 50 K. For nitroxides, this temperature is generally regarded as the best compromise between signal intensity and T_{1e} relaxation time for pure EPR experiments.[158] In hyperfine spectroscopy, not only electron but also nuclear relaxation needs to be considered. The nuclear relaxation times can be much longer than the electron relaxation, but EPR experiments to measure them are not readily available, and so the effect of nuclear relaxation has to be determined indirectly. In our test, nuclear relaxation and saturation effects appeared not to influence the hyperfine spectroscopy experiments for nitroxide and tyrosyl radicals.

6.2.1 HYSCORE experiments

HYSCORE experiments at the two EPR frequencies were performed with maximum microwave power and short, broadband pulses to increase the probability of exciting allowed and forbidden electron coherences. Measurements with two different τ-values (see Fig. 6.1, A) were performed: one value was chosen, so that the maximum signal around the ^{17}O Larmor frequency was detected and the other with minimal signal. This was done to catch all nuclear transitions that might otherwise be obscured in a single measurement. The ^{17}O HYSCORE spectra at 34 GHz (Figure 6.3, A/C/E) show signal at $\sim$ 6.9 MHz while the signals in the 94 GHz spectra are centered at $\sim$ 19.3 MHz (Figure 6.3, B/D/F), which are the ^{17}O Larmor frequencies at the respective fields (Tab. 6.1). The full HYSCORE spectra of the nitroxides contain additional signals in the (+,+) and (-,+)-quadrants (most pronounced in the 94 GHz experiments, see (Fig. 6.16-6.21) which can be assigned to the ^{14}N nucleus of the nitroxide moiety. The full tyrosyl spectra only contain additional signal along the diagonal in the (-,+)-quadrant (also present in the nitroxide spectra), which can be assigned to artefacts from imperfect phase cycling.
The ^{17}O signal at both frequencies is spread across a range of $\pm$4 MHz along the anti-

diagonal for the two nitroxide radicals $T_6^\bullet$ and $T_5^\bullet$ while the tyrosyl radicals signal only spans a range of ±0.5 MHz. The 34 and 94 GHz nitroxide spectra are broadened along the diagonal, with individual ridges identifiable (arrows, Fig. 6.3, A and C) in the 34 GHz spectra. HYSCORE experiments performed at other principal *g*-tensor orientations show little variation in the observed signal (Sec. 6.7.5). The 34 GHz nitroxide spectra contain pronounced signal close to the ^{17}O Larmor frequency (dashed circles) in addition to the broad signals, which is not present in the 94 GHz spectra. The tyrosyl spectra contain no discernible coupling ridges or structure and the major difference between the 34 and 94 GHz spectra is an overall reduced intensity at higher field, only apparent in the full spectra (Fig. 6.21) due to the normalization procedure.

All ^{17}O signals in the HYSCORE experiments appeared in the (+,+)-quadrant, which means that the coupling to organic radicals at 34 and 94 GHz occurs in the weak coupling case, i.e. $A < \omega_I$. The spread of signal across the anti-diagonal in the nitroxide spectra is evidence of hyperfine coupling with coupling tensor components up to 8 MHz. The spread across the diagonal and the observed individual ridges are evidence of significant nuclear quadrupole

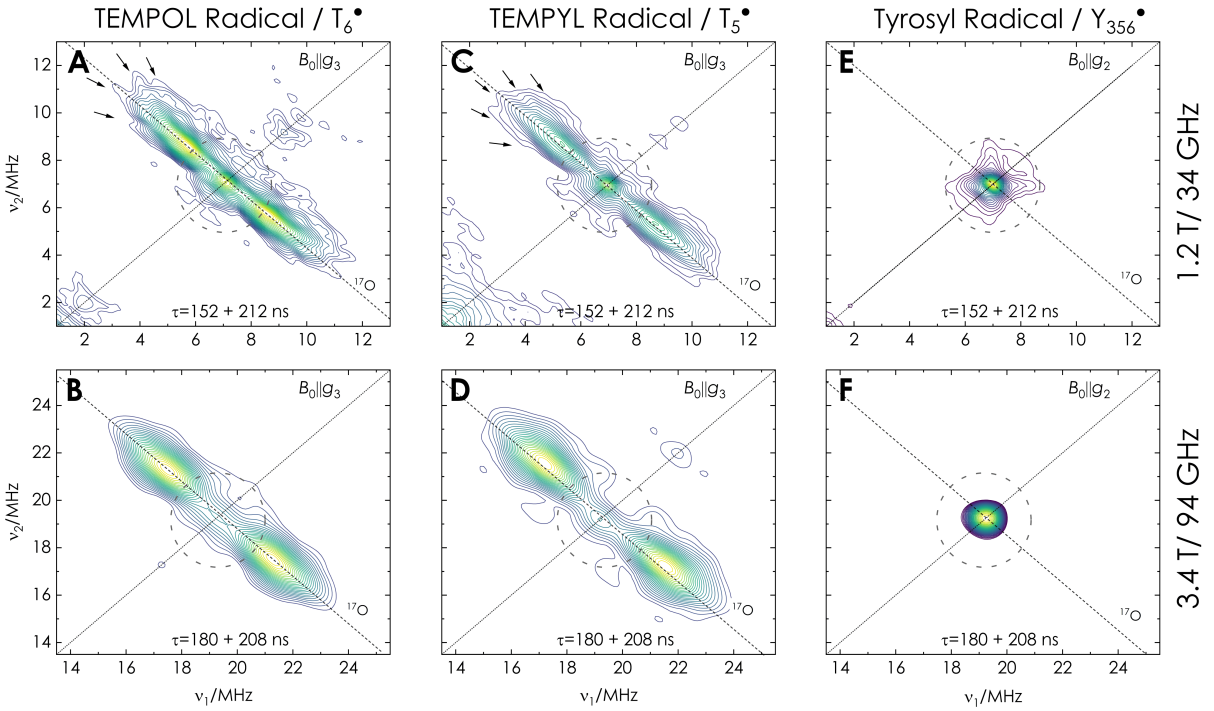

Figure 6.3: Experimental HYSCORE spectra ((+,+)-quadrant) of $T_6^\bullet$ (**A**/**B**), $T_5^\bullet$ (**C**/**D**) and $Y_{356}^\bullet$ (**E**/**F**) recorded at 34 GHz (**A**/**C**/**E**) and 94 GHz (**B**/**D**/**F**) microwave frequency. Experiments were performed with two τ-values (given in the Figure) and summed. The ^{17}O Larmor frequency is shown as a dashed line. Spectra are symmetrized along the diagonal and normalized to the ^{17}O signal. The full spectra including the (-,+)-quadrant are shown in Figure 6.16-6.21. Arrows show the ridges corresponding to the nuclear quadrupole transitions. Dashed circles indicate the signals corresponding to small hyperfine coupling interactions, which are suppressed at higher magnetic field.

coupling of similar size for both radicals. The overall intensity distribution at 34 GHz also suggests more small couplings in the $T_5^{\bullet}$ then in the $T_6^{\bullet}$ radical. The two-dimensional nature of the HYSCORE experiment and especially the selectivity for strong vs weak coupling in the different quadrants allows a successful separation of ^{17}O from ^{14}N signal. The very intense ^{14}N signal observed for $B_0 \| g_1$ and g_2 at 94 GHz (Fig. 6.17/6.19) is caused by the match of nuclear Larmor frequency (~ 10.5 MHz) and hyperfine coupling size ($A = 13/18$ MHz). The tyrosyl spectra give evidence for only small ^{17}O couplings $A < 1$ MHz, in accordance with our earlier work (Chapter 5).[15] Signals close to the center of the 94 GHz spectra (Fig. 6.3, dashed circle), i.e. signals corresponding to small hyperfine couplings, are suppressed at the higher magnetic field. This is caused by the increasing difference between hyperfine or quadrupole coupling and Larmor frequency. Additionally, small pseudo-secular hyperfine coupling B also decreases the transition probability (see Eq. (2.89)). For the two nitroxide radicals this means that the 94 GHz spectra consist only of the larger coupling contributions. (Fig. 6.3, B and D). In case of the $Y_{356}^{\bullet}$ radical, the signal is still detectable at 94 GHz but the intensity is notably reduced. An abundance of "matrix" ^{17}O nuclei, i.e. distant nuclei with very small dipolar coupling, is present in the three samples, since $H_2{}^{17}O$ is the solvent. It is therefore not possible to determine, whether the signals originate purely from the matrix or other nuclei with small hyperfine couplings $A < 1$ MHz.

6.2.2 EDNMR experiments

ELDOR-detected NMR experiments were performed with high-turning angle pulses of 20 µs at 34 GHz and 30 µs at 94 GHz. The detection was performed with a selective echo sequence with $\pi/2$-pulses of 100 ns ($t_\pi = 2t_{\pi/2}$) at both microwave frequencies. Experiments were performed with different microwave field strength $\omega_1/2\pi$ of the HTA pulse.

Experiments with strong HTA pulses ($\omega_1/2\pi > 2$ MHz), given in the supporting information, showed intense signals for all three radicals with offsets $\Delta\nu_{\mathrm{EDNMR}} = \pm 6.9$ MHz and ± 19.3 MHz at 34 and 94 GHz, respectively, which can be assigned to ^{17}O nuclei (Fig. 6.22-6.24). The 34 GHz spectra of all three radicals contain additional symmetric signals at ± 51.5 MHz, which are ^{1}H resonances. While the strong ^{17}O signals of all radicals resemble Gaussian peaks with a width of ~ 2 MHz, the nitroxide radicals show additional, broader features at either side of the peak. These are obscured in the 34 GHz EDNMR spectra due to the overlap with the central hole (Fig. 6.22-6.24). The nitroxide spectra also show signals originating from the strongly coupled nitroxide nitrogen (^{14}N), which are asymmetric around the central hole.

Experiments performed with lower HTA power ($\omega_1/2\pi < 1$ MHz) show a significant reduction of the strong Gaussian signal at the ^{17}O Larmor frequency and reveal broad

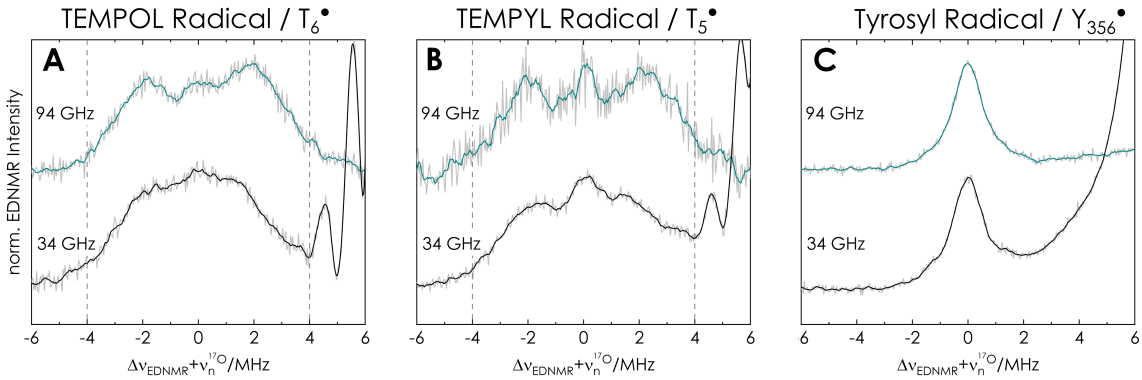

Figure 6.4: Experimental EDNMR spectra $T_6^\bullet$ (**A**), $T_5^\bullet$ (**B**) and $Y_{356}^\bullet$ (**C**) recorded at 34 GHz (black) and 94 GHz (cyan) microwave frequency. Experiments were performed with low microwave field strengths $\omega_1/2\pi = 0.5 - 0.7$ MHz to suppress the central Gaussian signal for the two nitroxide radicals. Higher microwave power ($\omega_1/2\pi = 2.2$ MHz) was used for the $Y_{356}^\bullet$ radical since lower power produced almost no detectable signal. Spectra are shown at the left side of the central hole (negative offsets). The full spectra, including the central hole, are shown in Figure (Fig. 6.27/6.26). Experiments of the nitroxide radicals (**A**/**B**) are shown at the $B_0 \| g_3$ position, where no ^{14}N signal overlaps the ^{17}O resonances. Experiments of the tyrosyl radical (**C**) are shown at the $B_0 \| g_2$ position of maximum signal intensity. Untreated spectra are shown in light gray and 4th order SG filtered (20 point window) spectra in black and cyan.

signals, spanning a range of ± 4 MHz for the two nitroxide radicals (Figure 6.4, A and B). The 94 GHz spectra of both radicals show a broad doublet with maxima at ±2 MHz. The overall ^{17}O signal intensity relative to the central hole and compared to the ^{14}N signal is about twice as large for the $T_6^\bullet$ than the $T_5^\bullet$ radical (see Fig. 6.25). This effect is obscured in Figure 6.4, since the ^{17}O signal is normalized to its absolute intensity.

In the 34 GHz spectra, the Gaussian signal at the Larmor frequency is still more intense then the doublet and partially overlaps with the central hole (black, artefacts between +4 and +6 MHz) due to the small Larmor frequency of ^{17}O at 34 GHz. EDNMR experiments performed at the $B_0 \| g_1$ and g_2 positions in the EPR spectrum show that the ^{17}O signal strongly overlaps with ^{14}N resonances of the nitroxide nitrogen at 94 GHz. A similar overlap, however to a smaller extent is also present in the 34 GHz spectra (Fig. 6.27/6.26). The only resonance position that has exclusively oxygen resonances around the ^{17}O Larmor frequency is the $B_0 \| g_3$ position, which was confirmed by control measurements with unlabelled sample.

The tyrosyl spectra at low power show almost no detectable signal (Fig. 6.24) and medium power produces only the Gaussian signal spanning around ±1 MHz (Fig. 6.4, C) The 94 GHz EDNMR spectra are generally easier to interpret, since the ^{17}O signal is shifted 13 MHz further away from the central hole than at 34 GHz and no overlap of signal with the central hole impedes the assignment.

The high-power EDNMR spectra of all three radicals show an abundance of weakly

coupled ^{17}O nuclei with hyperfine couplings $A < 2$ MHz at both magnetic fields. Signals corresponding to such nuclei were also present in all 34 GHz HYSCORE spectra. The EDNMR spectra recorded with low microwave power give evidence of nuclei with hyperfine couplings up to 8 MHz for the two nitroxide radicals, which is the same coupling range observed in the HYSCORE spectra. Signal intensities are linked to the turning angle of the HTA pulse, that is a product of the microwave power and the transition probability. This is why the signals of nuclei with small couplings are reduced in the low power spectra. Even though they are much more abundant than the strongly coupled nuclei (since all samples contain $H_2{}^{17}O$ as solvent and therefore a lot of matrix nuclei), the turning angle becomes too small to produce significant signal intensity.
The spectral resolution of the EDNMR spectrum allows no distinction between weakly coupled ($0.1 < A < 1$ MHz) and matrix ($A \lesssim 0.1$ MHz) nuclei. The transition probability is also affected by the relative size of hyperfine coupling and nuclear Larmor frequency. The transition probability of small couplings is therefore higher at 34 GHz and the corresponding signal is more intense than in the 94 GHz spectra. The EDNMR spectra of the tyrosyl radical show no indication of couplings larger than 2 MHz, also in analogy to the HYSCORE spectra. Due to its one-dimensional nature, ^{14}N signal overlap is a problem which renders the ^{17}O signals of nitroxides almost un-interpretable at resonance positions other than $B_0 \| g_3$. The overlapping signal is most intense at 94 GHz, which follows the same trend observed in the HYSCORE spectra. This is especially problematic for the $T_6^\bullet$ radical at $B_0 \| g_1$ (Fig. 6.27) where a clear doublet structure might be misinterpreted as ^{17}O coupling if no background measurements are recorded. The EDNMR experiment cannot distinguish between hyperfine and quadrupole coupling contributions.

6.2.3 ENDOR experiments

We performed Davies and Mims ENDOR experiments at Q- and W-band frequencies. Davies ENDOR experiments were optimized for the observation of medium sized hyperfine couplings ($A \sim 1 - 10$ MHz) by choosing a long, selective preparation pulse of 400 ns. Mims ENDOR experiments were optimized for the observation of small hyperfine couplings ($A \sim 0.2 - 1.5$ MHz) by performing short, broadband microwave pulses and by choosing a τ-value of 390 ns.[15] Experiments were recorded for the three canonical g-tensor orientations in the EPR spectrum (Sec. 6.7.7, Fig. 6.13).
Figure 6.5 shows representative spectra recorded at $B_0 \| g_3$ for the two nitroxide spectra, since they contain no underlying ^{14}N signal. The ENDOR spectra of the tyrosyl radical are shown for the $B_0 \| g_2$ position because the signal intensity needed to be maximized. Davies ENDOR spectra of the two nitroxide radicals (Fig. 6.5, A and C) show broad signals around the ^{17}O Larmor frequency at both microwave frequencies. The shape varies between

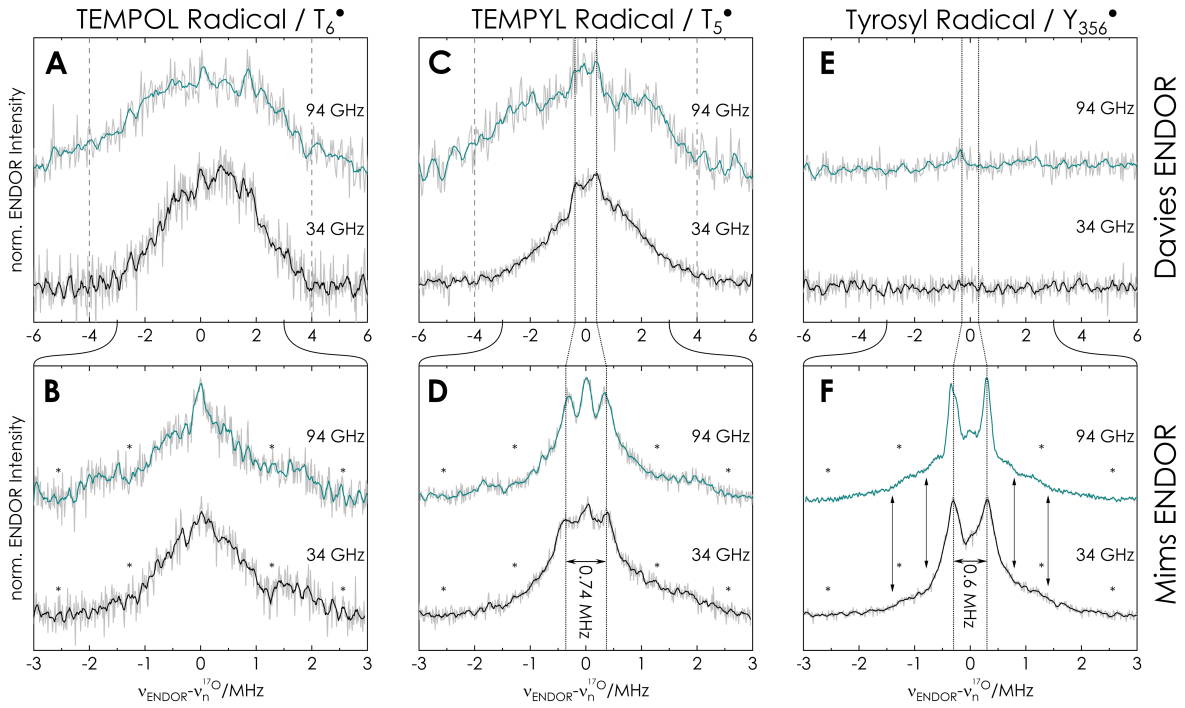

Figure 6.5: Experimental Davies (**A**/**C**/**E**) and Mims (**B**/**D**/**F**) ENDOR spectra of $T_6^\bullet$ (**A**/**B**), $T_5^\bullet$ (**C**/**D**) and $Y_{356}^\bullet$ (**E**/**F**) recorded at 34 GHz (black) and 94 GHz (cyan) microwave frequency. All nitroxide spectra shown are recorded at the $B_0 \| g_3$ position to avoid underlying ^{14}N signal. The tyrosyl spectra are shown at the $B_0 \| g_2$ position since the signal intensity is maximized there. Davies ENDOR spectra were recorded with 400 ns preparation pulse and selective detection (200/400 ns echo) for the nitroxide radicals but broadband detection (20/40 ns echo) for the tyrosyl radical. Mims ENDOR was recorded with short, broadband pulses ($6 - 12$ ns) and a τ-value of 390 ns. The radio-frequency pulses were uniformly 40 µs long. Untreated spectra are shown in light gray and 4$^{\text{th}}$ order SG filtered (20 point window) spectra in black and cyan. Asterisks indicate theoretical ($I = 1/2$) Mims blindspots for τ = 390 ns. The additional blindspot at the zero frequency is not marked.

fields and respective nitroxide radical but the majority of the intensity is spread across a range of ±4 MHz for all four spectra (dashed gray lines). Davies ENDOR spectra of the tyrosyl radical show no signal at either frequency (Fig. 6.5, E). The $T_6^\bullet$ Davies spectra show a small matrix line at the Larmor frequency, which is most pronounced at $B_0 \| g_2$ (Fig. 6.28) but otherwise only the broad features. The $T_5^\bullet$ Davies spectra on the other hand contain a matrix line, broad features and additionally a sharp doublet structure in the center of the spectrum with a splitting of ~ 0.8 MHz (Fig. 6.5, C, dotted black lines). The doublet is present at both frequencies and different g-tensor orientations but appears most pronounced in the 94 GHz at $B_0 \| g_2$ (Fig. 6.30).

The 34 and 94 GHz Mims ENDOR spectra of $T_6^\bullet$ (Fig. 6.5, B) contain an intense matrix line at the center of the spectrum and broad, unstructured signal with apparent shoulders at ±1.3 and ±2.6 MHz. This shape is uniform for all g-tensor orientations (Fig. 6.28). The shoulders correspond to the Mims blindspots that would be expected for $I = 1/2$ nuclei

(asterisks, also see Sec. 2.3.3).

The $T_5^\bullet$ Mims ENDOR spectra contain the same doublet structure (Fig. 6.5, D, dotted line) observed in the Davies ENDOR with a splitting of 0.74 MHz in addition to an intense matrix line as observed for $T_6^\bullet$. Two peaks are observable, but not well separated in the 34 GHz spectra (black), whereas they are clearly distinguishable in the 94 GHz spectra (cyan). Experiments at the other *g*-tensor orientations (Fig. 6.31) show that the doublet is isotropic with only small differences in peak width. The spectra also contain shoulders at the positions of the Mims blindspots (asterisks).

The Mims ENDOR spectra of $Y_{356}^\bullet$ show a clearly separated doublet with a splitting of 0.6 MHz at both EPR frequencies (Fig. 6.5, F, dotted line). In contrast to the two nitroxide spectra, the doublet is the most intense signal in absence of a clear matrix line. The spectra contain additional shoulders at ± 0.7 and ± 1.4 MHz (arrows). The sharp doublet signal shows a generally smaller linewidth than observed in the nitroxide $T_5^\bullet$ but the trend of narrower signals at the higher field (cyan vs. black) is preserved. Additional shoulders at the theoretical $I = {}^1/_2$ blind spots are not discernible in the $Y_{356}^\bullet$ Mims spectra.

The Davies ENDOR spectra of the two nitroxide radicals show the same spread of signals observed in the EDNMR and HYSCORE spectra with coupling components up to 8 MHz. The spectral hole at the center of the ENDOR spectrum significantly reduces contributions from weakly coupled nuclei ($A < 0.5$ MHz). Due to its one-dimensional nature and the mostly broad and featureless signal, the Davies ENDOR does not allow a distinction between influence of hyperfine vs. quadrupole coupling, which the HYSCORE experiments do. The sharp doublet observed for $T_5^\bullet$ but not the $T_6^\bullet$ radical in both ENDOR experiments confirms the presence of well-defined small hyperfine couplings. This signal was fully suppressed in the EDNMR spectra and only the ENDOR spectra show the clear coupling structure.

The nitroxide ENDOR spectra, in analogy to the EDNMR spectra, have varying and sometimes significant contributions of ^{14}N signal (Fig. 6.28 and 6.30). The contributions vary strongly for the different *g*-tensor orientations and could only be identified by performing control measurements with nitroxide samples containing unlabeled water. As observed in the EDNMR and HYSCORE spectra, the ^{14}N contributions do not overlay the ^{17}O signal at the $B_0 \| g_3$ position, where the ^{14}N hyperfine coupling is very large.

The Davies ENDOR experiments of the tyrosyl radical showed no signal while the Mims spectra revealed clearly defined coupling structure. While Davies is generally not well suited for small hyperfine couplings (*vide infra*), slightly larger couplings were readily observed in the spectra of $T_5^\bullet$. This may be rationalized by the three times longer phase memory time of the nitroxide vs the tyrosyl radical (see Fig. 6.34). Due to the long preparation pulse in the Davies experiment, only a small amount of the spins is excited and a significant delay τ has to be used to record the broad echo. This reduces the signal intensity to a bare minimum in case of $Y_{356}^\bullet$. The Mims experiment, on the other hand, has an intrinsically

larger signal intensity due to the broadband excitation and the significantly shorter pulse delay time in which T_2 relaxation occurs (390 vs. 1000 ns).
The Mims ENDOR spectra of $Y^{\bullet}_{356}$ are the only spectra in which shoulders, that are assigned to nuclear quadrupole transitions, were resolved. We have previously reported the trend of narrowing ^{17}O ENDOR signals for the tyrosyl radical. This trend is again readily identifiable in both $T^{\bullet}_{5}$ and $Y^{\bullet}_{356}$ Mims ENDOR spectra and affects the sharp, isotropic signals, which belong to the central nuclear transition of the ^{17}O nucleus. This is caused by: firstly, the higher orientation-selectivity at higher fields, meaning that generally less spins contribute to the ENDOR spectrum and secondly, the reduction of higher order nuclear quadrupole broadening of these transitions (see Fig. 6.35).

6.2.4 Experiment summary

The spectroscopy methods all show the presence of coupled ^{17}O nuclei around the three radicals. The best performing experiments are summarized in Figure 6.6. All methods indicate the presence of nuclei with hyperfine couplings up to 8 MHz (grey dashed lines) for the two nitroxide radicals while they show only weakly coupled nuclei with hyperfine couplings smaller than 1 MHz for the tyrosyl radical. The broadband hf techniques HYSCORE and Mims ENDOR are more sensitive than the selective EDNMR and Davies ENDOR experiments for all radicals. This is most pronounced for the tyrosyl radical, largely due to the significantly shorter phase memory time of $Y^{\bullet}_{356}$ compared to $T^{\bullet}_{6}$ and $T^{\bullet}_{5}$ (Fig. 6.34). 34 GHz experiments show stronger ^{17}O signals than 94 GHz experiments, which can be explained by the smaller orientation-selectivity when using identical pulse lengths in EDNMR and Davies ENDOR, especially at the $B_0 \| g_3$ position. For Mims and HYSCORE, it is explained by the higher microwave power at this frequency allowing for shorter pulses with larger excitation bandwidths. 34 GHz HYSCORE experiments of the nitroxides suggest a clearly defined nuclear quadrupole coupling which cannot be distinguished from the other two experiments.
A clearly defined hyperfine coupling structure of the moderately coupled ^{17}Onuclei (1 – 8 MHz), i.e. clearly distinguishable tensor features, cannot be discerned from any of the hyperfine spectroscopy experiments of the nitroxide radicals. Nevertheless, the distribution is experimentally best resolved in 34 GHz HYSCORE as well as 94 GHz EDNMR and Davies ENDOR. Mims ENDOR at 94 GHz best resolves clearly defined hyperfine couplings of 0.74 and 0.6 MHz for the $T^{\bullet}_{5}$ and $Y^{\bullet}_{356}$ radicals (dotted lines), respectively. The Mims ENDOR spectra of $Y^{\bullet}_{356}$ also show the evidence of nuclear quadrupole coupling.

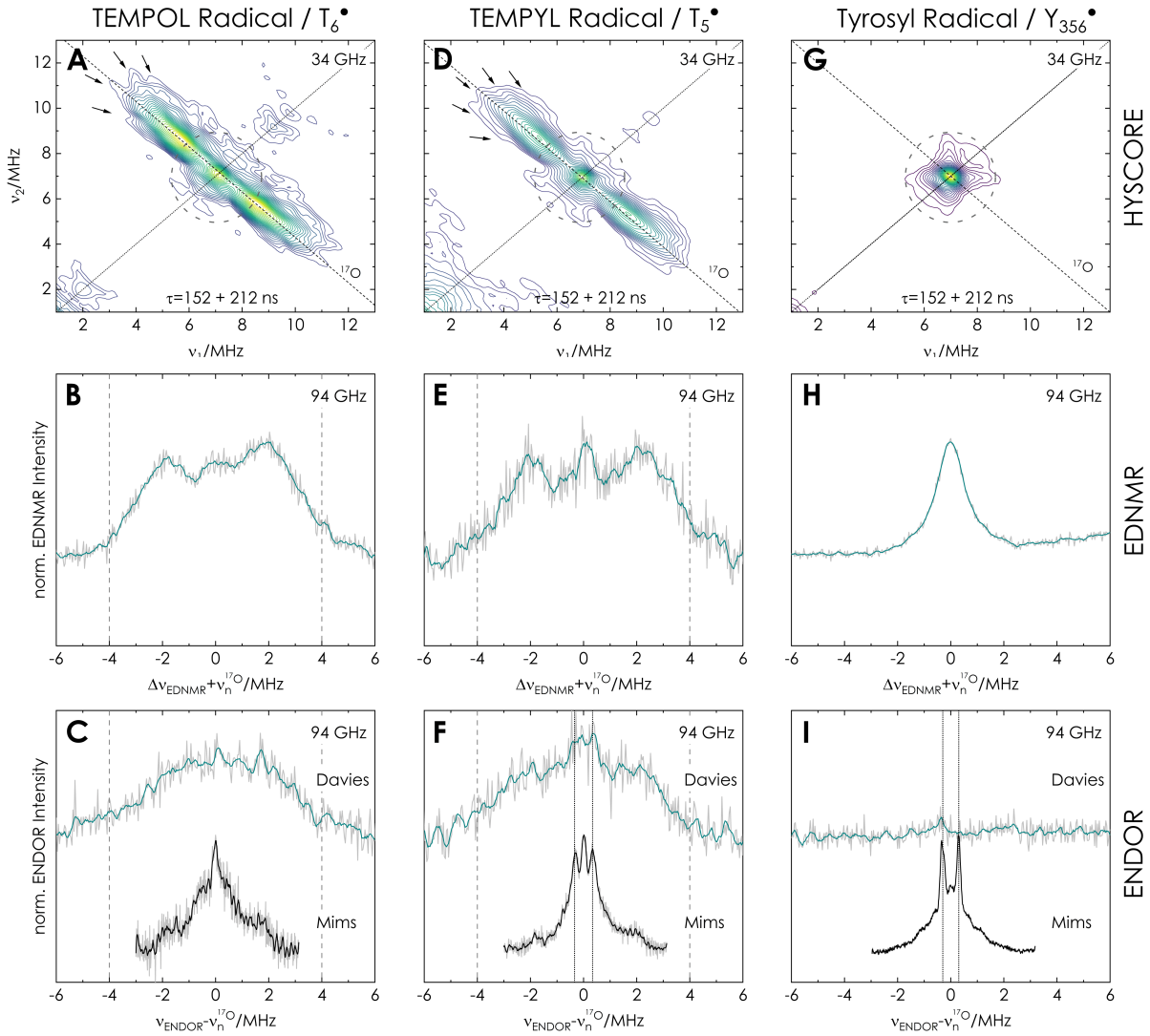

Figure 6.6: Comparison of ^{17}O hyperfine spectroscopy experiments of the three radicals $T_6^\bullet$ (**A**/**B**/**C**), $T_5^\bullet$ (**D**/**E**/**F**) and $Y_{356}^\bullet$ (**G**/**H**/**I**). HYSCORE experiments are best performed at 34 GHz (**A**/**D**/**G**). EDNMR experiments are best performed at 94 GHz (**B**/**E**/**H**). Davies (cyan) and Mims (black) ENDOR experiments are best performed at 94 GHz (**C**/**F**/**I**).

6.3 Computational results

6.3.1 Structural models

EPR parameters calculated from molecular models on the density functional theory level have shown great agreement with experimental results.[55] In order to interpret the observed ^{17}O hyperfine spectra, we have therefore calculated a series of DFT radical models (Fig. 6.7, A/D/G), each containing a single water molecule fixed at specific dihedral angles θ(C-N(C)-$O_{PC}\cdots H_{H_2O}$) between the respective radical ring and the hydrogen atom of the water molecule (see Fig. 6.13). No other parameters were fixed during geometry optimization, resulting in bond distances $r(O_{PC}\cdots H_{H_2O})$ of $1.8 - 1.9$ Ångstrom with $O_{PC}\cdots H_{H_2O}$-O angles of $\sim 175^\circ$ in all models. This falls within the definition of a moderate hydrogen-bond.[159] After restricted geometry optimization, we calculated the EPR parameters including the ^{17}O hyperfine coupling of the water oxygen atoms from these models.

We previously used this method to elucidate the binding structure of water around three tyrosyl radicals.[15] Here, we employ it again since a dipole model, often used for ^{1}H/^{2}H couplings, proved unable to predict ^{17}O couplings in water molecules. The results for the $Y^{\bullet}_{356}$ radical (originally shown in Fig. 5.14[15]) are reproduced in Fig. 6.7 to emphasize similarities and differences between nitroxide and tyrosyl radicals. We note here, that all calculations are gas-phase calculations, even though the polarity of the solvent was considered for the coupling parameter calculations by the use of a CPCM model. This is in stark contrast to the actual binding situation the radicals exhibit in solution, where multiple layers of solvation spheres and the protein environment determine the exact binding geometry. The models can nevertheless be used to gain an understanding of the relative relationship between coupling parameters and binding structure.

We have chosen the dihedral angle θ between the ring plan eof the respective radical and the water molecule (Fig. 6.13) as variable, since it can be used to scan the majority of the available coordination space around the radical oxygen atom. Previous studies have shown, that the angle τ(N(C)-$O_{PC}\cdots H_{H_2O}$) (Fig. 6.13) of a water molecule coordinated to a sp^2 hybridized oxygen atom in nitroxides or carbonyls is expected to be $\sim 120^\circ$ in line with the oxygen lone-pairs.[159] Deviations from this angle are caused by restrictions to the available coordination space. The coordination space around the nitroxide group is restricted by the two methyl groups, whereas the space around the tyrosyl oxygen is unrestricted.

The six-membered ring of the $T^{\bullet}_{6}$ radical assumes a chair-like conformation (Fig. 6.7, A), leaving more space above the NO group ($\theta = 90^\circ$) than below ($\theta = 270^\circ$), while the coordination space in the ring plane ($\theta = 0/180^\circ$) is at the same time restricted. The five-membered ring of the $T^{\bullet}_{5}$ radical is planar (Fig. 6.7, D), due to the double bond between the two carbon atoms in the back of the ring, restricting the coordination space above and

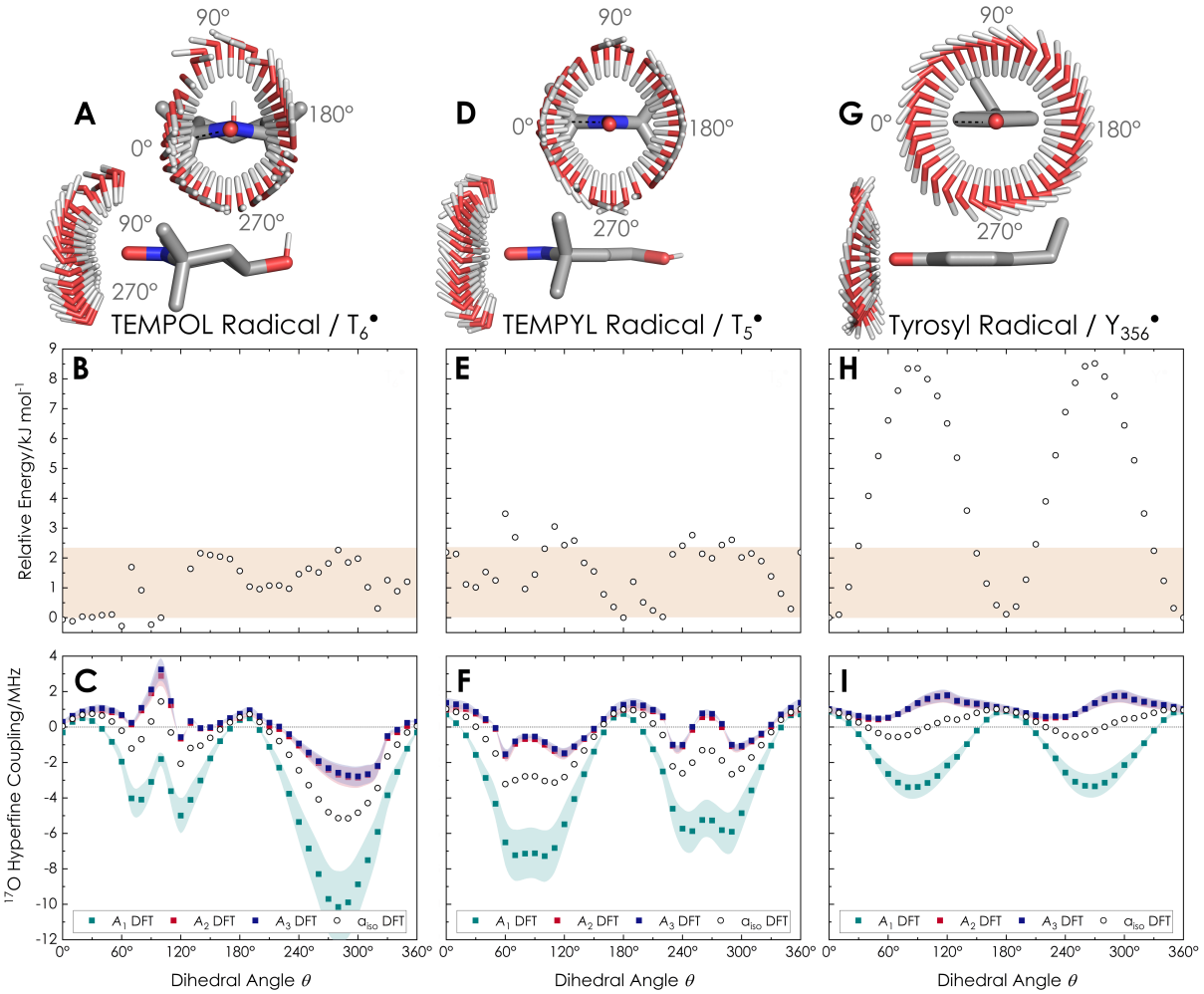

Figure 6.7: DFT models of the radicals with one water molecule (**A**/**D**/**G**) fixed at specific dihedral angles θ(C-N(C)-O$_{PC}$···H$_{H_2O}$). The structure with 0° is marked by a dashed black line and the angles given in grey. **B**/**E**/**H**: Relative energy of the calculated structures, $\theta = 0°$ structure set as the zero-point. Orange area represents an interval of thermal energy ($k_B T$) at 298 K. **C**/**F**/**I**: Calculated hyperfine coupling tensor components ($A_1 < A_2 < A_3$) and isotropic hyperfine coupling a_{iso}. An error estimate of 20 % is shown as shaded area.

below the ring equally while leaving more space for in-plane coordination.

A comparison of the relative energies of the individual models shows that the two nitroxide radicals have no clear energetic minimum, whereas the tyrosyl radical shows two symmetric minima for in-plane ($\theta = 0/180°$) coordination of a water molecule (see Fig. 6.7, B/E/H). Figure 6.7, C, F and I shows, how the ^{17}O hyperfine coupling components ($A_1 < A_2 < A_3$) depend on the water coordination geometry. In all three radicals, coordination of the water molecule in the ring plane leads to small positive couplings, indicative of mostly isotropic hyperfine couplings of $\sim 0.5 - 1$ MHz with small dipolar contributions. For the $T_6^{\bullet}$ radical, the isotropic coupling is observed for angles θ that are $10 - 20°$ larger than 0° or 180°, which is a result of the non-planar six-membered ring. Coordination of the water molecules perpendicular to the ring planes lead to very anisotropic coupling tensors with one large

and negative coupling tensor component (cyan squares) in the three radicals.
This can be explained by the spin-density of the radicals (see Fig. 6.13): the large positive spin density is distributed above and below the oxygen atom while only small amounts of negative spin density are distributed in-plane . Perpendicular coordination therefore leads to "closer" and therefore stronger interaction between ^{17}O nucleus and spin density.
The $T_6^\bullet$ calculations show hyperfine couplings up to -10 MHz for coordination below ($\theta = 270°$) the ring while coordination above the ring ($\theta = 90°$) leads to couplings of up to 4 MHz. This can be explained by the asymmetry in the two coordination spaces, allowing the water molecules to coordinate closer to the center of the N-O bond ($\tau \sim 100°$) for the more open space above the ring as compared to the space below the ring where the water interacts mostly with the oxygen nucleus ($\tau \sim 120°$). The $T_5^\bullet$ calculations show a more symmetric behavior of the hyperfine coupling with couplings up to $-8/-6$ MHz for $\theta = 90/270°$, respectively. This is in line with the symmetric coordination space above and below the ring which leads to τ angles of $\sim 110°$. Small deviations from the symmetric behavior may be caused by the slightly tilted NO group in the $T_5^\bullet$ models.
The $Y_{356}^\bullet$ calculations show a completely symmetric behavior of the hyperfine couplings with components up to -3 MHz for perpendicular coordination of the water molecule ($\theta = 90/270°$, $\tau \sim 120°$). The difference in maximum hyperfine coupling between the nitroxides and tyrosyl radical may be explained by the different spin density distribution of the radicals. The spin density of the nitroxides is almost fully located on the NO group with ~ 50 % on the oxygen atoms (Fig. 6.13 and Loewdin spin population analysis[135]), while it is distributed across the aromatic ring of the tyrosyl radical with ~ 30 % located on the oxygen atom.
The ^{17}O nuclear quadrupole coupling tensor components do not change significantly with the coordination geometry for either of the radicals (see Fig. 6.37). Since the quadrupole coupling depends on the electric field gradient around the nucleus, which is mostly defined by two lone-pairs of the oxygen as well as the two bound hydrogen nuclei, a change of the quadrupole coupling as a function of θ was also not expected.
For all three radicals, in-plane coordination of a water molecule leads to the transfer of small amounts of spin density (< 0.1 %) onto the ^{17}O nucleus via the hydrogen-bond, giving rise to isotropic couplings up to 1 MHz with small amounts of through space dipolar coupling (< 0.4 MHz). Out of plane coordination leads to larger spin density transfer (up to 1 %) and much larger hyperfine couplings of up to -10 MHz. For these coordination's, the dipolar contribution may no longer be estimated from the point-dipole model.
The g- tensor orientation of all three radicals is similar, with g_1 and g_2 spanning the ring plane and g_1 oriented along the N(C)-O bond direction, while g_3 is oriented perpendicular to the ring plane (Fig. 6.13). The DFT calculations show, that large hyperfine coupling components at the perpendicular orientation (A_1) are aligned with the g_3 component of

the g-tensor, making the $B_0 \| g_3$ resonance position the most sensitive for such couplings. Models show that, in the absence of external structural influences, no energetically preferred coordination motif is expected for the two nitroxide radicals. Similar calculations by *Bras et al.*, performed in the course of an infrared spectroscopy study of the TEMPO radical that is structurally very similar to TEMPOL, came to the same conclusion.[160] The opposite situation occurs for the tyrosyl radical, for which an energetically preferred in-plane coordination of the water molecule should be expected. They also show that small variations in coordination structure result in large changes of the hyperfine coupling parameters, which means that sharp spectral features have to be the result of a clearly defined coordination geometry. Single models can therefore be used to interpret the $Y^{\bullet}_{356}$ spectra, while a different methodology is necessery to rationalize the broad $T^{\bullet}_{6}$ and $T^{\bullet}_{5}$ spectra.

6.3.2 Molecular dynamics simulations

A computational method that is well suited to the task of probing the structural variety in solutions is the molecular dynamics simulation.[161] We therefore performed MD simulations of a single nitroxide radical ($T^{\bullet}_{6}$ or $T^{\bullet}_{5}$) in a mixture of H_2O and glycerol (v/v: 8:2). The MD parameters of the nitroxide radicals were adapted to explicitly include the oxygen lone-pairs (see Sec. 6.7.11) following the methodology first described by *Stendardo et al.*[161] The lone-pairs of the oxygen atom are crucial for the description of hydrogen-bonding.

To emulate the experimental conditions, we simulated the freezing of the sample by reduction of the internal temperature to 50 K until molecular motion stopped. This was repeated a total of 100 times with slightly different starting conditions to acquire a statistical average of structures. From the final structures, the three closest water (or glycerol) molecules to the nitroxide radical and their 3 neighbors (9 solvent molecules in total) were selected and the rest discarded. Using DFT, we calculated the EPR parameters of the radical and the three closest water molecules without further geometric optimization. Figure 6.8 summarizes the most important results of the MD simulations.

The water molecules fill the coordination space around the nitroxide group, as expected, with a lot more structural variation than the limited DFT model showed. Generally, coordination with $\tau(\text{N-O}_{\text{PC}}\cdots\text{H}_{\text{H}_2\text{O}})$ angles $< 150°$ is present, which is also in accordance with the DFT optimized structures (Fig. 6.8, A/H). Two sets of water molecules can be distinguished by looking at the distribution of $\text{O}_{\text{PC}}\cdots\text{H}_{\text{H}_2\text{O}}$ distances (Fig. 6.8, B/E). The biggest peak in the distribution occurs at 1.8 Å, i.e. the equilibrium hydrogen-bond distance observed in all DFT models. A second, much broader, peak shows the unbound waters with distances larger than 2.3 Å.

The hydrogen-bound waters are mostly found at the two perpendicular orientations ($\theta =$

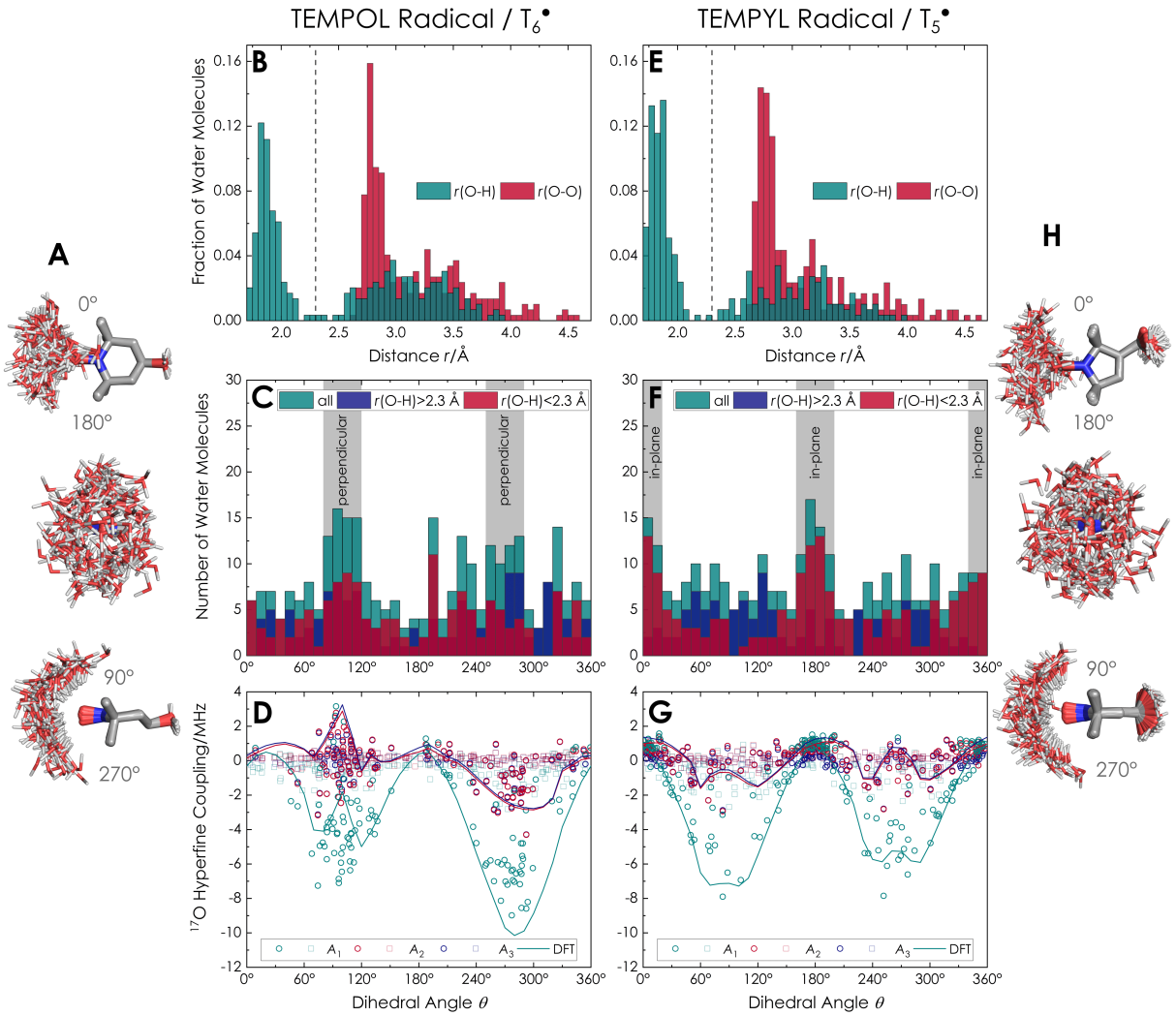

Figure 6.8: Molecular dynamics simulations of the two nitroxide radicals. **A**/**H**: Overlay of the 100 MD runs aligned to the respective nitroxide radical (**A**: $T_6^\bullet$, **F**: $T_5^\bullet$), including the 3 closest water molecules, for which the coupling parameters were calculated. **B**/**E**: Distribution of $O_{PC}\cdots H_{H_2O}$ (cyan) and $O_{PC}\cdots O_{H_2O}$ (red) distances observed for the molecules around the nitroxides oxygen atoms. Dashed line indicates the distinction between hydrogen-bound (r(O···H)< 2.3 Å) and distant waters (r(O···H)> 2.3 Å). **C**/**F**: Dihedral angle θ(C-N-$O_{PC}\cdots H_{H_2O}$) distribution of all (cyan) water molecules and distribution of hydrogen-bound (red) vs. distant waters (blue). **D**/**G**: Calculated ^{17}O hyperfine coupling tensor components ($A_1 < A_2 < A_3$) of the hydrogen-bound (circles) and distant (squares) water molecules. The calculation results of the previous DFT optimized structures are shown as solid lines for comparison.

90/270°) for the $T_6^\bullet$ radical and the in-plane orientations ($\theta = 0/180°$) for the $T_5^\bullet$ radical (Fig. 6.8, D/F, red). The more distant water molecules ($r(O_{PC}\cdots H_{H_2O}) > 2.3\,Å$) are more or less uniformly distributed around the nitroxide groups for both radicals (Fig. 6.8, D/F, blue).

The calculated hyperfine couplings of the MD generated structures, shown as open symbols in Figure 6.8, D and G, fall into the boundaries of the couplings calculated from the DFT optimized structures (solid lines, compare Fig. 6.7). Because the binding structures are much more diverse, a broad distribution of hyperfine couplings can be observed for the closely bound waters (circles), which fits very well to the observed broad coupling features in all hyperfine spectroscopy experiments of the nitroxide radicals. The more distant, unbound waters predominantly have hyperfine couplings smaller than 1 MHz and may therefore be counted as "matrix" waters (squares).

6.4 Interpretation and discussion

At the beginning of this study we asked two questions: "*Can we detect water molecules around organic radicals using ^{17}O hyperfine spectroscopy*?" and "*Which hyperfine spectroscopy method is best suited to the task*?". The answer to the first question has a simple answer: "*Yes*". We could show that all methods, performed at 34 or at 94 GHz, detect the presence of ^{17}O nuclei around the three organic radicals, albeit with varying sensitivities and resolution.

The second question, not surprisingly, has no simple answer. A short answer would have to be that: "*It depends on the hyperfine coupling size*." This answer summarizes the most important and least satisfying result of our study: Knowledge about the hyperfine couplings that are expected are a prerequisite for the choice of experiment. The following discussion of the three radicals will showcase this:

6.4.1 The tyrosyl radical

We will begin with the tyrosyl radical because it showed the smallest and most defined coupling features of the three investigated radicals and the hyperfine coupling parameters are known from our previous study.[15] $Y_{356}^\bullet$ is coordinated by a single hydrogen-bound ($r(O_{PC}\cdots H_{H_2O}) = 1.9 \pm 0.1\,Å$) water molecule oriented close to the ring plane ($\theta = 20 \pm 20°$) of the radical with $\boldsymbol{A} = [0.46; 0.66; 0.70]$ MHz and $\boldsymbol{P} = [-0.02; -0.32; 0.34]$ MHz (Figure 6.9, C). As discussed in Section 6.3.1, the ^{17}O hyperfine coupling tensor of an in-plane water molecule is comprised of a significant isotropic and a small dipolar contribution. The nuclear quadrupole coupling tensor is equivalent to the known tensor of pure $H_2{}^{17}O$ in ice.[134] Specific signals assignable to hyperfine and quadrupole coupling features are

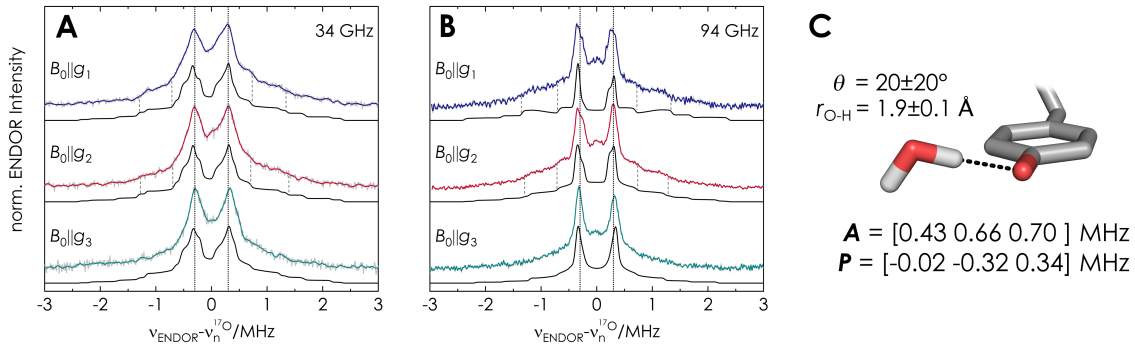

Figure 6.9: Simulation of 34 GHz/1.2 T (**A**) and 94 GHz/3.35 T (**B**) ^{17}O Mims ENDOR spectroscopy experiments performed on the tyrosyl radical $Y_{356}^{\bullet}$ in *E. coli* RNR. Experiments shown in color with simulations shown in black. **C**: Coordination motif and coupling parameters. 94 GHz ENDOR spectra and coordination structure reproduced from Ref. [15].

only resolved in the Mims ENDOR spectra of this radical. Simulations with the previously published hyperfine and quadrupole couplings reproduce the experimental Mims ENDOR spectra very well (Figure 6.9, A/B).

At both fields, the spectra are comprised of the typical narrow doublet, split by the isotropic hyperfine coupling ($\sim$ 0.6 MHz) and broadened by a small dipolar coupling ($\sim$ 0.1 MHz), corresponding to the central nuclear transition ($m_I(^{17}\mathrm{O}) = +1/2 \rightarrow -1/2$) of $I = 5/2$ nuclei and broad shoulders, which correspond to the other nuclear transitions.

The decreased line width of the central doublet observed at the higher field is reproduced by the simulation, which confirms the earlier explanation of increased orientation-selectivity and decreased quadrupole broadening. It is important to note that this requires simulations which consider the full coupling Hamiltonian instead of the high-field approximation, where the central transitions are unaffected by quadrupole coupling (see Ch. 4). Our experiments clearly show, that the *fingerprint* of in-plane water molecules at tyrosyl radicals can be detected with ^{17}O Mims ENDOR spectroscopy at common Q-band EPR frequencies and that high-field, orientation-selective Mims ENDOR at W-band provides the information necessary to determine water binding structures.

6.4.2 The TEMPOL radical

The binding structure of water around the TEMPOL radical in solution was not known prior to this study. A recent gas-phase IR spectroscopy study showed both perpendicular and in-plane coordination to a TEMPOL analogue[160] and a proton and deuterium ENDOR spectroscopy study of TEMPOL in isopropyl-alcohol solution suggested the presence of multiple H-bond motifs for this radical.[162]

All ^{17}O hyperfine spectroscopy methods show broad ^{17}O coupling features. The largest

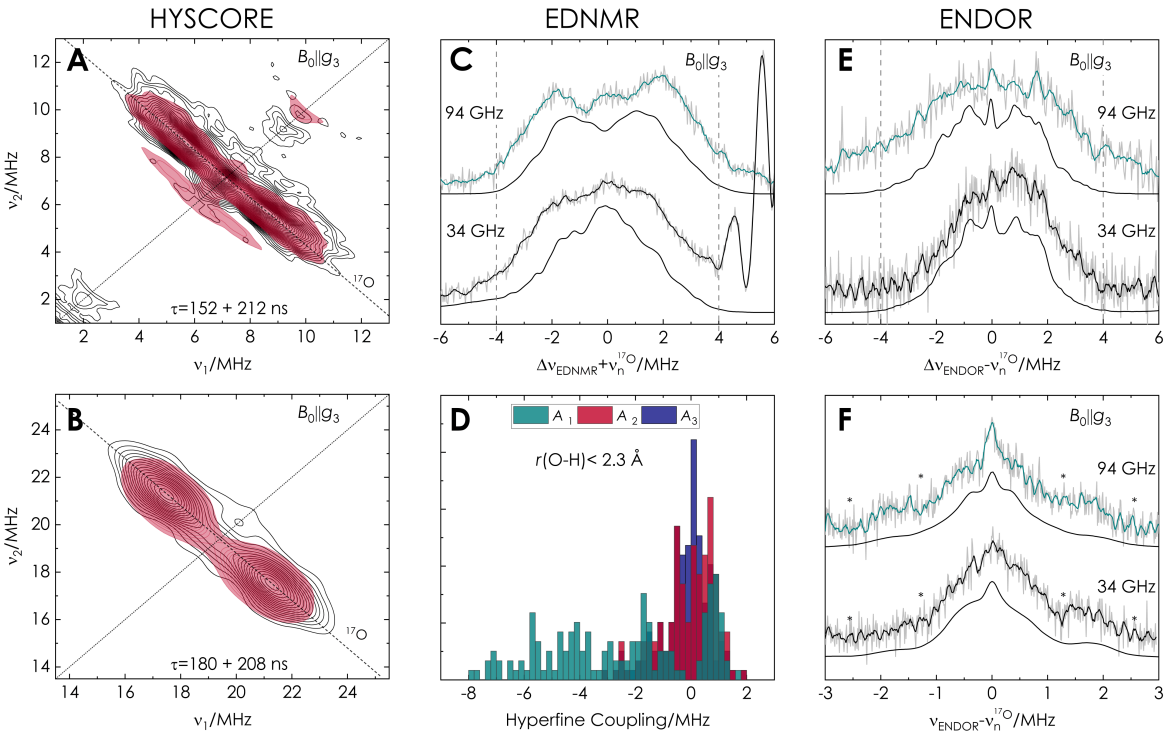

Figure 6.10: Simulation of TEMPOL/$T_6^\bullet$ hf spectra with a distribution of ^{17}O tensors (**D**) derived from MD simulations. **A**/**B**: HYSCORE simulations (red) reproduce the experimental spectra (black) at 34 (**A**) and 94 GHz (**B**). The 34 GHz spectra show resolution of the quadrupole coupling along the anti-diagonal. **C**: EDNMR simulations (black) of the experiments performed at 34 (black) and 94 GHz (cyan) show the difference in contribution of small hyperfine couplings and reproduce the width of the spectra. **D**: The hyperfine coupling components for hydrogen-bound water molecules show a broad distribution of A_1 (cyan) values, while $A_{2,3}$ (red, blue) are predominantly in the range of 0 ± 1.5 MHz. **E**: Davies ENDOR simulations (black) of the experiments performed at 34 (black) and 94 GHz (cyan) reproduce the broader distribution at 94 GHz. The sharp simulation features are artefacts of the limited amount of simulated hf coupling tensors with small linewidth. **F**: Mims ENDOR simulations (black) reproduce the experiments performed at 34 (black) and 94 GHz (cyan). The positions of the broad shoulders correspond to the theoretical Mims blindspot positions marked by asterisks.

distribution with a range of up to 8 MHz is observed at the $B_0 \| g_3$ position. From the DFT models it is clear, that the $B_0 \| g_3$ spectral position is the most sensitive to the structural variations of water molecules. The increased orientation-selectivity at 94 GHz makes the EDNMR and ENDOR experiments at the higher field more suitable to detect these couplings but at the same time reduces signal intensity which results in the poor signal to noise even for long measurements.

The MD simulations of the $T_6^\bullet$ radical show mostly perpendicular coordination of the closely bound water molecules, which is in good agreement with the large couplings observed experimentally. The absence of a defined coordination geometry in the MD, as observed for the tyrosyl radical, is also in good agreement with the broad, featureless distribution in the experiments. The simulation approach for the hf spectroscopy experiments is

therefore different than for the tyrosyl radical, where the spectra are reproduced by a single hyperfine and quadrupole coupling tensor. The broad coupling features may be represented by a combination of two coupling tensors with very broad linewidth parameters, but this would represent the structural variety in the sample only very poorly. Instead, we simulated the hyperfine spectra for all DFT calculated coupling tensors from the MD study. The quadrupole coupling tensor was set to the same values used for the tyrosyl radical ($\boldsymbol{P} = [-0.02; -0.32; 0.34]$ MHz) for all simulations.

The experimental spectra were then simulated as a sum of the individual tensor simulations with linewidths comparable to the simulations utilized for the tyrosyl radical (~ 0.1 MHz) and are shown in Figure 6.10. HYSCORE and Mims ENDOR simulations calculated a density operator evolution while EDNMR and Davies ENDOR simulations calculated the transitions from a static Hamiltonian (see Sec. 4). A sum of coupling tensor components for the hydrogen-bound water molecules ($r(O_{PC}\cdots H_{H_2O}) < 2.3$, Fig. 6.10, D) reproduces the broad coupling features in all three types of hf spectroscopy experiments. Significant deviations between spectra and simulation can mainly be observed for the Davies ENDOR, where the simulation does not cover the full width of the experimental 94 GHz spectrum and contains shoulders which the experiment does not exhibit (Fig. 6.10, E). This may be explained by the limited set of simulated tensors (3 waters x 100 models) used to simulate these spectra, which is not a full sampling of all possible coordinations, and the high orientation-selectivity of the Davies ENDOR experiments and simulations.

The experimental hyperfine spectra combined with the DFT and MD analysis allows us to concluded that no clearly defined binding motif for water exist for the six-membered $T_6^\bullet$ radical, but that perpendicular is preferred over in-plane binding.

6.4.3 The TEMPYL radical

In analogy to the $T_6^\bullet$ radical, the binding structure of water around the nitroxide $T_5^\bullet$ was not known. The ^{1}H/^{2}H ENDOR study of hydrogen-bound isopropyl-alcohol concluded that hydrogen-bond coordination occurs exclusively in-plane for this radical.[162] The hyperfine spectra of $T_5^\bullet$ show strong similarities but also marked differences compared to the $T_6^\bullet$ spectra. Similar broad ^{17}O coupling features in a range of up to 8 MHz are present at all canonical g-tensor orientations in the three experiment types with the largest distribution observed at the $B_0 \| g_3$ position. The EDNMR and 94 GHz HYSCORE spectra of $T_5^\bullet$ show mainly an overall reduced ^{17}O signal intensity compared to $T_6^\bullet$. Only the ENDOR spectra of $T_5^\bullet$ reveal additional, sharp ^{17}O couplings of ~ 1 MHz, which resemble the signals observed for the tyrosyl radical. In contrast to the tyrosyl radical, these signals can also be observed in the Davies ENDOR spectra, which can be explained by the larger overall radical concentration (~ 80 vs 200 µM) and the 3-fold longer relaxation time of $T_5^\bullet$. The

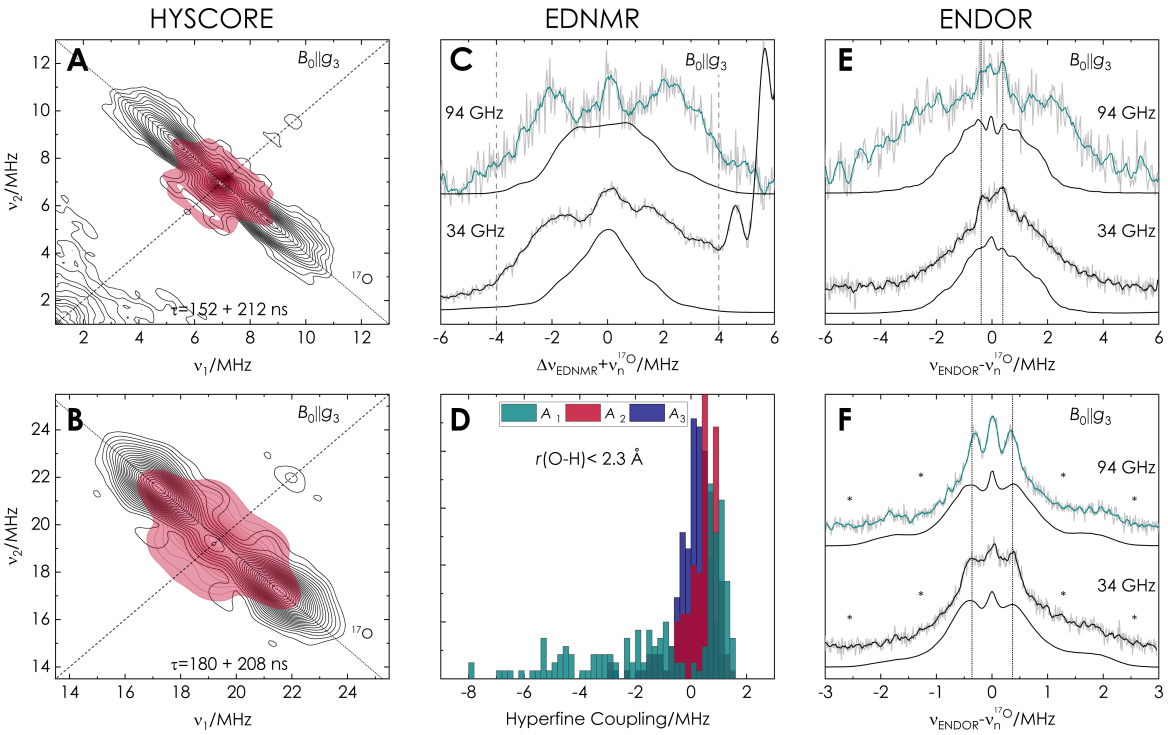

Figure 6.11: Simulation of TEMPYL/$T_5^\bullet$ hf spectra with a distribution of ^{17}O tensors (**D**) derived from MD simulations. **A**/**B**: HYSCORE simulations (red) only reproduce the center of the experimental spectra (black) at 34 (**A**) and 94 GHz (**B**). **C**: EDNMR simulations (black) of the experiments performed at 34 (black) and 94 GHz (cyan) overestimate the small hyperfine couplings and underestimate the width of the spectra. **D**: The hyperfine coupling components for hydrogen-bound water molecules show a broad distribution of A_1 (cyan) but a clear majority of $A_{1,2}$ and A_3 in the range of 1 ± 1 MHz. **E**: Davies ENDOR simulations (black) of the experiments performed at 34 (black) and 94 GHz (cyan) do not reproduce the broader distribution at 94 GHz. The sharp doublet with a splitting of 0.7 MHz (dotted grey lines) are broader in the simulation than in the experiment and barely visible in the 34 GHz simulation. **F**: Mims ENDOR simulations (black) are broader than the experiments performed at 34 (black) and 94 GHz (cyan). The positions of the sharp doublet with a splitting of 0.7 MHz is reproduced but the difference in line-width is obscured in the simulations.

94 GHz Mims ENDOR spectra best resolve the clear doublet structure with a splitting of 0.74 MHz, while the broadening at lower field makes them hard to distinguish.

From the DFT analysis it is clear, that such couplings correspond to water molecules coordinated in the plane of the nitroxide radicals ring. The MD simulations are in accordance with this spectroscopic observation, indicating the preference for in-plane coordination for hydrogen-bound waters. The same simulation approach used for the $T_6^\bullet$ radical was employed, using the sum of calculated hyperfine tensors predicted by the MD/DFT analysis. Figure 6.11 shows the simulations of all hyperfine spectroscopy experiments which, in contrast to $T_5^\bullet$, do not agree with the experimental spectra. In all simulations, the broad distribution of hyperfine couplings is underestimated, showing a narrower coupling range. The sensitivity of the $B_0||g_3$ spectral position for large couplings associated with

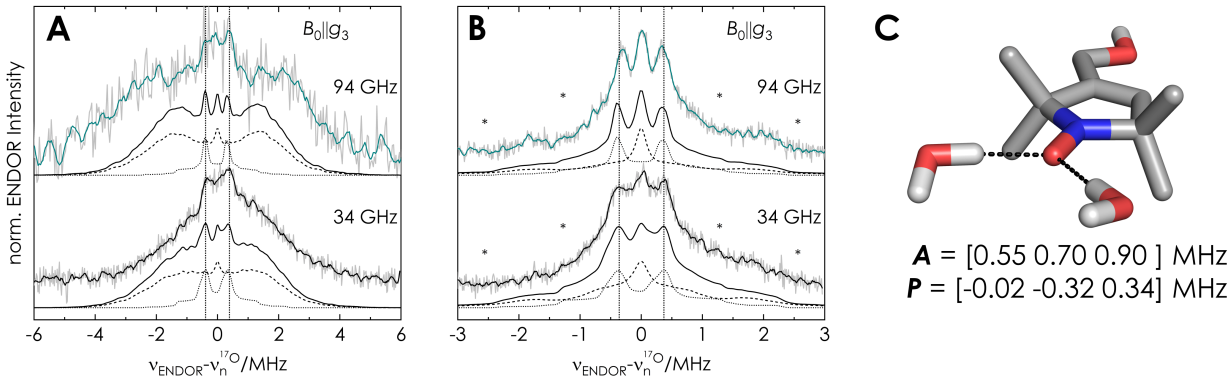

Figure 6.12: Alternative simulation of TEMPYL/$T_5^\bullet$ ENDOR spectra with a combination of a broad distribution of ^{17}O tensors and a single hyperfine coupling tensor. **A**/**B**: ENDOR simulations (black) with a combination of a broad (dashed line) tensor distribution and a single coupling tensor (dotted line) with a relative weight of 55/45 (±10)%, respectively. Davies ENDOR simulations (**A**) represent the experimental spectra better than in Fig. 6.11. Mims ENDOR simulations (**B**) reproduce the experimental spectra very well, especially the different linewidths at 34 vs. 94 GHz. **C**: In-plane coordination of water molecules to $T_5^\bullet$ at a dihedral angle of $\theta = 0/180°$ with corresponding hyperfine and quadrupole coupling tensor. Simulations do not distinguish between the two angles.

perpendicular water binding means that this coordination mode is underestimated by the molecular dynamics simulations. This is reflected by the distribution of hyperfine couplings of the hydrogen-bound waters (Figure 6.11, D), which is dominated by small couplings in the $0-1$ MHz range. The sharp coupling features in the Davies and Mims ENDOR spectra are reproduced qualitatively by the MD simulations but appear too broad (Figure 6.11, E/F). The different linewidths observed in the 34 and 94 GHz Mims ENDOR spectra are also not reproduced by the simulations, which indicates that the MD overestimates the structural variety of the in-plane coordination.

We therefore used an alternative simulation approach for the ENDOR spectra by combining a broad tensor distribution similar to the $T_6^\bullet$ MD results with a single hyperfine coupling tensor ($\boldsymbol{A} = [0.55; 0.70; 0.90]$ MHz) with the orientation and coupling size close to the predicted DFT tensor of an in-plane ($\theta = 0/180°$) water molecule.

They are shown in Figure 6.12 and fit the experimental data better than the pure MD simulations, reproducing the linewidth differences between 34 and 94 GHz experiments in the same way observed for the tyrosyl radical. The coordination geometry of water molecules, shown in the same figure, represents only the binding motif responsible for the sharp coupling features. It should be noted that the simulation can neither distinguish between 0 or 180° coordination, nor between one or two coordinated water molecules. The relative intensity of the sharp and broad coupling features in the ENDOR simulations are approx. 45 and 55 %, respectively. Since the broad coupling features are the only contribution to the 94 GHz HYSCORE and EDNMR spectra, this also explains their reduced signal intensity

compared to the $T_6^\bullet$ spectra.
We conclude that water molecules coordinate to the $T_5^\bullet$ radical both perpendicular and in-plane, with a rather well-defined coordination geometry for the latter motif. MD simulations qualitatively describe the presence of this preferred binding mode but overestimate the structural distribution.

6.5 Conclusion

We have shown the application of HYSCORE, EDNMR and ENDOR spectroscopy at two different EPR frequencies to detect ^{17}O-labelled water molecules around three biologically relevant radicals. Our experiments show, that the ^{17}O nucleus is a good hyperfine spectroscopy target to unambiguously assign spectral signatures to water molecules.
The choice of the best method depends on the size of the ^{17}O hyperfine coupling. HYSCORE, EDNMR and Davies ENDOR are well suited to resolve hyperfine couplings in the range of $1 - 8$ MHz, which were observed for both nitroxide radicals as broad spectroscopic features. The advantage of HYSCORE over EDNMR and ENDOR lies in the spectral separation of strongly and weakly coupled nuclei, important for nitroxide radicals due to the strongly coupled ^{14}N nucleus, as well as in the resolution of nuclear quadrupole coupling separated from hyperfine coupling. The disadvantage lies in the long acquisition times of the 2D datasets and the spectral blindspots.
Mims ENDOR is the only method capable of resolving isotropic ^{17}O hyperfine couplings smaller than 1 MHz, which were observed for the five-membered nitroxide $T_5^\bullet$ and the tyrosyl radical $Y_{356}^\bullet$. Mims experiments at the common Q-band frequency yield ENDOR spectra with characteristic spectral features while experiments at the higher W-band frequency significantly improve the spectral resolution due to the reduction of nuclear quadrupole coupling and increased orientation-selectivity. The small coupling features resolved by Mims can be completely missed in HYSCORE and EDNMR spectra due to their limited resolution and may also disappear in Davies ENDOR experiments if the relaxation time of the investigated radical is fast enough. A combination of HYSCORE and Mims ENDOR should be the preferred experimental approach if the binding mode is unknown, since it is unlikely that spectral features are missed in this approach.
Small structural models of the three radicals showed that the ^{17}O hyperfine coupling is very sensitive to the binding motif of the hydrogen-bound water molecules due to the asymmetric spin density distribution of the oxygen-centered radicals. While large hyperfine couplings are indicative of perpendicular coordination above and below the ring, small isotropic couplings correspond to in-plane coordination. The ^{17}O hyperfine spectra show a clearly defined in-plane coordination for the $Y_{356}^\bullet$ radical. This is linked to the enzyme environment and the energetic preference of the ideal hydrogen-bond. Our earlier ^{17}O

Mims ENDOR work had established water molecules at the $Y^{\bullet}_{356}$ as well as two other tyrosyl radicals in the RNR enzyme.[15] These works hint at the mechanistic significance of the structured water molecules in biological proton-coupled electron transfer and open the possibility for study in other enzymes with tyrosyl radicals.
The broad ^{17}O hyperfine spectra of the nitroxides on the other hand represent a large variety of binding motifs in the bulk solution, which was supported by MD simulations. The six-membered nitroxide radical $T^{\bullet}_{6}$ exhibits mostly perpendicular water coordination without a clearly preferred binding mode. The five-membered $T^{\bullet}_{5}$ radical on the other hand shows both variable perpendicular binding as well as a clearly defined in-plane binding mode. The difference between the two nitroxides results from their methyl group arrangement, due to the difference between a chair-like six membered ring and a planar five membered ring.
Our results give the first link between ^{17}O hyperfine spectra and structural information about nitroxide-water hydrogen-bond geometries. The hydrogen-bond environment around nitroxide radicals has previously been investigated by indirect measurement of its effects on the *g*-values and nitrogen hyperfine as well as quadrupole coupling tensors.[163–166] From these works, qualitative information about hydration amount and number of hydrogen-bonds could be gained. The earlier work of *Nalepa et al.* using ^{17}O EDNMR and Davies ENDOR of a TEMPOL had resolved similarly broad ^{17}O signals, but gave no link to structural information.[50] Our work shows that ^{17}O hyperfine signatures can be used to derive structural information around nitroxides and distinguish between different coordination modes in bulk solutions.

6.6 Experimental section

Substances, sample preparation and experimental setup are described in Chapter 3.

HYSCORE experiments HYSCORE experiments were recorded with the pulse sequence $\pi/2-\tau-\pi/2-t_1-\pi-t_2-\pi/2-\tau-$echo with maximum microwave power resulting in 6 ns and 12 ns $\pi/2$ pulses at 34 and 94 GHz, respectively. A 16-step phase cycle was used to remove unwanted echo contributions. Experiments were performed with two inter-pulse delays τ chosen to either maximize ($\tau = n/\nu_{\mathrm{Larmor}}$) or minimize ($\tau = (n+0.5)/\nu_{\mathrm{Larmor}}$) the signal at the respective nuclear Larmor frequency of ^{17}O. The center of the produced echo (32 ns) was integrated to yield the time traces. The experimental datasets comprised a total of 300 by 300 data points. The time domain data was baseline corrected (third-order polynomial), apodized with a hamming function, zero-filled and Fourier-transformed to yield the frequency spectrum with a resolution of 0.1 MHz. Frequency spectra were normalized to the ^{17}O signal.

EDNMR experiments EDNMR experiments were performed with the pulse sequence $t_{HTA} - t_d - \pi/2 - \tau - \pi - \tau -$ echo. The microwave frequency of the detection echo was set to the operating frequency of the resonator and the power adjusted to produce $\pi/2$-pulses of 100 ns and π-pulses of 200 ns, checked by mw nutation experiments. The power of the HTA pulse was adjusted for each experiment individually and the $\omega_1/2\pi$ determined as twice the HWHM of a Lorentz fit to the central blindspot. Experiments were performed with 20 µs HTA pulses at 34 GHz and 30 µs HTA pulses at 94 GHz. A long delay t_d of 10 µs was chosen to allow a full relaxation of any coherences produced by the HTA pulse. Experiments with shorter delays showed no significant gain in EDNMR signal (data not shown). The τ-value in the detection echo was set to 1400 ns, which ensures a sufficient delay between the end of the spectrometer dead time and the echo ($\sim$ 1000 ns), while limiting signal loss due to relaxation. The experiments were performed with a 2-step phase cycle of the $\pi/2$ to remove long FIDs produced by the π-pulse. The echo was integrated in a range of $\pm$1000 ns around its maximum to increase the spectral resolution. Experimental data was processed by subtracting an aforementioned Lorentz fit to the central hole and normalized to the ^{17}O signal.

ENDOR experiments ENDOR experiments were performed with the Davies $\pi_{sel.} - \pi(rf) - t_d - \pi/2 - \tau - \pi - \tau -$ echo and Mims pulse sequence $\pi/2 - \tau - \pi/2 - \pi(rf) - t_d - \pi/2 - \tau -$ echo. The microwave power was adjusted to produce $\pi/2$-pulses of 200 ns and π-pulses of 400 ns for Davies ENDOR and $\pi/2$-pulses of $6 - 40$ ns for Mims ENDOR, respectively, checked by mw *Rabi* nutation experiments. The radio-frequency power was adjusted to produce 40 µs pulses at 34 and 94 GHz, respectively, checked by rf *Rabi* nutation experiments. The radio-frequency was swept stochastically to reduce heating and saturation effects and the entire echo was integrated to yield the ENDOR spectra.[139] ENDOR experiments were recorded in batches of $5 - 100$ scans as a 2D dataset. The batches were individually phase corrected to account for phase drifts during long acquisition and then summed. The sum spectra were baseline corrected (first-order polynomial) and normalized to the maximum intensity.

DFT calculations DFT models were calculated using the *Orca* 4.0.1.2 software package.[73] Geometry optimization was performed using the BP86[74,75] combined with Ahlrichs' triple-ζ quality basis set def2-TZVP[76,77] and the RIJCOSX[78] approximation(def 2/J auxiliary basis set). The SCF calculations were supplemented with Grimmes dispersion correction (d3bj).[79,80] SCF energies, magnetic properties and coupling parameters were calculated from the geometry optimized structures using the B3LYP[75,81,82] combined with the EPR-II basis set[83] for the entire model. The RIJCOSX approximation and dispersion correction were also used. The water and protein environment was approximated by a conductor-like

polarization model (CPCM) with polarity epsilon of 80 and 24 for the nitroxides and the tyrosyl radical, respectively.

MD simulations MD simulations were performed using the *Gromacs* 2018.4 software package.[167] A detailed description of the methodology is given under Section 6.7.11.

Spectral simulations Spectral simulations were performed using the *EasySpin* 5.2.33 software package.[70,142] HYSCORE simulations were performed using the `saffron` routine. Simulated time traces for the individual τ-values and were summed to give the overall time trace. The sum of all time traces was zero filled, Fourier transformed to yield frequency domain simulations with 0.1 MHz resolution and normalized to the ^{17}O signal. EDNMR spectra were simulated using a modified version of the `horseradish` routine, developed by *Wili et al.*[72] (see Ch. 4). Simulated spectra were summed and normalized to the ^{17}O signal. Davies ENDOR spectra were simulated using the `salt` routine utilizing full tensor diagonalization (`Opt.Method='matrix'`). Individual spectra were summed, normalized to the maximum signal and convolved with an inverted Lorentzian line-shape to account for the spectral hole in the center of the spectrum. Mims ENDOR spectra were simulated using the `saffron` routine. Individual spectra were summed and then normalized to the maximum signal.

6.7 Supporting information

6.7.1 ^{17}O hf studies of water molecules at transition metal ions

Table 6.2: Summary of selected publications using ^{17}O hyperfine spectroscopy to investigate water binding to transition metal ions.

PC	System	A_1	A_2	A_3	a_{iso}	P_1	P_2	P_3	Reference	Experiment
Mn(II)	Ras GDP	6.27	6.86	10.1	7.74	-0.238	0.238	0	*Bennati et al.*[103]	ENDOR
Mn(II)	$Mn(H_2O)_6$	-7.5	-6.5	-6.5	-6.83	-0.3	0.3	0	*Baute et al.*[44]	ENDOR
Mn(II)	$Mn(H_2O)_6$	-6.3	-6.3	-10	-7.53	-0.35	0.35	0	*Tan et al.*[147]	ENDOR ESEEM
Gd(III)	Gd(MS-325)	1.44	0.405	0.405	0.75	-0.325	0.325	0	*Raitsimring et al.*[150]	ENDOR
Fe(III)	CytP450	2.9	2.45	2.45	2.6	-0.33	0.329	0.01	*Thomann et al.*[48]	ESEEM
Fe(III)	CytP450	4.2-4.5	-	-	1.5-2	-	-	-	*Goldfarb et al.*[148]	ENDOR ESEEM
Cu(II)	Tutton Salt	0.13	0.23	-3.81	-1.15	0.318	-0.307	-0.11	*Colaneri et al.*[49]	ESEEM
Fe(III)	RNR	34	21	17	24	0.3	-0.25	-0.05	*Burdi et al.*[149]	ENDOR
Mn(II)	$Mn(H_2O)_6$	-9.8	-5.6	-7.1	7.5	-0.1	0.5	0.5	*Cox et al.*[47]	EDNMR
Mn(II)	PSII	5 2.1	5.1 0.2	3.3 2	4.5 1.4	-	-	-	*Rapatskiy et al.*[46]	EDNMR

[a] all coupling values given in MHz.

6.7.2 EPR characterization

Table 6.3: EPR simulation parameters of $T_6^\bullet$, $T_5^\bullet$ and $Y_{356}^\bullet$.

Radical	g_1	g_2	g_3	Nuclei	A_1	A_2	A_3	P_1	P_2	P_3
$T_6^\bullet$	2.0093 2.0088	2.00615	2.0022	N	19.5	18.9	105	1.2	0.54	−1.7
$T_5^\bullet$	2.0082	2.0061	2.0022	N	13.3	13.3	104	1.2	0.4	−1.7
$Y_{356}^\bullet$	2.0062	2.0045	2.0022	H_β H^a H^b	61 −5 −3	52 −21 −19	57 −24 −24	-	-	-

[a] Simulation of experimental $T_6^\bullet$ spectra was performed as a 1:1 mixture of two spectra with different g_1 values to account for different H-bond environments.[166]
[b] Euler angles $\alpha,\beta,\gamma = 90°,90°, \pm 20°$ were used.[26]

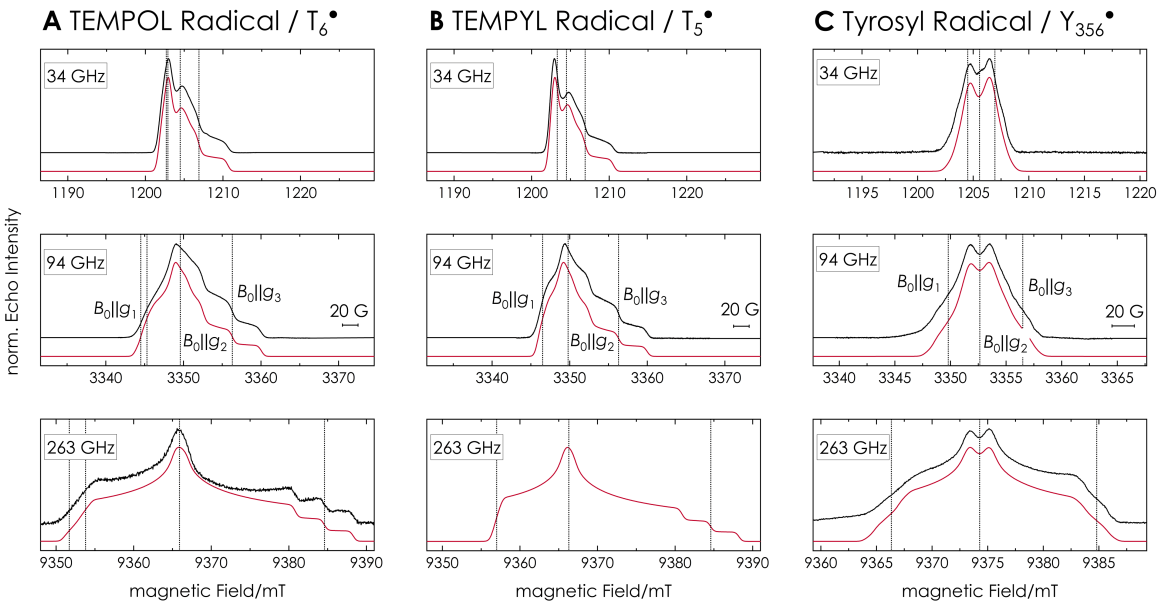

Figure 6.13: Echo-detected field sweep spectra of the $T_6^\bullet$ (**A**), $T_5^\bullet$ (**B**) and $Y_{356}^\bullet$ (**C**) radicals recorded at three different microwave frequencies. Experiment is shown in black with simulations shown in red. Simulations were performed with *EasySpin*, using full matrix diagonalization and parameters are specified in Table 6.3. Resonance fields corresponding to the canonical g-tensor orientations ($B_0 \| g_{1,2,3}$) are marked by dotted lines. Differences between simulation and experimental spectra are most likely caused by different relaxation behavior across the EPR line. $T_5^\bullet$ experimental spectrum at 263 GHz is missing due to technical problems with the spectrometer.

6.7.3 HYSCORE of $I = 5/2$ nuclei

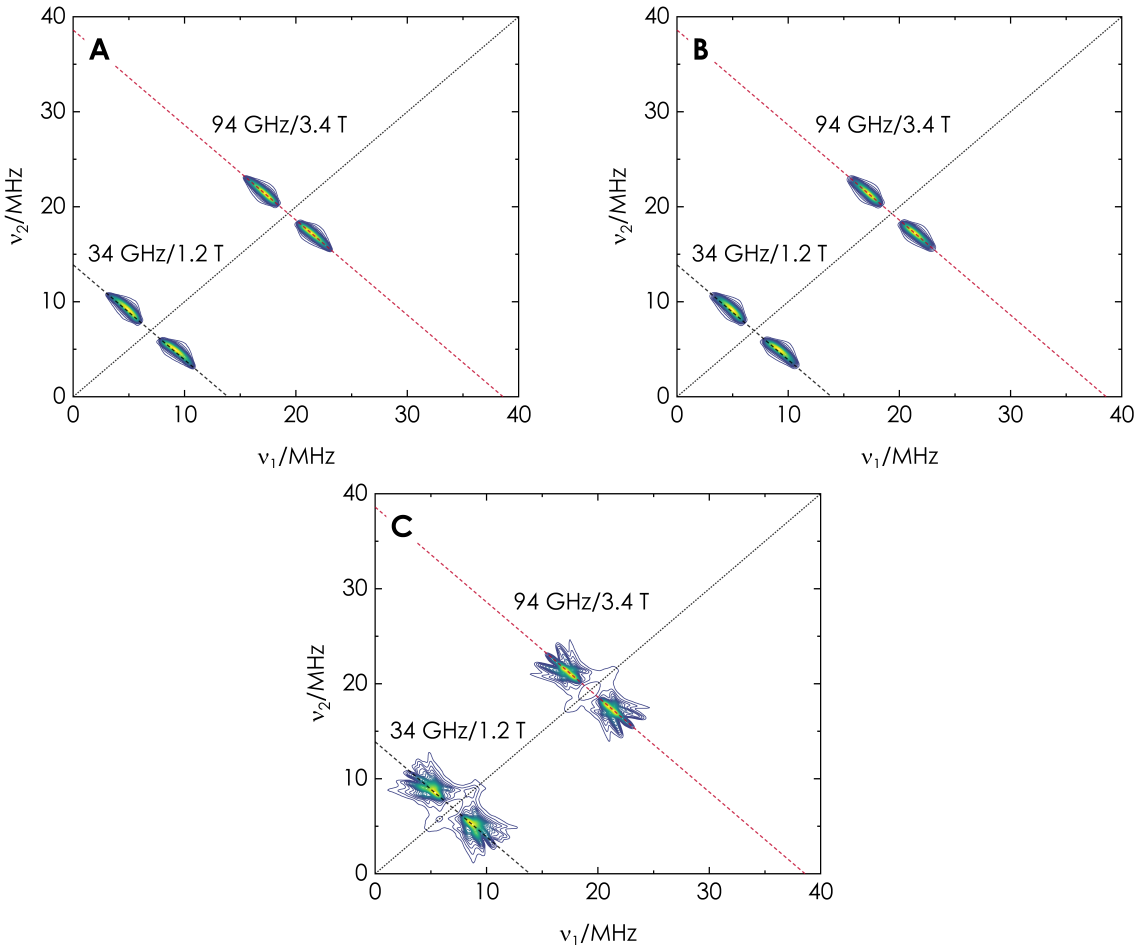

Figure 6.14: Simulated HYSCORE spectra of a coupled $S = 1/2, I = 5/2$ spin system. Hyperfine coupling tensor $\boldsymbol{A} = 4 + [-2; -2; 4]$ MHz in combination with **A**: no quadrupole coupling ($\boldsymbol{P} = [0; 0; 0]$ MHz), **B**: small quadrupole coupling ($\boldsymbol{P} = [-0.002; -0.032; 0.034]$ MHz) and **C**: large quadrupole coupling ($\boldsymbol{P} = [-0.02; -0.32; 0.34]$ MHz). Spectra are simulated using the *EasySpin* function `saffron`, which calculates a time evolution of the density matrix.

6.7.4 Mims blindspots

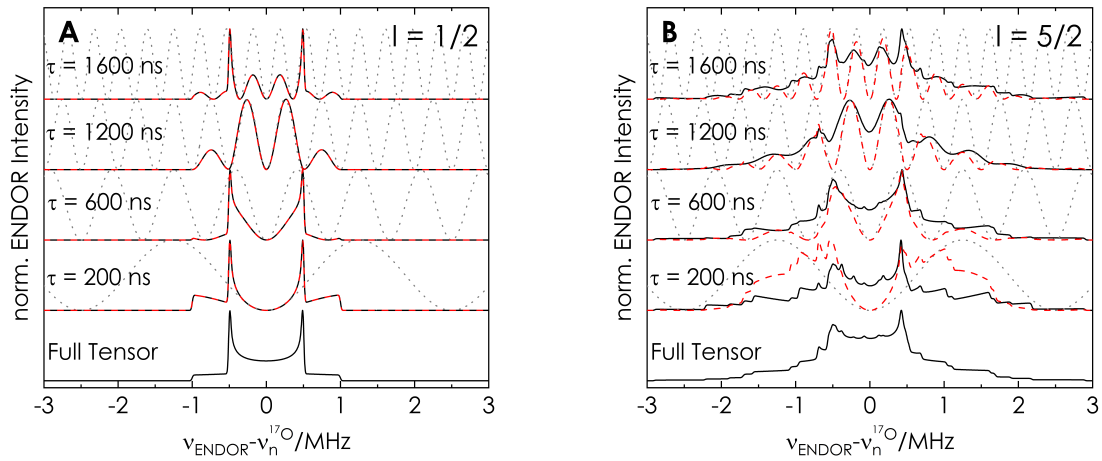

Figure 6.15: Simulated Mims ENDOR spectra of a nuclear spin $I = 1/2$ (**A**) and $I = 5/2$ (**B**) with a hyperfine coupling tensor $\boldsymbol{A} = [-2; 1; 1]$ MHz and a quadrupole coupling tensor ($I = 5/2$ only) $\boldsymbol{P} = [-0.2; -0.2; 0.4]$ MHz. Simulated spectra using the *EasySpin* function `saffron`, which calculates the spectrum through density matrix evolution, shown in black. Theoretical Mims blindspot function (Eq. 2.82) is shown as gray dotted lines. Red dashed lines show the product of the full tensor simulation (bottom) with the respective blindspot function. The two methods produce identical results in case of a spin $I = 1/2$ (**A**) nucleus, while significant deviations are present for a nuclear spin $I = 5/2$ (**B**).

6.7.5 Experimental HYSCORE spectra

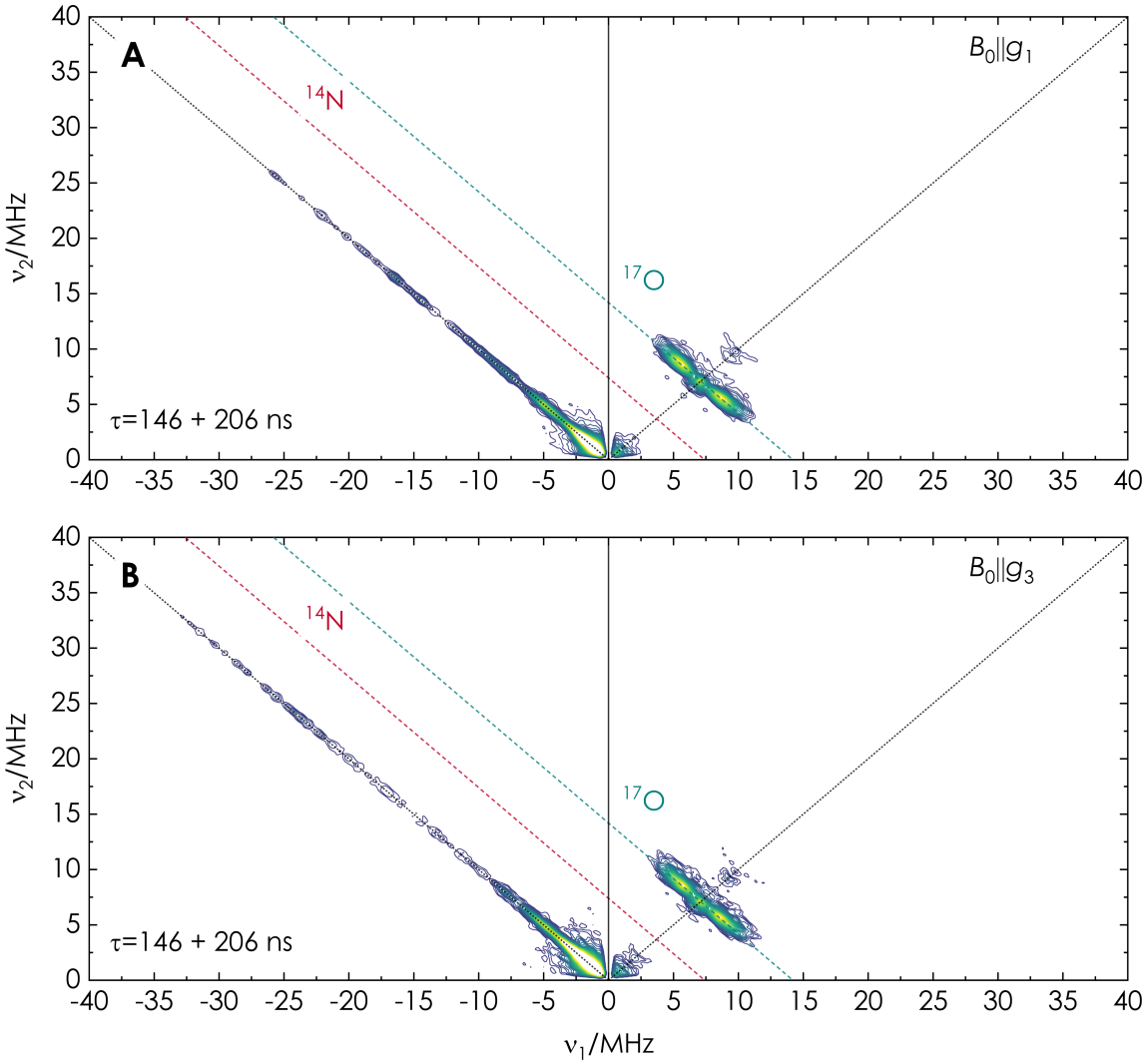

Figure 6.16: 34 GHz HYSCORE spectra of $T_6^{\bullet}$ recorded at the $B_0 \| g_1$ (**A**) and $B_0 \| g_3$ (**B**) positions in the EPR line. Experimental parameters: 50 K, pulse sequence: $\pi/2 - \tau - \pi/2 - t_1 - \pi - t_2 - \pi/2 - \tau -$ echo, $\pi/2 = 6$ ns, $\tau = 146/206$ ns, d$t = 10$ ns, $t_1/t_2 = 100 \rightarrow 3090$ ns, 16-step phase cycle, 6 shot/point, 3 ms SRT, 15 h per spectrum.

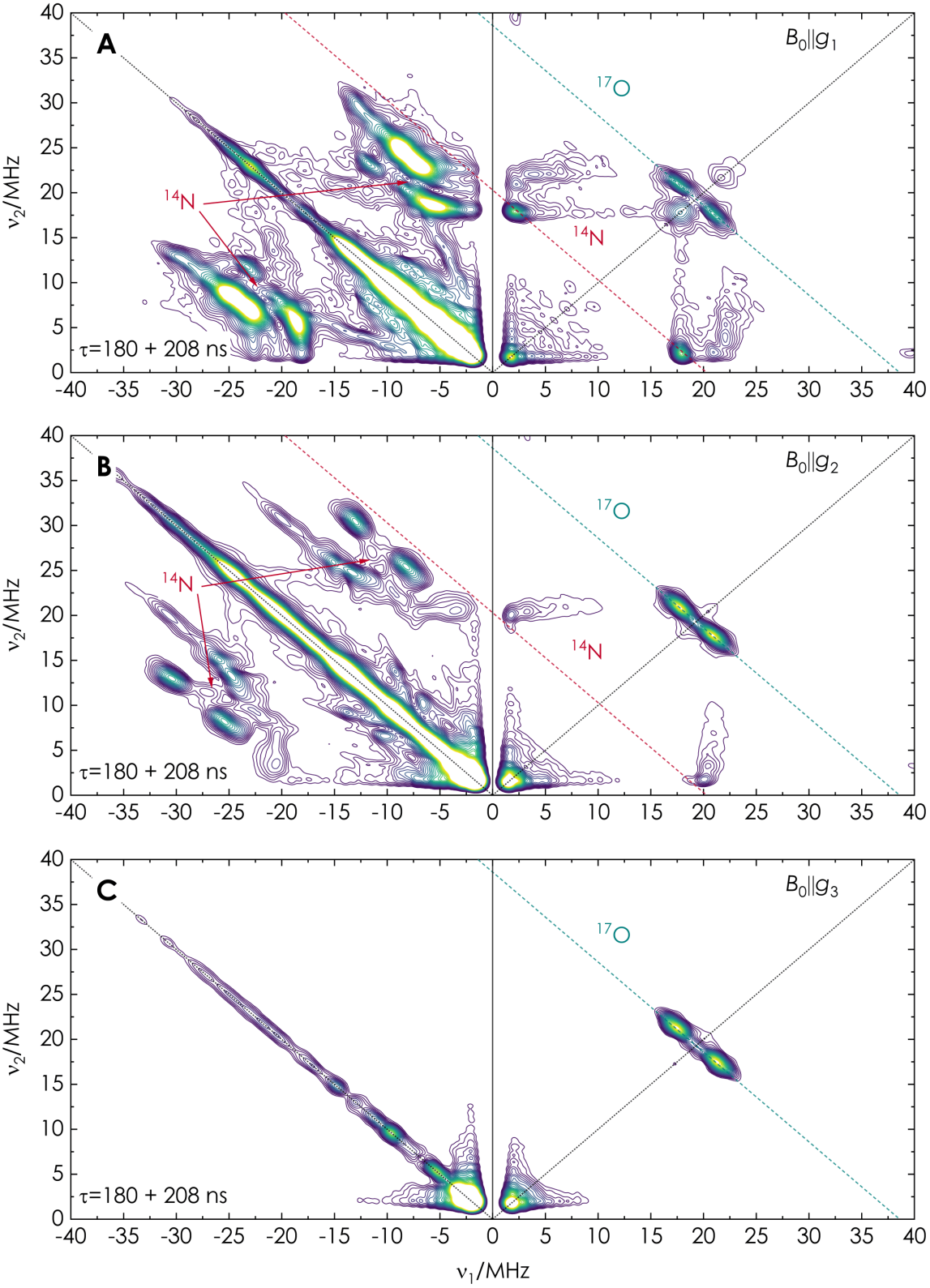

Figure 6.17: 94 GHz HYSCORE spectra of $T_6^{\bullet}$ recorded at the $B_0 \| g_1$ (**A**), $B_0 \| g_2$ (**B**) and $B_0 \| g_3$ (**C**) positions in the EPR line. Experimental parameters: 50 K, pulse sequence: $\pi/2 - \tau - \pi/2 - t_1 - \pi - t_2 - \pi/2 - \tau -$ echo, $\pi/2 = 10$ ns, $\tau = 180/208$ ns, $dt = 4$ ns, $t_1/t_2 = 100 \rightarrow 1296$ ns, 16-step phase cycle, 3 shot/point, 6 ms SRT, 15 h per spectrum.

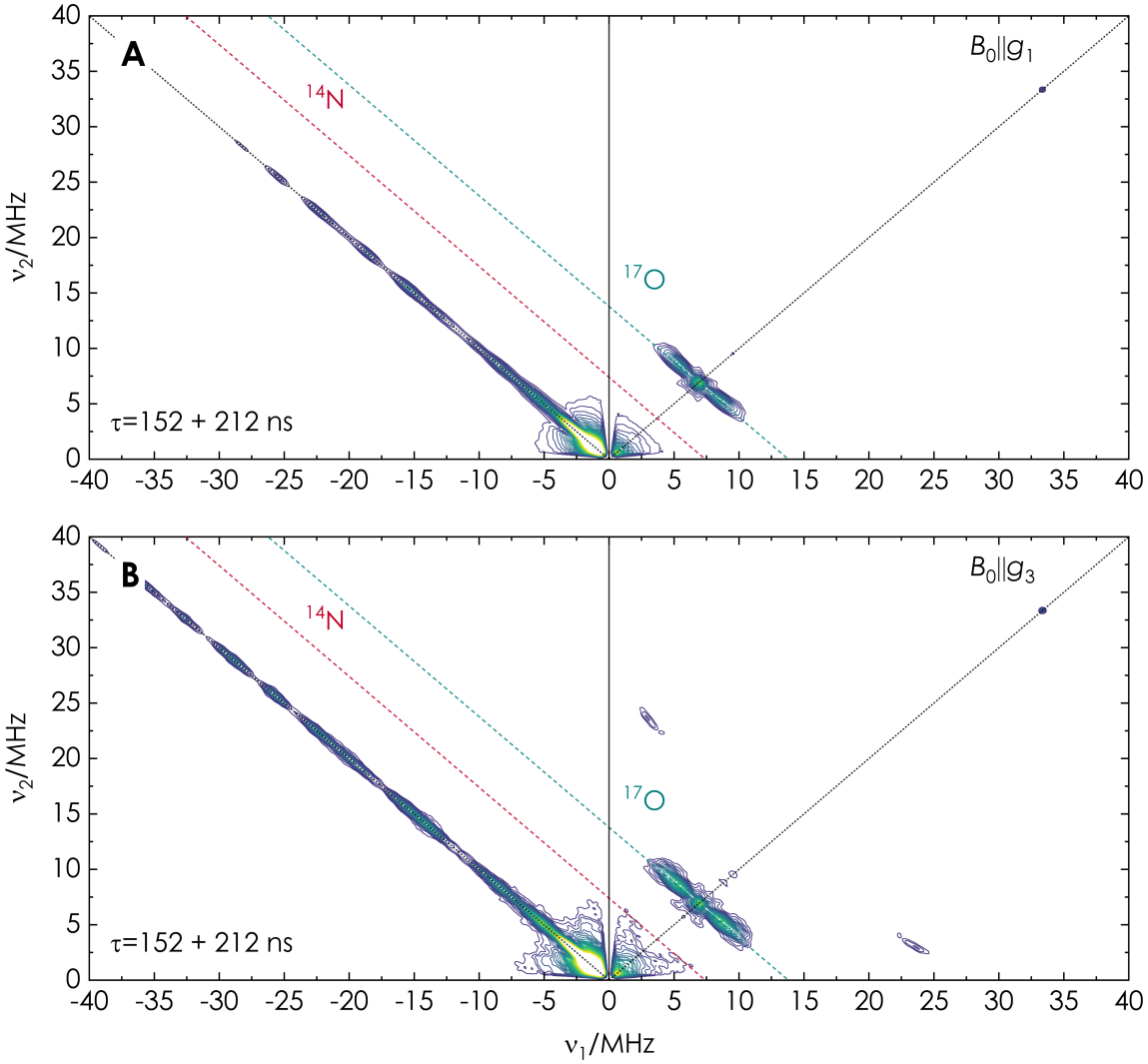

Figure 6.18: 34 GHz HYSCORE spectra of $T_5^{\bullet}$ recorded at the $B_0 \| g_1$ (**A**) and $B_0 \| g_3$ (**B**) positions in the EPR line. Experimental parameters: 50 K, pulse sequence: $\pi/2 - \tau - \pi/2 - t_1 - \pi - t_2 - \pi/2 - \tau -$ echo, $\pi/2 = 6$ ns, $\tau = 140/200$ ns, d$t = 10$ ns, $t_1/t_2 = 100 \rightarrow 3090$ ns, 16-step phase cycle, 5 shot/point, 3 ms SRT, 12 h per spectrum.

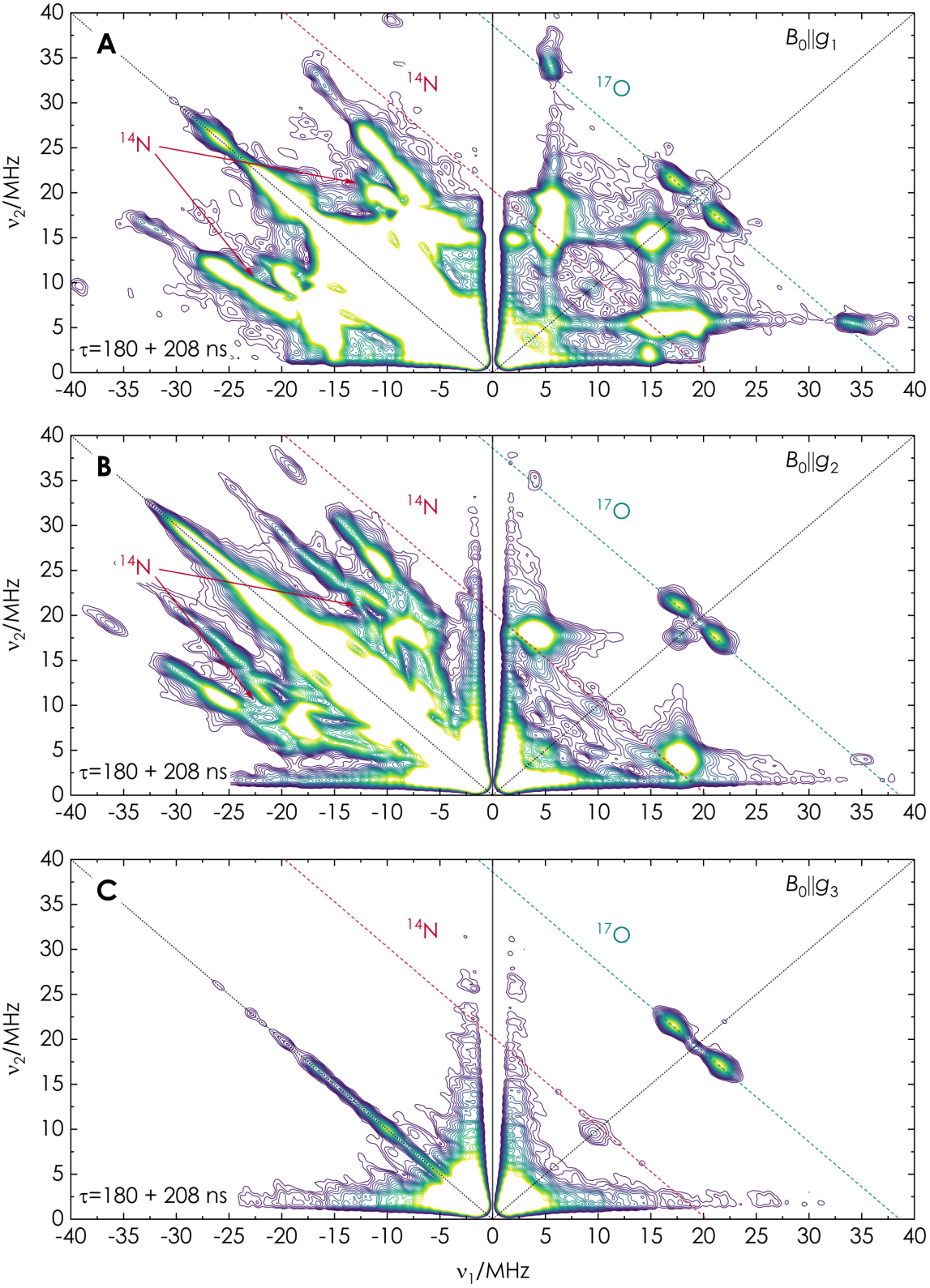

Figure 6.19: 94 GHz HYSCORE spectra of $T_5^{\bullet}$ recorded at the $B_0 \| g_1$ (**A**), $B_0 \| g_2$ (**B**) and $B_0 \| g_3$ (**C**) positions in the EPR line. Experimental parameters: 50 K, pulse sequence: $\pi/2 - \tau - \pi/2 - t_1 - \pi - t_2 - \pi/2 - \tau -$ echo, $\pi/2 = 12$ ns, $\tau = 180/208$ ns, $dt = 4$ ns, $t_1/t_2 = 100 \rightarrow 1296$ ns, 16-step phase cycle, 3 shot/point, 5 ms SRT, 12 h per spectrum.

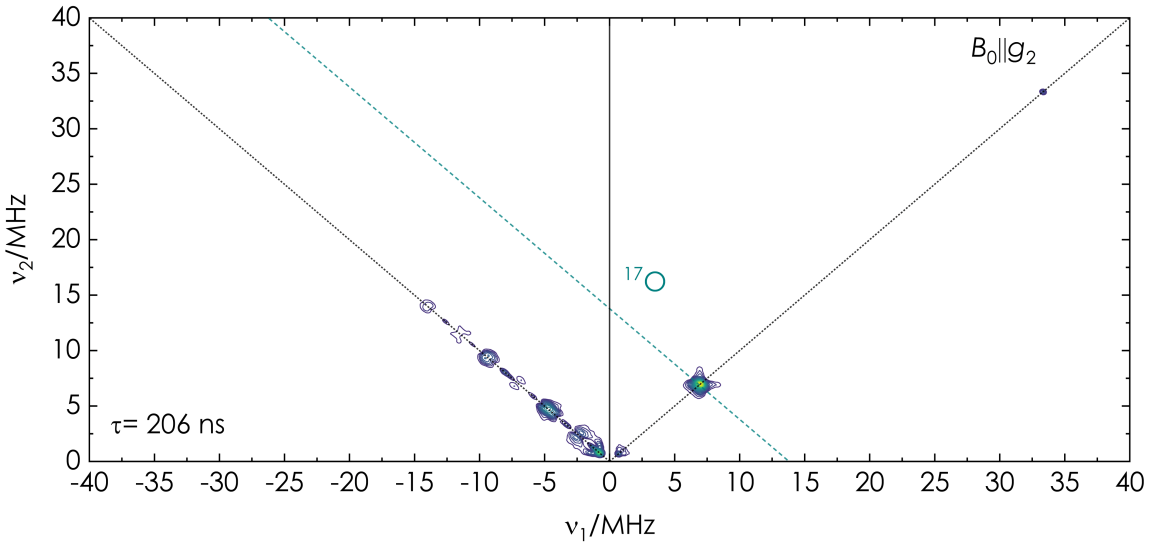

Figure 6.20: 34 GHz HYSCORE spectrum of $Y^{\bullet}_{356}$ recorded at the $B_0 \| g_2$ position in the EPR line. Experimental parameters: 50 K, pulse sequence: $\pi/2 - \tau - \pi/2 - t_1 - \pi - t_2 - \pi/2 - \tau -$ echo, $\pi/2 = 6$ ns, $\tau = 206$ ns, $dt = 10$ ns, $t_1/t_2 = 100 \rightarrow 3090$ ns, 16-step phase cycle, 6 shot/point, 3 ms SRT, 7.5 h.

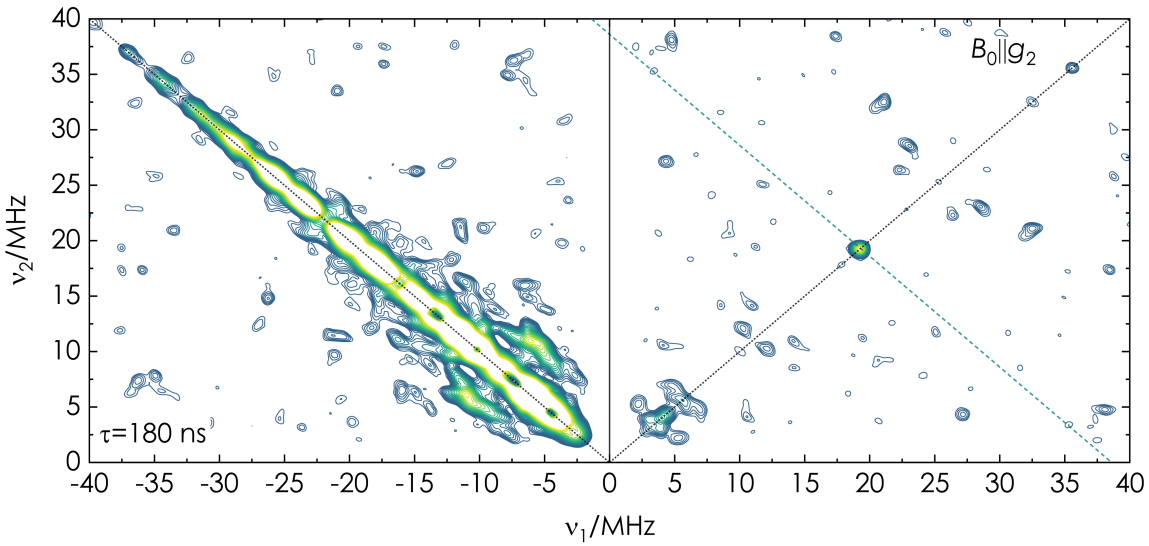

Figure 6.21: 34 GHz HYSCORE spectrum of $Y^{\bullet}_{356}$ recorded at the $B_0 \| g_2$ position in the EPR line. Experimental parameters: 50 K, pulse sequence: $\pi/2 - \tau - \pi/2 - t_1 - \pi - t_2 - \pi/2 - \tau -$ echo, $\pi/2 = 10$ ns, $\tau = 180$ ns, $dt = 4$ ns, $t_1/t_2 = 100 \rightarrow 1296$ ns, 16-step phase cycle, 3 shot/point, 5 ms SRT, 6 h.

6.7.6 Experimental EDNMR spectra

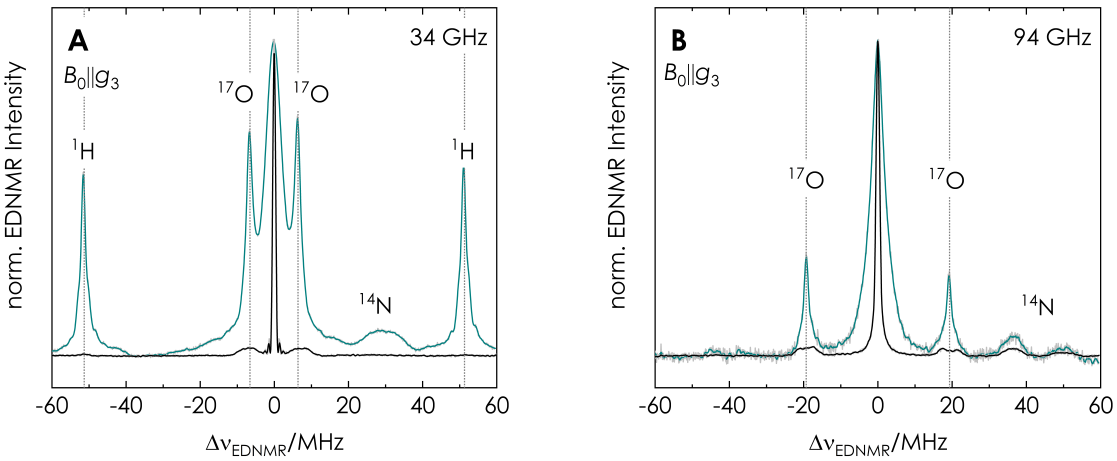

Figure 6.22: Power-dependent EDNMR spectra of $T_6^\bullet$ recorded at 34 GHz (**A**) and 94 GHz (**B**) at the $B_0 \| g_3$ position in the EPR line. Experiments with high microwave-power HTA are shown in cyan and with low mw-power are shown in black. $\omega_1/2\pi$ and acquisition times were: **A**: 3 MHz/2 h and 0.4 MHz/9 h, **B**: 2 MHz/2 h and 0.5 MHz/9 h. Spectra are normalized to the central hole. Experimental parameters: 50 K, pulse sequence: $t_{HTA} - t_d - \pi/2 - \tau - \pi - \tau -$ echo, $t_{HTA} = 20/30$ µs, $t_d = 10$ µs, $\pi/2 = 100$ ns, 2-step phase cycle, 20 shot/point, 3/5 ms SRT.

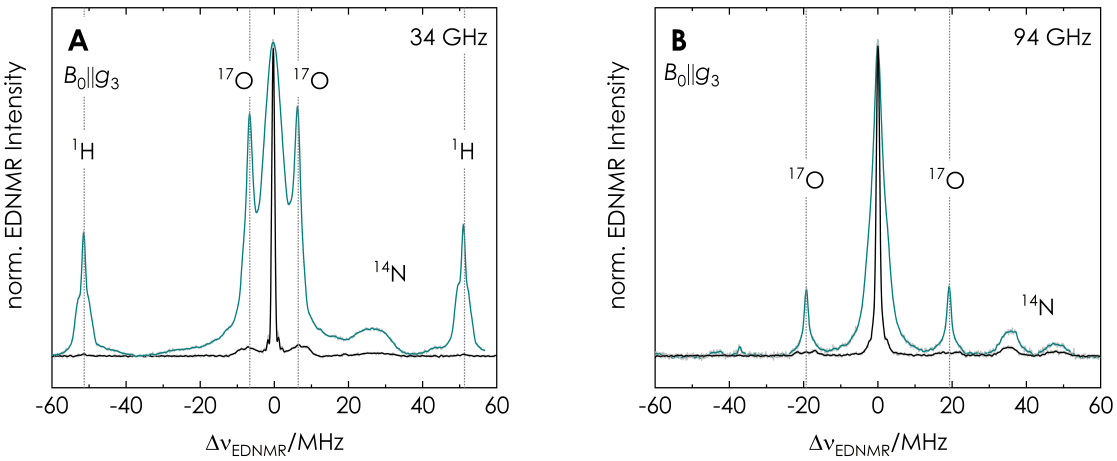

Figure 6.23: Power-dependent EDNMR spectra of $T_5^\bullet$ recorded at 34 GHz (**A**) and 94 GHz (**B**) at the $B_0 \| g_3$ position in the EPR line. Experiments with high microwave-power HTA are shown in cyan and with low mw-power are shown in black. $\omega_1/2\pi$ and acquisition times were: **A**: 3 MHz/2 h and 0.4 MHz/9 h, **B**: 2 MHz/2 h and 0.5 MHz/9 h. Spectra are normalized to the central hole. Experimental parameters: 50 K, pulse sequence: $t_{HTA} - t_d - \pi/2 - \tau - \pi - \tau -$ echo, $t_{HTA} = 20/30$ µs, $t_d = 10$ µs, $\pi/2 = 100$ ns, 2-step phase cycle, 20 shot/point, 3/5 ms SRT.

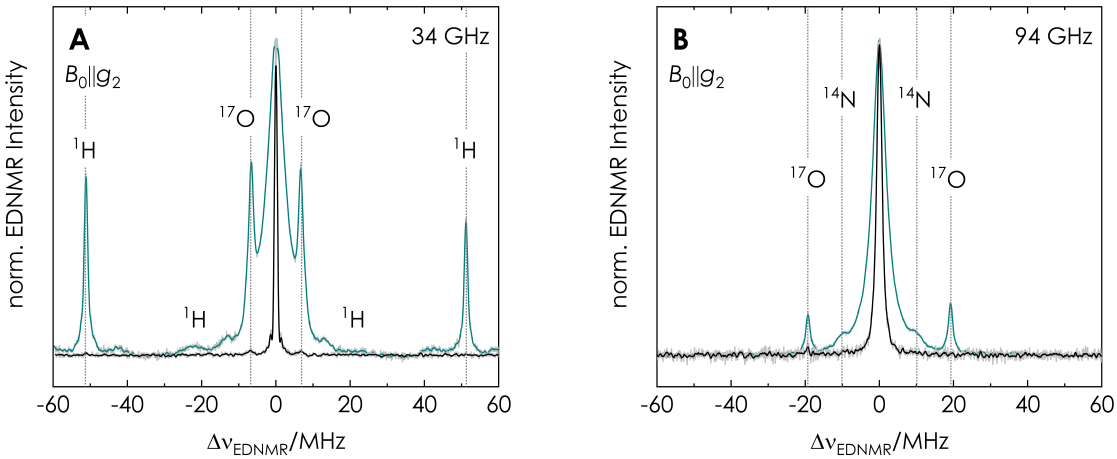

Figure 6.24: Power-dependent EDNMR spectra of $Y^{\bullet}_{356}$ recorded at 34 GHz (**A**) and 94 GHz (**B**) at the $B_0 \| g_2$ position in the EPR line. Experiments with high microwave-power HTA are shown in cyan and with low mw-power are shown in black. $\omega_1/2\pi$ and acquisition times were: **A**: 3 MHz/4.5 h and 0.4 MHz/13 h, **B**: 2.3 MHz/3 h and 0.8 MHz/9 h. Spectra are normalized to the central hole. Experimental parameters: 50 K, pulse sequence: $t_{HTA} - t_d - \pi/2 - \tau - \pi - \tau -$ echo, $t_{HTA} = 20/30$ µs, $t_d = 10$ µs, $\pi/2 = 100$ ns, 2-step phase cycle, 20 shot/point, 3/5 ms SRT.

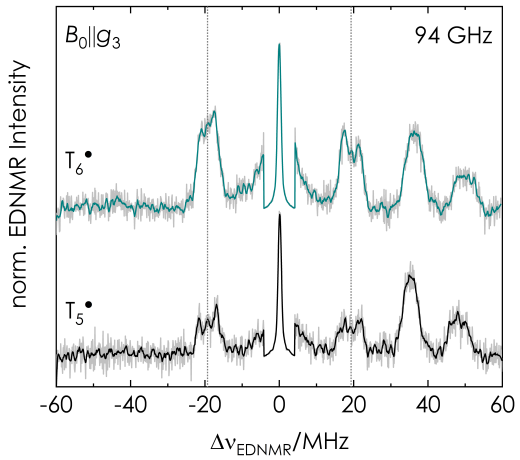

Figure 6.25: EDNMR comparison of $T^{\bullet}_6$ (cyan) and $T^{\bullet}_5$ (black) recorded at 94 GHz at the $B_0 \| g_3$ position in the EPR line. ^{17}O Larmor frequency marked by dotted grey line. Spectra are normalized and the central hole is scaled to 5 % of its original intensity. Experimental parameters: 50 K, pulse sequence: $t_{HTA} - t_d - \pi/2 - \tau - \pi - \tau -$ echo, $t_{HTA} = 20/30$ µs, $\omega_1/2\pi = 0.4$ MHz, $t_d = 10$ µs, $\pi/2 = 100$ ns, 2-step phase cycle, 20 shot/point, 3/5 ms SRT.

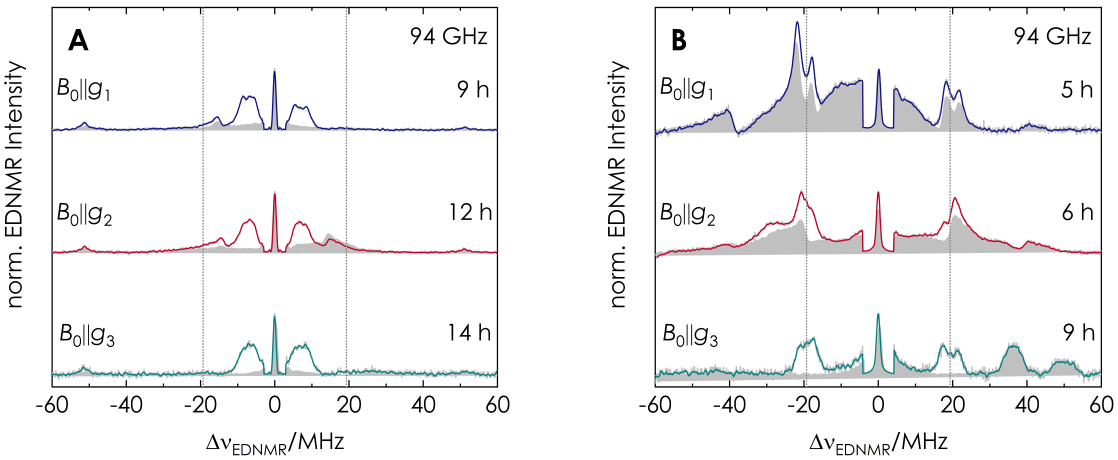

Figure 6.26: Orientation-selective EDNMR spectra of $T_6^\bullet$ recorded at 34 GHz (**A**) and 94 GHz (**B**) at the $B_0\|g_1$ (blue), $B_0\|g_2$ (red) and $B_0\|g_3$ (cyan) positions in the EPR line. Background measurements recorded with unlabelled water are shown in grey. ^{17}O Larmor frequency marked by dotted grey line. Spectra are normalized and the central hole is scaled to 5 % of its original intensity. Experimental parameters: 50 K, pulse sequence: $t_{HTA}-t_d-\pi/2-\tau-\pi-\tau-$echo, $t_{HTA}=20/30$ µs, $\omega_1/2\pi=0.35-0.5$ MHz, $t_d=10$ µs, $\pi/2=100$ ns, 2-step phase cycle, 20 shot/point, 3/5 ms SRT.

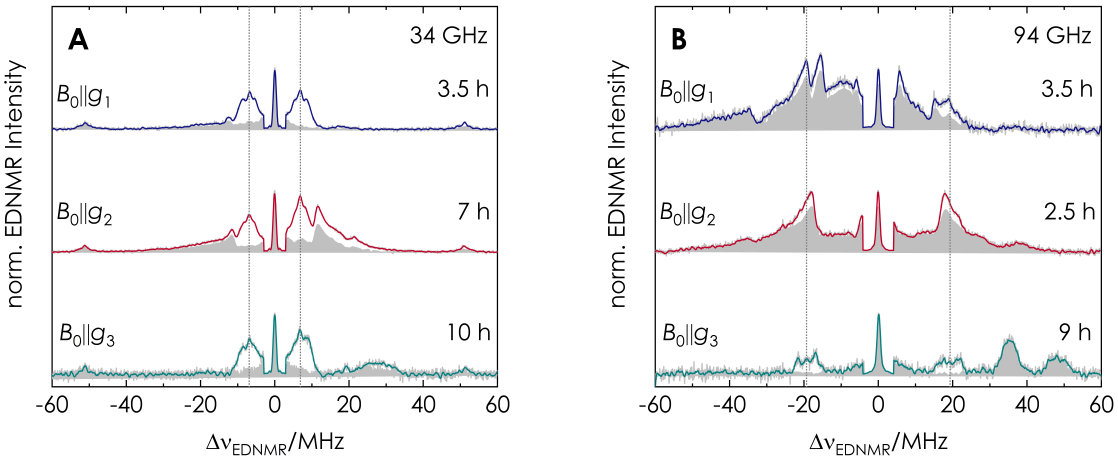

Figure 6.27: Orientation-selective EDNMR spectra of $T_5^\bullet$ recorded at 34 GHz (**A**) and 94 GHz (**B**) at the $B_0\|g_1$ (blue), $B_0\|g_2$ (red) and $B_0\|g_3$ (cyan) positions in the EPR line. Background measurements recorded with unlabelled water are shown in grey. ^{17}O Larmor frequency marked by dotted grey line. Spectra are normalized and the central hole is scaled to 5 % of its original intensity. Experimental parameters: 50 K, pulse sequence: $t_{HTA}-t_d-\pi/2-\tau-\pi-\tau-$echo, $t_{HTA}=20/30$ µs, $\omega_1/2\pi=0.35-0.5$ MHz, $t_d=10$ µs, $\pi/2=100$ ns, 2-step phase cycle, 20 shot/point, 3/5 ms SRT.

6.7.7 Experimental ENDOR spectra

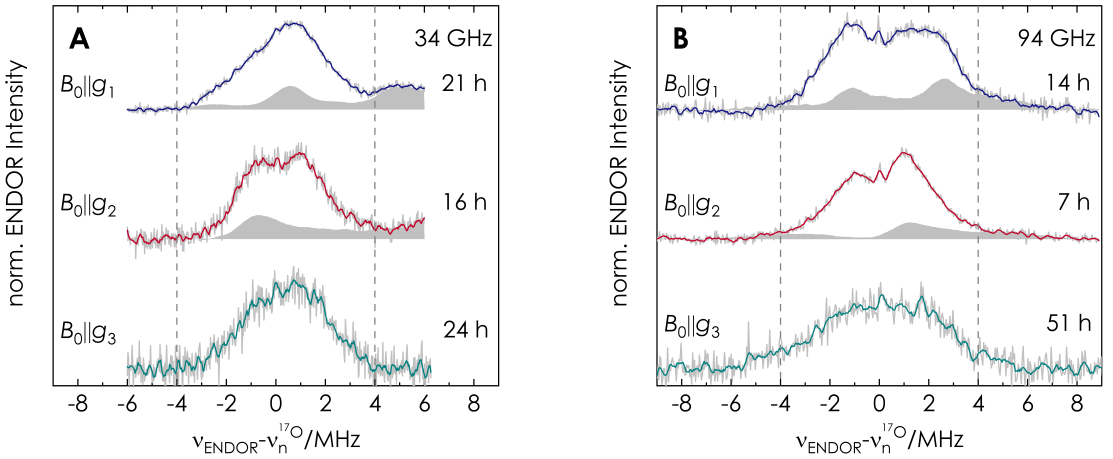

Figure 6.28: Orientation-selective Davies ENDOR spectra of $T_6^{\bullet}$ recorded at 34 GHz (**A**) and 94 GHz (**B**) at the $B_0 \| g_1$ (blue), $B_0 \| g_2$ (red) and $B_0 \| g_3$ (cyan) positions in the EPR line. Background measurements recorded with unlabelled water are shown in grey. Experimental parameters: 50 K, pulse sequence: $\pi_{sel.} - \pi(rf) - t_d - \pi/2 - \tau - \pi - \tau -$ echo, $\pi_{sel.} = 400$ ns, rf = 40 µs, $\pi/2 = 200$ ns, 30 shot/point, random rf acquisition, 3/5 ms SRT, 24 kHz rf sweep interval. Acquisition time of the spectra is written in the Figure.

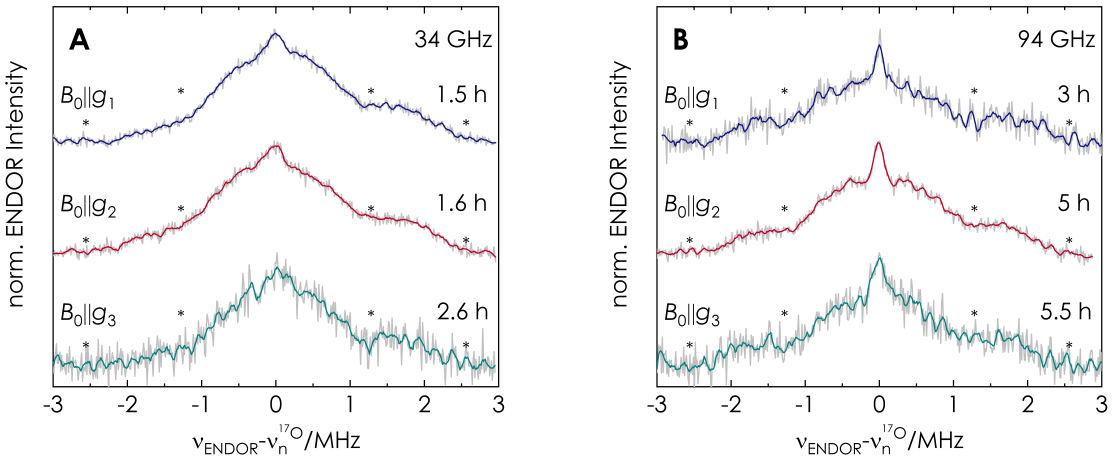

Figure 6.29: Orientation-selective Mims ENDOR spectra of $T_6^{\bullet}$ recorded at 34 GHz (**A**) and 94 GHz (**B**) at the $B_0 \| g_1$ (blue), $B_0 \| g_2$ (red) and $B_0 \| g_3$ (cyan) positions in the EPR line. Experimental parameters: 50 K, pulse sequence: $\pi/2 - \tau - \pi/2 - \pi(rf) - t_d - \pi/2 - \tau -$ echo, $\pi/2 = 6/12$ ns, $\tau = 390$ ns, rf = 40 µs, 20 shot/point, random rf acquisition, 3/5 ms SRT, 12 kHz rf sweep interval. Acquisition time of the spectra is written in the Figure.

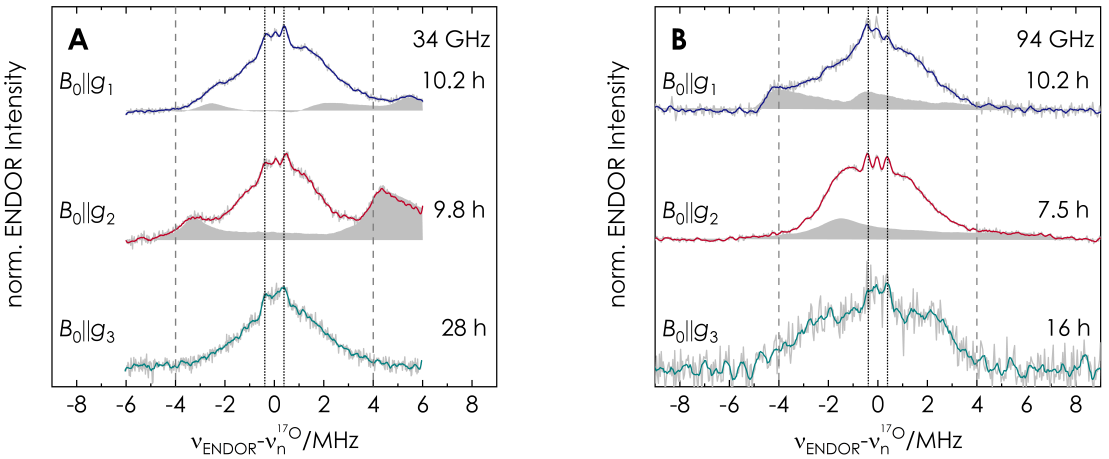

Figure 6.30: Orientation-selective Davies ENDOR spectra of $T_5^{\bullet}$ recorded at 34 GHz (**A**) and 94 GHz (**B**) at the $B_0||g_1$ (blue), $B_0||g_2$ (red) and $B_0||g_3$ (cyan) positions in the EPR line. Background measurements recorded with unlabelled water are shown in grey. Experimental parameters: 50 K, pulse sequence: $\pi_{sel.} - \pi(rf) - t_d - \pi/2 - \tau - \pi - \tau -$ echo, $\pi_{sel.} = 400$ ns, rf = 40 µs, $\pi/2 = 200$ ns, 30 shot/point, random rf acquisition, 3/5 ms SRT, 24 kHz rf sweep interval. Acquisition time of the spectra is written in the Figure.

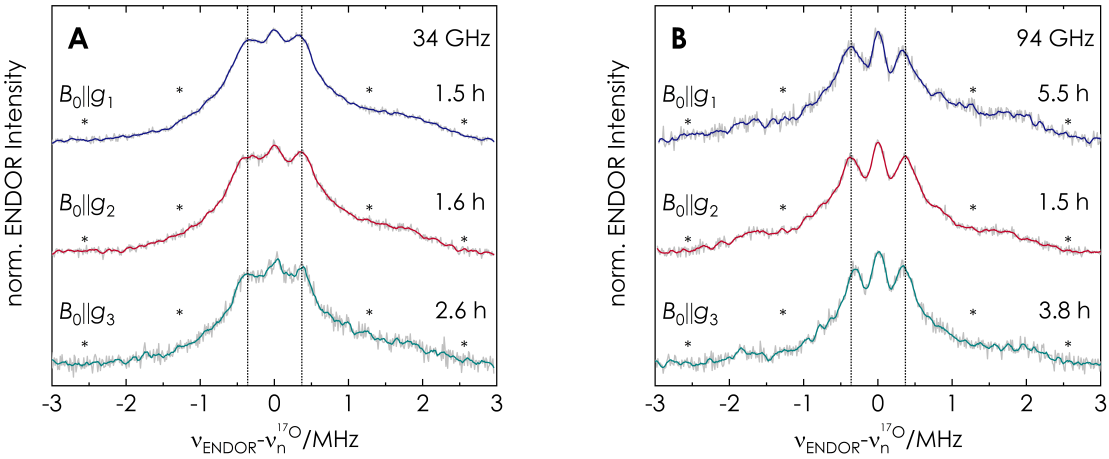

Figure 6.31: Orientation-selective Mims ENDOR spectra of $T_5^{\bullet}$ recorded at 34 GHz (**A**) and 94 GHz (**B**) at the $B_0||g_1$ (blue), $B_0||g_2$ (red) and $B_0||g_3$ (cyan) positions in the EPR line. Experimental parameters: 50 K, pulse sequence: $\pi/2 - \tau - \pi/2 - \pi(rf) - t_d - \pi/2 - \tau -$ echo, $\pi/2 = 40$ ns, $\tau = 390$ ns, rf = 40 µs, 30 shot/point, random rf acquisition, 3/5 ms SRT, 12 kHz rf sweep interval. Acquisition time of the spectra is written in the Figure.

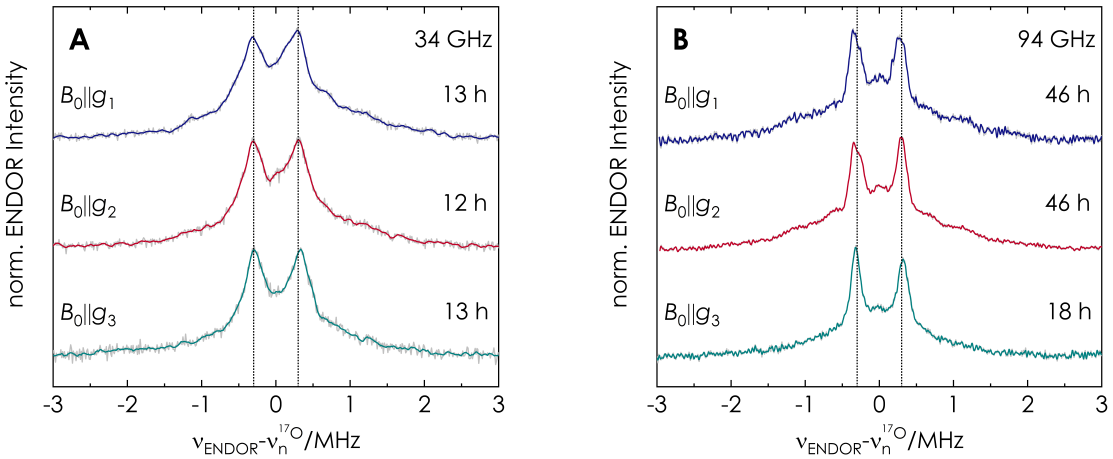

Figure 6.32: Orientation-selective Mims ENDOR spectra of $Y^{\bullet}_{356}$ recorded at 34 GHz (**A**) and 94 GHz (**B**) at the $B_0 \| g_1$ (blue), $B_0 \| g_2$ (red) and $B_0 \| g_3$ (cyan) positions in the EPR line. Experimental parameters: 50 K, pulse sequence: $\pi/2 - \tau - \pi/2 - \pi(\mathrm{rf}) - t_d - \pi/2 - \tau -$ echo, $\pi/2 = 40$ ns, $\tau = 390$ ns, rf $= 40$ µs, 30 shot/point, random rf acquisition, 3/5 ms SRT, 12/6 kHz rf sweep interval. Acquisition time of the spectra is written in the Figure.

6.7.8 Relaxation properties

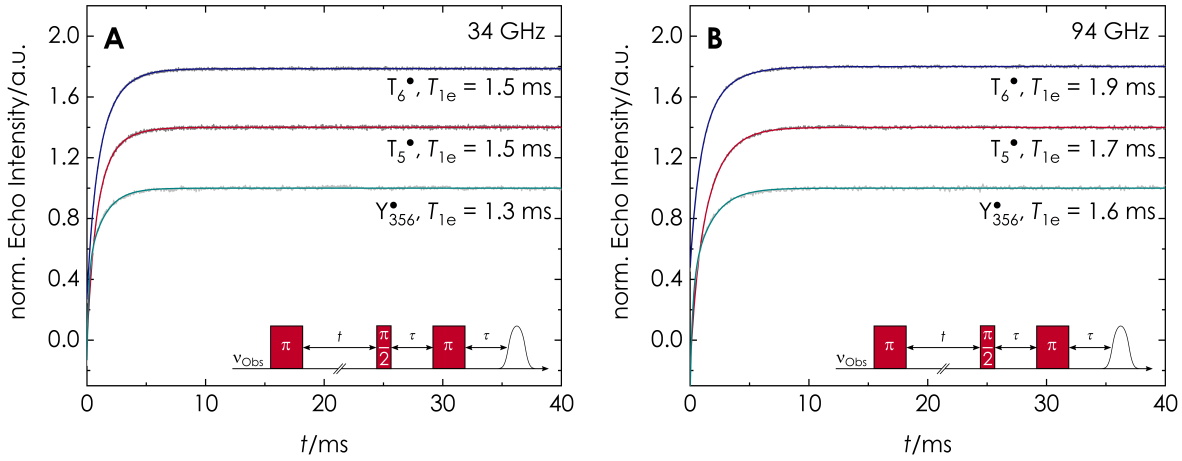

Figure 6.33: Inversion recovery measurements (grey) with bi-exponential fits (color) of $T_6^\bullet$ (blue), $T_5^\bullet$ (red) and $Y_{356}^\bullet$ (cyan) recorded at 34 GHz (**A**) and 94 GHz (**B**) at the $B_0 \| g_2$ positions in the EPR line. Experimental parameters: 50 K, pulse sequence: $\pi - t - \pi/2 - \tau - \pi - \tau -$ echo, $\pi/2 = 6/12$ ns, 100 shot/point.

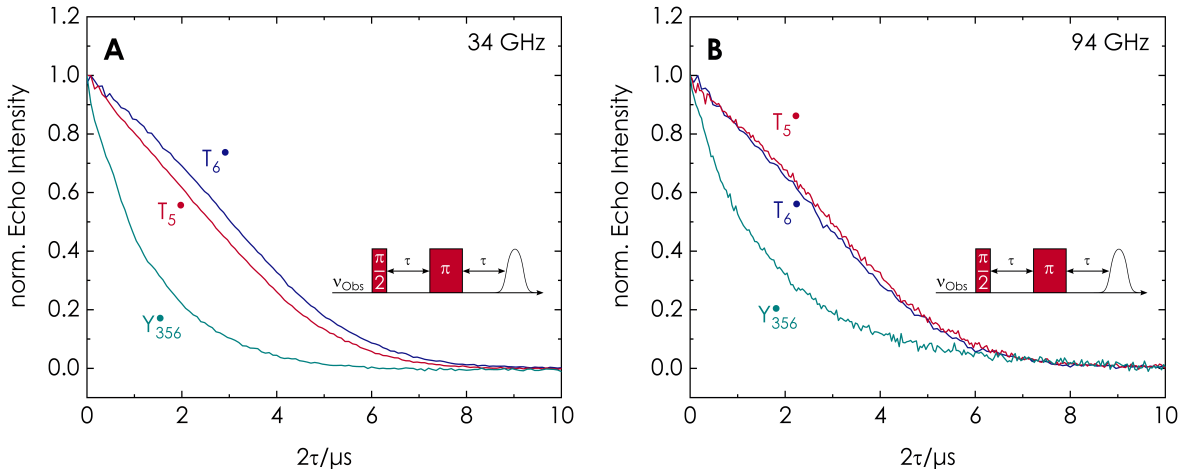

Figure 6.34: Phase memory time measurements of $T_6^\bullet$ (blue), $T_5^\bullet$ (red) and $Y_{356}^\bullet$ (cyan) recorded at 34 GHz (**A**) and 94 GHz (**B**) at the $B_0 \| g_2$ positions in the EPR line. Experimental parameters: 50 K, pulse sequence: $\pi/2 - \tau - \pi - \tau -$ echo, $\pi/2 = 6/12$ ns, 100 shot/point.

6.7.9 Nuclear quadrupole broadening

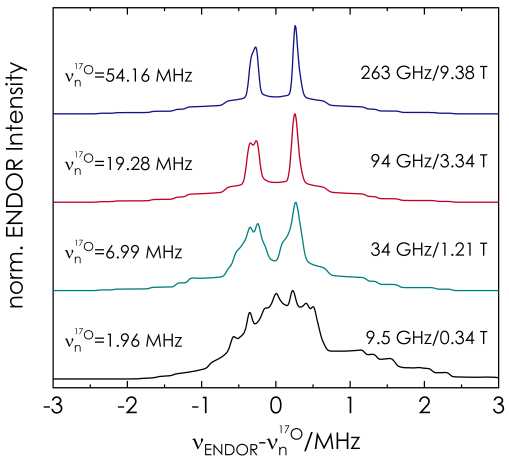

Figure 6.35: Simulation of the full ENDOR spectrum expected for an electron spin $S = 1/2$ with $g = g_e = 2.0023$ coupled to a nuclear spin $I = 5/2$ with $\boldsymbol{A} = [0.5; 0.5; 0.7]$ MHz and $\boldsymbol{P} = [-0.02; -0.32; 0.34]$ MHz.

6.7.10 DFT models

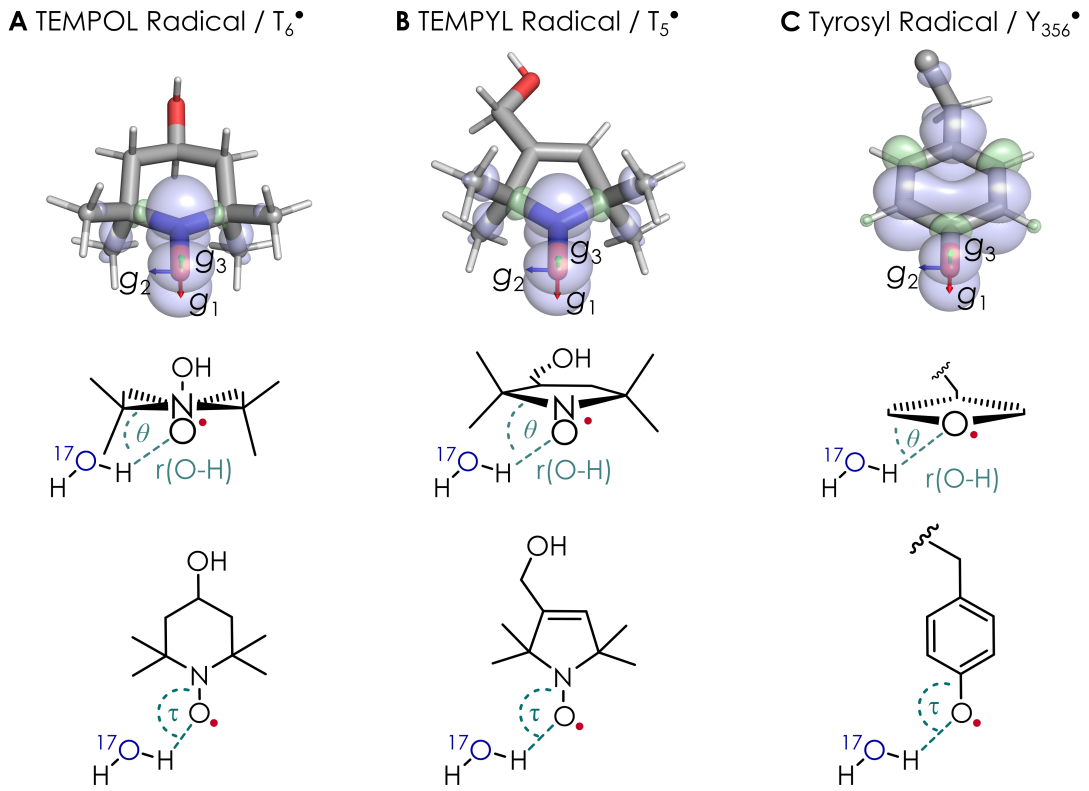

Figure 6.36: Overview of the three oxygen-centered radicals $T^{\bullet}_{6}$ (**A**), $T^{\bullet}_{5}$ (**B**) and $Y^{\bullet}_{356}$ (**C**) investigated in this study. Top: DFT optimized structures and spin density of the radicals. Positive (light blue) and negative (light green) spin density at the ±0.002 a.u. level. Orientation of the g-tensor within the molecular frame is marked by arrows (red: g_1, blue: g_2, green: g_3). Bottom: Lewis structures with a water molecule coordinated at a distance $r(O_{PC}\cdots H_{H_2O})$ with dihedral angle θ(C-N(C)-$O_{PC}\cdots H_{H_2O}$) and angle τ(N(C)-$O_{PC}\cdots H_{H_2O}$) (cyan).

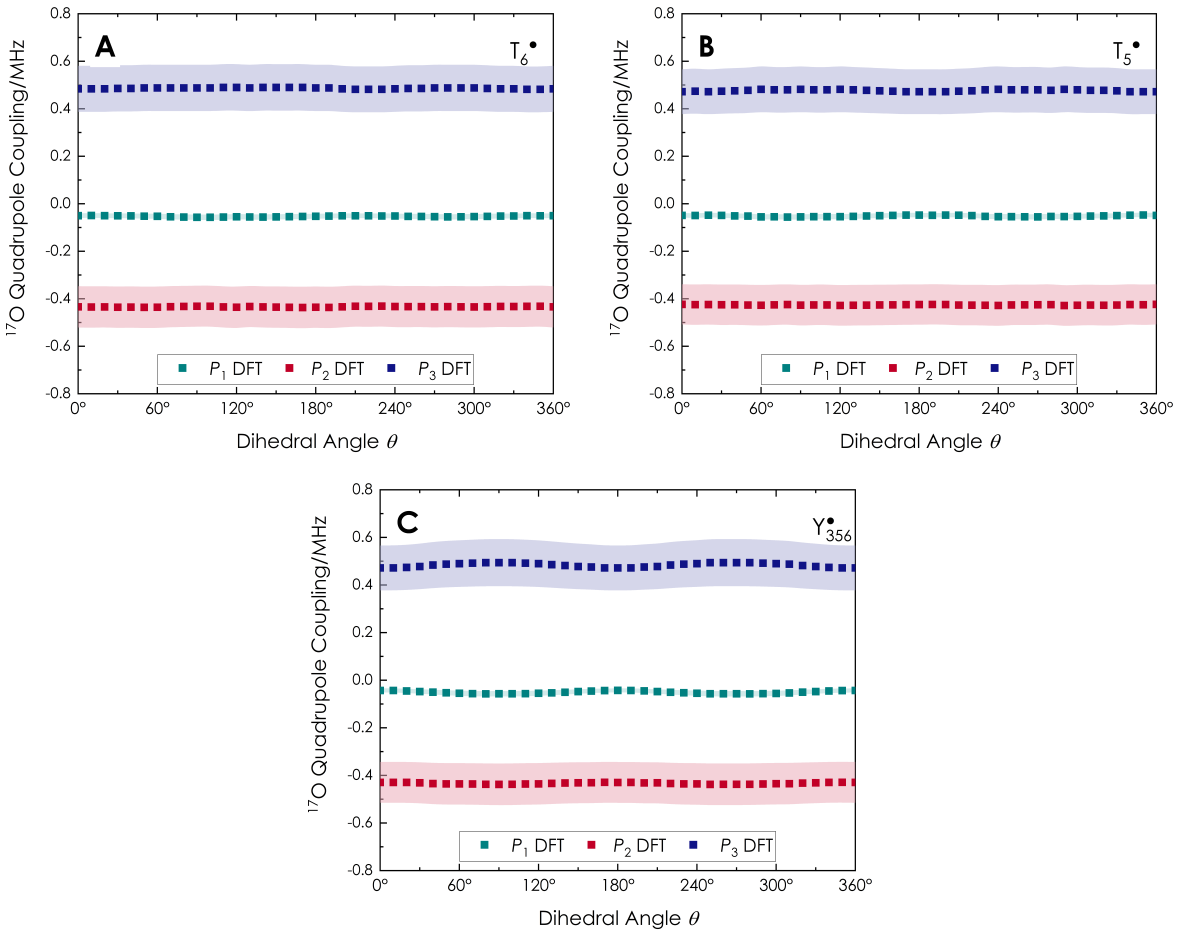

Figure 6.37: DFT calculated nuclear quadrupole tensor components of the individual radical models of $T_6^\bullet$ (**A**), $T_5^\bullet$ (**B**) and $Y_{356}^\bullet$ (**C**). The values change only slightly as a function of θ. 20 % confidence interval of DFT calculated coupling constants are marked by colored areas.

6.7.11 Molecular dynamics simulations

All MD simulations were performed with *Gromacs* 2018.4.[167] For water molecules, the default `tip3p` model was used as included in the *Gromacs* installation. Topologies for glycerol and the $T_6^\bullet$ and $T_5^\bullet$ radicals were constructed in a semi-automatic pipeline:
The geometries of the respective molecules were first optimized by DFT (*Orca* 4.2.1 using B3LYP/def2-TZVPP).[73] For the optimized geometry, a Hartee-Fock calculation was performed for the subsequent determination of atomic charges by RESP fitting using the *Multifn* 3.6 program[168,169], following the recommendations for obtaining parameters compatible to the amber force field.[170] For this purpose the results of the quantum chemical calculations were converted using the `orca_2mkl` module in combination with the `-molden` flag, the result of which can be read-in to *Multiwfn*. Identical charges on atoms related by molecular symmetry were enforced directly in the RESP fitting procedure. The final charges used for glycerol and the radicals are summarized in Figures 6.38-6.40. The optimized structures and atomic charges were combined in `*.mol2` files, which were used as input to *acpype*[171] for the construction of initial topology files, using the `c user` and `a amber` flags.
Following this, the parameters (bond, angles, dihedrals) related to the radical moiety were adjusted manually using literature values specifically developed for nitroxide radicals.[161] The dihedral parameters given in the latter reference as periodic-type format were translated to *Ryckaert-Bellemans* coefficients for consistency with the *acpype* output.
At this stage, two lone-pairs were also included at the nitroxide oxygen atom following the literature approach. Charges for the nitroxide oxygen atoms were evenly distributed to the oxygen atom itself and its two lone-pairs, in analogy to the literature approach. Notably, we found the introduction of an addition dihedral potential (which is explicitly set to 0 in 7) to be required to prevent the undesirable and physically nonsensical rotation of the lone-pairs around the nitroxide N-O bond for certain modes of water coordination.
The $T_5^\bullet$ radical features a double bond within the 5-membered ring, for which the amber force field is not explicitly parametrized. We chose to treat this group with the parameters used in the amber force field for the 5-membered ring in the tryptophan sidechain, which should behave very similar. In cases where definitions for bonded parameters were lacking in the original amber forcefield implementation, we resorted to default values (particularly for the dihedral angles) by treating the sp^2 carbons like the CA atom type intended for aromatic carbon atoms. For the improper dihedrals we used values given for a similar situation in [161]. We note, that very similar parameters result if the `-a GAFF` option of *acpype* is used. An overview of relevant bonded parameters is given in Table 6.5.
In order to test the topologies obtained in this fashion, we performed energy minimization of water complexes of the $T_5^\bullet$ and $T_6^\bullet$ radicals, analogous to [161]. The different steric

demand of the methyl groups resulting from the variation of the ring atom arrangements in the two radicals (see Figure 6.41) is reflected by the optimized hydrogen-bond lengths and bond angles summarized in Table 6.4.

For the MD simulations, the respective radical was placed in a pre-equilibrated solvent box containing approximately 20 % glycerol (v/v) in water (78 glycerol molecules, 15017 water molecules), reflecting the experimental conditions. Notably, the concentration of the radical within the simulation box is ca. 1 mM and thus five times higher than in the experiment. However, further increase of the box size is unfavorable in terms of computational demand. Since only a single radical is present, the simulation implicitly disregards any possible radical-radical interactions.

The complete simulation box was equilibrated for 500 ps in the nvt ensemble and 1000 ps in the npt ensemble, after which a stable density was obtained, close to the expected value (ca. 0.99 g cm^{-3}). Due to the fast fluctuation of the nitroxide oxygen lone-pairs, simulation time steps of 0.2 fs were used throughout. Subsequently two different paths were followed: Firstly, the simulation was allowed to develop for 2000 ps at a temperature of 300 K to assess the dynamic behavior at ambient temperature. Secondly, a total of 100 annealing runs were performed for each radical using different initial particle velocities (by supplying unique random seeds to the velocity generation).

Each run consisted of 3 phases. First, the system was allowed to reach a pseudo-random state based on its initial velocities, which consequently differs between the various runs. To determine the required length of this stage, the system RMDS was used, which indicated complete loss of any structural auto-correlation within ca. 1000 ps. Hence, for the first phase the system was allowed to develop for 1000 ps. Following this, the system temperature was decreased linearly over 800 ps to the experimental value of 50 K. Finally, the system was allowed to settle for a further 200 ps at the target temperature to allow for a complete settling of the structure.

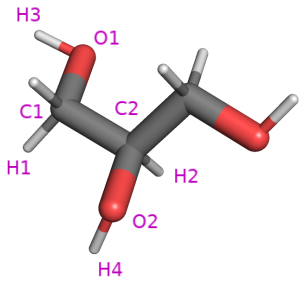

Atom	Atom type	Partial charge/e
C1	CT	0.082325
C2	CT	0.392255
O1	OH	-0.709847
O2	OH	-0.733242
H1	HO	0.051033
H2	HO	0.050074
H3	H1	0.449474

Figure 6.38: Labeling scheme and atomic charges for glycerol.

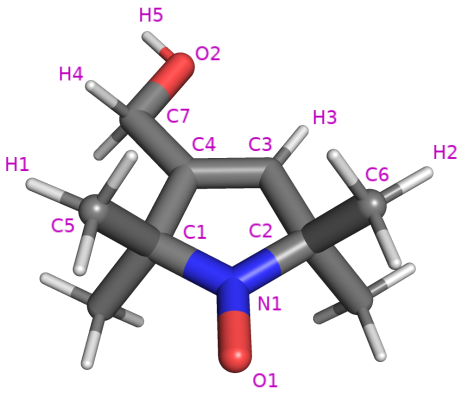

Atom	Atom type	Partial charge/e
C1	CT	0.385580
C2	CT	0.511891
C3	CW[a]	-0.447150
C4	C*[a]	-0.084100
C5	CT	-0.365870
C6	CT	-0.372210
C7	CT	0.392070
N1	NN[b]	0.060150
O1	NO[b]	-0.124980[c]
O2	OH	-0.695951
H1	NH[b]	0.096160
H2	NH[b]	0.093130
H3	H4[a]	0.228990
H4	H1	-0.031570
H5	HO	0.427060

Figure 6.39: Labeling scheme and atomic charges for $T_5^\bullet$. [a]These atom types are used in the *amber* force field for the 5-membered ring in the tryptophan side chain. [b]These atom types were introduced in [161] for nitroxide radicals. [c]Additional charges of -0.125 e were used on the lone-pairs, thus the total charge of the oxygen atom is -0.374980 e.

For the calculation of ^{17}O interaction parameters using DFT, only the close environment of the nitroxide oxygen atom was included, as for more remote molecules, no significant hyperfine interactions are expected. Thus, as a first shell the water molecules closest to the oxygen atom were included. In cases, where glycerol was among the closest three neighboring molecules, the molecule was also included in the calculation but not considered for the calculation of hyperfine couplings. In these cases, only two first-shell water neighbors are included for the calculation of interaction parameters. Importantly, to obtain meaningful results for the ^{17}O electric field gradients, which in turn determine the quadrupole interaction, the nearest neighbors of the first-shell water molecules were included as well. Thus, the precise number and types of molecules differs between the various frames in the trajectories and between the individual annealing runs. For efficient handling of these quite large data sets, a Python script was used for automatic creation and analysis of the DFT calculations.

Bond/Angle	$T_5^\bullet$ complex	$T_6^\bullet$ complex
NO-HW	1.859/1.860 Å	1.957/1.920 Å
NO-OW	2.817/2.811 Å	2.911/2.872 Å
NN-NO-HW	123.4/121.7°	130.4/127.9°

Table 6.4: Optimized parameters (from molecular mechanics parametrization) of $T_5^\bullet$ and $T_6^\bullet$ complexes with two water molecules, see Fig. 6.41.

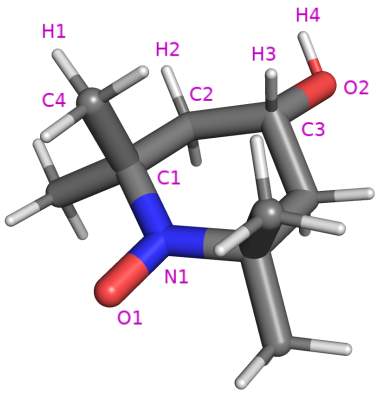

Atom	Atom type	Partial charge/e
C1	CT	0.568924
C2	CT	-0.663448
C3	CT	0.576191
C4	CT	-0.404915
N1	NN[a]	-0.084919
O1	NO[a]	-0.104956[b]
O2	OH	-0.617854
H1	NH[a]	0.102004
H2	HC	0.176154
H3	H1	-0.032712
H4	HO	0.354295

Figure 6.40: Labeling scheme and atomic charges for $T_6^\bullet$. [a]These atom types were introduced in [161] for nitroxide radicals. [b]Additional charges of -0.105 e were used on the lone-pairs, thus the total charge of the oxygen atom is -0.314956 e.

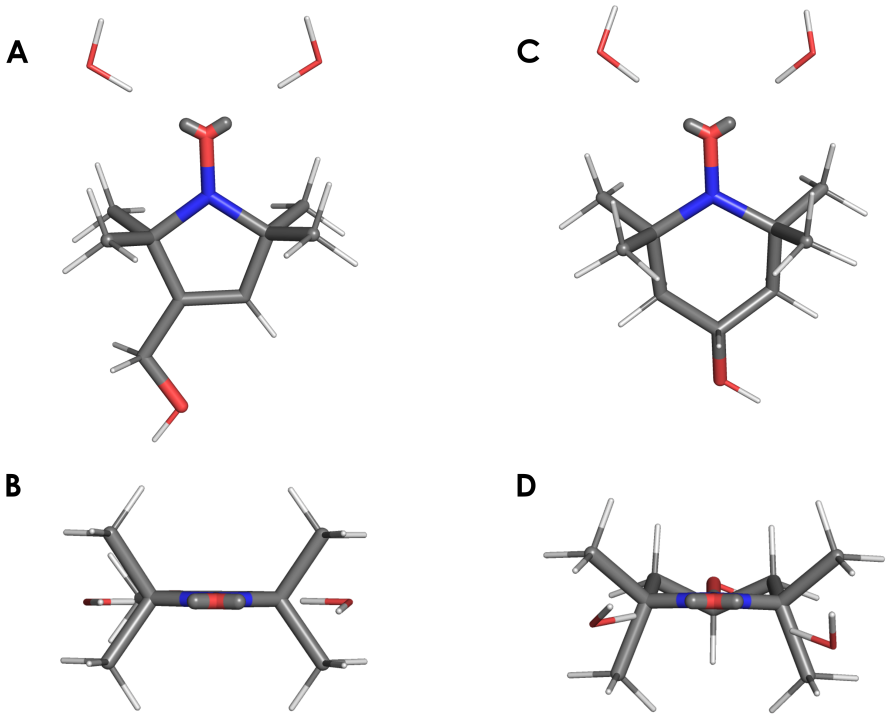

Figure 6.41: Optimized structures (from molecular mechanics parametrization) of $T_5^\bullet$ (**A**/**B**) and $T_6^\bullet$ (**C**/**D**) complexes with two water molecules.

Table 6.5: Bond parameters used for the $T_5^{\bullet}$ MD simulations.

bond parameters		
bond	involved atom types	amber bond type used
C1-C4	CT-C*	CT-C*
C2-C3	CT-CW	CT-C*
C3-C4	CW-C*	CW-C*
C3-H3	CW-H4	CW-H4
C4-C7	C*-CT	CT-C*
angle parameters		
angle	involved atom types	amber angle type used
N1-C1-C4	NN-CT-C*	NN-CT-CAa
N1-C2-C3	NN-CT-CW	NN-CT-CAa
C1-C4-C3	CT-C*-CW	CT-CA-CA
C1-C4-C7	CT-C*-CT	CT-CA-CA
C3-C4-C7	CT-C*-CW	CT-CA-CA
C2-C3-C4	CT-CW-C*	CT-CA-CA
C2-C3-C3	CT-CW-H4	C*-CW-H4
C4-C3-H3	C*-CW-H4	C*-CW-H4
C4-C7-O2	C*-CT-OH	CT-CT-OH
C4-C7-H4	C*-CT-H1	CT-CT-H1
dihedral parameters		
dihedral	involved atom types	amber dihedral type used
O1-N1-C1-C4	NO-NN-CT-C*	NO-NN-CT-CT[(a)]
O1-N1-C2-C3	NO-NN-CT-CW	NO-NN-CT-CT[(a)]
N1-C1-C4-C3	NN-CT-C*-CW	X-CA-CT-X[(b)]
N1-C1-C4-C7	NN-CT-C*-CT	X-CA-CT-X[(b)]
N1-C2-C3-C4	NN-CT-CW-C*	X-CA-CT-X[(b)]
N1-C2-C3-H3	NN-CT-CW-H4	X-CA-CT-X[(b)]
H1-C5-C1-C4	NH-CT-CT-C*	NH-CT-CT-CT[(a)]
H2-C6-C2-C3	NH-CT-CT-CW	NH-CT-CT-CT[(a)]
C5-C1-C4-C3	CT-CT-C*-CW	X-CA-CT-X[(b)]
C5-C1-C4-C7	CT-CT-C*-CT	X-CA-CT-X[(b)]
C6-C2-C3-C4	CT-CT-CW-C*	X-CA-CT-X[(b)]
C6-C2-C3-H3	CT-CT-CW-H4	X-CA-CT-X[(b)]
C1-C4-C3-C2	CT-C*-CW-CT	NA-C*-CW-CT
C1-C4-C3-H3	CT-C*-CW-H4	NA-C*-CW-H4
C2-C3-C4-C7	CT-CW-C*-CT	NA-C*-CW-CT
C7-C4-C3-H3	CT-C*-CW-H4	NA-C*-CW-H4
C3-C4-C7-O2	CW-C*-CT-OH	X-CA-CT-X[(b)]
C1-C4-C7-O2	CT-C*-CT-OH	X-CA-CT-X[(b)]
C3-C4-C7-H4	CW-C*-CT-H1	X-CA-CT-X[(b)]
C1-C4-C7-H4	CT-C*-CT-H1	X-CA-CT-X[(b)]
C4-C7-O2-H5	C*-CT-OH-HO	CT-CT-OH-HO
LP1-O1-N1-C1	LP-NO-NN-CT	No. of paths: 2, V·n (kcal mol^{-1}): 12.0
LP2-O1-N1-C1	LP-NO-NN-CT	Φ_0: 180°, n=2
improper dihedral parameters		
improper	involved atom types	amber improper type used
C4-C2-C3-H3	C*-CT-CW-H4	CA-CA-CA-Cla
C3-C1-C4-C7	CW-CT-C*-CT	CA-CA-CA-Cla

[(a)] type taken from [161].
[(b)] amber default, which is a zero potential.

7 Conclusion and outlook

Three challenges have previously discouraged the use of the ^{17}O hyperfine spectroscopy to study water binding to organic radicals: Firstly, the low gyromagnetic ratio of ^{17}O leading to a small sensitivity; secondly, it's high nuclear spin leading to quadrupole broadening; thirdly, the hydrogen-bond coordination of water molecules to oxygen-centered organic radicals, which leads to PC$\cdots^{17}$O distances $\gtrsim 3$ Å. The experiments, theoretical models and spectral simulations of this thesis have shown, that the method can be used effectively for hydrogen-bound water molecules despite these challenges. They will be addressed individually in the following section. The relationship between ^{17}O hyperfine couplings and coordination geometry will be discussed. Finally, ongoing work and further applications will be mentioned.

Sensitivity and Resolution The low sensitivity the ^{17}O nucleus leads to generally long acquisition times to produce interpretable hyperfine spectra. The experiments show that spectroscopy methods employing broadband excitation, i.e. HYSCORE and Mims ENDOR, generally perform better than the selective excitation methods EDNMR and Davies ENDOR due to the larger amount of spins contributing to the spectra. The same argument also explains, why hf experiments generally show larger sensitivity at lower field, where resonances are less spread out due to g-tensor anisotropy.

HYSCORE is particularly useful for the detection of ^{17}O since it separates hyperfine and quadrupole coupling in different spectral dimensions. The additional separation of strongly and weakly coupled nuclei is of great value for nitroxide radicals, as ^{17}O resonances are easily distinguished from the intense nitrogen resonances. The intrinsic resolution of the HYSCORE experiment is well suited for hyperfine couplings larger than 1 MHz but prevents the distinction of small hyperfine coulings (< 1 MHz). The experiment is most sensitive at 34 GHz due to the smaller orientation-selectivity and the increased modulation depth for the specific ^{17}O hyperfine couplings in the range of $1 - 8$ MHz.

EDNMR experiments performed with powerful (large ω_1) high-turning angle pulses can

show the presence of ^{17}O signals with high sensitivity while lower powered HTA pulses can establish the presence of large (>1 MHz) ^{17}O hyperfine couplings, albeit with significantly reduced sensitivity. Detailed hyperfine and quadrupole coupling parameters, especially for small (< 1 MHz) hyperfine couplings, can however not be distinguished from the experiments. This is due to the intrinsically low resolution and also because the EDNMR transition probabilities are zero for canonical the hyperfine and quadrupole tensor orientations that contain the most valuable information. Additionally, strong overlap of nitrogen resonances hinder the analysis of ^{17}O signals in the case of nitroxide radicals. To acquire pure ^{17}O EDNMR spectra, experiments have to be performed at the $B_0 \| g_3$ position, which however has the lowest overall signal intensity. The experiment is best performed at 94 GHz to avoid overlap of ^{17}O signals with the central blindspot.

The selective excitation of Davies ENDOR leads to relatively low sensitivity and long acquisition times. Small hyperfine couplings are difficult to detect due to the spectral hole of the preparation pulse. The Mims ENDOR experiment, on the other hand, is the only experiment suited to resolve small ^{17}O hyperfine couplings (< 1 MHz). ^{17}O Mims ENDOR spectra are less affected by the Mims blindspot function than comparable spectra of $I = 1/2$ nuclei, due to the presence of considerable quadrupole coupling. Apart from the spectral blindspot function, ENDOR spectra contain the full hyperfine and quadrupole tensor information. The specific *fingerprint* signature of in-plane water molecules can be detected with Mims ENDOR at all three investigated frequencies (see Fig. 7.1). ^{17}O ENDOR experiments of nitroxide radicals, like EDNMR, suffer from the underlying nitrogen signals, which need to be identified by background measurements. Measurements at the $B_0 \| g_3$ position can and should be made to avoid the overlap but suffer from the poor signal intensity.

The highest concentration sensitivity so far was achieved by 94 GHz Mims ENDOR, with which a hydrogen-bound water molecule was detected around a sample of $Y^{\bullet}_{356}$ with a concentration of $\sim$ 1µM.[16] In the future, the sensitivity of Mims ENDOR experiments may be increased by the application of broadband excitation pulses.[11,172] This could especially benefit experiments at high field, where arbitrary waveform generator technology is now available. The same technology might be used to increase performance of EDNMR experiments by performing the initial HTA as Gaussian pulse.[8,173,174]

Quadrupole broadening The high nuclear spin of ^{17}O may lead to significant quadrupole broadening effects of the detected signals. The central nuclear transition ($m_I(^{17}\mathrm{O}) = +1/2 \rightarrow -1/2$) is affected when the difference between nuclear Larmor frequency and hyperfine as well as quadrupole coupling is small. Mims ENDOR experiments in this work showed that quadrupole broadening affects the spectra at EPR frequencies of 34 and 94 GHz. They also showed that the effect can be significantly reduced at the higher frequencies, especially

at 263 GHz where signals with linewidths $\lesssim$ 0.1 MHz can be detected (see Fig. 7.1). The effect can be reproduced by spectral simulations, which do not use the high-field approximation but consider the full hyperfine and quadrupole coupling Hamiltonian in a tensor diagonalization approach. Experiments and simulations show that it is the combined effect of reduced nuclear quadrupole broadening and increased orientation selectivity. The narrow ^{17}O signals recorded with 263 GHz Mims ENDOR experiments can be used to resolve the binding of one versus two water molecules, which was an open question prior to this work.[26]

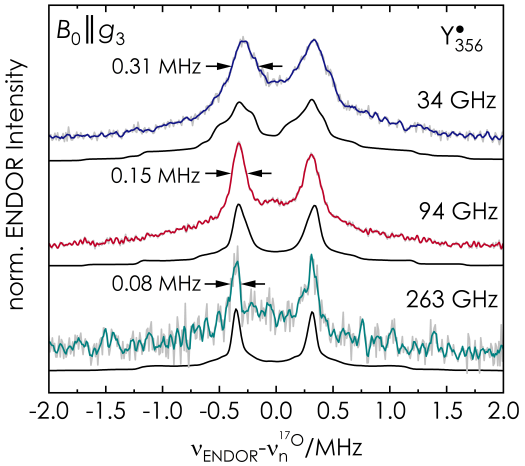

Figure 7.1: Mims ENDOR experiments of $Y^{\bullet}_{356}$ at 34 (blue), 94 (red) and 263 GHz (cyan). Simulations are shown in black. The effect of narrowing linewidths at higher magnetic fields is indicated by arrows and reproduced by the simulations.

PC···O_{H_2O} distance The hydrogen-bond coordination of water to organic radicals leads to PC-O distances of $\gtrsim$ 3 Å. Due to the small gyromagnetic ratio of ^{17}O, this would result in dipolar couplings of $\lesssim$ 0.2 MHz, if the system could be considered in the point-dipole approximation. Such couplings would be hard to detect due to the additional quadrupole broadening (see. Fig. 7.2, A). The experiments of this thesis have shown that hydrogen-bond coordination leads to spin density transfer onto the ^{17}O nucleus, sufficient to produce isotropic couplings that are readily resolvable with Mims ENDOR spectroscopy (see Fig. 7.2, B).

Recent ^{19}F Mims ENDOR experiments performed in our group have shown that much smaller hyperfine couplings in the range of $\sim$ 0.02 MHz can be resolved, corresponding to PC···F distances of $\sim$ 15 Å.[14] While such long distances are not feasible with ^{17}O due to it's small gyromagnetic ratio, the resolution of hyperfine couplings in the kHz range would allow the detection of second sphere water molecules at distances of $\sim$ 5 Å. This is potentially very interesting for applications in RNR, where hydrogen bond networks might be of key importance for the PCET mechanism.[131,133] Mims ENDOR resolution of small

couplings is mainly limited by the choice of τ-value, which is in turn limited by the phase memory time T_m.[14,15,61] Therefore methods to prolong the T_m can be employed to increase the detectable PC···O_{H_2O} distance. These methods have been developed for the PELDOR technique and usually rely on the deuteration of the solvent and cryoprotectant[175–177] as well as the entire biomolecule[178,179]. The deuteration of $H_2{}^{17}O$ is rather problematic and therefore deuteration of the radical itself might be the more reasonable approach.[177] Deuterated nitroxide radicals are available and tyrosyl residues Y_{122}[121,122] and Y_{356}[26] have been deuterated in the RNR enzyme, making them interesting candidates for future ^{17}O Mims ENDOR studies.

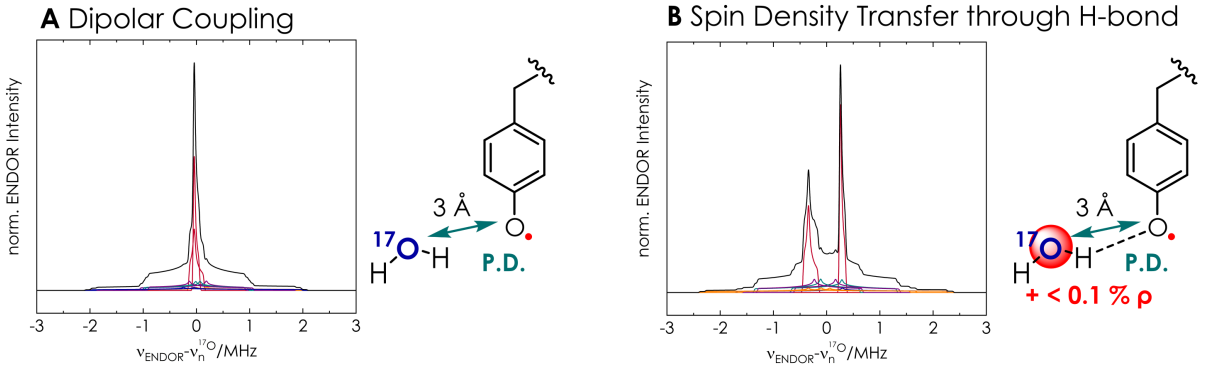

Figure 7.2: Effect of spin density transfer through hydrogen-bond interaction. **A**: Assumption of pure dipolar coupling over 3 Å results in no discernible hyperfine coupling structure. **B**: Hydrogen-bonding leads to spin density transfer onto the ^{17}O nucleus, resulting in detectable isotropic coupling.

Relationship between ^{17}O hyperfine coupling and coordination geometry Small DFT models of organic-radical water complexes have shown the strong dependence of ^{17}O hyperfine couplings on the coordination geometry around tyrosyl and nitroxide radicals. The asymmetric spin density distribution around oxygen-centered organic radicals is mainly responsible for this effect. Coordination of water molecules in the ring-plane of the radicals, i.e. with the ideal hydrogen-bond geometry to the lone pairs of oxygen, leads to small, isotropic hyperfine couplings. Perpendicular coordination, on the other hand, leads to large, anisotropic hyperfine couplings, since the majority of the spin density is located here and the effective distance to the ^{17}O nucleus is shorter.

The most sensitive resonance position within the EPR spectra is $B_0 \| g_3$, as g_3 is aligned directly perpendicular to the ring plane for such radicals, in line with the spin density. Additionally, the largest ^{17}O hyperfine coupling component is also aligned in this direction. This allows for a clear distinction between the two coordination modes from hf spectra, even in bulk water with a lot of structural variety. In the case of specific coordination in protein environments, the sensitivity of the ^{17}O couplings can be used to determine dihedral angles with approximately 20° accuracy.

Perspective applications Tyrosyl radicals are the most common radicals encountered in enzymatic systems[156,157] and water molecules around essential tyrosine resides have been crystallographically identified. Photosystem II houses two essential tyrosyl radicals, Y_D and Y_Z, with interesting water molecules, which are part of proton-coupled electron transfer reactions.[38,41] Both of them could be investigated with ^{17}O hyperfine spectroscopy. Another interesting tyrosyl intermediate in PCET reactions is Y_8 in the blue light using flavine adenine dinucleotide (BLUF) domaine, present in many bacterial photoreceptors.[116] Water has not been established around this intermediate but ^{17}O hf spectroscopy could be used to do so.

Derivatives of the nitroxide radicals investigated in this work are routinely used as spin probes in diamagnetic biomolecules. They are used for inter- and intramolecular distance measurements or as mobility probes.[151–153] ^{17}O hyperfine spectroscopy offers a new possibility to use them for the detection of structured water domains.

Beyond these, different organic radicals, such as DOPA, cysteine or tryptophane radicals exist in biomolecular machines.[156] All of them could be investigated with the established ^{17}O hyperfine spectroscopy methods.

The use of ^{17}O hyperfine spectroscopy for organic radicals can also be expanded beyond water molecules. Our group, in collaboration with the group of Prof. Tittmann, has recently incorporated ^{17}O-labelled tyrosines into the α-subunit of ribonucleotide reductase.[16] This was done to detect a direct hydrogen bond between the $Y^{\bullet}_{356}$ radical in β and the ^{17}O-Y_{731} residue with ^{17}O Mims ENDOR spectroscopy. Our experiments so far could not detect ^{17}O signatures but we hope to expand the applications in the future.

To increase the information content gain from ^{17}O signals, advanced hyperfine spectroscopy methods may be applied in the future. Especially spectroscopy experiments, which allow the detection of correlation frequencies between nuclei coupled to the same electron spin, are of particular interest. Such methods include multi-dimensional EDNMR,[180] THYSCOS,[181] DONUT-HYSCORE[182] or TRIPLE.[183] A specific question for such an experiment is the involvement of the arginine residue R_{411} in water binding to $Y^{\bullet}_{356}$ in RNR. Efforts to perform ^{17}O-$^{14,15}N$ correlation experiments are currently being made, to establish the binding of water and arginin to the same spin system.

Bibliography

[1] E. Ravera, G. Parigi, C. Luchinat, "Perspectives on paramagnetic NMR from a life sciences infrastructure", *J. Magn. Reson.* **2017**, *282*, 154–169, DOI 10.1016/j.jmr.2017.07.013.

[2] A. J. Pell, G. Pintacuda, C. P. Grey, "Paramagnetic NMR in solution and the solid state", *Prog. Nucl. Magn. Reson. Spectrosc.* **2019**, *111*, 1–271, DOI 10.1016/j.pnmrs.2018.05.001.

[3] G. Feher, E. A. Gere, "Polarization of Phosphorus Nuclei in Silicon", *Phys. Rev.* **1956**, *103*, 501–503, DOI 10.1103/PhysRev.103.501.

[4] W. Mims, "Pulsed endor experiments", *Proc. R. Soc. London* **1965**, *283*, 452–457, DOI 10.1098/rspa.1965.0034.

[5] E. R. Davies, "A new pulse endor technique", *Phys. Lett. A* **1974**, *47*, 1–2, DOI 10.1016/0375-9601(74)90078-4.

[6] S. A. Dikanov, Y. Tsvetkov, *Electron Spin Echo Envelope Modulation (ESEEM) Spectroscopy*, CRC Press, **1992**.

[7] P. Höfer, A. Grupp, H. Nebenführ, M. Mehring, "Hyperfine sublevel correlation (hyscore) spectroscopy: a 2D ESR investigation of the squaric acid radical", *Chem. Phys. Lett.* **1986**, *132*, 279–282, DOI 10.1016/0009-2614(86)80124-5.

[8] P. Schosseler, T. Wacker, A. Schweiger, "Pulsed ELDOR detected NMR", *Chem. Phys. Lett.* **1994**, *224*, 319–324, DOI 10.1016/0009-2614(94)00548-6.

[9] D. Goldfarb, Y. Lipkin, A. Potapov, Y. Gorodetsky, B. Epel, A. M. Raitsimring, M. Radoul, I. Kaminker, "HYSCORE and DEER with an upgraded 95GHz pulse EPR spectrometer", *J. Magn. Reson.* **2008**, *194*, 8–15, DOI 10.1016/j.jmr.2008.05.019.

[10] L. Rapatskiy, W. M. Ames, M. Perez-Navarro, A. Savitsky, J. J. Griese, T. Weyhermuller, H. S. Shafaat, M. Hogbom, F. Neese, D. A. Pantazis, N. Cox, "Characterization of Oxygen Bridged Manganese Model Complexes Using Multifrequency (17)O-Hyperfine EPR Spectroscopies and Density Functional Theory", *J. Phys. Chem. B* **2015**, *119*, 13904–21, DOI 10.1021/acs.jpcb.5b04614.

[11] N. Wili, G. Jeschke, "Chirp echo Fourier transform EPR-detected NMR", *J. Magn. Reson.* **2018**, *289*, 26–34, DOI 10.1016/j.jmr.2018.02.001.

[12] N. Cox, A. Nalepa, W. Lubitz, A. Savitsky, "ELDOR-detected NMR: A general and robust method for electron-nuclear hyperfine spectroscopy?", *J. Magn. Reson.* **2017**, *280*, 63–78, DOI 10.1016/j.jmr.2017.04.006.

[13] I. Tkach, I. Bejenke, F. Hecker, A. Kehl, M. Kasanmascheff, I. Gromov, I. Prisecaru, P. Hofer, M. Hiller, M. Bennati, "(1)H high field electron-nuclear double resonance spectroscopy at 263GHz/9.4T", *J. Magn. Reson.* **2019**, *303*, 17–27, DOI 10.1016/j.jmr.2019.04.001.

[14] A. Meyer, S. Dechert, S. Dey, C. Hobartner, M. Bennati, "Measurement of Angstrom to Nanometer Molecular Distances with (19) F Nuclear Spins by EPR/ENDOR Spectroscopy", *Angew. Chem. Int. Ed. Engl.* **2020**, *59*, 373–379, DOI 10.1002/anie.201908584.

[15] F. Hecker, J. Stubbe, M. Bennati, "Detection of Water Molecules on the Radical Transfer Pathway of Ribonucleotide Reductase by (17)O Electron-Nuclear Double Resonance Spectroscopy", *J. Am. Chem. Soc.* **2021**, *143*, 7237–7241, DOI 10.1021/jacs.1c01359.

[16] A. Meyer, A. Kehl, C. Cui, F. A. K. Reichardt, F. Hecker, L.-M. Funk, K.-T. Pan, H. Urlaub, K. Tittmann, J. Stubbe, M. Bennati, "19F Electron Nuclear Double Resonance reveals interaction be-tween redox active tyrosines across the ab interface of E. coli ribo-nucleotide reductase", *submitted* **2022**.

[17] S. Milikisiyants, R. Chatterjee, A. Weyers, A. Meenaghan, C. Coates, K. V. Lakshmi, "Ligand environment of the S2 state of photosystem II: a study of the hyperfine interactions of the tetranuclear manganese cluster by 2D 14N HYSCORE spectroscopy", *J. Phys. Chem. B* **2010**, *114*, 10905–11, DOI 10.1021/jp1061623.

[18] N. Cox, M. Retegan, F. Neese, D. A. Pantazis, A. Boussac, W. Lubitz, "Photosynthesis. Electronic structure of the oxygen-evolving complex in photosystem II prior to O-O bond formation", *Science* **2014**, *345*, 804–8, DOI 10.1126/science.1254910.

[19] T. Spatzal, M. Aksoyoglu, L. Zhang, S. L. Andrade, E. Schleicher, S. Weber, D. C. Rees, O. Einsle, "Evidence for interstitial carbon in nitrogenase FeMo cofactor", *Science* **2011**, *334*, 940, DOI 10.1126/science.1214025.

[20] A. Adamska-Venkatesh, S. Roy, J. F. Siebel, T. R. Simmons, M. Fontecave, V. Artero, E. Reijerse, W. Lubitz, "Spectroscopic Characterization of the Bridging Amine in the Active Site of [FeFe] Hydrogenase Using Isotopologues of the H-Cluster", *J. Am. Chem. Soc.* **2015**, *137*, 12744–7, DOI 10.1021/jacs.5b06240.

[21] G. Rao, L. Tao, D. L. M. Suess, R. D. Britt, "A [4Fe-4S]-Fe(CO)(CN)-L-cysteine intermediate is the first organometallic precursor in [FeFe] hydrogenase H-cluster bioassembly", *Nat. Chem.* **2018**, *10*, 555–560, DOI 10.1038/s41557-018-0026-7.

[22] M. Horitani, K. Shisler, W. E. Broderick, R. U. Hutcheson, K. S. Duschene, A. R. Marts, B. M. Hoffman, J. B. Broderick, "Radical SAM catalysis via an organometallic intermediate with an Fe-[5'-C]-deoxyadenosyl bond", *Science* **2016**, *352*, 822–5, DOI 10.1126/science.aaf5327.

[23] L. Tao, S. A. Pattenaude, S. Joshi, T. P. Begley, T. B. Rauchfuss, R. D. Britt, "Radical SAM Enzyme HydE Generates Adenosylated Fe(I) Intermediates En Route to the [FeFe]-Hydrogenase Catalytic H-Cluster", *J. Am. Chem. Soc.* **2020**, *142*, 10841–10848, DOI 10.1021/jacs.0c03802.

[24] T. Argirevic, C. Riplinger, J. Stubbe, F. Neese, M. Bennati, "ENDOR spectroscopy and DFT calculations: evidence for the hydrogen-bond network within alpha2 in the PCET of E. coli ribonucleotide reductase", *J. Am. Chem. Soc.* **2012**, *134*, 17661–70, DOI 10.1021/ja3071682.

[25] T. U. Nick, W. Lee, S. Kossmann, F. Neese, J. Stubbe, M. Bennati, "Hydrogen bond network between amino acid radical intermediates on the proton-coupled electron transfer pathway of E. coli alpha2 ribonucleotide reductase", *J. Am. Chem. Soc.* **2015**, *137*, 289–98, DOI 10.1021/ja510513z.

[26] T. U. Nick, K. R. Ravichandran, J. Stubbe, M. Kasanmascheff, M. Bennati, "Spectroscopic Evidence for a H Bond Network at Y356 Located at the Subunit Interface of Active E. coli Ribonucleotide Reductase", *Biochemistry* **2017**, *56*, 3647–3656, DOI 10.1021/acs.biochem.7b00462.

[27] V. Srinivas, H. Lebrette, D. Lundin, Y. Kutin, M. Sahlin, M. Lerche, J. Eirich, R. M. M. Branca, N. Cox, B. M. Sjoberg, M. Hogbom, "Metal-free ribonucleotide reduction powered by a DOPA radical in Mycoplasma pathogens", *Nature* **2018**, *563*, 416–420, DOI 10.1038/s41586-018-0653-6.

[28] E. J. Blaesi, G. M. Palowitch, K. Hu, A. J. Kim, H. R. Rose, R. Alapati, M. G. Lougee, H. J. Kim, A. T. Taguchi, K. O. Tan, T. N. Laremore, R. G. Griffin, C. Krebs, M. L. Matthews, A. Silakov, J. Bollinger, J. M., B. D. Allen, A. K. Boal, "Metal-free class Ie ribonucleotide reductase from pathogens initiates catalysis with a tyrosine-derived dihydroxyphenylalanine radical", *Proc. Natl. Acad. Sci. U.S.A.* **2018**, *115*, 10022–10027, DOI 10.1073/pnas.1811993115.

[29] P. Ball, "Water as an active constituent in cell biology", *Chem. Rev.* **2008**, *108*, 74–108, DOI 10.1021/cr068037a.

[30] F. A. Tezcan, B. R. Crane, J. R. Winkler, H. B. Gray, "Electron tunneling in protein crystals", *Proc. Natl. Acad. Sci. U.S.A.* **2001**, *98*, 5002–5006, DOI 10.1073/pnas.081072898.

[31] I. M. van Amsterdam, M. Ubbink, O. Einsle, A. Messerschmidt, A. Merli, D. Cavazzini, G. L. Rossi, G. W. Canters, "Dramatic modulation of electron transfer in protein complexes by crosslinking", *Nat. Struct. Mol. Biol.* **2002**, *9*, 48–52, DOI 10.1038/nsb736.

[32] J. Lin, I. A. Balabin, D. N. Beratan, "The nature of aqueous tunneling pathways between electron-transfer proteins", *Science* **2005**, *310*, 1311–1313, DOI 10.1126/science.1118316.

[33] A. de la Lande, S. Marti, O. Parisel, V. Moliner, "Long distance electron-transfer mechanism in peptidylglycine alpha-hydroxylating monooxygenase: a perfect fitting for a water bridge", *J. Am. Chem. Soc.* **2007**, *129*, 11700–7, DOI 10.1021/ja0703291.

[34] H. Luecke, B. Schobert, H. T. Richter, J. P. Cartailler, J. K. Lanyi, "Structure of bacteriorhodopsin at 1.55 A resolution", *J. Mol. Biol.* **1999**, *291*, 899–911, DOI 10.1006/jmbi.1999.3027.

[35] H. J. Sass, G. Buldt, R. Gessenich, D. Hehn, D. Neff, R. Schlesinger, J. Berendzen, P. Ormos, "Structural alterations for proton translocation in the M state of wild-type bacteriorhodopsin", *Nature* **2000**, *406*, 649–53, DOI 10.1038/35020607.

[36] K. Linke, F. M. Ho, "Water in Photosystem II: structural, functional and mechanistic considerations", *Biochim. Biophys. Acta* **2014**, *1837*, 14–32, DOI 10.1016/j.bbabio.2013.08.003.

[37] K. Saito, J. R. Shen, T. Ishida, H. Ishikita, "Short hydrogen bond between redox-active tyrosine Y(Z) and D1-His190 in the photosystem II crystal structure", *Biochemistry* **2011**, *50*, 9836–44, DOI 10.1021/bi201366j.

[38] A. Sirohiwal, F. Neese, D. A. Pantazis, "Microsolvation of the Redox-Active Tyrosine-D in Photosystem II: Correlation of Energetics with EPR Spectroscopy and Oxidation-Induced Proton Transfer", *J. Am. Chem. Soc.* **2019**, *141*, 3217–3231, DOI 10.1021/jacs.8b13123.

[39] U. Uhlin, H. Eklund, "Structure of ribonucleotide reductase protein R1", *Nature* **1994**, *370*, 533–9, DOI 10.1038/370533a0.

[40] M. Eriksson, U. Uhlin, S. Ramaswamy, M. Ekberg, K. Regnström, B.-M. Sjöberg, H. Eklund, "Binding of allosteric effectors to ribonucleotide reductase protein R1: reduction of active-site cysteines promotes substrate binding", *Structure* **1997**, *5*, 1077–1092, DOI 10.1016/s0969-2126(97)00259-1.

[41] Y. Umena, K. Kawakami, J. R. Shen, N. Kamiya, "Crystal structure of oxygen-evolving photosystem II at a resolution of 1.9 A", *Nature* **2011**, *473*, 55–60, DOI 10.1038/nature09913.

[42] M. Cohn, H. C. Urey, "Oxygen Exchange Reactions of Organic Compounds and Water", *J. Am. Chem. Soc.* **1938**, *60*, 679–687, DOI 10.1021/ja01270a052.

[43] E. Tiesinga, P. J. Mohr, D. B. Newell, B. N. Taylor, CODATA Recommended Values of the Fundamental Physical Constants: 2018, Web Page.

[44] D. Baute, D. Goldfarb, "The 17O hyperfine interaction in V17O(H217O)52+ and Mn(H217O)62+ determined by high field ENDOR aided by DFT calculations", *J. Phys. Chem. A* **2005**, *109*, 7865–71, DOI 10.1021/jp052132q.

[45] M. Bennati, T. F. Prisner, "New developments in high field electron paramagnetic resonance with applications in structural biology", *Rep. Prog. Phys.* **2005**, *68*, 411–448, DOI 10.1088/0034-4885/68/2/r05.

[46] L. Rapatskiy, N. Cox, A. Savitsky, W. M. Ames, J. Sander, M. M. Nowaczyk, M. Rogner, A. Boussac, F. Neese, J. Messinger, W. Lubitz, "Detection of the water-binding sites of the oxygen-evolving complex of Photosystem II using W-band 17O electron-electron double resonance-detected NMR spectroscopy", *J. Am. Chem. Soc.* **2012**, *134*, 16619–34, DOI 10.1021/ja3053267.

[47] N. Cox, W. Lubitz, A. Savitsky, "W-band ELDOR-detected NMR (EDNMR) spectroscopy as a versatile technique for the characterisation of transition metal–ligand interactions", *Mol. Phys.* **2013**, *111*, 2788–2808, DOI 10.1080/00268976.2013.830783.

[48] H. Thomann, M. Bernardo, D. Goldfarb, P. M. H. Kroneck, V. Ullrich, "Evidence for Water Binding to the Fe Center in Cytochrome P450cam Obtained by 17O Electron Spin-Echo Envelope Modulation Spectroscopy", *J. Am. Chem. Soc.* **1995**, *117*, 8243–8251, DOI 10.1021/ja00136a023.

[49] M. J. Colaneri, J. Vitali, "Probing Axial Water Bound to Copper in Tutton Salt Using Single Crystal (17)O-ESEEM Spectroscopy", *J. Phys. Chem. A* **2018**, *122*, 6214–6224, DOI 10.1021/acs.jpca.8b04075.

[50] A. Nalepa, M. Malferrari, W. Lubitz, G. Venturoli, K. Mobius, A. Savitsky, "Local water sensing: water exchange in bacterial photosynthetic reaction centers embedded in a trehalose glass studied using multiresonance EPR", *Phys. Chem. Chem. Phys.* **2017**, *19*, 28388–28400, DOI 10.1039/c7cp03942e.

[51] A. Schweiger, G. Jeschke, *Principles of Pulsed Electron Paramagnetic Resonance*, Oxford University Press, **2001**.

[52] D. Goldfarb, S.Stoll, *EPR Spectroscopy: Fundamentals and Methods*, Wiley, **2018**.

[53] P. Gast, E. J. J. Groenen, "EPR Interactions - g -Anisotropy" in *eMagRes*, **2016**, pp. 1435–1444, DOI 10.1002/9780470034590.emrstm1500.

[54] A. Kehl, M. Hiller, F. Hecker, I. Tkach, S. Dechert, M. Bennati, A. Meyer, "Resolution of chemical shift anisotropy in (19)F ENDOR spectroscopy at 263 GHz/9.4 T", *J. Magn. Reson.* **2021**, *333*, 107091, DOI 10.1016/j.jmr.2021.107091.

[55] F. Neese, "Quantum Chemistry and EPR Parameters" in *eMagRes*, **2017**, pp. 1–22, DOI 10.1002/9780470034590.emrstm1505.

[56] M. Bennati, "EPR Interactions - Hyperfine Couplings" in *eMagRes*, **2017**, pp. 271–282, DOI 10.1002/9780470034590.emrstm1503.

[57] S. Stoll, "Pulse EPR" in *eMagRes*, **2017**, pp. 23–38, DOI 10.1002/9780470034590.emrstm1510.

[58] A. Feintuch, S. Vega, "Spin Dynamics" in *eMagRes*, **2017**, pp. 427–452, DOI 10.1002/9780470034590.emrstm1506.

[59] C. Gemperle, A. Schweiger, "Pulsed electron-nuclear double resonance methodology", *Chem. Rev.* **1991**, *91*, 1481–1505, DOI 10.1021/cr00007a011.

[60] N. B. Asanbaeva, A. A. Sukhanov, A. A. Diveikina, O. Y. Rogozhnikova, D. V. Trukhin, V. M. Tormyshev, A. S. Chubarov, A. G. Maryasov, A. M. Genaev, A. V. Shernyukov, G. E. Salnikov, A. A. Lomzov, D. V. Pyshnyi, E. G. Bagryanskaya, "Application of W-band (19)F electron nuclear double resonance (ENDOR) spectroscopy to distance measurement using a trityl spin probe and a fluorine label", *Phys. Chem. Chem. Phys.* **2022**, *24*, 5982–6001, DOI 10.1039/d1cp05445g.

[61] P. P. Zanker, G. Jeschke, D. Goldfarb, "Distance measurements between paramagnetic centers and a planar object by matrix Mims electron nuclear double resonance", *J. Chem. Phys.* **2005**, *122*, 024515, DOI 10.1063/1.1828435.

[62] P. E. Doan, N. S. Lees, M. Shanmugam, B. M. Hoffman, "Simulating suppression effects in Pulsed ENDOR, and the 'hole in the middle' of Mims and Davies ENDOR Spectra", *Appl. Magn. Reson.* **2010**, *37*, 763–779, DOI 10.1007/s00723-009-0083-6.

[63] D. Goldfarb, "ELDOR-Detected NMR" in *eMagRes*, **2017**, pp. 101–114, DOI 10.1002/9780470034590.emrstm1516.

[64] A. Nalepa, K. Mobius, W. Lubitz, A. Savitsky, "High-field ELDOR-detected NMR study of a nitroxide radical in disordered solids: towards characterization of heterogeneity of microenvironments in spin-labeled systems", *J. Magn. Reson.* **2014**, *242*, 203–13, DOI 10.1016/j.jmr.2014.02.026.

[65] S. Van Doorslaer, "Hyperfine Spectroscopy: ESEEM" in *eMagRes*, **2017**, pp. 51–70, DOI 10.1002/9780470034590.emrstm1517.

[66] C. Do, J. Hatfield, S. Patel, D. Vasudevan, C. Tirla, N. S. Mills, "Dications of benzylidene-fluorene and diphenylmethylidene fluorene: the relationship between magnetic and energetic measures of antiaromaticity", *J. Org. Chem.* **2011**, *76*, 181–7, DOI 10.1021/jo101871q.

[67] E. C. Minnihan, D. D. Young, P. G. Schultz, J. Stubbe, "Incorporation of fluorotyrosines into ribonucleotide reductase using an evolved, polyspecific aminoacyl-tRNA synthetase", *J. Am. Chem. Soc.* **2011**, *133*, 15942–5, DOI 10.1021/ja207719f.

[68] W. Lee, M. Kasanmascheff, M. Huynh, A. Quartararo, C. Costentin, I. Bejenke, D. G. Nocera, M. Bennati, C. Tommos, J. Stubbe, "Properties of Site-Specifically Incorporated 3-Aminotyrosine in Proteins To Study Redox-Active Tyrosines: Escherichia coli Ribonucleotide Reductase as a Paradigm", *Biochemistry* **2018**, *57*, 3402–3415, DOI 10.1021/acs.biochem.8b00160.

[69] K. R. Ravichandran, A. T. Taguchi, Y. Wei, C. Tommos, D. G. Nocera, J. Stubbe, "A >200 meV Uphill Thermodynamic Landscape for Radical Transport in Escherichia coli Ribonucleotide Reductase Determined Using Fluorotyrosine-Substituted Enzymes", *J. Am. Chem. Soc.* **2016**, *138*, 13706–13716, DOI 10.1021/jacs.6b08200.

[70] S. Stoll, A. Schweiger, "EasySpin, a comprehensive software package for spectral simulation and analysis in EPR", *J. Magn. Reson.* **2006**, *178*, 42–55, DOI 10.1016/j.jmr.2005.08.013.

[71] S. Stoll, B. Kasumaj, "Phase Cycling in Electron Spin Echo Envelope Modulation", *Appl. Magn. Reson.* **2008**, *35*, 15–32, DOI 10.1007/s00723-008-0140-6.

[72] N. Wili, S. Richert, B. Limburg, S. J. Clarke, H. L. Anderson, C. R. Timmel, G. Jeschke, "ELDOR-detected NMR beyond hyperfine couplings: a case study with Cu(ii)-porphyrin dimers", *Phys. Chem. Chem. Phys.* **2019**, *21*, 11676–11688, DOI 10.1039/c9cp01760g.

[73] F. Neese, "The ORCA program system", *Wiley Interdisciplinary Reviews: Computational Molecular Science* **2012**, *2*, 73–78, DOI 10.1002/wcms.81.

[74] J. P. Perdew, "Density-functional approximation for the correlation energy of the inhomogeneous electron gas", *Phys. Rev. B* **1986**, *33*, 8822–8824, DOI 10.1103/physrevb.33.8822.

[75] A. D. Becke, "Density-functional exchange-energy approximation with correct asymptotic behavior", *Phys. Rev. A* **1988**, *38*, 3098–3100, DOI 10.1103/physreva.38.3098.

[76] A. Schäfer, C. Huber, R. Ahlrichs, "Fully optimized contracted Gaussian basis sets of triple zeta valence quality for atoms Li to Kr", *J. Chem. Phys.* **1994**, *100*, 5829–5835, DOI 10.1063/1.467146.

[77] F. Weigend, R. Ahlrichs, "Balanced basis sets of split valence, triple zeta valence and quadruple zeta valence quality for H to Rn: Design and assessment of accuracy", *Phys. Chem. Chem. Phys.* **2005**, *7*, 3297–305, DOI 10.1039/b508541a.

[78] F. Neese, F. Wennmohs, A. Hansen, U. Becker, "Efficient, approximate and parallel Hartree–Fock and hybrid DFT calculations. A 'chain-of-spheres' algorithm for the Hartree–Fock exchange", *Chem. Phys.* **2009**, *356*, 98–109, DOI 10.1016/j.chemphys.2008.10.036.

[79] S. Grimme, J. Antony, S. Ehrlich, H. Krieg, "A consistent and accurate ab initio parametrization of density functional dispersion correction (DFT-D) for the 94 elements H-Pu", *J. Chem. Phys.* **2010**, *132*, 154104, DOI 10.1063/1.3382344.

[80] S. Grimme, S. Ehrlich, L. Goerigk, "Effect of the damping function in dispersion corrected density functional theory", *J. Comput. Chem.* **2011**, *32*, 1456–65, DOI 10.1002/jcc.21759.

[81] C. Lee, W. Yang, R. G. Parr, "Development of the Colle-Salvetti correlation-energy formula into a functional of the electron density", *Phys. Rev. B: Cond. Mat.* **1988**, *37*, 785–789, DOI 10.1103/physrevb.37.785.

[82] A. D. Becke, "Density-functional thermochemistry. III. The role of exact exchange", *J. Chem. Phys.* **1993**, *98*, 5648–5652, DOI 10.1063/1.464913.

[83] V. Barone, "Structure, Magnetic Properties and Reactivities of Open-Shell Species from Density Functional and Self-Consistent Hybrid Methods" in *Recent Advances in Density Functional Methods, Part1*, **1996**, p. 287.

[84] H. J. Hogben, M. Krzystyniak, G. T. Charnock, P. J. Hore, I. Kuprov, "Spinach–a software library for simulation of spin dynamics in large spin systems", *J. Magn. Reson.* **2011**, *208*, 179–94, DOI 10.1016/j.jmr.2010.11.008.

[85] R. Rizzato, M. Bennati, "Cross-Polarization Electron-Nuclear Double Resonance Spectroscopy", *Chem. Phys. Chem.* **2015**, *16*, 3769–73, DOI 10.1002/cphc.201500938.

[86] I. Bejenke, R. Zeier, R. Rizzato, S. J. Glaser, M. Bennati, "Cross-polarisation ENDOR for spin-1 deuterium nuclei", *Mol. Phys.* **2020**, *118*, DOI 10.1080/00268976.2020.1763490.

[87] L. Thelander, P. Reichard, "Reduction of ribonucleotides", *Annu. Rev. Biochem.* **1979**, *48*, 133–58, DOI 10.1146/annurev.bi.48.070179.001025.

[88] P. Reichard, "From RNA to DNA, why so many ribonucleotide reductases?", *Science* **1993**, *260*, 1773–7, DOI 10.1126/science.8511586.

[89] A. Hofer, M. Crona, D. T. Logan, B. M. Sjoberg, "DNA building blocks: keeping control of manufacture", *Crit. Rev. Biochem. Mol. Biol.* **2012**, *47*, 50–63, DOI 10.3109/10409238.2011.630372.

[90] Y. Aye, M. Li, M. J. Long, R. S. Weiss, "Ribonucleotide reductase and cancer: biological mechanisms and targeted therapies", *Oncogene* **2015**, *34*, 2011–21, DOI 10.1038/onc.2014.155.

[91] E. Guarino, I. Salguero, S. E. Kearsey, "Cellular regulation of ribonucleotide reductase in eukaryotes", *Semin. Cell Dev. Biol.* **2014**, *30*, 97–103, DOI 10.1016/j.semcdb.2014.03.030.

[92] B. L. Greene, G. Kang, C. Cui, M. Bennati, D. G. Nocera, C. L. Drennan, J. Stubbe, "Ribonucleotide Reductases: Structure, Chemistry, and Metabolism Suggest New Therapeutic Targets", *Annu. Rev. Biochem.* **2020**, *89*, 45–75, DOI 10.1146/annurev-biochem-013118-111843.

[93] M. D. Sintchak, G. Arjara, B. A. Kellogg, J. Stubbe, C. L. Drennan, "The crystal structure of class II ribonucleotide reductase reveals how an allosterically regulated monomer mimics a dimer", *Nat. Struct. Biol.* **2002**, *9*, 293–300, DOI 10.1038/nsb774.

[94] D. T. Logan, J. Andersson, B. M. Sjoberg, P. Nordlund, "A glycyl radical site in the crystal structure of a class III ribonucleotide reductase", *Science* **1999**, *283*, 1499–504, DOI 10.1126/science.283.5407.1499.

[95] J. Stubbe, M. R. Seyedsayamdost, "Discovery of a New Class I Ribonucleotide Reductase with an Essential DOPA Radical and NO Metal as an Initiator of Long-Range Radical Transfer", *Biochemistry* **2019**, *58*, 435–437, DOI 10.1021/acs.biochem.8b01238.

[96] A. Jordan, P. Reichard, "Ribonucleotide reductases", *Annu. Rev. Biochem.* **1998**, *67*, 71–98, DOI 10.1146/annurev.biochem.67.1.71.

[97] P. Nordlund, P. Reichard, "Ribonucleotide reductases", *Annu. Rev. Biochem.* **2006**, *75*, 681–706, DOI 10.1146/annurev.biochem.75.103004.142443.

[98] A. Graslund, M. Sahlin, "Electron paramagnetic resonance and nuclear magnetic resonance studies of class I ribonucleotide reductase", *Annu. Rev. Biophys. Biomol. Struct.* **1996**, *25*, 259–86, DOI 10.1146/annurev.bb.25.060196.001355.

[99] J. Stubbe, D. G. Nocera, C. S. Yee, M. C. Chang, "Radical initiation in the class I ribonucleotide reductase: long-range proton-coupled electron transfer?", *Chem. Rev.* **2003**, *103*, 2167–201, DOI 10.1021/cr020421u.

[100] P. Nordlund, B. M. Sjoberg, H. Eklund, "Three-dimensional structure of the free radical protein of ribonucleotide reductase", *Nature* **1990**, *345*, 593–8, DOI 10.1038/345593a0.

[101] N. Ando, E. J. Brignole, C. M. Zimanyi, M. A. Funk, K. Yokoyama, F. J. Asturias, J. Stubbe, C. L. Drennan, "Structural interconversions modulate activity of Escherichia coli ribonucleotide reductase", *Proc. Natl. Acad. Sci. U.S.A.* **2011**, *108*, 21046–51, DOI 10.1073/pnas.1112715108.

[102] E. C. Minnihan, N. Ando, E. J. Brignole, L. Olshansky, J. Chittuluru, F. J. Asturias, C. L. Drennan, D. G. Nocera, J. Stubbe, "Generation of a stable, aminotyrosyl radical-induced alpha2beta2 complex of Escherichia coli class Ia ribonucleotide reductase", *Proc. Natl. Acad. Sci. U.S.A.* **2013**, *110*, 3835–40, DOI 10.1073/pnas.1220691110.

[103] M. Bennati, M. M. Hertel, J. Fritscher, T. F. Prisner, N. Weiden, R. Hofweber, M. Sporner, G. Horn, H. R. Kalbitzer, "High-frequency 94 GHz ENDOR characterization of the metal binding site in wild-type Ras x GDP and its oncogenic mutant G12V in frozen solution", *Biochemistry* **2006**, *45*, 42–50, DOI 10.1021/bi051156k.

[104] M. R. Seyedsayamdost, C. T. Chan, V. Mugnaini, J. Stubbe, M. Bennati, "PELDOR spectroscopy with DOPA-beta2 and NH2Y-alpha2s: distance measurements between residues involved in the radical propagation pathway of E. coli ribonucleotide reductase", *J. Am. Chem. Soc.* **2007**, *129*, 15748–9, DOI 10.1021/ja076459b.

[105] M. R. Seyedsayamdost, J. Xie, C. T. Chan, P. G. Schultz, J. Stubbe, "Site-specific insertion of 3-aminotyrosine into subunit alpha2 of E. coli ribonucleotide reductase: direct evidence for involvement of Y730 and Y731 in radical propagation", *J. Am. Chem. Soc.* **2007**, *129*, 15060–71, DOI 10.1021/ja076043y.

[106] G. Kang, A. T. Taguchi, J. Stubbe, C. L. Drennan, "Structure of a trapped radical transfer pathway within a ribonucleotide reductase holocomplex", *Science* **2020**, *368*, 424–427, DOI 10.1126/science.aba6794.

[107] E. C. Minnihan, D. G. Nocera, J. Stubbe, "Reversible, long-range radical transfer in E. coli class Ia ribonucleotide reductase", *Acc. Chem. Res.* **2013**, *46*, 2524–35, DOI 10.1021/ar4000407.

[108] H. Eklund, U. Uhlin, M. Färnegårdh, D. T. Logan, P. Nordlund, "Structure and function of the radical enzyme ribonucleotide reductase", *Prog. Biophys. Mol. Biol.* **2001**, *77*, 177–268, DOI 10.1016/s0079-6107(01)00014-1.

[109] I. Climent, B. M. Sjoberg, C. Y. Huang, "Carboxyl-terminal peptides as probes for Escherichia coli ribonucleotide reductase subunit interaction: kinetic analysis of inhibition studies", *Biochemistry* **1991**, *30*, 5164–71, DOI 10.1021/bi00235a008.

[110] I. Climent, B. M. Sjoberg, C. Y. Huang, "Site-directed mutagenesis and deletion of the carboxyl terminus of Escherichia coli ribonucleotide reductase protein R2. Effects on catalytic activity and subunit interaction", *Biochemistry* **1992**, *31*, 4801–7, DOI 10.1021/bi00135a009.

[111] M. Ekberg, M. Sahlin, M. Eriksson, B. M. Sjoberg, "Two conserved tyrosine residues in protein R1 participate in an intermolecular electron transfer in ribonucleotide reductase", *J. Biol. Chem.* **1996**, *271*, 20655–9, DOI 10.1074/jbc.271.34.20655.

[112] F. Lendzian, M. Sahlin, F. MacMillan, R. Bittl, R. Fiege, S. Pötsch, B.-M. Sjöberg, A. Gräslund, W. Lubitz, G. Lassmann, "Electronic Structure of Neutral Tryptophan Radicals in Ribonucleotide Reductase Studied by EPR and ENDOR Spectroscopy", *J. Am. Chem. Soc.* **1996**, *118*, 8111–8120, DOI 10.1021/ja960917r.

[113] L. Saleh, J. Bollinger, J. M., "Cation mediation of radical transfer between Trp48 and Tyr356 during O2 activation by protein R2 of Escherichia coli ribonucleotide reductase: relevance to R1-R2 radical transfer in nucleotide reduction?", *Biochemistry* **2006**, *45*, 8823–30, DOI 10.1021/bi060325d.

[114] K. Yokoyama, A. A. Smith, B. Corzilius, R. G. Griffin, J. Stubbe, "Equilibration of tyrosyl radicals (Y356*, Y731*, Y730*) in the radical propagation pathway of the Escherichia coli class Ia ribonucleotide reductase", *J. Am. Chem. Soc.* **2011**, *133*, 18420–32, DOI 10.1021/ja207455k.

[115] J. Stubbe, W. A. van der Donk, "Ribonucleotide reductases: radical enzymes with suicidal tendencies", *Chem. Biol.* **1995**, *2*, 793–801, DOI 10.1016/1074-5521(95)90084-5.

[116] A. Migliore, N. F. Polizzi, M. J. Therien, D. N. Beratan, "Biochemistry and theory of proton-coupled electron transfer", *Chem. Rev.* **2014**, *114*, 3381–465, DOI 10.1021/cr4006654.

[117] B. M. Sjöberg, M. Karlsson, H. Jörnvall, "Half-site reactivity of the tyrosyl radical of ribonucleotide reductase from Escherichia coli", *J. Biol. Chem.* **1987**, *262*, 9736–9743, DOI 10.1016/s0021-9258(18)47996-3.

[118] A. Ehrenberg, P. Reichard, "Electron Spin Resonance of the Iron-containing Protein B2 from Ribonucleotide Reductase", *J. Biol. Chem.* **1972**, *247*, 3485–3488, DOI 10.1016/s0021-9258(19)45166-1.

[119] B. M. Sjöberg, P. Reichard, A. Gräslund, A. Ehrenberg, "The tyrosine free radical in ribonucleotide reductase from Escherichia coli", *J. Biol. Chem.* **1978**, *253*, 6863–6865, DOI 10.1016/s0021-9258(17)37999-1.

[120] M. Bennati, C. T. Farrar, J. A. Bryant, S. J. Inati, V. Weis, G. J. Gerfen, P. Riggs-Gelasco, J. Stubbe, R. G. Griffin, "Pulsed electron-nuclear double resonance (ENDOR) at 140 GHz", *J. Magn. Reson.* **1999**, *138*, 232–43, DOI 10.1006/jmre.1999.1727.

[121] Y. Pokern, B. Eltzner, S. F. Huckemann, C. Beeken, J. Stubbe, I. Tkach, M. Bennati, M. Hiller, "Statistical analysis of ENDOR spectra", *Proc. Natl. Acad. Sci. U.S.A.* **2021**, *118*, DOI 10.1073/pnas.2023615118.

[122] M. Hiller, I. Tkach, H. Wiechers, B. Eltzner, S. Huckemann, Y. Pokern, M. Bennati, "Distribution of H^{β} Hyperfine Couplings in a Tyrosyl Radical Revealed by 263 GHz ENDOR Spectroscopy", *Appl. Magn. Reson.* **2021**, DOI 10.1007/s00723-021-01411-5.

[123] M. R. Seyedsayamdost, S. Y. Reece, D. G. Nocera, J. Stubbe, "Mono-, di-, tri-, and tetra-substituted fluorotyrosines: new probes for enzymes that use tyrosyl radicals in catalysis", *J. Am. Chem. Soc.* **2006**, *128*, 1569–79, DOI 10.1021/ja055926r.

[124] T. S. Young, P. G. Schultz, "Beyond the canonical 20 amino acids: expanding the genetic lexicon", *J. Biol. Chem.* **2010**, *285*, 11039–44, DOI 10.1074/jbc.R109.091306.

[125] K. Yokoyama, U. Uhlin, J. Stubbe, "Site-specific incorporation of 3-nitrotyrosine as a probe of pKa perturbation of redox-active tyrosines in ribonucleotide reductase", *J. Am. Chem. Soc.* **2010**, *132*, 8385–97, DOI 10.1021/ja101097p.

[126] P. E. M. Siegbahn, L. Eriksson, F. Himo, M. Pavlov, "Hydrogen Atom Transfer in Ribonucleotide Reductase (RNR)", *J. Phys. Chem. B* **1998**, *102*, 10622–10629, DOI 10.1021/jp9827835.

[127] V. R. Kaila, G. Hummer, "Energetics of direct and water-mediated proton-coupled electron transfer", *J. Am. Chem. Soc.* **2011**, *133*, 19040–3, DOI 10.1021/ja2082262.

[128] E. C. Minnihan, M. R. Seyedsayamdost, U. Uhlin, J. Stubbe, "Kinetics of radical intermediate formation and deoxynucleotide production in 3-aminotyrosine-substituted Escherichia coli ribonucleotide reductases", *J. Am. Chem. Soc.* **2011**, *133*, 9430–40, DOI 10.1021/ja201640n.

[129] M. Kasanmascheff, W. Lee, T. U. Nick, J. Stubbe, M. Bennati, "Radical transfer in E. coli ribonucleotide reductase: a NH2Y731/R411A-alpha mutant unmasks a new conformation of the pathway residue 731", *Chem. Sci.* **2016**, *7*, 2170–2178, DOI 10.1039/c5sc03460d.

[130] B. L. Greene, A. T. Taguchi, J. Stubbe, D. G. Nocera, "Conformationally Dynamic Radical Transfer within Ribonucleotide Reductase", *J. Am. Chem. Soc.* **2017**, *139*, 16657–16665, DOI 10.1021/jacs.7b08192.

[131] C. R. Reinhardt, P. Li, G. Kang, J. Stubbe, C. L. Drennan, S. Hammes-Schiffer, "Conformational Motions and Water Networks at the alpha/beta Interface in E. coli Ribonucleotide Reductase", *J. Am. Chem. Soc.* **2020**, *142*, 13768–13778, DOI 10.1021/jacs.0c04325.

[132] C. R. Reinhardt, E. R. Sayfutyarova, J. Zhong, S. Hammes-Schiffer, "Glutamate Mediates Proton-Coupled Electron Transfer Between Tyrosines 730 and 731 in Escherichia coli Ribonucleotide Reductase", *J. Am. Chem. Soc.* **2021**, *143*, 6054–6059, DOI 10.1021/jacs.1c02152.

[133] C. Cui, B. L. Greene, G. Kang, C. L. Drennan, J. Stubbe, D. G. Nocera, "Gated Proton Release during Radical Transfer at the Subunit Interface of Ribonucleotide Reductase", *J. Am. Chem. Soc.* **2021**, *143*, 176–183, DOI 10.1021/jacs.0c07879.

[134] D. T. Edmonds, A. Zussman, "Pure quadrupole resonance of 17O in ice", *Phys. Lett. A* **1972**, *41*, 167–169, DOI 10.1016/0375-9601(72)91097-3.

[135] P.-O. Löwdin, "On the Non-Orthogonality Problem Connected with the Use of Atomic Wave Functions in the Theory of Molecules and Crystals", *J. Chem. Phys.* **1950**, *18*, 365–375, DOI 10.1063/1.1747632.

[136] Q. Lin, M. J. Parker, A. T. Taguchi, K. Ravichandran, A. Kim, G. Kang, J. Shao, C. L. Drennan, J. Stubbe, "Glutamate 52-b at the a/b subunit interface of Escherichia coliclass Ia ribonucleotide reductase is essential for conformational gating of radical transfer", *J. Biol. Chem.* **2017**, *292*, 9229–9239, DOI 10.1074/jbc.M117.783092.

[137] H. J. Jakobsen, H. Bildsøe, M. Brorson, G. Wu, P. L. Gor'kov, Z. Gan, I. Hung, "High-Field17O MAS NMR Reveals1J(17O-127I) with its Sign and the NMR Crystallography of the Scheelite Structures for NaIO4and KIO4", *J. Phys. Chem. C* **2015**, DOI 10.1021/acs.jpcc.5b03721.

[138] E. G. Keeler, V. K. Michaelis, M. T. Colvin, I. Hung, P. L. Gor'kov, T. A. Cross, Z. Gan, R. G. Griffin, "(17)O MAS NMR Correlation Spectroscopy at High Magnetic Fields", *J. Am. Chem. Soc.* **2017**, *139*, 17953–17963, DOI 10.1021/jacs.7b08989.

[139] W. Bruggemann, J. R. Niklas, "Stochastic ENDOR", *J. Magn. Reson.* **1994**, *108*, 25–29, DOI 10.1006/jmra.1994.1084.

[140] B. Epel, D. Arieli, D. Baute, D. Goldfarb, "Improving W-band pulsed ENDOR sensitivity—random acquisition and pulsed special TRIPLE", *J. Magn. Reson.* **2003**, *164*, 78–83, DOI 10.1016/s1090-7807(03)00191-5.

[141] R. Rizzato, M. Bennati, "Enhanced sensitivity of electron-nuclear double resonance (ENDOR) by cross polarisation and relaxation", *Phys. Chem. Chem. Phys.* **2014**, *16*, 7681–5, DOI 10.1039/c3cp55395g.

[142] S. Stoll, R. D. Britt, "General and efficient simulation of pulse EPR spectra", *Phys. Chem. Chem. Phys.* **2009**, *11*, 6614–25, DOI 10.1039/b907277b.

[143] K. R. Ravichandran, E. C. Minnihan, Y. Wei, D. G. Nocera, J. Stubbe, "Reverse Electron Transfer Completes the Catalytic Cycle in a 2,3,5-Trifluorotyrosine-Substituted Ribonucleotide Reductase", *J. Am. Chem. Soc.* **2015**, *137*, 14387–95, DOI 10.1021/jacs.5b09189.

[144] M. Sahlin, L. Petersson, A. Graslund, A. Ehrenberg, B. M. Sjoberg, L. Thelander, "Magnetic interaction between the tyrosyl free radical and the antiferromagnetically coupled iron center in ribonucleotide reductase", *Biochemistry* **1987**, *26*, 5541–8, DOI 10.1021/bi00391a049.

[145] C. C. Lawrence, M. Bennati, H. V. Obias, G. Bar, R. G. Griffin, J. Stubbe, "High-field EPR detection of a disulfide radical anion in the reduction of cytidine 5'-diphosphate by the E441Q R1 mutant of Escherichia coli ribonucleotide reductase", *Proc. Natl. Acad. Sci. U.S.A.* **1999**, *96*, 8979–84, DOI 10.1073/pnas.96.16.8979.

[146] S. Pribitzer, D. Mannikko, S. Stoll, "Determining electron-nucleus distances and Fermi contact couplings from ENDOR spectra", *Phys. Chem. Chem. Phys.* **2021**, *23*, 8326–8335, DOI 10.1039/d1cp00229e.

[147] X. Tan, M. Bernardo, H. Thomann, C. P. Scholes, "17O hyperfine and quadrupole interactions for water ligands in frozen solutions of high spin Mn2+", *J. Chem. Phys.* **1995**, *102*, 2675–2690, DOI 10.1063/1.468644.

[148] D. Goldfarb, M. Bernardo, H. Thomann, P. M. H. Kroneck, V. Ullrich, "Study of Water Binding to Low-Spin Fe(III) in Cytochrome P450 by Pulsed ENDOR and Four-Pulse ESEEM Spectroscopies", *J. Am. Chem. Soc.* **1996**, *118*, 2686–2693, DOI 10.1021/ja951307e.

[149] D. Burdi, J.-P. Willems, P. Riggs-Gelasco, W. E. Antholine, J. Stubbe, B. M. Hoffman, "The Core Structure of X Generated in the Assembly of the Diiron Cluster of Ribonucleotide Reductase: 17O2and H217O ENDOR", *J. Am. Chem. Soc.* **1998**, *120*, 12910–12919, DOI 10.1021/ja9824270.

[150] A. M. Raitsimring, A. V. Astashkin, D. Baute, D. Goldfarb, P. Caravan, "W-Band17O Pulsed Electron Nuclear Double Resonance Study of Gadolinium Complexes with Water", *J. Chem. Phys. A* **2004**, *108*, 7318–7323, DOI 10.1021/jp040306i.

[151] N. Kocherginsky, H. M. Swartz, *Nitroxide Spin Labels*, CRC Press, New York, **1995**.

[152] E. Bordignon, "EPR Spectroscopy of Nitroxide Spin Probes" in *eMagRes*, **2017**, pp. 235–254, DOI 10.1002/9780470034590.emrstm1513.

[153] S. A. Shelke, S. T. Sigurdsson, "Site-Directed Nitroxide Spin Labeling of Biopolymers" in *Structural Information from Spin-Labels and Intrinsic Paramagnetic Centres in the Biosciences*, (Eds.: C. R. Timmel, J. R. Harmer), Springer Berlin Heidelberg, Berlin, Heidelberg, **2013**, pp. 121–162, DOI 10.1007/430_2011_62.

[154] C. Song, K. N. Hu, C. G. Joo, T. M. Swager, R. G. Griffin, "TOTAPOL: a biradical polarizing agent for dynamic nuclear polarization experiments in aqueous media", *J. Am. Chem. Soc.* **2006**, *128*, 11385–90, DOI 10.1021/ja061284b.

[155] C. Sauvee, M. Rosay, G. Casano, F. Aussenac, R. T. Weber, O. Ouari, P. Tordo, "Highly efficient, water-soluble polarizing agents for dynamic nuclear polarization at high frequency", *Angew. Chem. Int. Ed. Engl.* **2013**, *52*, 10858–61, DOI 10.1002/anie.201304657.

[156] J. Stubbe, W. A. van Der Donk, "Protein Radicals in Enzyme Catalysis", *Chem. Rev.* **1998**, *98*, 705–762, DOI 10.1021/cr9400875.

[157] C. W. Hoganson, C. Tommos, "The function and characteristics of tyrosyl radical cofactors", *Biochim Biophys Acta* **2004**, *1655*, 116–22, DOI 10.1016/j.bbabio.2003.10.017.

[158] O. Schiemann, C. A. Heubach, D. Abdullin, K. Ackermann, M. Azarkh, E. G. Bagryanskaya, M. Drescher, B. Endeward, J. H. Freed, L. Galazzo, D. Goldfarb, T. Hett, L. Esteban Hofer, L. Fabregas Ibanez, E. J. Hustedt, S. Kucher, I. Kuprov, J. E. Lovett, A. Meyer, S. Ruthstein, S. Saxena, S. Stoll, C. R. Timmel, M. Di Valentin, H. S. McHaourab, T. F. Prisner, B. E. Bode, E. Bordignon, M. Bennati, G. Jeschke, "Benchmark Test and Guidelines for DEER/PELDOR Experiments on Nitroxide-Labeled Biomolecules", *J. Am. Chem. Soc.* **2021**, *143*, 17875–17890, DOI 10.1021/jacs.1c07371.

[159] T. Steiner, "The Hydrogen Bond in the Solid State", *Angew. Chem. Int. Ed.* **2002**, *41*, 48–76, DOI 10.1002/1521-3773(20020104)41:1<48::Aid-anie48>3.0.Co;2-u.

[160] E. M. Bras, T. L. Fischer, M. A. Suhm, "The Hydrates of TEMPO: Water Vibrations Reveal Radical Microsolvation", *Angew. Chem. Int. Ed. Engl.* **2021**, *60*, 19013–19017, DOI 10.1002/anie.202104496.

[161] E. Stendardo, A. Pedone, P. Cimino, M. Cristina Menziani, O. Crescenzi, V. Barone, "Extension of the AMBER force-field for the study of large nitroxides in condensed phases: an ab initio parameterization", *Phys. Chem. Chem. Phys.* **2010**, *12*, 11697–11709, DOI 10.1039/C001481H.

[162] A. Savitsky, A. Nalepa, T. Petrenko, M. Plato, K. Möbius, W. Lubitz, "Hydrogen-Bonded Complexes of Neutral Nitroxide Radicals with 2-Propanol Studied by Multifrequency EPR/ENDOR", *Appl. Magn. Reson.* **2021**, DOI 10.1007/s00723-021-01442-y.

[163] R. Owenius, M. Engström, M. Lindgren, M. Huber, "Influence of Solvent Polarity and Hydrogen Bonding on the EPR Parameters of a Nitroxide Spin Label Studied by 9-GHz and 95-GHz EPR Spectroscopy and DFT Calculations", *J. Chem. Phys. A* **2001**, *105*, 10967–10977, DOI 10.1021/jp0116914.

[164] P. Gast, R. T. Herbonnet, J. Klare, A. Nalepa, C. Rickert, D. Stellinga, L. Urban, K. Mobius, A. Savitsky, H. J. Steinhoff, E. J. Groenen, "Hydrogen bonding of nitroxide spin labels in membrane proteins", *Phys. Chem. Chem. Phys.* **2014**, *16*, 15910–6, DOI 10.1039/c4cp01741b.

[165] E. Bordignon, A. I. Nalepa, A. Savitsky, L. Braun, G. Jeschke, "Changes in the Microenvironment of Nitroxide Radicals around the Glass Transition Temperature", *J. Phys. Chem. B* **2015**, *119*, 13797–806, DOI 10.1021/acs.jpcb.5b04104.

[166] A. Nalepa, K. Möbius, M. Plato, W. Lubitz, A. Savitsky, "Nitroxide Spin Labels—Magnetic Parameters and Hydrogen-Bond Formation: A High-Field EPR and EDNMR Study", *Appl. Magn. Reson.* **2018**, *50*, 1–16, DOI 10.1007/s00723-018-1073-3.

[167] S. Pronk, S. Pall, R. Schulz, P. Larsson, P. Bjelkmar, R. Apostolov, M. R. Shirts, J. C. Smith, P. M. Kasson, D. van der Spoel, B. Hess, E. Lindahl, "GROMACS 4.5: a high-throughput and highly parallel open source molecular simulation toolkit", *Bioinformatics* **2013**, *29*, 845–54, DOI 10.1093/bioinformatics/btt055.

[168] C. I. Bayly, P. Cieplak, W. Cornell, P. A. Kollman, "A well-behaved electrostatic potential based method using charge restraints for deriving atomic charges: the RESP model", *J. Phys. Chem.* **2002**, *97*, 10269–10280, DOI 10.1021/j100142a004.

[169] T. Lu, F. Chen, "Multiwfn: a multifunctional wavefunction analyzer", *J. Comput. Chem.* **2012**, *33*, 580–92, DOI 10.1002/jcc.22885.

[170] T. Fox, P. A. Kollman, "Application of the RESP Methodology in the Parametrization of Organic Solvents", *J. Phys. Chem. B* **1998**, *102*, 8070–8079, DOI 10.1021/jp9717655.

[171] A. W. Sousa da Silva, W. F. Vranken, "ACPYPE - AnteChamber PYthon Parser interfacE", *BMC Res. Notes* **2012**, *5*, 367, DOI 10.1186/1756-0500-5-367.

[172] J. B. Verstraete, W. K. Myers, M. Foroozandeh, "Chirped ordered pulses for ultra-broadband ESR spectroscopy", *J. Chem. Phys.* **2021**, *154*, 094201, DOI 10.1063/5.0038511.

[173] T. Wacker, G. A. Sierra, A. Schweiger, "The Concept of FID-detected Hole-burning in Pulsed EPR Spectroscopy", *Isr. J. Chem.* **1992**, *32*, 305–322, DOI 10.1002/ijch.199200038.

[174] T. Hetzke, A. M. Bowen, T. F. Prisner, "ELDOR-detected NMR at Q-Band", *Appl. Magn. Reson.* **2017**, *48*, 1375–1397, DOI 10.1007/s00723-017-0927-4.

[175] M. Huber, M. Lindgren, P. Hammarström, L. G. Mårtensson, U. Carlsson, G. R. Eaton, S. S. Eaton, "Phase memory relaxation times of spin labels in human carbonic anhydrase II: pulsed EPR to determine spin label location", *Biophys. Chem.* **2001**, *94*, 245–256, DOI 10.1016/s0301-4622(01)00239-3.

[176] R. Dastvan, B. E. Bode, M. P. Karuppiah, A. Marko, S. Lyubenova, H. Schwalbe, T. F. Prisner, "Optimization of transversal relaxation of nitroxides for pulsed electron-electron double resonance spectroscopy in phospholipid membranes", *J. Phys. Chem. B* **2010**, *114*, 13507–16, DOI 10.1021/jp1060039.

[177] E. R. Canarie, S. M. Jahn, S. Stoll, "Quantitative Structure-Based Prediction of Electron Spin Decoherence in Organic Radicals", *J. Phys. Chem. Lett.* **2020**, *11*, 3396–3400, DOI 10.1021/acs.jpclett.0c00768.

[178] H. El Mkami, R. Ward, A. Bowman, T. Owen-Hughes, D. G. Norman, "The spatial effect of protein deuteration on nitroxide spin-label relaxation: implications for EPR distance measurement", *J. Magn. Reson.* **2014**, *248*, 36–41, DOI 10.1016/j.jmr.2014.09.010.

[179] T. Schmidt, M. A. Walti, J. L. Baber, E. J. Hustedt, G. M. Clore, "Long Distance Measurements up to 160 A in the GroEL Tetradecamer Using Q-Band DEER EPR Spectroscopy", *Angew. Chem. Int. Ed. Engl.* **2016**, *55*, 15905–15909, DOI 10.1002/anie.201609617.

[180] I. Kaminker, T. D. Wilson, M. G. Savelieff, Y. Hovav, H. Zimmermann, Y. Lu, D. Goldfarb, "Correlating nuclear frequencies by two-dimensional ELDOR-detected NMR spectroscopy", *J. Magn. Reson.* **2014**, *240*, 77–89, DOI 10.1016/j.jmr.2013.12.016.

[181] A. Potapov, D. Goldfarb, "The Mn(2+)-bicarbonate complex in a frozen solution revisited by pulse W-band ENDOR", *Inorg. Chem.* **2008**, *47*, 10491–8, DOI 10.1021/ic8011316.

[182] D. Goldfarb, V. Kofman, J. Libman, A. Shanzer, R. Rahmatouline, S. Van Doorslaer, A. Schweiger, "Double Nuclear Coherence Transfer (DONUT)-HYSCORE: A New Tool for the Assignment of Nuclear Frequencies in Pulsed EPR Experiments", *J. Am. Chem. Soc.* **1998**, *120*, 7020–7029, DOI 10.1021/ja973271r.

[183] B. Epel, D. Goldfarb, "Two-dimensional pulsed TRIPLE at 95 GHz", *J. Magn. Reson.* **2000**, *146*, 196–203, DOI 10.1006/jmre.2000.2139.

Appendix

A Resonator bandwidth measurements

The microwave power $\nu_1 = \omega_1/2\pi$ depends on the quality factor of the microwave resonator Q and is described by the following expression:

$$\nu_1 = \nu_{1,\max} \cdot \sqrt{1 + \left(2 \cdot Q \cdot \frac{\nu_{mw} - \nu_0}{\nu_0}\right)^2} \tag{A.1}$$

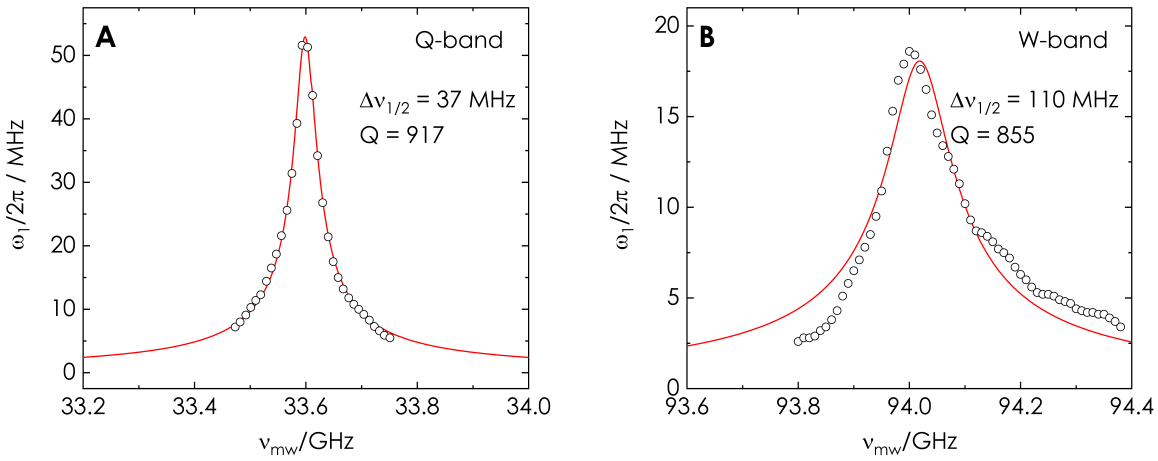

Figure A.1: Resonator bandwidths of the Q- (**A**) and W-band (**B**) spectrometers. Experimental microwave powers (black circles) were determined by microwave Nutation experiments. Resonator quality factors Q were determined by a least square fit of Eq. (A.1) to the experimental data (red). Measurements were performed with 0.1 % ^{1}H-BDPA samples at 50 K.

B Rf heating

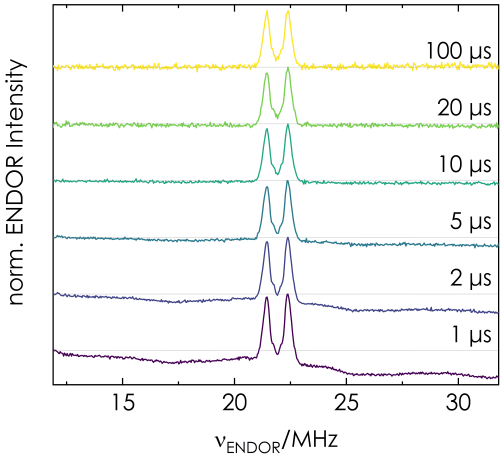

Figure B.1: Experimental Mims ENDOR spectra of ^{2}H BDPA in PS as a function of delay time t_d (given in figure) between rf pulse and microwave readout. Experiments recorded at 94 GHz EPR frequency and a temperature of 50 K with a rf pulse of 40 µs. Spectra are not baseline corrected but normalized to maximum intensity of the ENDOR signal. Dotted grey lines show the relative baseline.

C Static Hamiltonian simulation code

```
%% ENDOR simulation script
%%%%%%%%%%%
clear
tic
%% Natural Constants and Conversion Factors
H = 6.62607015 * 10^-34;          % J*s Planck Constant
MU_B = 9.274010783 * 10^-24;      % J/T Bohr Magneton
MU_N = 5.0507837461 * 10^-27;     % J/T nuclear Magneton
G_E =  2.00231930436256;          % G-factor electron

Nucleus_EPR='14N';
Nucleus_ENDOR='17O';
%g_N_EPR = 0.40376100;            % g_N of 14N, reference see line 33
%g_N_ENDOR = -0.7575 ;            % g_N of 17O,
g_N_EPR=nucgval(Nucleus_EPR);     % Easyspin
g_N_ENDOR=nucgval(Nucleus_ENDOR); % Easyspin
% unless other Ref given: National Institute of Standard and Technology 2019

%% Parameters for Simulation %%%%%%%%%%
Ntheta = 200;                     % No.of increments for the powder average
```

```
Nphimax = 200;
g = diag([2.00913    2.00633    2.00233]); % g_xyz values of nitroxide radical

Nuclei_ENDOR = ([2.5]);               % ENDOR spin quantum number(s)
Ni_ENDOR = size(Nuclei_ENDOR,2);      % number of coupled nuclei for ENDOR

Nuclei_EPR = ([1]);               % EPR spin quantum number
Ni_EPR = size(Nuclei_EPR,2);      % number of coupled nuclei for EPR spectrum

%ENDOR Nucleus

A_ten=[0.43 0.66 0.7 ]; %in MHz
A_Frame=[0 0 0]; % ind deg
P_ten=[-0.02 -0.32 0.34]; %in MHz
P_Frame=[0 0 0]; % in deg

% A_ten=[1 1 2]; %in MHz
% A_Frame=[0 0 0]; % ind deg
% P_ten=[0 0 0]; %in MHz
% P_Frame=[0 0 0]; % in deg

% HF coupling constants
L(1,1:3) = A_ten;
L(1,4:6) = A_Frame;
L(1,7:9) = P_ten;
L(1,10:12) = P_Frame;

% EPR Nucleus
M(1,1:3) = [13,13,94];                    % 14N values in MHz
M(1,4:6) = [0,0,0]    ;                   % alpha ,beta, gamma
M(1,7:9) = [+1.3 +0.5 -1.8];              % Quadrupole values in MHz
M(1,10:12) = [0,0,0];                     % Euler angles

% Measurement Parameters
FreqMeas = 94e9;                          % MW frequencz in Hz
FieldOffset=0.0;                         % correction factor for 263 GHz spectrometer in
    Gauss
Endordelta = 0.001;   % resolution of ENDOR spectrum, in MHz (i.e. histogram bin size)
EndorSw = 6;          % RF sweep range for simulation, MHz
endormin = -EndorSw/2;
endormax = EndorSw/2;

% Linewidth parameters.
lw = 20;                % line broadening for EPR  [MHz]
lwEnd = 0.06;         % line broadening for ENDOR [MHz]
```

```
65
66  % Field positions for ENDOR detection in Gauss
67  % 94 GHz W-band
68  ObsField{1}=33425;              % B||g1
69  ObsField{2}=33470;              % B||g2
70  ObsField{3}=33535;              % B||g3
71
72  % Field Correction with Offset
73  for i=1:length(ObsField)
74      ObsField{i}=ObsField{i}-FieldOffset;
75  end
76
77  chosenfield = 2; % Observerfield
78  larmor = larmorfrq(Nucleus_ENDOR,ObsField{chosenfield}/10);
79
80  % Frequency range for calculation of EPR spectrum at 94 GHz
81  freq_min = 93.3e9; % in Hz
82  freq_max = 94.4e9; % in Hz
83  delta_freq = 1e6;  % in Hz
84
85  % Mims blindspot calculation
86  Mims_blindspot = false;
87  tau = 850;                  % in ns
88
89  %excitation pulse length in ENDOR
90  probe_pi=80;         % pulse length for a mw pi pulse in ns
91
92  %simulation mode
93  transition_probability = true ; %calculate with Ix operator ?
94
95  % what will be plotted
96  plot_EPR  = false;      % plot EPR?
97  plot_ENDOR = true;      % plot ENDOR?
98  plot_sum_ENDOR = false; % plot summed ENDOR spectrum over all orientations
99
100 % save results?
101 save_EPR = false;       % EPR?
102 save_ENDOR = false;     % ENDOR?
103 save_sum_ENDOR = false; % summed ENDOR spectrum over all orientations
104
105 %%%%%%%%%%%%%%%%%%% SIMULATION %%%%%%%%%%%%%%%%%%%
106 %% Spin Operator Definitions
107 % Adapted from Easyspin/Examples/Varia/Spinopxyz.m
108 % Define the Electron Spin operators in S eigenbasis
109 S = 1/2;
```

```
S_id = eye(2*S+1);
Sz0 = diag(S:-1:-S);
Svalues = sqrt((1:2*S).*(2*S:-1:1));
Sp0 = diag(Svalues,+1);
Sm0 = diag(Svalues,-1);
Sx0 = (Sp0 + Sm0)/2;
Sy0 = (Sp0 - Sm0)/2i;

%Define the EPR Nuclear Spin operators in I eigenbasis
I_EPR = Nuclei_EPR;
I_id_EPR = eye(2*I_EPR+1);
Iz0_EPR = diag(I_EPR:-1:-I_EPR);
Ivalues_EPR = sqrt((1:2*I_EPR).*(2*I_EPR:-1:1));
Ip0_EPR = diag(Ivalues_EPR,+1);
Im0_EPR = diag(Ivalues_EPR,-1);
Ix0_EPR = (Ip0_EPR + Im0_EPR)/2;
Iy0_EPR = (Ip0_EPR - Im0_EPR)/2i;

%Define the ENDOR Nuclear Spin operators in I eigenbasis
I_ENDOR = Nuclei_ENDOR;
I_id_ENDOR = eye(2*I_ENDOR+1);
Iz0_ENDOR = diag(I_ENDOR:-1:-I_ENDOR);
Ivalues_ENDOR = sqrt((1:2*I_ENDOR).*(2*I_ENDOR:-1:1));
Ip0_ENDOR = diag(Ivalues_ENDOR,+1);
Im0_ENDOR = diag(Ivalues_ENDOR,-1);
Ix0_ENDOR = (Ip0_ENDOR + Im0_ENDOR)/2;
Iy0_ENDOR = (Ip0_ENDOR - Im0_ENDOR)/2i;

% Transform EPR operators into the (S= 1/2, I = 1) eigenbasis
Sx_EPR=kron(Sx0,I_id_EPR);
Sy_EPR=kron(Sy0,I_id_EPR);
Sz_EPR=kron(Sz0,I_id_EPR);
Sop_EPR={Sx_EPR; Sy_EPR; Sz_EPR};

Ix_EPR=kron(S_id,Ix0_EPR);
Iy_EPR=kron(S_id,Iy0_EPR);
Iz_EPR=kron(S_id,Iz0_EPR);
Iop_EPR={Ix_EPR;Iy_EPR;Iz_EPR};

% Transform ENDOR operators into the large eigenbasis
Sx_ENDOR=kron(Sx0,I_id_ENDOR);
Sy_ENDOR=kron(Sy0,I_id_ENDOR);
Sz_ENDOR=kron(Sz0,I_id_ENDOR);
Sop_ENDOR={Sx_ENDOR; Sy_ENDOR; Sz_ENDOR};

```

```
Ix_ENDOR=kron(S_id,Ix0_ENDOR);
Iy_ENDOR=kron(S_id,Iy0_ENDOR);
Iz_ENDOR=kron(S_id,Iz0_ENDOR);
Iop_ENDOR={Ix_ENDOR;Iy_ENDOR;Iz_ENDOR};

%% Parameter calculation
B = [0    0    ObsField{chosenfield}]*10^-4; % in T
% transform ENDOR coupling tensors into g Frame
for k = 1:Ni_ENDOR
    alpha = L(k,4)*pi/180;
    beta = L(k,5)*pi/180;
    gamm = L(k,6)*pi/180;
    RA(1,1) = cos(beta)*cos(alpha)*cos(gamm) - sin(alpha)*sin(gamm);
    RA(1,2) = cos(beta)*sin(alpha)*cos(gamm) + cos(alpha)*sin(gamm);
    RA(1,3) = -sin(beta)*cos(gamm);
    RA(2,1) = -cos(beta)*cos(alpha)*sin(gamm) - sin(alpha)*cos(gamm);
    RA(2,2) = -cos(beta)*sin(alpha)*sin(gamm) + cos(alpha)*cos(gamm);
    RA(2,3) = sin(beta)*sin(gamm);
    RA(3,1) = sin(beta)*cos(alpha);
    RA(3,2) = sin(beta)*sin(alpha);
    RA(3,3) = cos(beta);

    X = RA*diag(L(k,1:3))*RA';
    A_g_ENDOR((k-1)*3+1:(k-1)*3+3,:) = X; % A TENSOR in g Frame

    if size(L,2)>6
        alphaQ = L(k,10)*pi/180;
        betaQ = L(k,11)*pi/180;
        gammQ = L(k,12)*pi/180;
        RQ(1,1) = cos(betaQ)*cos(alphaQ)*cos(gammQ) - sin(alphaQ)*sin(gammQ);
        RQ(1,2) = cos(betaQ)*sin(alphaQ)*cos(gammQ) + cos(alphaQ)*sin(gammQ);
        RQ(1,3) = -sin(betaQ)*cos(gammQ);
        RQ(2,1) = -cos(betaQ)*cos(alphaQ)*sin(gammQ) - sin(alphaQ)*cos(gammQ);
        RQ(2,2) = -cos(betaQ)*sin(alphaQ)*sin(gammQ) + cos(alphaQ)*cos(gammQ);
        RQ(2,3) = sin(betaQ)*sin(gammQ);
        RQ(3,1) = sin(betaQ)*cos(alphaQ);
        RQ(3,2) = sin(betaQ)*sin(alphaQ);
        RQ(3,3) = cos(betaQ);
        Y = RQ*diag(L(k,7:9))*RQ';
        P_g_ENDOR((k-1)*3+1:(k-1)*3+3,:) = Y; % Q TENSOR in g Frame
    end
end

% transform EPR coupling tensors into g Frame
for k = 1:Ni_EPR
```

```
    alpha = M(k,4)*pi/180;
    beta = M(k,5)*pi/180;
    gamm = M(k,6)*pi/180;
    RA(1,1) = cos(beta)*cos(alpha)*cos(gamm) - sin(alpha)*sin(gamm);
    RA(1,2) = cos(beta)*sin(alpha)*cos(gamm) + cos(alpha)*sin(gamm);
    RA(1,3) = -sin(beta)*cos(gamm);
    RA(2,1) = -cos(beta)*cos(alpha)*sin(gamm) - sin(alpha)*cos(gamm);
    RA(2,2) = -cos(beta)*sin(alpha)*sin(gamm) + cos(alpha)*cos(gamm);
    RA(2,3) = sin(beta)*sin(gamm);
    RA(3,1) = sin(beta)*cos(alpha);
    RA(3,2) = sin(beta)*sin(alpha);
    RA(3,3) = cos(beta);

    X = RA*diag(M(k,1:3))*RA';
    A_g_EPR((k-1)*3+1:(k-1)*3+3,:) = X; % A tensor in g Frame

    if size(M,2)>6
        alphaQ = M(k,10)*pi/180;
        betaQ = M(k,11)*pi/180;
        gammQ = M(k,12)*pi/180;
        RQ(1,1) = cos(betaQ)*cos(alphaQ)*cos(gammQ) - sin(alphaQ)*sin(gammQ);
        RQ(1,2) = cos(betaQ)*sin(alphaQ)*cos(gammQ) + cos(alphaQ)*sin(gammQ);
        RQ(1,3) = -sin(betaQ)*cos(gammQ);
        RQ(2,1) = -cos(betaQ)*cos(alphaQ)*sin(gammQ) - sin(alphaQ)*cos(gammQ);
        RQ(2,2) = -cos(betaQ)*sin(alphaQ)*sin(gammQ) + cos(alphaQ)*cos(gammQ);
        RQ(2,3) = sin(betaQ)*sin(gammQ);
        RQ(3,1) = sin(betaQ)*cos(alphaQ);
        RQ(3,2) = sin(betaQ)*sin(alphaQ);
        RQ(3,3) = cos(betaQ);
        Y = RQ*diag(M(k,7:9))*RQ';
        P_g_EPR((k-1)*3+1:(k-1)*3+3,:) = Y; % Q TENSOR in g Frame
    end
end

% Frequency Axis of EPR Spectrum
Npts_epr_freq=round((freq_max - freq_min)/delta_freq);
freq = linspace(freq_min,freq_max,Npts_epr_freq);
epr_amp_tensor_freq = zeros(Npts_epr_freq,1);

% Number of points in ENDOR dimension
NptsE = round(EndorSw/Endordelta)+1;

%ENDOR PREPARATION FUNCTION
W1 = pi/(probe_pi*1e-9);      %in rad/s-1

```

```
% Calculate list of theta and phi values to allow parfor loop for EPR
or_all=0;
for ii = 1:Ntheta
    theta = ii*pi/Ntheta;
    Nphi = round(sin(theta)*Nphimax);
    for jj = 1:Nphi
        or_all=or_all+1;
        phi = (jj-1)*pi*2/(Nphi-1);
        orientation_list(or_all,:)=[or_all theta phi];
    end
end

%% EPR calculation
tic
parfor ii = 1:or_all
    %initialyze arrays
    temp_epr_amp_tensor_freq=zeros(Npts_epr_freq,1);

    %retrieve previously generated variables
    orientation=orientation_list(ii,:);
    orientation_id=orientation(1);
    theta=orientation(2);
    phi=orientation(3);
    A_g_EPR_or=A_g_EPR*1e6; %in Hz, HF Couplings for EPR
    P_g_EPR_or=P_g_EPR*1e6; % in Hz, NQ Couplings for EPR

    A_g_ENDOR_or=A_g_ENDOR*1e6;
    P_g_ENDOR_or=P_g_ENDOR*1e6;

    R1 = zeros(3);

    % Rotation matrix into lab system
    R1(1,1) = cos(theta)*cos(phi);
    R1(1,2) = cos(theta)*sin(phi);
    R1(1,3) = -sin(theta);
    R1(2,1) = -sin(phi);
    R1(2,2) = cos(phi);
    R1(2,3) = 0;
    R1(3,1) = sin(theta)*cos(phi);
    R1(3,2) = sin(theta)*sin(phi);
    R1(3,3) = cos(theta);

    % g tensor rotation into Lab frame
    grot = R1*g*R1';

```

```
290     %ENDOR Nuclei
291     A_ENDOR=zeros(3,3,Ni_ENDOR);
292     P_ENDOR=zeros(3,3,Ni_ENDOR);
293
294     for m = 1:Ni_ENDOR
295         hf2 = A_g_ENDOR_or((m-1)*3+1:(m-1)*3+3,:);
296         X2 = R1*hf2*R1';
297         A_ENDOR(:,:,m)=X2;
298
299         qq2 = P_g_ENDOR_or((m-1)*3+1:(m-1)*3+3,:);
300         Y2 = R1*qq2*R1';
301         P_ENDOR(:,:,m)=Y2;
302     end
303
304     % EPR Nuclei
305     A_EPR=zeros(3,3,Ni_EPR);
306     P_EPR=zeros(3,3,Ni_EPR);
307     for m = 1:Ni_EPR
308         hf2 = A_g_EPR_or((m-1)*3+1:(m-1)*3+3,:);
309         X2 = R1*hf2*R1';
310         A_EPR(:,:,m)=X2;
311
312         qq2 = P_g_EPR_or((m-1)*3+1:(m-1)*3+3,:);
313         Y2 = R1*qq2*R1';
314         P_EPR(:,:,m)=Y2;
315     end
316
317     %EPR Calculation
318     H_HF_EPR=zeros(size(Sz_EPR));
319     H_NQI_EPR=zeros(size(Sz_EPR));
320
321     H_EZ_EPR = MU_B*grot(3,3)*B(3)*Sz_EPR/H; %in Hz
322     H_NZ_EPR = MU_N*g_N_EPR*(B(1)*Ix_EPR + B(2)*Iy_EPR + B(3)*Iz_EPR)/H; %in Hz
323
324     H_HF_EPR = Iz_EPR * A_EPR(3,3) * Sz_EPR + Ix_EPR *(A_EPR(1,3)^2+A_EPR(2,3)^2)^0.5 *
            Sz_EPR % H_HF = ASzIz + BSzIx
325
326     %Calculate EPR NQI Hamiltonian Q*I*I in Hz
327     for m = 1:Ni_EPR
328         for k=1:size(Iop_EPR,1)
329             for t=1:size(Iop_EPR,1)
330                 H_NQI_EPR = H_NQI_EPR + P_EPR(k,t,m)*Iop_EPR{k}*Iop_EPR{t};
331             end
332         end
333     end
```

```
334
335     %Calculate the EPR Spin Hamiltonian in Hz (neglecting 19F for orientation selection)
336     H_S_EPR = H_EZ_EPR - H_NZ_EPR + H_HF_EPR + H_NQI_EPR;
337
338     % Diagonalize and calculate eigenvalues of the EPR Hamiltonian
339     [V_EPR,E_EPR] = eig(H_S_EPR); % E ... Hamiltonian Elements, V... eigenvectors
340     V_EPR=round((V_EPR),9); % round necessary for following calculation
341     E_EPR=real(diag(E_EPR));
342
343     %initiallyze freq matrices
344     freq_EPR = zeros(1,length(V_EPR)*length(V_EPR));
345     trans_prob_EPR = zeros(1,length(V_EPR)*length(V_EPR));
346
347     % Calculate transitions between all elements
348     q=1;
349     for x=1:length(V_EPR)
350         for y=1:length(V_EPR)
351             trans_prob_EPR(q)=abs(round((V_EPR(:,x))'*Sx_EPR*(V_EPR(:,y)),9))^2; %<x|S_x|
                    y>^2 , x/y are the eigenvectors
352             freq_EPR(q)= abs(E_EPR(x)-E_EPR(y)); %in Hz, Transition Frequency
353
354             %Select EPR Transitions with frequency threshhold value (1 GHz)
355             if freq_EPR(q)<1e9
356                 trans_prob_EPR(q)=0;
357             end
358             q=q+1;
359         end
360     end
361
362     EPR_Resonances =[freq_EPR' trans_prob_EPR' grot(3,3)*ones(length(freq_EPR),1)];
363
364     %EPR Frequency Spectrum
365     for p = 1:length(EPR_Resonances)
366         if trans_prob_EPR(p)>0
367             bin_freq = round((EPR_Resonances(:,1)- freq_min)/delta_freq) + 1; %scale
                    resonance to freq axis bin
368             temp_epr_amp_tensor_freq(bin_freq(p)) = temp_epr_amp_tensor_freq(bin_freq(p))
                     + EPR_Resonances(p,2);
369         end
370     end
371
372     Resonances{ii} = EPR_Resonances;
373     ENDOR_values{ii} = [A_ENDOR,P_ENDOR]; % parameters for ENDOR calculation
374
375     epr_amp_tensor_freq=epr_amp_tensor_freq+temp_epr_amp_tensor_freq; %EPR intensities
```

```
376
377 end
378 toc
379
380 %% Orientation selection for ENDOR
381 n_res = size(Resonances{1},1);
382 params_all = zeros(or_all*n_res,size(Resonances{1},2)+1);
383 ENDOR_params_all = zeros(size(ENDOR_values{1},1),size(ENDOR_values{1},2),or_all*n_res);
384 tic
385 count=0;
386 for ii = 1:or_all
387     %retrieve arrays
388     Res = Resonances{ii};
389     for jj = 1:n_res
390         count=count+1;
391         trans_prob =  Res(jj,2);
392         if trans_prob > 0
393             Deltaom =(Res(jj,1)-FreqMeas)*2*pi; % mw offset between resonance and
                    excitation frequency
394             scalefactor =((Deltaom^2)-(W1^2))/((Deltaom^2)+(W1^2));
395             scalefactor =(1-scalefactor)/2;
396             if scalefactor > 1e-3
397                 SF=scalefactor;
398             else
399                 SF=0;
400             end
401             params_all(count,1:3) = Res(jj,:);
402             params_all(count,4) = SF;
403             ENDOR_params_all(:,:,count) = ENDOR_values{ii};
404         end
405     end
406 end
407 toc
408
409 %sort out non excited resonances by discarding entries with scalefactor 0
410 Params_sel= params_all(logical(params_all(:,4)),:);
411 ENDOR_params_sel=ENDOR_params_all(:,:,logical(params_all(:,4)));
412
413 %% ENDOR Calculation
414 tic
415 trans_sel=size(Params_sel,1);
416 endor_amp_full = zeros(NptsE,1);
417 endor_amp_perturb = zeros(NptsE,1);
418 parfor jj = 1:trans_sel
419     % Initiallyze empty HF and NQI tensors
```

```
    H_HF_full=zeros(size(Sz_ENDOR));
    H_NQI_full=zeros(size(Sz_ENDOR));

    % Set HF and P Tensors from precalculated values
    A_ENDOR=ENDOR_params_sel(:,1:3,jj);
    P_ENDOR=ENDOR_params_sel(:,4:6,jj);
    scalefactor=Params_sel(jj,4);
    EPR_trans_prob = Params_sel(jj,2);
    g_sel=Params_sel(jj,3);
    % ------------------ HAMILTONIANS ------------------------------
    %Calculate Electron and Nuclear Zeeman Terms
    H_EZ_full = MU_B*g_sel*B(3)*Sz_ENDOR/H; %in Hz
    H_EZ_perturb = H_EZ_full;

    for m=1:Ni_ENDOR %% Here we need a loop over multiple Nuclei !!

        H_NZ_full = MU_N*g_N_ENDOR*(B(1)*Ix_ENDOR + B(2)*Iy_ENDOR + B(3)*Iz_ENDOR)/H;
        H_NZ_perturb = H_NZ_full;

        for k=1:size(Sop_ENDOR,1)
            for t=1:size(Iop_ENDOR,1)
                H_HF_full = H_HF_full + A_ENDOR(k,t,m)*Sop_ENDOR{k}*Iop_ENDOR{t};
            end
        end

        %Calculate first order perturb HF
        H_HF_perturb=A_ENDOR(3,3,m)*Sz_ENDOR*Iz_ENDOR;

        %Calculate full NQI Hamiltonian Q*I*I in MHZ
        for k=1:size(Iop_ENDOR,1)
            for t=1:size(Iop_ENDOR,1)
                H_NQI_full = H_NQI_full + P_ENDOR(k,t,m)*Iop_ENDOR{k}*Iop_ENDOR{t};
            end
        end

        %Calculate first order perturb NQI
        H_NQI_perturb=P_ENDOR(3,3,m)/2*(3*Iz_ENDOR*Iz_ENDOR-I_ENDOR*(I_ENDOR+1)*eye(size(
            Iz_ENDOR)));

        %Calculate the Full Spin Hamiltonian
        H_S_full = H_EZ_full - H_NZ_full + H_HF_full + H_NQI_full;
        H_S_perturb = H_EZ_perturb - H_NZ_perturb + H_HF_perturb + H_NQI_perturb;

        % Calculate the eigenvalues of the Hamiltonian
        [V_full,E_full] = eig(H_S_full);
```

```
464         V_full=round((V_full),9);
465         [V_perturb,E_perturb] = eig(H_S_perturb);
466         V_perturb=round((V_perturb),9);
467 
468         %Sort the eigenvectors of the system into energetic order, this is
469         %necessary to calculate the ENDOR transitions in the simple model
470         %as differences of adjacent levels
471         [~,Ind_full]=max(abs(transpose(V_full)));
472         [~,Ind_perturb]=max(abs(transpose(V_perturb)));
473 
474         E_sort_full=E_full(Ind_full,Ind_full);
475         E_sort_full=real(diag(E_sort_full));
476 
477         E_sort_perturb=E_perturb(Ind_perturb,Ind_perturb);
478         E_sort_perturb=real(diag(E_sort_perturb));
479 
480         E_full=real(diag(E_full));
481         E_perturb = real(diag(E_perturb));
482 
483         %initiallyze matices for transistion probability calculation
484         freq_SF_full=zeros(1,length(V_full)*length(V_full));
485         freq_SF_perturb=zeros(1,length(V_full)*length(V_full));
486         trans_prob_full=zeros(1,length(V_full)*length(V_full));
487         trans_prob_perturb=zeros(1,length(V_full)*length(V_full));
488 
489         % initiallyze matrices for simple adjacent subtraction calculation
490         freq_simple_full=zeros(1,length(E_sort_full)-1);
491         freq_simple_perturb=zeros(1,length(E_sort_perturb)-1);
492 
493         if transition_probability==true %Calculate nuclear Frequencies via the Ix
                operator
494             q=1;
495             for x=1:length(V_full)
496                 for y=1:length(V_full)
497                     trans_prob_full(q)=abs(round((V_full(:,x))'*Ix_ENDOR*(V_full(:,y)),3)
                        )^2;
498                     trans_prob_perturb(q)=abs(round((V_perturb(:,x))'*Ix_ENDOR*(V_perturb
                        (:,y)),3))^2;
499                     freq_SF_full(q)= abs(E_full(x)-E_full(y));
500                     freq_SF_perturb(q)= abs(E_perturb(x)-E_perturb(y));
501                     q=q+1;
502                 end
503             end
504         else % Calculate nuclear frequencies as difference between adjacent energy levels
505 
```

```
            for z=2:length(E_sort_full)
                freq_simple_full(z-1)=abs(E_sort_full(z)-E_sort_full(z-1));
                freq_simple_perturb(z-1)=abs(E_sort_perturb(z)-E_sort_perturb(z-1));
            end
            %Find Transition with largest Frequency -> this is the
            %transition between ms manifolds
            [max_freq_full,max_freq_ind_full]=max(abs(freq_simple_full));
            [max_freq_perturb,max_freq_ind_perturb]=max(abs(freq_simple_perturb));

            %Delete central transistion between electron spin manifolds
            freq_simple_full(max_freq_ind_full)=[];
            freq_simple_perturb(max_freq_ind_perturb)=[];

        end

        %initiallize temporary ENDOR spectra matrices, necessary for PARFOR
        temp_amp_full = zeros(NptsE,1);
        temp_amp_perturb = zeros(NptsE,1);
        ebinmax = NptsE;
        if transition_probability==true
            ebin_full = round((freq_SF_full/1e6 - (endormin+larmor))/Endordelta)+1;
            for k = 1:length(ebin_full)      % take only resonances in desired spectral
                range
                if      0 < ebin_full(k)
                    if ebin_full(k) <= ebinmax
                        temp_amp_full(ebin_full(k)) = temp_amp_full(ebin_full(k)) +
                            scalefactor*trans_prob_full(k);
                    end
                end
            end

            ebin_perturb = round((freq_SF_perturb/1e6 - (endormin+larmor))/Endordelta)+1;
            for k = 1:length(ebin_perturb)      % take only resonances in desired
                spectral range
                if      0 < ebin_perturb(k)
                    if ebin_perturb(k) <= ebinmax
                        temp_amp_perturb(ebin_perturb(k)) = temp_amp_perturb(ebin_perturb
                            (k)) + scalefactor*trans_prob_perturb(k);
                    end
                end
            end
        else % Line intesity is uniformly one
            ebin_full = round((freq_simple_full/1e6 - (endormin+larmor))/Endordelta)+1;
            ebin_perturb = round((freq_simple_perturb/1e6 - (endormin+larmor))/Endordelta
                )+1;
```

```
546             for k = 1:length(ebin_full)      % take only resonances in desired spectral
                    range
547                 if      0 < ebin_full(k)
548                     if ebin_full(k) <= ebinmax
549                         temp_amp_full(ebin_full(k)) = temp_amp_full(ebin_full(k)) +
                                scalefactor;
550                     end
551                 end
552             end %full
553             for k = 1:length(ebin_perturb)      % take only resonances in desired
                    spectral range
554                 if      0 < ebin_perturb(k)
555                     if ebin_perturb(k) <= ebinmax
556                         temp_amp_perturb(ebin_perturb(k)) = temp_amp_perturb(ebin_perturb
                                (k)) + scalefactor;
557                     end
558                 end
559             end
560         end % trans prob if
561         endor_amp_full=endor_amp_full+temp_amp_full*EPR_trans_prob;
562         endor_amp_perturb=endor_amp_perturb+temp_amp_perturb*EPR_trans_prob;
563
564     end %Ni_ENDOR loop
565 end % ori loop
566 toc
567
568 %% CONVOLUTION
569 % Convolve EPR with a Gaussian
570 Delta=(lw*10^6*pi/((freq_max - freq_min)*sqrt(2*log(2))))^2;  % Conversion of line width
        to line broadening factor
571 Intens1_tensor_freq = ifft(epr_amp_tensor_freq);
572 Intens_tensor_freq = zeros(1,Npts_epr_freq);
573 for i = 1:Npts_epr_freq
574     Intens_tensor_freq(i) = Intens1_tensor_freq(i)*exp(-Delta*i^2/2);   % Gaussian line
            shape
575 end
576 Intens1_tensor_freq = fft(Intens_tensor_freq);
577 Intens1_tensor_freq=Intens1_tensor_freq-Intens1_tensor_freq(1); % Subtract first
        datapoint to account for FFT baseline offset
578 ConvolvedEPR = real(Intens1_tensor_freq/max(real(Intens1_tensor_freq)));
579
580 % Convolve the Endor dimension with a Lorentzian line width
581
582 Deltaend = lwEnd*pi/(EndorSw);          % Conversion of line width into a linebroadening
        factor used for FT
```

```
endintens=zeros(1,NptsE);
endintens1 = ifft(endor_amp_full);
for ii = 1:NptsE
    endintens(ii) = endintens1(ii)*exp(-Deltaend*ii);   % Lorentzian line shape
end
endamp_conv = real(fft(endintens));
endamp_conv = endamp_conv - endamp_conv(1); % Subtract first datapoint to account for FFT baseline offset

% normalization of ENDOR spectrum
amplitude_full=(endamp_conv-min(endamp_conv))/(max(endamp_conv)-min(endamp_conv));
Deltaend = lwEnd*pi/(EndorSw);          % Conversion of line width into a linebroadening factor used for FT
endintens=zeros(1,NptsE);
endintens1 = ifft(endor_amp_perturb);
for ii = 1:NptsE
    endintens(ii) = endintens1(ii)*exp(-Deltaend*ii);   % Lorentzian line shape
end
endamp_conv = real(fft(endintens));
endamp_conv = endamp_conv - endamp_conv(1); % Subtract first datapoint to account for FFT baseline offset

% normalization of ENDOR spectrum
amplitude_perturb=(endamp_conv-min(endamp_conv))/(max(endamp_conv)-min(endamp_conv));
endfreq=linspace(EndorSw/(-2),EndorSw/(2),NptsE);

% EPR field axis
g_axis = freq*H/(MU_B * B(3));
field_axis=zeros(1,Npts_epr_freq);
for ii = 1:size(g_axis,2)
    field_axis(ii) = H*FreqMeas/(MU_B*g_axis(ii)); % in T
end

%% PLOTTING AND SAVING
% plot EPR spectrum
if plot_EPR == true
    %Visualize excitation window
    Deltaom_ex =(freq-FreqMeas)*2*pi;
    scalefactor_ex=zeros(length(Deltaom_ex),1);
    for i=1:length(Deltaom_ex)
        sf_ex =((Deltaom_ex(i)^2)-(W1^2))/((Deltaom_ex(i)^2)+(W1^2));
        scalefactor_ex(i) =(1-sf_ex)/2;
    end
    figure('Renderer','painters')
    box on
```

```
    hold on
    plot(freq*10^-9,ConvolvedEPR)
    plot(freq*10^-9,scalefactor_ex);
    xline(FreqMeas*10^-9);
    xlabel('mw Frequency/GHz')
    ylabel('norm. Intensity/a.u.')
    hold off
    figure('Renderer','painters')
    plot(field_axis*1e3,ConvolvedEPR)
    xlabel('magnetic Field/mT')
    ylabel('norm. Intensity/a.u.')
end
% save EPR spectrum
if save_EPR == true
    data_EPR=[field(:) ConvolvedEPR(:)];
    save('EPR','data_EPR','-ascii');
end
%plot the simulated spectra and measured ENDOR spectra
if plot_ENDOR == true
    figure
    hold on
    plot(endfreq,amplitude_full);
    plot(endfreq,amplitude_perturb+1);
    hold off
    data=[endfreq(:) amplitude_full(:)];
end
%save the simulated spectra
if save_ENDOR==true
    cur_amplitude=amplitude_full{ff};
    data=[endfreq(:) cur_amplitude(:)];
    save(['AM100_263_sim_',num2str(chosenfield),'.dat'],'data','-ascii');
end
```

D Spin dynamics simulation code

```
% Example for simulating small quantum systems
% relevant to nuclear magnetic resonance.
% The system consists of an electron spin
% and a nuclear spin.
% Robert Zeier, 2016, zeier@tum.de
% (adapted from cosy_demo.m by
% Michael Tesch, 2016, michael.tesch@tum.de)
% adapted version Oct 2020 AK
% selective mw pulse operator Sx instead SxIa
```

```
% selective RF pulse operator Iy for all RF positions
% powder pattern as sum over all possible orientations
% adapted version April2021 FH
% Orientation Preselection Implemented

clear
tic
%--------------------SPIN SYSTEM PARAMETERS ------------------------------
g=[2.00263   2.00260    2.00257]; % diagonal g Tensor
% g=[2.0063   2.0042    2.00257]; % diagonal g Tensor
g = diag(g);
g2 = g*g;
g_iso=(g(1,1)+g(2,2)+g(3,3))/3;

%ENDOR Nuclei
A_ten=[-2 1 1]; %in MHz
A_frame=[0 0 0]; % in deg
Q_ten=[0 0 0]; %in MHz
Q_frame=[0 0 0]; % in deg

% A_ten=[0.43 0.66 0.7]; %in MHz
% A_frame=[49 168 -67]; % in deg
% Q_ten=[-0.02 -0.32 0.34]; %in MHz
% Q_frame=[-39 87 -22]; % in deg

L(1,1:3) = A_ten*10^6;           % Hf constants /CONST1
L(1,4:6) = A_frame;              % Euler angles alpha ,beta, gamma !!!
L(1,7:9) = Q_ten*10^6;
L(1,10:12) = Q_frame;
Ni_ENDOR = size(L,1);

%EPR Nuclei
% M(1,1:3) = [20 20 90]*10^6;
% M(1,4:6) = [0 0 0];
Nuc_Spin_EPR = [1];
Mi_EPR=BuildSpace(Nuc_Spin_EPR); % Generate Nuclear Spin orientations for EPR calculation
Ni_EPR=0;

%Define the Electron Spin operators in general
S = 1/2;
id_S = eye(2*S+1);
Svalues = sqrt((1:2*S).*(2*S:-1:1));
sigma_Sp = diag(Svalues,+1);
sigma_Sm = diag(Svalues,-1);
sigma_Sx = (sigma_Sp + sigma_Sm)/2;
```

```
55 sigma_Sy = (sigma_Sp - sigma_Sm)/2i;
56 sigma_Sz = diag(S:-1:-S);
57
58 %Define the Nuclear Spin operators in general
59 I = 1/2;
60 id_I = eye(2*I+1);
61 Ivalues = sqrt((1:2*I).*(2*I:-1:1));
62 sigma_Ip = diag(Ivalues,+1);
63 sigma_Im = diag(Ivalues,-1);
64 sigma_Ix = (sigma_Ip + sigma_Im)/2;
65 sigma_Iy = (sigma_Ip - sigma_Im)/2i;
66 sigma_Iz = diag(I:-1:-I);
67
68 % alpha and beta operators % REDIFINE FOR GENERAL CASE
69 alpha_S = [1 0; 0 0];
70 beta_S = [0 0; 0 1];
71 alpha_I = [1 0; 0 0];
72 beta_I = [0 0; 0 1];
73
74 % spin operators
75 Sx = kron(sigma_Sx, id_I);
76 Sy = kron(sigma_Sy, id_I);
77 Sz = kron(sigma_Sz, id_I);
78 Sop={Sx; Sy; Sz};
79 Ix = kron(id_S, sigma_Ix);
80 Iy = kron(id_S, sigma_Iy);
81 Iz = kron(id_S, sigma_Iz);
82 Iop={Ix;Iy;Iz};
83
84 % Have to be redefined for the general case
85 Sa = kron(alpha_S, id_I);
86 Sb = kron(beta_S, id_I);
87 Ia = kron(id_S, alpha_I);
88 Ib = kron(id_S, beta_I);
89
90 %MW pulse Length
91 tp_MW = 100; % in ns
92 tau = 1000;
93 % tau = [200 400] ; % in ns
94 % tau   = [200 400 600 1000 1200 1400 1600] ; % in ns
95 tp_RF = 60; %in us
96
97 %Consider Ideal pulses (no Hfree during pulses)
98 ideal_pulse=1; %disable Hfree during mw Pulses
99
```

```
%time intervals
t1 = tp_MW*10^(-9); %seconds pi/2 pulse
t2 = tau*10^(-9);   %seconds delay
t3 = tp_MW*10^(-9);  %seconds pi/2 pulse
t4 = 1*10^(-6);   %seconds delay
t5 = tp_RF*10^(-6); %seconds  RF
t6 = 1*10^(-6); %seconds delay
t7 = tp_MW*10^(-9); %seconds  pi/2
t8 = tau*10^(-9); %seconds delay

%Parameters for Powder Averaging

Ntheta = 100;
Nphimax = Ntheta;

%----------------CONSTANT DEFINITIONS-------------------------------
k_B=2.0836618E10; %Boltzmann Constant Hz K-1
ge=28024.95266E6; %MHz/Tesla
gn=42.576E6;% proton Larmor MHz/Tesla
CONST1=2.81; %G to MHz conversion
T = 298;          %K
Temp_Eff=1;

% sel_trans = -1;                       % preparation selective on +1=alpha EPR
    transition or -1=beta EPR transition
omega_1e = pi/(2*t1);    % MW amplitude pi/2 pulse
omega_1n = pi/t5;        % RF amplitude pi pulse

% omega1e in T for orientation preselection
pulsewidth = omega_1e/(2*pi*1e6*CONST1*1e4);

FreqMeas=94*10^9;    % in Hz
vmw = FreqMeas; %Microwave Frequency
FieldOffset=0*10^-4; % in T
ObsField{1}=FreqMeas*6.62607*10^-34/(g(2,2)*9.27401*10^-24); % B||gy
vepr=FreqMeas*6.62607*10^-34/(9.27401*10^-24)-FieldOffset*g_iso;        %(g*B0)
fieldCenter=vepr/g_iso;

% EPR SPECTRUM Simulation Parameters
plot_EPR = 0; %Plot EPR Spectrum 1 = yes, 0 = no
deltafield = 0.01*10^-4; %EPR Field sweep interval in T
fieldrange = 200*10^-4; %Sweep around Center in T
DeltaEPR = 0.001; % EPR Gaussian Line Broadening

%EPR x-axis definition
```

```
144 fieldmin = fieldCenter-fieldrange/2;  % Field sweep range for simulation
145 fieldmax = fieldCenter+fieldrange/2;
146 Npts = round((fieldmax - fieldmin)/deltafield)+1; % number of points in Field dimension
147 field = linspace(fieldmin,fieldmax,Npts);
148
149 % ENDOR Spectrum Parameters
150 res_EN = 0.01*10^6;   % in Hz
151 range_EN = 2*max(abs(L(1,1:3)));           % ENDOR x-axis width
152 range_EN = 6e6;           % ENDOR x-axis width
153
154 ff = 1;
155 v_L = gn*ObsField{ff}*10^6;                     % Hz    Nuclar larmor frequency
156 % range_EN = 16*10^6;           % ENDOR x-axis width
157
158 plot_ENDORtens = 1; %Calculate and plot ENDOR Spectrum without time domaine 1 = yes, 0 =
        no
159 om1r = 25*10^6; %in MHz
160 om1=1.55*om1r;
161
162 %ENDOR Line Broadening
163 Lorentian = 0;  %Lorentian broadening yes=1, no=0
164 Deltaend_L = 0.02;
165 Gaussian = 1;   %Gaussian broadening yes=1, no=0
166 Deltaend_G = 0.001;
167 slots_iter_EN = range_EN/res_EN;                % 1001;
168 start_EN = v_L-range_EN/2;                      % max(abs(L(1,1:3)));   % ENDOR start x-
        axis
169 step_EN = range_EN/(slots_iter_EN-1);           % X-Axis steps
170 x_coords = zeros(slots_iter_EN,1);
171 for aa = 1:slots_iter_EN
172     x_coords(aa) = start_EN + (aa-1)*step_EN-v_L;
173 end
174
175 % FOR PURE TENSOR SIMULATION
176 endor_amp_tens=zeros(slots_iter_EN,1);
177 endor_freq_tens=x_coords*10^(-6);
178 endormin=endor_freq_tens(1);
179 endormax=endor_freq_tens(end);
180 endstep=res_EN*10^-6;
181 Deltaend_tens=0.004;
182 %----------------------Tensor Rotation-----------------------------------------
183 for k = 1:Ni_EPR
184     alpha = M(k,4)*pi/180;
185     beta = M(k,5)*pi/180;
186     gamm = M(k,6)*pi/180;
```

```
    R(1,1) = cos(beta)*cos(alpha)*cos(gamm) - sin(alpha)*sin(gamm);
    R(1,2) = cos(beta)*sin(alpha)*cos(gamm) + cos(alpha)*sin(gamm);
    R(1,3) = -sin(beta)*cos(gamm);
    R(2,1) = -cos(beta)*cos(alpha)*sin(gamm) - sin(alpha)*cos(gamm);
    R(2,2) = -cos(beta)*sin(alpha)*sin(gamm) + cos(alpha)*cos(gamm);
    R(2,3) = sin(beta)*sin(gamm);
    R(3,1) = sin(beta)*cos(alpha);
    R(3,2) = sin(beta)*sin(alpha);
    R(3,3) = cos(beta);
    X = R*diag(M(k,1:3))*R';
    A_EPR((k-1)*3+1:(k-1)*3+3,:) = X;
end

for k = 1:Ni_ENDOR
    alpha = L(k,4)*pi/180;
    beta = L(k,5)*pi/180;
    gamm = L(k,6)*pi/180;
    R(1,1) = cos(beta)*cos(alpha)*cos(gamm) - sin(alpha)*sin(gamm);
    R(1,2) = cos(beta)*sin(alpha)*cos(gamm) + cos(alpha)*sin(gamm);
    R(1,3) = -sin(beta)*cos(gamm);
    R(2,1) = -cos(beta)*cos(alpha)*sin(gamm) - sin(alpha)*cos(gamm);
    R(2,2) = -cos(beta)*sin(alpha)*sin(gamm) + cos(alpha)*cos(gamm);
    R(2,3) = sin(beta)*sin(gamm);
    R(3,1) = sin(beta)*cos(alpha);
    R(3,2) = sin(beta)*sin(alpha);
    R(3,3) = cos(beta);
    X = R*diag(L(k,1:3))*R';
    A((k-1)*3+1:(k-1)*3+3,:) = X;

    if exist('Q_ten','var')==1
        alphaQ = L(k,10)*pi/180;
        betaQ = L(k,11)*pi/180;
        gammQ = L(k,12)*pi/180;
        RQ(1,1) = cos(betaQ)*cos(alphaQ)*cos(gammQ) - sin(alphaQ)*sin(gammQ);
        RQ(1,2) = cos(betaQ)*sin(alphaQ)*cos(gammQ) + cos(alphaQ)*sin(gammQ);
        RQ(1,3) = -sin(betaQ)*cos(gammQ);
        RQ(2,1) = -cos(betaQ)*cos(alphaQ)*sin(gammQ) - sin(alphaQ)*cos(gammQ);
        RQ(2,2) = -cos(betaQ)*sin(alphaQ)*sin(gammQ) + cos(alphaQ)*cos(gammQ);
        RQ(2,3) = sin(betaQ)*sin(gammQ);
        RQ(3,1) = sin(betaQ)*cos(alphaQ);
        RQ(3,2) = sin(betaQ)*sin(alphaQ);
        RQ(3,3) = cos(betaQ);
        Y = RQ*diag(L(k,7:9))*RQ';
        Q((k-1)*3+1:(k-1)*3+3,:) = Y;
    end
```

```
end
% preallocate ------------
epr_amp = zeros(Npts,1);
endor_amp_time=zeros(1,slots_iter_EN);
endor_amp_time_tau{length(tau)}=(zeros(1,slots_iter_EN));
endamp_2d_G_conv=zeros(1,slots_iter_EN);
endamp_2d_L_conv=zeros(1,slots_iter_EN);
endintens = zeros(1,slots_iter_EN);
endintens1=zeros(slots_iter_EN,1);
Nint = 8;
Nori=0;
ObsField=ObsField{ff};
or=1;
tmp_epr = zeros(Npts,1);

%----------------------Oreintation Preselection-----------------------------
for ii = 1:Ntheta
    theta = ii*pi/Ntheta;
    Nphi = round(sin(theta)*Nphimax)*1;
    for jj = 1:Nphi
        phi = (jj-1)*pi*2/(Nphi);
        dc = [cos(phi)*sin(theta) sin(phi)*sin(theta) cos(theta)];              %
            direction cosine vector
        geff = (dc*g2*dc')^.5; % effective g-Value for given theta and phi combination
        B = vepr/geff; %effective B field for given theta and phi
        veff = geff*ObsField*9.27401*10^-24/(6.62607*10^-34); % Resonance frequency for
            geff at ObsField in GHz

        HF_zz=zeros(1,Ni_ENDOR);
        for m = 1:Ni_ENDOR
            HF_zz(m) = ...
                (sin(theta))^2*(cos(phi))^2*A(3*m-2,1)...           %A11
                +(sin(theta))^2*(sin(phi))^2*A(3*m-1,2)...          %A22
                +(cos(theta))^2*A(3*m,3)...                         %A33
                +2*(sin(theta))^2*sin(phi)*cos(phi)*A(3*m-2,2)...   %A12
                +2*sin(theta)*cos(theta)*cos(phi)*A(3*m-2,3)...     %A13
                +2*sin(theta)*cos(theta)*sin(phi)*A(3*m-1,3);       %A23
        end

        HF_zz_EPR=zeros(1,Ni_ENDOR);
        for m = 1:Ni_EPR
            HF_zz_EPR(m) = ...
                (sin(theta))^2*(cos(phi))^2*A_EPR(3*m-2,1)...           %A11
                +(sin(theta))^2*(sin(phi))^2*A_EPR(3*m-1,2)...          %A22
                +(cos(theta))^2*A_EPR(3*m,3)...                         %A33
```

```
            +2*(sin(theta))^2*sin(phi)*cos(phi)*A_EPR(3*m-2,2)...   %A12
            +2*sin(theta)*cos(theta)*cos(phi)*A_EPR(3*m-2,3)...     %A13
            +2*sin(theta)*cos(theta)*sin(phi)*A_EPR(3*m-1,3);       %A23
    end

    NQI_zz=zeros(1,Ni_ENDOR);
    for m = 1:Ni_ENDOR
        NQI_zz(m) = ...
            (sin(theta))^2*(cos(phi))^2*Q(3*m-2,1)...           %Q11
            +(sin(theta))^2*(sin(phi))^2*Q(3*m-1,2)...          %Q22
            +(cos(theta))^2*Q(3*m,3)...                         %Q33
            +2*(sin(theta))^2*sin(phi)*cos(phi)*Q(3*m-2,2)...   %Q12
            +2*sin(theta)*cos(theta)*cos(phi)*Q(3*m-2,3)...     %Q13
            +2*sin(theta)*cos(theta)*sin(phi)*Q(3*m-1,3);       %Q23
    end

    if Ni_EPR>0
        E = B + Mi_EPR*(HF_zz_EPR./CONST1*10^(-10))'; %calculate EPR Resonance with
            HF only
        bin = round((E - fieldmin)/deltafield) + 1;
    else
        E=B;
        bin = round((E - fieldmin)/deltafield) + 1;
    end
    for p = 1:length(bin)
        tmp_epr(bin(p)) = tmp_epr(bin(p)) + 1; % Add resonances to EPR spectrum
    end

    DeltaB=zeros(2,1);
    for l = 1:length(E)
        DeltaB(l) = field(bin(l)) - ObsField; % Magnetic field offset in T
        if abs(DeltaB(l)) <= abs(5*pulsewidth)
            scalefactor = (DeltaB(l)^2 - pulsewidth^2)/(DeltaB(l)^2 + pulsewidth^2);
            scalefactor = (1-scalefactor)/2;
        else
            scalefactor= 0;
        end
    end
    S=((veff-vmw)^2-(omega_1e)^2)/((veff-vmw)^2+(omega_1e)^2);
    S=(1-S)/2;
    %Select only those parameters, for which scalefactor > 0
    if scalefactor>0
        geff_sel(or)=geff;
        B_sel(or)=B;
        HF_zz_sel{or}=HF_zz;
```

```
            NQI_zz_sel{or}=NQI_zz;
            S_sel(or) = scalefactor;
            W_sel(or)=1; %Weight of the orientation
            or = or +1;
        end
    end
    epr_amp=epr_amp+tmp_epr;
end
%--------------------ENDOR Calculation-----------------------------------
parfor ii = 1:length(B_sel)
    tmp_endor_time = zeros(1,slots_iter_EN); % for time domaine simulation
    tmp_endor_tens =zeros(1,slots_iter_EN); % for tensor simulation
    res=0;

    %Set precalculated orientation dependent values
    geff = geff_sel(ii);
    B = B_sel(ii); %effective B field for given theta and phi
    veff = geff*ObsField*9.27401*10^-24/(6.62607*10^-34); % Resonance frequency for geff
        at ObsField in GHz
    HF_zz=HF_zz_sel{ii};
    NQI_zz=NQI_zz_sel{ii};
    S=S_sel(ii)*W_sel(ii);

    % Temperature Effect calculation
    if Temp_Eff==1
        E = ge*B*Sz  ; %Energy from electron zeeman
        for m=1:Ni_ENDOR
            E = E - gn*B*Iz + HF_zz(m) * Sz*Iz;
        end
        Boltz=expm(-E/(k_B*T)); % calculate Boltzmann factor
        rho0=Boltz/trace(Boltz); % calculate density matrix with Temp Effect
    else
        rho0 = -Sz; % calculate density matrix without Temp Effect
    end
    %Loop over individual nuclei
    for tt = 1:length(tau)
        for m=1:Ni_ENDOR
            %Calculate half ENDOR spectrum
            switch I
                case 1/2
                    res =  HF_zz(m)/2/10^6;
                case 1
                    res(1) = (HF_zz(m)/2+1.5*NQI_zz(m))/10^6;
                    res(2) = (HF_zz(m)/2-1.5*NQI_zz(m))/10^6;
                case 5/2
```

```
                res(1) = (HF_zz(m)/2)/10^6;
                res(2) = (HF_zz(m)/2-1.5*NQI_zz(m))/10^6;
                res(3) = (HF_zz(m)/2+1.5*NQI_zz(m))/10^6;
                res(4) = (HF_zz(m)/2-3*NQI_zz(m))/10^6;
                res(5) = (HF_zz(m)/2+3*NQI_zz(m))/10^6;
            end
            ebin = round((res - endormin)/endstep)+1;
            ebinmax = round((endormax - endormin)/endstep);
            for k = 1:length(ebin)      % take only resonances in desired spectral range

                if      0 < ebin(k)
                    if ebin(k) <= ebinmax
                        tmp_endor_tens(ebin(k)) = tmp_endor_tens(ebin(k)) + 1*S;
                    end
                end
            end
            for kk=-I:I
                v_off_S = kk*HF_zz(m);
                for a = 1:slots_iter_EN
                    v_RF = (start_EN+step_EN*(a-1));     %Increments x-Axis  (RF
                        increment)
                    v_off_I = (v_L - v_RF);              %Calculates nuclear offset for
                        each RF increment

                    %Calculate the Free evolution hamiltonian

                    Hfree = 2*pi*v_off_S*Sz + 2*pi*v_off_I*Iz + 2*pi*HF_zz(m)*(Sz*Iz) +
                        pi*NQI_zz(m)*(3*Iz*Iz-I*(I+1)*eye(size(Iz)));

                    %Select between nonideal and ideal pulses
                    if ideal_pulse==1
                        Hnonsel = omega_1e*Sx;
                    else
                        Hnonsel = Hfree + omega_1e*Sx;
                    end
                    HRF = Hfree + omega_1n*Iy;
                    %Calculate the propagators
                    U1 = expm(-1i*Hnonsel*t1);
                    U2 = expm(-1i*Hfree*t2);
                    U3 = expm(-1i*Hnonsel*t3);
                    U4 = expm(-1i*Hfree*t4);
                    U5 = expm(-1i*HRF*t5);
                    U6 = expm(-1i*Hfree*t6);
                    U7 = expm(-1i*Hnonsel*t7);
                    U8 = expm(-1i*Hfree*t8);
```

```
405
406                     %Evolve the densitymatrix
407                     rho = rho0;
408                     rho = U1*rho*U1';
409                     rho = U2*rho*U2';
410                     rho = U3*rho*U3';
411                     rho = U4*rho*U4';
412                     rho = U5*rho*U5';
413                     rho = U6*rho*U6';
414                     rho = U7*rho*U7';
415                     rho = U8*rho*U8';
416
417                     t9 = 1/((HF_zz(m))*Nint); %Calculate t9 as multiple of Couling
                            constant
418                     U9 = expm(-1i * Hfree * t9);
419                     value_Sy=0;
420
421                     for b=1:Nint
422                         rho = U9*rho*U9';
423                         value_Sy = value_Sy+real(trace(rho*Sy));
424                     end
425                     tmp_endor_time(a) = tmp_endor_time(a)+(value_Sy/Nint)*S;
426                 end
427             end
428         end
429         endor_amp_time=endor_amp_time+tmp_endor_time;
430         endor_amp_tens=endor_amp_tens+tmp_endor_tens;
431     end
432 end
433 calculationtime=toc;
434 %----------------------ENDOR Convolution-------------------------------------
435 %----------------------------------------------------------------------------
436 %TENSOR Spectrum
437 %Convolve with Gaussian
438 endintens_ten = zeros(1,slots_iter_EN);
439 endintens1_ten = ifft(endor_amp_tens(:));
440 for i = 1:slots_iter_EN
441     endintens_ten(i) = endintens1_ten(i)*exp(-Deltaend_tens*i^2/2);   % Lorentzian line
            shape
442 end
443 endintens_ten(1)=0.5*endintens_ten(1);
444 endintens_ten(:) = real(fft(endintens_ten));
445 %Flip and ADD
446 endintens_ten2 = fliplr(endintens_ten);
447 endintens_ten = endintens_ten + endintens_ten2;
```

```
endintens_ten = endintens_ten/max(endintens_ten);

%Time Domaine Spectrum
%Lorentian
if Lorentian == 1
    endintens1 = ifft(endor_amp_time(:));
    for i = 1:slots_iter_EN
        endintens(i) = endintens1(i)*exp(-Deltaend_L*i);   % Lorentzian line shape
    end
    endintens(1)=0.37*endintens(1);
    endamp_2d_L_conv(:) = real(fft(endintens));
end

%Gaussian
if Gaussian == 1
    endintens1 = ifft(endor_amp_time(:));
    for i = 1:slots_iter_EN
        endintens(i) = endintens1(i)*exp(-Deltaend_G*i^2/2);   % Gaussian line shape
    end
    endintens(1)=0.5*endintens(1);
    endamp_2d_G_conv(:) = -abs(fft(endintens));
end

%Normalize to Number of Orientations
endamp_2d_L_conv(:)=endamp_2d_L_conv(:)/or;
endamp_2d_G_conv(:)=endamp_2d_G_conv(:)/or;

if Lorentian==1
    endamp_fin=endamp_2d_L_conv(:)-endamp_2d_L_conv(1);
    endamp_fin=endamp_fin/max(endamp_fin);
end
if Gaussian==1
    endamp_fin=endamp_2d_G_conv(:)-endamp_2d_G_conv(1);
    endamp_fin=endamp_fin/max(endamp_fin);
end

%------------------Easyspin Calculation-----------------------------------------
tic
switch I
    case 1/2
        Nuc='1H';
    case 1
        Nuc='2H';
    case 5/2
        Nuc='17O';
```

```
end
Sys.g=diag(g)';
if exist('Q_ten','var')==1
    Sys=nucspinadd(Sys,Nuc,A_ten,A_frame,Q_ten,Q_frame);
else
    Sys=nucspinadd(Sys,Nuc,A_ten,A_frame);
end
Sys.lwEndor=0.1;
Exp.Sequence='MimsENDOR';
% Exp.tau=(t1+t2)*10^6;
Exp.tau=(t2)*10^6;
Exp.nPoints=slots_iter_EN;
Exp.mwFreq=FreqMeas/10^9;
Exp.Field=ObsField*1000;
Exp.ExciteWidth=1e6;
SW=abs(x_coords(1)*10^(-6));
Exp.Range=[larmorfrq(Nuc,Exp.Field)-SW larmorfrq(Nuc,Exp.Field)+SW];
Opt.nKnots=90;
Opt_p.nKnots=Opt.nKnots;
Opt_p.Method='perturb1';
Opt_t.nKnots=Opt.nKnots;
Opt_t.Method='matrix';
[x_saf,spec_saf]=saffron(Sys,Exp,Opt_p);
[x_sal_p,spec_sal_p]=salt(Sys,Exp,Opt_p);
% [x_sal_t,spec_sal_t]=salt(Sys,Exp,Opt_t);

spec_saf=spec_saf/max(spec_saf);
spec_sal_p=spec_sal_p/max(spec_sal_p);
% spec_sal_t=spec_sal_t/max(spec_sal_t);

bsfunc=(sin(2*pi*Exp.tau*10^-6*(x_sal_p-larmorfrq(Nuc,Exp.Field))*10^6).^2);
spec_sal_p_bsfunc=spec_sal_p.*bsfunc;
spec_sal_p_bsfunc=spec_sal_p_bsfunc/max(spec_sal_p_bsfunc);
calculationtime_ES=toc;

%-----------------------Plotting-----------------------------------------------
%-----------------------EPR Spectrum-------------------------------------------
if plot_EPR==1
    %Gauss Convolution
    eprintens1 = ifft(epr_amp);
    eprintens = zeros(1,Npts);
    for i = 1:Npts
        eprintens(i) = eprintens1(i)*exp(-DeltaEPR*i^2/2);   % Gaussian line shape
    end
    eprintens(1) = 0.5*eprintens(1);
```

```
    eprintens1 = fft(eprintens);
    eprintens1 = real(eprintens1/max(real(eprintens1)));
    %Calculation of Excitation Function
    SF=zeros(1,length(field));
    for i=1:length(field)
        DeltaB=field(i)-ObsField;
        SF(i) = (DeltaB^2 - pulsewidth^2)/(DeltaB^2 + pulsewidth^2);
        SF(i) = (1-SF(i))/2;
    end
    SF=SF/max(SF);
    %Plotting
    figure('Renderer','painters')
    hold on
    plot(field,eprintens1,'k','Linewidth',1.2)
    plot(field,SF,'r','Linewidth',1)
    legend({'EPR Spectrum','Excitation Function'});
end
%----------------------ENDOR Spectrum-----------------------------------------
fig=figure('Position',[200 200 1000 500],'Renderer','painters');
box on
hold on
plot(x_coords*10^(-6),endamp_fin)
plot(x_saf-larmorfrq(Nuc,Exp.Field),spec_saf)
plot(x_sal_p-larmorfrq(Nuc,Exp.Field),spec_sal_p_bsfunc)
if plot_ENDORtens ==1
    plot(x_sal_p-larmorfrq(Nuc,Exp.Field),spec_sal_p-1)
    plot(endor_freq_tens,endintens_ten-1)
    legend({'AK Mims', 'ES Mims','ES Tensor * BS','ES Tensor','MB Tensor'})
else
    legend({'AK Mims', 'ES Mims','ES Tensor * BS'})
end
ylim([-1.1 1.1])
xlim([endormin endormax])
formatSpec = A = [%0.1f;%0.1f;%0.1f], Q=[%0.1f;%0.1f;%0.1f], tau = %d, Ntheta = %d;
str = sprintf(formatSpec,A_ten(1),A_ten(2),A_ten(3),Q_ten(1),Q_ten(2),Q_ten(3),tau,Ntheta
    );
title(str)
formatSpec='Mims_tau_%d_I_%0.1f_A_%0.1f_%0.1f_%0.1f_Q_%0.1f_%0.1f_%0.1f_Ntheta_%d_tcalc_%
    ds';
str=sprintf(formatSpec,tau,I,A_ten(1),A_ten(2),A_ten(3),Q_ten(1),Q_ten(2),Q_ten(3),Ntheta
    ,round(calculationtime));
str_figname=[str,'.fig'];
str_filename=[str,'.mat'];
% savefig(fig,str_figname,'compact')
% save(str_filename)
```

```
580 fprintf('Calculation Time AK: %d min %0.2f sec\n', floor(calculationtime/60), round(rem(
        calculationtime,60),2));
581 fprintf('Calculation Time ES: %d min %0.2f sec\n', floor(calculationtime_ES/60), round(
        rem(calculationtime_ES,60),2));
582 fig=figure('Position',[200 200 700 500],'Renderer','painters');
583 box on
584 hold on
585 plot(x_coords*10^(-6),endamp_fin+1,'Linewidth',1.2)
586 plot(x_saf-larmorfrq(Nuc,Exp.Field),spec_saf,'Linewidth',1.2)
587 legend({'Time Domaine ENDOR', 'Easy Spin Mims'})
588 ylim([-0.1 2.1])
589 xlim([-3 3])
```

Acknowledgment

First and foremost, I would like to acknowledge and thank my PhD advisor and mentor, Prof. Dr. Marina Bennati. I began my scientific journey in her group as a bachelor's student and returned for my master's and eventually my PhD thesis. I remember vividly the enthusiasm, with which she explained the basics of EPR instrumentation to me in my first personal meeting with her. Her guidance throughout my time in the lab made this thesis possible and the freedom she gave, allowed me to explore the world of scientific research way beyond the boarders of my dissertation topic.

I would like to thank my thesis advisory committee members Prof. Dr. Christian Griesinger and Prof. Dr. Martin A. Suhm for fruitful and challenging discussions during my TAC meetings, which extended the boundaries of my doctoral project.

My sincere gratitude goes to Prof. Dr. JoAnne Stubbe, who welcomed me into her lab at MIT and taught me the wondrous world of ribonucleotide reductases. I firmly believe that her fascination for every new piece of data and her rigorousness in their interpretation made me a better scientist.

A special thank you goes to Dr. Igor Tkach, whose technical expertise and unbelievable patience helped solve the countless difficulties associated with high-end EPR spectroscopy.

Thank you to my former colleague Dr. Isabel Bejenke for the guidance during my master's thesis and the beginning of my PhD project. For endless scientific and more often also non-scientific discussions, but also for soup dumplings in New York, table tennis sessions, rhubarb liquor and making fun of me while rowing on a lake.

I would like to thank my office mate throughout bachelor, master and PhD, Marcel Levien. Thank you for great team work, be it organizing teaching and exams or the moving of an EPR spectrometer from one lab to another. Also thank you for climbing sessions, skat evenings, an unforgettable month in Thailand and much more.

I would like to acknowledge my other great colleagues Dr. Tomas Orlando, Dr. Markus Hiller, Dr. Andreas Meyer, Dr. Luming Yang, Annemarie Kehl and Maik Reinhard for the awesome working atmosphere, for enjoyable pen and paper games with gorgonzola pizza

and for two great seasons of MPI beach volleyball league.
Another special thanks goes to Brigitta Angerstein for her invaluable assistance in the lab and the great teamwork in all matters concerning helium as well as Monika Froemel for assistance with all sorts of administrative tasks, especially the procurement of a J1 student visa for the US. Our group would be quite lost without the two of you.
I would like to thank my student-coworkers Lisa Fries and Marvin Lenjer, whom I had the pleasure to supervise during their respective bachelor's and in Lisa's case also master's thesis. Your projects turned out way better than we initially expected and helped bring along my PhD project greatly. I hope I could convey some of my love for science to you and wish you all the best for your future careers.
A great thank you goes to the friends, who supported me during my PhD time and did not get mad when appointments had to be canceled because the spectrometer did not behave. Thank you Leo, Ferdinand, Calle, Stella, Darius, Roland, Marco, Chris, Freddy and many more.
Last, I want to thank my family. My brother Philipp, my parents Heike and Joachim. You have encouraged me to pursue a PhD and have supported me everyday since. Without you, this work would not have been possible. A final acknowledgement goes to my grandfather Ernst: you sparked my love for science, which brought me to where I am today. Thank you!

Publications

F. Hecker, L. Fries, M. Hiller, M. Chiesa, M. Bennati, "^{17}O hyperfine spectroscopy to detect water binding to biologically relevant radicals: a comparative study of nitroxide and tyrosyl radicals" *to be submitted*.

C. J. Schürmann, T. T. Teuteberg; A. C. Stückl; P. N. Ruth; F. Hecker, R. Herbst-Irmer; R. A. Mata and D. Stalke "Trapping X-ray Radiation Damage from Homolytic Se–C Bond Cleavage in BnSeSeBn Crystals (Bn=benzyl, $CH_2C_6H_5$)" *Angew. Chem.*, **2022**, e202203665.

A. Meyer, A. Kehl, C. Cui, F. A. K. Reichardt, F. Hecker, L.-M. Funk, K.-T. Pan, H. Urlaub, K. Tittmann, J. Stubbe, and M. Bennati "^{19}F Electron Nuclear Double Resonance reveals interaction between redox active tyrosines across the $\alpha\beta$ interface of *E. coli* ribonucleotide reductase", *J. Am. Chem. Soc.* **2022**, https://doi.org/10.1021/jacs.2c02906.

F. Hecker, J. Stubbe, M. Bennati, "Detection of Water Molecules on the Radical Transfer Pathway of Ribonucleotide Reductase by ^{17}O Electron-Nuclear Double Resonance Spectroscopy" *J. Am. Chem. Soc.* **2021**, *143* (19), 7237-7241.

A. Kehl, M. Hiller, F. Hecker, I. Tkach, S. Dechert, M. Bennati, A. Meyer "Resolution of chemical shift anisotropy in ^{19}F ENDOR spectroscopy at 263 GHz/9.4 T" *J. Magn. Res.*, **2021**, *333*, 107091.

I. Tkach, I. Bejenke, F. Hecker, A. Kehl, M. Kasanmascheff, I. Gromov, I. Prisecaru, P.

Höfer, M. Hiller, M. Bennati "^{1}H high field electron-nuclear double resonance spectroscopy at 263 GHz/9.4 T" *J. Magn. Res.*, **2019**, *303*, 17-27.

J. Altnöder, K. Krüger, D. Borodin, L. Reuter, D. Rohleder, F. Hecker, R. A. Schulz, X. Nguyen, H. Preiß, M. Eckhoff, M. Levien, M. Suhm "The Guinness Molecules for the Carbohydrate Formula" *Chem. Rec.*, **2014**, *6*, 1116-1133.